# Modeling of Fluid-Structure Interactions with the Least-Squares FEM

Von der Fakultät für Ingenieurwissenschaften,
Abteilung Bauwissenschaften
der Universität Duisburg-Essen
zur Erlangung des akademischen Grades
Doktor-Ingenieur
genehmigte Dissertation

von

Solveigh Averweg, M.Sc.

| | |
|---|---|
| Hauptberichter: | Prof. Dr.-Ing. habil. Jörg Schröder |
| Korreferenten: | Univ.-Prof. Marek Behr, Ph.D. |

| | |
|---|---|
| Tag der Einreichung: | 02. Juni 2022 |
| Tag der mündlichen Prüfung: | 12. Mai 2023 |

Fakultät für Ingenieurwissenschaften,
Abteilung Bauwissenschaften
der Universität Duisburg-Essen
Institut für Mechanik
Prof. Dr.-Ing. habil. J. Schröder

**Berichte des Instituts für Mechanik, Universität Duisburg-Essen**
Nr. 28

**Herausgeber:**
Prof. Dr.-Ing. habil. J. Schröder

**Organisation und Verwaltung:**
Prof. Dr.-Ing. habil. J. Schröder
Institut für Mechanik
Fakultät für Ingenieurwissenschaften
Abteilung Bauwissenschaften
Universität Duisburg-Essen
Universitätsstraße 15
45141 Essen
Tel.: 0201 / 183 - 2682
Fax.: 0201 / 183 - 2680

Institut für Mechanik
Abteilung Bauwissenschaften
Fakultät für Ingenieurwissenschaften
Universität Duisburg-Essen
Universitätsstraße 15
45141 Essen

ISBN-13 978-3-9821811-4-1

# Vorwort

Die vorliegende Arbeit entstand während meiner Tätigkeit als wissenschaftliche Mitarbeiterin am Institut für Mechanik (Abteilung Bauwissenschaften, Fakultät für Ingenieurwissenschaften) an der Universität Duisburg-Essen im Rahmen des durch die Deutsche Forschungsgemeinschaft (DFG) finanzierten Projektes SCHW 1355/3-1, 1355/3-2 und SCHR 570/31-1, 570/31-2. An dieser Stelle möchte ich der DFG für die finanzielle Unterstützung danken und all jenen meinen persönlichen Dank aussprechen, die zum Gelingen dieser Arbeit beigetragen haben.
An erster Stelle gilt mein Dank meinem geschätzten Doktorvater Prof. Jörg Schröder, der mir die Möglichkeit gab unter seiner Leitung zu promovieren. Insbesondere möchte ich mich bedanken für die gute Förderung während der Zeit am Institut für Mechanik und das entgegengebrachte Vertrauen in der gesamten Phase meiner Promotion. Dieses hat mir vorallem während und nach der Phase der Pandemie die Möglichkeit gegeben selbstständig arbeiten zu können und die Finalisierung meiner Arbeit erleichtert. Mein weiterer Dank gilt Prof. Marek Behr für die Übernahme des Korreferats und das entgegengebrachte Interesse an meiner Dissertation. Über die ausführliche Begutachtung und die fachlichen Hinweise mit Schwerpunkt auf das Thema der Fluid-Struktur-Interaktion habe ich mich sehr gefreut. Ebenso möchte ich mich recht herzlich für die Mitwirkung in der Prüfungskommission bei Frau Prof. Dr.-Ing. habil. Natalie Stranghöner, Frau Prof. Dr.-Ing. habil. Carolin Birk und Herrn Prof. Dr.-Ing. habil. André Niemann bedanken. Ein besonderer Dank gilt Alexander Schwarz der mich bereits während meines Studiums im Rahmen der Bachelor- und Masterarbeit betreut hat, und ohne den ich diese Promotion vielleicht nie begonnen hätte. Er hatte immer ein offenes Ohr und war jederzeit bereit sein breites Fachwissen und seine Lebenserfahrung zu teilen. In diesem Zuge danke ich auch Carina Schwarz herzlichst für ihre Unterstützung und ihre enorme Hilfsbereitschaft. Sie stand ebenfalls von Beginn an immer mit Rat und Tat zur Seite.
Ein herzliches Dankeschön möchte ich meinen ehemaligen Kolleginnen und Kollegen des Instituts für Mechanik für die tolle Zusammenarbeit und die positive Atmosphäre aussprechen. Ich möchte mich für die immer vorhandene Unterstützung sowie den fachlichen als auch persönlichen Austausch bei meinen Kollegen/-innen Joachim Bluhm, Dominik Brands, Simon Fausten, Philipp Hartwig, Sonja Hellebrand, Markus von Hoegen, Simon Kugai, Matthias Labusch, Veronica Lemke, Sascha Maassen, Simon Maike, Rainer Niekamp, Yasemin Özmen, Mangesh Pise, Markus Prangs, Maximilian Reichel, Sabine Ressel, Mohammad Sarhil, Maximilian Scheunemann, Lisa Scheunemann, Serdar Serdas, Steffen Specht, Karl Steeger, Julia Sunten und Nils Viebahn bedanken.
Abschließend gilt mein besonderer Dank meinen Freunden und vorallem meiner Familie für ihre fortwährende, bedingungslose Unterstützung.

Essen, Oktober 2023 Solveigh Averweg

**DOI:** 10.17185/duepublico/79170
**URN:** urn:nbn:de:hbz:465-20231024-083019-4

# Abstract

For years, the development and advancement of numerical methods for the calculation of physical phenomena has been the objective of numerous research. With the available computational capacity nowadays, the simulation of more complex problems such as fluid-structure interaction (FSI) is becoming increasingly demanded. FSI applications require not only the stable and accurate solution of the individual domains, but also the consideration of the interaction at the interface. Here, the least-squares finite element method (LSFEM) offers a possibility of monolithic coupling with inherent fulfillment of the interface conditions. The present work aims to investigate different approaches to solve FSI problems using the LSFEM. For this purpose, different formulations for the calculation of fluid flows based on the incompressible Navier-Stokes equations and for elastic solid deformations based on linear and hyperelastic material behavior are considered. A main focus is on the time discretization of these approaches including the application and analysis of high-order methods and adaptive time-stepping based on embedded Runge-Kutta methods. Another important aspect of investigation is the coupling of the presented least-squares formulations to solve FSI problems with large deformations, taking into account the fluid in an Arbitrary-Lagrangian-Eulerian (ALE) description, the hyperelastic solid formulation, and the deformation of the background mesh. Furthermore, different formulations for the calculation of flows of non-Newtonian fluids are investigated, which are, for example, suitable for the simulation of blood flows.

# Zusammenfassung

Die Entwicklung und Optimierung numerischer Methoden für die Berechnung physikalischer Phänomene ist seit Jahren Gegenstand zahlreicher Forschungsarbeiten. Mit der heute zur Verfügung stehenden Rechenkapazität wird die Simulation von immer komplexeren Problemen wie der Fluid-Struktur-Interaktion (FSI) zunehmend wichtiger. FSI Anwendungen erfordern nicht nur die stabile und präzise Lösung der einzelnen Teilgebiete, sondern auch die Berücksichtigung der Wechselwirkung an der Schnittstelle. Hier bietet die Least-Squares Finite-Elemente-Methode (LSFEM) eine Möglichkeit der monolithischen Kopplung mit inhärenter Erfüllung der Übergangsbedingungen. Die vorliegende Arbeit soll dazu beitragen, verschiedene Ansätze zur Lösung von FSI-Problemen mithilfe der LSFEM zu untersuchen. Dazu werden verschiedene Formulierungen für die Berechnung von Fluidströmungen auf Basis der inkompressiblen Navier-Stokes-Gleichungen und für elastische Festkörperverformungen auf Basis von linearem und hyperelastischem Materialverhalten betrachtet. Ein Hauptaugenmerk liegt dabei auf der zeitlichen Diskretisierung dieser Ansätze, einschlielich der Anwendung und Analyse von Methoden höherer Ordnung und adaptiver Zeitschrittsteuerung mittels eingebetteter Runge-Kutta-Verfahren. Ein weiterer wichtiger Untersuchungsaspekt ist die Kopplung der vorgestellten Least-Squares Formulierungen zur Lösung von FSI-Problemen mit großen Verformungen unter Berücksichtigung des Fluids in einer Arbitrary-Lagrangian-Eulerian (ALE) Beschreibung, der Solidformulierung für Hyperelastizität und des Ansatzes für die Verformung des Hintergrundnetzes. Darüber hinaus werden verschiedene Formulierungen für die Berechnung von Strömungen nicht-Newtonscher Flüssigkeiten untersucht, die sich z.B. für die Modellierung von Blutströmungen eignen.

# Contents

1 Introduction 1

1.1 Motivation . . . 1

1.2 State of the art . . . 2

1.2.1 LSFEM for fluid and solid dynamics . . . 2

1.2.2 Finite element methods for FSI problems . . . 5

1.3 Outline . . . 9

2 Basic aspects of continuum mechanics 11

2.1 Kinematics . . . 11

2.1.1 Configuration and motion . . . 12

2.1.2 Eulerian and Lagrangian description . . . 13

2.1.3 Material time derivative . . . 13

2.1.4 Deformation gradient and strain measures . . . 15

2.2 Concept of stresses . . . 17

2.2.1 Surface traction . . . 17

2.2.2 Stress tensors . . . 18

2.2.3 Stress deviator and hydrostatic pressure . . . 18

2.3 Balance principles . . . 19

2.3.1 Conservation of mass . . . 19

2.3.2 Balance of linear momentum . . . 20

2.3.3 Balance of angular momentum . . . 21

2.4 Constitutive equations for elastic structures . . . 22

2.4.1 Description for hyperelastic material behavior . . . 23

2.4.2 Description for linear elastic material behavior . . . 24

2.5 Constitutive equations for fluid dynamics . . . 24

2.5.1 Flow characteristics . . . 24

2.5.2 Fluid properties . . . 25

2.5.3 Description for Newtonian fluids . . . 27

2.5.4 Description for non-Newtonian fluids . . . 28

3 Spatial discretization using least-squares finite elements 30

3.1 The finite element discretization . . . 30

3.2 Interpolation functions . . . 33

3.2.1 Function spaces and norms . . . 33

3.2.2 Lagrange interpolating polynomials for triangles . . . . . . . . . . . 34
3.2.3 Raviart-Thomas interpolation functions for triangles . . . . . . . . 37
3.3 The least-squares finite element method . . . . . . . . . . . . . . . . . . . . 39
3.3.1 Advantages and disadvantages . . . . . . . . . . . . . . . . . . . . . 39
3.3.2 Construction aspects of the LSFEM for nonlinear systems . . . . . 41
3.3.3 Boundary and initial conditions . . . . . . . . . . . . . . . . . . . . . 42
3.3.4 Interpolation spaces for mixed least-squares formulations . . . . . . 43
3.4 Assimilation of data to numerical simulations . . . . . . . . . . . . . . . . . 43
3.4.1 Data preparation using the Kriging interpolation method . . . . . . 44
3.4.2 Data assimilation using the LSFEM . . . . . . . . . . . . . . . . . . 45

**4 LSFEM for Newtonian fluids 47**
4.1 Stress-velocity-pressure formulation for fluid dynamics . . . . . . . . . . . . 47
4.2 Stress-velocity formulation for fluid dynamics . . . . . . . . . . . . . . . . . 49
4.2.1 Discretization and assembly aspects . . . . . . . . . . . . . . . . . . 50

**5 LSFEM for non-Newtonian fluids 51**
5.1 SV formulation for incompressible non-Newtonian fluids in 2D . . . . . . . 52
5.2 Numerical examples: Steady flow of non-Newtonian fluids in 2D . . . . . . 52
5.2.1 Flow in a square domain with analytical solution . . . . . . . . . . 53
5.2.2 Lid driven cavity flow of non-Newtonian fluid . . . . . . . . . . . . 55
5.2.3 Flow over a backward facing step with parameter study . . . . . . . 57
5.2.4 Channel flow with smooth contraction 4:1 and data assimilation . . 62
5.3 SVP formulation for incompressible non-Newtonian fluids in 3D . . . . . . 65
5.4 Numerical examples: Steady flow of non-Newtonian fluids in 3D . . . . . . 66
5.4.1 Flow in a cubical domain with analytical solution . . . . . . . . . . 66
5.4.2 Steady blood flow in a carotid artery bifurcation . . . . . . . . . . 67
5.4.3 Carotid bifurcation model - assimilation of experimental data . . . 72
5.4.4 Carotid bifurcation model - assimilation of numerical data . . . . . 75

**6 LSFEM for elastic solid dynamics 77**
6.1 Stress-velocity formulation for linear elastic materials . . . . . . . . . . . . 77
6.2 Stress-velocity formulation for hyperelastic materials . . . . . . . . . . . . 79

**7 Time discretization schemes for fluid and solid dynamics 82**
7.1 Brief introduction to the basic concept . . . . . . . . . . . . . . . . . . . . 83
7.2 Overview on some time integration methods for first-order ODEs . . . . . . 85

7.2.1 Implicit Euler . . . . . . . . . . . . . . . . . . . . . . . . . . . . . 85
7.2.2 Crank-Nicolson method . . . . . . . . . . . . . . . . . . . . . . . . 85
7.2.3 The family of Runge-Kutta methods . . . . . . . . . . . . . . . . . 85
7.2.4 Simple example: Advection equation in 1D . . . . . . . . . . . . . . 87
7.3 Time integration methods for least-squares SV formulations . . . . . . . . 93
7.3.1 Implicit Euler method for least-squares SV formulations . . . . . . 94
7.3.2 Newmark method for least-squares SV formulations . . . . . . . . . 94
7.3.3 Houbolt method for least-squares SV formulations . . . . . . . . . . 95
7.3.4 Crank-Nicolson method for least-squares SV formulations . . . . . . 95
7.3.5 SDIRK methods for least-squares SV formulations . . . . . . . . . . 97
7.4 Numerical examples: Unsteady flow of Newtonian fluids . . . . . . . . . . 99
7.4.1 Unsteady Taylor-Green vortex . . . . . . . . . . . . . . . . . . . . . 99
7.4.2 Unsteady flow around a cylinder . . . . . . . . . . . . . . . . . . . . 103
7.5 Numerical example: Dynamic structure problem . . . . . . . . . . . . . . . 108
7.6 Adaptive time stepping methods . . . . . . . . . . . . . . . . . . . . . . . 110
7.6.1 Error estimation based on embedded Runge-Kutta schemes . . . . . 111
7.6.2 Automatic step-size control . . . . . . . . . . . . . . . . . . . . . . . 112
7.7 Numerical examples: Time adaptivity for fluid and solid dynamics . . . . . 114
7.7.1 Flow around a cylinder with time dependent inflow . . . . . . . . . 115
7.7.2 Vibration of a linear elastic cantilever beam . . . . . . . . . . . . . 120

**8 LSFEM for dynamic fluid-structure interaction problems 129**
8.1 The coupled LS stress-velocity formulations for dynamic FSI problems . . . 130
8.1.1 Monolithic coupling conditions for SV formulations . . . . . . . . . 131
8.2 Numerical examples: Dynamic FSI problems with small deformations . . . 132
8.2.1 Steady flow around a cylinder with flag . . . . . . . . . . . . . . . . 132
8.2.2 Channel with flow over a wall . . . . . . . . . . . . . . . . . . . . . 136
8.3 The fluid formulation with a moving domain . . . . . . . . . . . . . . . . . 138
8.3.1 The Arbitrary-Lagrangian-Eulerian framework . . . . . . . . . . . . 138
8.3.2 Stress-velocity fluid formulation in ALE description . . . . . . . . . 140
8.3.3 Mesh motion techniques . . . . . . . . . . . . . . . . . . . . . . . . 141
8.3.4 Mesh motion based on linear elasticity with local stiffening . . . . . 142
8.4 Numerical examples: Mesh motion and fluid in ALE description . . . . . . 144
8.4.1 Dynamic flag with large deformations in moving mesh domain . . . 144
8.4.2 Channel flow with moving background mesh . . . . . . . . . . . . . 151

8.5 Numerical examples: Dynamic FSI problems with large deformations . . . 153
    8.5.1 Channel flow with contracting linear elastic walls . . . . . . . . . . 154
    8.5.2 Unsteady flow around a cylinder with flag . . . . . . . . . . . . . . . 157

**9 Conclusion and Outlook 167**

**A Appendix: Spatial discretization 171**
A.1 Lagrange shape functions . . . . . . . . . . . . . . . . . . . . . . . . . . . . . 171

**B Appendix: LSFEM for non-Newtonian fluids 172**
B.1 Algorithmic procedure for implementation of LS SV formulation to solve steady flow of non-Newtonian fluids in 2D including data assimilation . . . 172
B.2 Algorithmic procedure for implementation of LS SVP formulation to solve steady flow of non-Newtonian fluids in 3D including data assimilation . . . 173
B.3 Body force for flow of non-Newtonian fluid in cubical domain . . . . . . . . 174

**C Appendix: Time discretization 175**
C.1 Butcher tableaus for applied ESDIRK schemes . . . . . . . . . . . . . . . . . 175
C.2 Butcher tableaus for applied embedded ESDIRK and SDIRK schemes . . . 175

**D Appendix: LSFEM for FSI 178**
D.1 Algorithmic procedure for implementation of LS SV formulations to solve dynamic FSI problems . . . . . . . . . . . . . . . . . . . . . . . . . . . . . 178

**List of Figures/Tables 179**

**References 189**

# 1 Introduction

The aim of this work is the development and investigation of different approaches based on the least-squares finite element method (LSFEM) for the solution of fluid and structural problems with the objective of coupling these approaches to solve systems involving the interaction between a fluid flow and a structural deformation. An essential point of study therein is the discretization of space and time of the considered least-squares formulations, including time adaptivity. Furthermore, different formulations suitable for the simulation of non-Newtonian fluids are investigated in the context of this thesis. This chapter provides a brief background motivation and an introduction regarding the subjects that will be discussed. Then, a literature review of relevant topics in the context of this thesis follows. The scope and outline of the thesis are presented at the end of this chapter.

## 1.1 Motivation

In the last decades the numerical treatment of multi-physics problems has attracted increasing interest due to the large number of application fields and notable progress that has been made regarding computing power, making reliable simulations feasible. Advanced mathematical models provide an accurate representation of underlying physical phenomena, enabling precise and efficient analysis of highly complex engineering problems, which were, previously, strongly dependent on more expensive and effortful experimental evaluations. The mechanical coupling of different physical fields is present in a wide range of mechanisms in reality. For instance, **fluid-structure interaction** (FSI) plays an important role not only in traditional engineering, such as mechanical and civil engineering, but also in a wide variety of fields ranging from aeronautics and aerospace to biomechanics. Improved computations of, e.g., vibrating lightweight constructions induced by wind effects enhance the prediction of failures, which may actually prevent catastrophes like the collapsing of bridges or light roof structures, for instance. Another interesting example for the application of FSI can be found, for instance, in biomechanical engineering, where blood flow in deformable vessels in the human arterial system can be simulated. Such simulations can help to improve the quality of artificial blood vessels and predict the rupture of aneurysms during certain medical treatments or surgeries.

The term FSI implies a two-way interaction of a fluid flow and a moving and/or deforming solid. In this process, the fluid exerts surface forces on the solid body caused by its flow motion, which leads to deformations or displacements. In turn, the structure movement leads to a change in the fluid domain, which affects the flow. Thus, there is a mutual interaction between a flowing medium and a solid structure, which are coupled at their common interface. A crucial aspect in the numerical solution of FSI problems is the treatment of the coupling conditions at the interface. In the context of this work, the focus is on the application of the **least-squares finite element method** (LSFEM), which provides, in combination with suitable approximation spaces, a direct possibility to satisfy the coupling conditions without additional numerical treatment.

Despite the technological progress in recent years, the solution of such multi-physics problems remains a challenging task. To reduce the computational effort or to facilitate implementations, it is common to use models based on simplifications, e.g. with respect to the material behavior. A frequent simplification is, for example, the assumption of Newtonian flow behavior in the simulation of blood flows. However, this assumption can only be used in a very limited range without loss of accuracy. In many applications, blood cannot be simplified as a Newtonian fluid. In fact, for a correct description of the blood rheology it is very important to consider the shear thinning behavior of blood by using **non-Newtonian fluid** models. These enable a correct and accurate calculation of relevant quantities such as viscosity and wall shear stresses, which is a crucial point, for example, in evaluating the occurrence of thrombosis and the development of aneurysms. The present thesis involves the study of various aspects in the solution of non-Newtonian fluid flows using the LSFEM in two and three dimensions.

A possibility to increase the accuracy of the calculation of e.g. the mentioned wall shear stresses is the **assimilation of data** into numerical simulations. More precisely, e.g. patient-specific velocity measurements can be performed and used to reduce possible model inaccuracies and to obtain results which are closer to reality. The least-squares finite element method used in this work offers the advantage that the assimilation of data is straightforward to implement and can be executed without any significant additional computational effort.

A general disadvantage of the LSFEM is that the system of equations to be solved can become very large due to many degrees of freedom and consequently the computational effort is often high compared to other finite element methods based on different variational approaches. Therefore, especially when considering complex dynamic systems as in the case of FSI calculations, it is important that the formulations are highly accurate and efficient at the same time. One of the most important aspects in dynamic systems, involving long-term computations, is the **time discretization**. There are numerous different approaches to numerical integration in time-dependent problems, often distinguished in their key properties such as stability and order of accuracy. In the course of this work, different time integration methods in combination with the LSFEM are investigated for the solution of fluid, structural and FSI problems. The focus is on accuracy and efficiency of the chosen approaches. Apart from methods with constant time step sizes, also algorithms with adaptive time step control are considered for improving efficiency.

## 1.2 State of the art

This section aims to give a general overview of existing methods related to the thematics considered in this thesis. The focus is on the application of the least-squares finite element method for the solution of time-dependent fluid, structure and FSI problems. In this context, the current state of the LSFEM in the different areas is discussed. A more detailed overview of the background and the general ideas of the LSFEM can be found in the textbooks and literature reviews by, e.g., Jiang [219], Bochev and Gunzburger [53] and Kayser-Herold and Matthies [229].

### 1.2.1 LSFEM for fluid and solid dynamics

The least-squares finite element method, which was subject to intense research starting already in the mid-1970s, represents an alternative variational approach to the well-known (mixed) Galerkin method in the field of finite element analysis. Initial publications on the use of the least-squares method in the field of FEM were, for example, by

Lynn and Arya [264]. From a mathematical point of view, several investigations regarding least-squares approaches also took place during this period, see, for example, Eason [136], Jespersen [216], and Fix and Gunzburger [150], Fix et al. [151]. A major drawback of this method was that it required high-order approximation functions for a good approximation quality, see e.g. Pontaza [309; 310], Kayser-Herold and Matthies [229] and Proot and Gerritsma [315]. The associated requirement in increased computational power led to infrequent application of the LSFEM. The interest in the method intensified when the available computational capacity increased significantly. Up to now, approaches based on the LSFEM exist in a wide variety of fields. A large part of application fields deals with the solution of flow problems, but also in the field of solid mechanics as well as FSI, there exist formulations based on the LSFEM. A brief summary of these is given in the following.

**Least-squares FEM for Newtonian fluids**

As mentioned before, a major effort in the development of the least-squares FEM lies in the field of fluid mechanics. In this context, there exists a large collection of works dealing with the solution of the Navier-Stokes and the Stokes equations, often based on the construction of first-order least-squares formulations. Several different least-squares formulations for both equations exist based on varying choices of the field variables.

Fundamentals in the field of LSFEM for solving flows with small Reynolds numbers are presented, for example, in the publications by Chang [96] and Jiang and Chang [220]. The latter introduces probably the best known and most widely used first-order formulation based on velocities, pressure, and vorticity. Further studies with this combination of unknown quantities include e.g. Jiang [217; 219], Bochev [46; 47], Bochev and Gunzburger [50; 51], Cai et al. [81] and Bochev et al. [55]. The main emphasis of these works is directed towards the study of these formulations from a mathematical point of view. Other publications on this topic, whose focus is rather on the application, are Tang and Tsang [381], Jiang et al. [221], Tang et al. [382; 383], Jiang [219] and Pontaza [311].

Apart from the formulations in which the vorticity is introduced in addition to the velocities and the pressure, other approaches exist based on adding a stress tensor as further unknown quantity. The number of publications on this least-squares formulation, of e.g. Bell and Surana [35; 36], Winterscheidt and Surana [421], Bochev and Gunzburger [52; 53], Ding and Tsang [128], Lee [258] and Nisters [294], indicates the popularity of this type as well. The addition of the stresses can lead, depending on the approximation, to a quite high number of degrees of freedom. The success of this formulation may be explained by the fact that the stress is a relevant quantity in many applications and its direct approximation allows a high computational accuracy. A slight reduction in the number of degrees of freedom can be achieved by eliminating the pressure by using the stress-pressure relation resulting from the constitutive law. Publications involving a velocity-stress formulation are, for instance, Cai et al. [86], Nisters and Schwarz [295], Schwarz et al. [352; 353] and Averweg et al. [9].

Another way to reformulate the Navier-Stokes equations is to include the velocity flux definition as in Cai et al. [82] and Bochev et al. [56; 57] or the velocity gradient as in Cai et al. [82]. Further variations consider for instance formulations in terms of stress and stream functions, cf. Bolton and Thatcher [62] and Bolton [60], or a the pressure gradient cf. Heys et al. [194], to mention a few. This collection provides only a brief overview of the least-squares FEM with respect to the construction based on different first-order formulations. Several other papers deal for example with the advantages and disadvantages of the method, i.e. low accuracy and mass loss or the application of adaptivity. An overview of these is given in the subchapter on this topic in Section 3.3.1. In most of the early investigations, the focus is on the solution of steady-state problems. But especially in the later years also transient problems are considered, using different time discretization methods for the integration. An overview of available numerical research studies on the solution of unsteady flow problems using LSFEM, e.g., by space-time methods and also sequential spatial and temporal discretizations, is included in Chapter 7 on time integration methods.

### Least-squares FEM for non-Newtonian fluids

The aforementioned studies deal with the solution of both the Stokes and Navier-Stokes equations for Newtonian fluids, which are characterized by a constant viscosity assumption. For many industrial and scientific applications this simplification is not necessarily valid, since many fluids are characterized by a viscosity that is not constant at a fixed pressure and temperature. As discussed in more detail in Section 2.5, non-Newtonian fluids can be roughly divided into viscoelastic fluids, time-dependent fluids, and generalized Newtonian fluids. In the last decades, many approaches based on different material models have been developed to numerically represent the various properties. At this point, an overview of existing research on non-Newtonian fluids in the context of LSFEM is presented.

A common fluid model which includes a partly elastic behavior, which is thus suitable for the modeling of viscoelastic fluids is, e.g., the Giesekus model, Giesekus [168]. Implementations of this model in the context of the LSFEM can be found in Nayak and Carey [288], Surana et al. [378], and Chen et al. [98], for instance. Other common models to simulate viscoelastic fluid behavior are the Phan-Thien-Tanner model, cf. Phan-Thien and Tanner [307], and a simplification thereof, the Oldroyd model, cf. Oldroyd [299]. These were investigated in Cai and Westphal [80], Lee [256] and Zhou and Hou [429], for example, focusing on convergence behavior, adaptive meshing, and residual weighting. A further modification represents the Maxwell model as studied e.g. in Bose and Carey [63] and Gerritsma [164].

Generalized Newtonian fluids, for which the shear stress is described as a function of the shear rate at the considered time and temperature, can be shear-thinning, shear-thickening, or plastic. A typical model to simulate primarily shear-thinning material behavior is the power-law equation, cf. Ostwald [301], as investigated in combination with the LSFEM by, e.g., Bell and Surana [36], Edgar and Surana [137], Dalimunthe and Surana [115], Vallala et al. [402], Surana et al. [377] and Waseem [411]. Some publications additionally examine the Carreau model, Carreau et al. [90], which can also be found in Chen et al. [98], Nickaeen [292] and Lee [257], for example. An extension thereof, the Carreau-Yasuda model, Yasuda et al. [427], has been investigated in the context of the LSFEM in Feng and Surana [147], Lee [259], Kim and Reddy [234; 235; 236; 237], Kim [233] and Averweg et al. [12].

**Least-squares FEM for elastic solids**

Due to several positive properties of the LSFEM, which are discussed in more detail in Chapter 3.3.1, a variety of mixed least-squares approaches has also been developed in the field of solid mechanics in the last decades, although less than for fluid dynamics. Initial formulations for linear elasticity derived from the approaches for the Stokes equations can be found, for example, in Cai et al. [81; 82]. Subsequently, several studies on first-order LS formulations based on displacements and displacement gradient were published, cf. Cai et al. [83; 84; 85] and Kim et al. [238], for instance. In further work dealing with the solution of linear elastic problems, the displacements and stresses were used as unknown field quantities, as in e.g. Cai and Starke [78; 79], Cai et al. [87], Schwarz [345], Schwarz et al. [349; 351] and Igelbüscher et al. [212]. Topics in these papers include among others the introduction of vector-valued interpolation functions of Raviart-Thomas type, see Raviart and Thomas [324], in $H(\text{div}, \Omega)$ for the stress approximation, and the use of the LS functional as an error estimator for adaptive mesh refinement. Additionally, in Bochev and Choi [48; 49] and De Sterck et al. [117; 118] studies can be found on the solution of partial differential equations of hyperbolic style using the LSFEM.

In the field of nonlinear solid mechanics, first investigations considering the constitutive law of St.Venant-Kirchhoff can be found in e.g. Manteuffel et al. [270]. Further publications using a Neo-Hookean type material law are Schwarz [345], Schwarz et al. [350; 354], Schröder et al. [341], Steeger [371] and Igelbüscher [211], for instance. Whereby in the work Schröder et al. [341] small and finite strain deformations are considered for isotropic and anisotropic material behavior. Aforementioned studies are conducted focussing on several application and performance aspects of the presented LS formulations from an engineering point of view. Research on the LSFEM for nonlinear material behavior with a mathematical focus can be found in Starke et al. [370], Müller et al. [284], Müller [282] and Müller and Starke [283], for instance.

### 1.2.2 Finite element methods for FSI problems

In FSI problems, different domains are connected, with the respective physical laws describing fluid flow and structural displacement valid in the individual domain. To compute these combined problems, in addition to the boundary and initial conditions, new conditions are imposed on the interface to ensure that equilibrium is satisfied. Hence, FSI problems can be practically divided into three subproblems, i.e. one for describing the fluid flow, one in which the solid deformations are calculated, and the third subproblem in which the equilibrium at the common interface is ensured. Due to the extremely broad spectrum of possible applications a wide range of research work on FSI problems has been carried out in the last decades. For a general overview on FSI methods of early work from the last century, one can refer to Cebral [94], Wall [408] and Dowell and Hall [133], for example. The authors list several papers related to FSI approaches, classified for example according to the complexity of the equations for the fluid and the structural domain. Further publications from this time with a classification into different application areas are given in, e.g., Steindorf [374] and Sieber [362]. For basic information on various aspects related to numerical methods for FSI problems, cf. textbooks Richter [327], Bazilevs et al. [27], Sigrist [364], and Souli and Benson [367], for instance.

A further subdivision of the different approaches to the computation of FSI problems can be performed based on the treatment of the coupling. Considering coupled problems a distinction can be made between partitioned and monolithic coupling procedures, cf. Zienkiewicz and Chan [430], Felippa and Park [143] and Park and Felippa [302]. In the former, the FSI problem is decoupled in two subproblems and separate equation systems for the fluid and solid domain are solved in turn, see e.g. Felippa et al. [144; 145], and Piperno et al. [308]. For example, the fluid solution is calculated first, then the resulting stresses are applied as boundary conditions for solving the solid equations. If these steps are performed once per time step this is also referred to as loose or weak coupling, and can lead to the occurrence of instabilities, see e.g. Leyland et al. [262], Le Tallec and Mouro [255], Rugonyi and Bathe [332]. The stability can be improved by iterating the process of solving the fluid and solid field equations in each time step, cf. Steindorf [374]. This is often termed implicit or strongly partitioned coupling. Main reasons for applying partitioned solution algorithms, are that existing codes for the fluid and solid domain can be used and that both domains can easily be discretized separately in space and/or time. With respect to spatial discretization, this allows, among other things, the coupling of different methods such as finite volume and finite element codes or the use of different mesh refinements. In the case of dynamic problems, different time integration algorithms or time step sizes may be chosen for the two domains. A substantial amount of research and development has been carried out in this area. Publications on partitioned coupling from the beginning of the 20th century are, for example, Matthies et al. [274], Matthies and Steindorf [275], Wall et al. [409], Förster et al. [153], Dettmer and Perić [125], and van Brummelen et al. [403]. Aspects of investigation in these articles are, for instance, the stability of strongly and weakly coupled partitioned schemes, multigrid methods, and the treatment of free surface flows. More recent studies are addressing, additionally to stability aspects, the solution of blood flows through arteries or the comparison of different partitioned coupling methods and their validation against experimental data, cf. Fernández et al. [148], Landajuela et al. [253], Serino et al. [355] and Schussnig et al. [344]. Another aspect of recent investigations is the application of NURBS-based coupling with a common spline interface of fluid and solid domain, see Hosters [199], Hosters et al. [200], Make [267] and Make et al. [268], for instance, which enables individual refinement of both domain, and a simplified transfer of quantities at the interface.

Besides the mentioned advantages, partitioned coupling approaches for FSI have some shortcomings, too. In case of large deformations in the solid domain, a large number of iterations per time step may be needed to obtain a converged solution, which can lead to high computational costs. Therefore, the staggered iterative solution procedure is most effectively used in case of a weak interaction between the fluid and the structure, and for more complex problems a monolithic approach may be superior, see for instance Rugonyi and Bathe [332], Michler et al. [280], Kayser-Herold [227] and Sheldon et al. [360]. To solve problems with strong interaction, as for example in the case of large structural displacements, the monolithic solution approach can be recommendable, where one global coefficient matrix for both domains and the coupling conditions is solved at once, cf. Heil et al. [181], Küttler et al. [247] and Langer and Yang [254], for instance. Further comparison between different partitioned and monolithic solution procedures can be found, among others, in

Dettmer and Perić [125; 126], Tezduyar et al. [389], Degroote et al. [121], Degroote [120].

In the area of solving FSI problems with monolithic approaches, there have also been immense research efforts and advances in recent years, and investigations have been carried out with a variety of different key aspects. One important point regarding complex numerical calculations is the performance and efficiency. Various recent studies address issues such as parallelization, multigrid methods and preconditioning, cf. Wu and Cai [425], Richter [328], Hessenthaler [183], Hessenthaler et al. [187], and Gee et al. [163]. Due to high demands on the accuracy of numerical solutions, high-order spatial discretizations are an ongoing research interest. In the context of fluid-structure interaction, some work has been devoted to this topic in the past years. For example, Persson et al. [306], Pena and Prud'homme [304], Froehle and Persson [156] and Chabannes et al. [95] use discontinuous higher order Galerkin approaches to discretize one or both domains of the coupled problem in order to achieve high accuracy. However, the discontinuity of the finite elements leads to an increased number of degrees of freedom. A possibility to reduce these is investigated by e.g. Sheldon et al. [359; 361], Neunteufel and Schöberl [289] and Fu and Kuang [157], which use hybrid discontinuous Galerkin approaches in their studies.

Due to the dynamic nature of fluid-structure interaction problems the choice of the temporal discretization method is an important aspect to be considered. The comparison of different time integration methods as well as the application of adaptive time stepping in connection with FSI problems can be found, for example, in Mayr et al. [278; 279]. Numerous contributions include space-time finite elements, among others Hübner et al. [205], Tezduyar and Sathe [387], Tezduyar et al. [390; 391], Sathe and Tezduyar [337], as well as some of those already mentioned. A recent review of existing space-time FE approaches to solving FSI problems can be found, e.g., in, Hughes et al. [209], Bazilevs et al. [32] and Tezduyar et al. [392]. Similar to adaptive time stepping methods, adaptivity was also applied in space, such as in Bathe and Zhang [22], Wick [416] and Jansson et al. [214].

A further relevant issue, which is inevitable as soon as significant deformations occur in the structure, is the consideration of the deformation of the fluid domain. Due to the relevance of this topic, there are again numerous different approaches. A common one is the use of the Arbitrary-Lagrangian-Eulerian (ALE) description, cf. Hughes et al. [207] and Donea et al. [131] in the fluid domain and the calculation of the background mesh as a kind of pseudo-material. However, there has also been much research on algorithms for re-meshing in the case of large deformations, which will not be discussed further at this point. An overview of some present work on mesh deformation is included in Section 8.3.

Due to the wide range of application fields of numerical FSI calculations the considered problems become continuously more specific. Some recent works in the field of mechanical engineering deal, for example, with the calculation of wind turbines or air blasts, see Bazilevs et al. [26; 28; 30; 31; 33]. In the field of medical engineering, there is a great deal of research in which, for example, the calculation of blood flow through vessels is studied, cf. Bazilevs et al. [24], Janela et al. [213], Balzani et al. [15; 17; 18], Hsu and Bazilevs [203], Terahara et al. [386] and

Schussnig et al. [344], or Hirschhorn et al. [196], for an overview on recent works. The focus of these works lies on the correct simulation of the blood behavior with the help of non-Newtonian material models or the exact modeling of the deformation of surrounding tissue, cf. Marino et al. [271] and von Hoegen et al. [406]. In addition to general models, patient-specific data are also taken into account, see e.g. Bazilevs et al. [25], Balzani et al. [16] and Schussnig and Fries [343].

A constantly ongoing topic in the development of numerical methods is the validation and verification of implemented algorithms on the basis of benchmark problems. The descriptions of some frequently used examples in the field of FSI can be found, among others, in Blom [44], Hron and Turek [202], Bathe and Ledezma [21], Hessenthaler et al. [184; 185; 186], Turek et al. [398]

Further publications that contain collections of research on advances in numerical methods for fluid-structure interaction problems are, for example, Bungartz and Schäfer [72], Schröder [342], Galdi and Rannacher [161], Bungartz et al. [73], Bodnár et al. [58], Bazilevs and Takizawa [23], and Frei et al. [155].

**Least-squares FEM for FSI problems**

A large part of the work mentioned so far is based on a finite element discretization with the continuous or discontinuous Galerkin method. In the context of this thesis, the focus is on the application of the least-squares finite element method. A major reason for using the LSFEM to solve fluid-structure problems is that mixed formulations can directly approximate the quantities that are shared at the interface between fluid and solid with high accuracy. If suitable approximation spaces in $H(\mathrm{div})$ and $H^1$ are applied for the stresses and velocities in both domains, this allows a direct fulfillment of the coupling conditions. Initial approaches using LS formulations do not take this into account, since only the fluid domain is discretized using the LSFEM, as in Lee et al. [261], Kayser-Herold and Matthies [228; 230], for example. The mixed LS fluid formulation therein is coupled with a Galerkin solid formulation. In the former publication, a partitioned scheme is applied to solve steady-state FSI problems. Therein, the domains are computed separately with an iterative update procedure until convergence is reached. Unsteady FSI computations are conducted in the two other works, whereby Kayser-Herold and Matthies [228] apply space-time methods including adaptivity, and in Kayser-Herold and Matthies [230] space and time discretization is performed sequentially.

Further developments including least-squares formulations for the fluid as well as solid domain are presented in Kayser-Herold [227] and Kayser-Herold and Matthies [231], for instance. In these studies, the Stokes and Navier-Stokes equations for the fluid domain, and the equations of linear elasticity for the solid domain, are reformulated into a first-order system by introducing the velocities and Cauchy stresses. In connection with stress approximations in $H(\mathrm{div}, \Omega)$ and standard interpolations for the velocities, a direct satisfaction of the coupling conditions is achieved. Similar approaches based on stress-velocity formulations for both the fluid and solid domain are investigated, for example, in Nisters et al. [297], Nisters [294], Averweg et al. [9]. Moreover, the authors Heys et al. [188; 189; 190] investigate different coupling procedures with a comparison in terms of accuracy and computational cost, and the model scalability with application to blood flow simulations. In Rasmussen et al. [322; 323] and Rasmussen [321], the LSFEM is applied to both fluid and solid domain discretization, and the formulations presented are tested with respect to monolithic coupling schemes and the sensitivity of the coupled system to residual weighting. Another research approach includes the application of sensitivity methods in the field of FSI based on the LSFEM, cf. Wickert et al. [419], Wickert and Canfield [418], Wickert [417], for instance.

## 1.3 Outline

In **Chapter 2** the essential basics of the concept of continuum mechanics are introduced. This includes the description of motion and deformation of bodies including Lagrangian and Eulerian frameworks, the concept of stresses, the balance equations and the constitutive relations required within this thesis.

A short introduction to the finite element method in general and to the specifics of the least-squares FEM is provided in **Chapter 3**. Furthermore, details on interpolation spaces and the construction of interpolation functions are given, including a brief explanation of implementation aspects. Since parts of this thesis involve the assimilation of data using the LSFEM, theoretical information regarding data preparation and implementation are presented in this chapter as well.

**Chapter 4** contains the derivation of least-squares finite element formulations for dynamic flow of incompressible Newtonian fluids based on the Navier-Stokes equations. The stress-velocity-pressure (SVP) and stress-velocity (SV) formulations are presented and information on the approximation is provided. The application of these formulations will be presented later, once the temporal discretization procedures have been introduced.

Least-squares finite element formulations for the solution of steady-state flow problems of non-Newtonian fluids are discussed in **Chapter 5**. The applied formulations and the viscosity model are explained and verified with the help of examples in 2D and 3D. Furthermore, the numerical examples contain several studies on the flow behavior as a function of the different viscosity model parameters. Another point of investigation in this chapter is the assimilation of numerical and experimental data into flow simulations of non-Newtonian fluids in 2D and 3D.

The subsequent **Chapter 6** deals with the derivation of LS formulations for solid mechanics problems. More precisely, formulations in terms of stresses and velocities are considered here, as the main objective of this work is the monolithic coupling of the LS fluid and solid formulations. Both linear elastic and hyperelastic material behavior is introduced for this purpose. Due to the inherent need of the stress-velocity (SV) formulation to be discretized in time, the formulation will be tested for standard application cases in the next chapter once time discretization methods have been presented.

As mentioned earlier, **Chapter 7** contains the explanation of time discretization methods utilized to solve the dynamic flow and solid problems with the LS stress-velocity formulations of the previous chapters. For this purpose, first basics of different time discretization methods are explained and a simple example in 1D is given to clarify their application to the solution of first-order partial differential equations. Furthermore, all necessary implementation aspects of the used discretization methods in connection with the SV formulations are explained and numerical examples are provided including the investigation of convergence orders. Another point of investigation in this chapter is the application of adaptive time stepping algorithms. For this purpose, the evaluation of error estimators based on embedded Runge-Kutta methods is explained and information on automatic time stepping is given. Moreover, the application of adaptivity in time is examined to solve flow and solid problems.

In **Chapter 8** the presented stress-velocity formulations for fluid and solid dynamics are monolithically coupled to solve fluid-structure interaction problems. First, the general idea of monolithic coupling and inherently fulfilled interface conditions using suitable function spaces is given and tested using numerical FSI examples with small deformations. Next, the necessary components for the handling of large deformations in FSI problems are specified. More precisely, the fluid formulation in an Arbitrary-Lagrangian-Eulerian description is introduced to account for deforming fluid domains. Furthermore, details are provided on how to calculate the movement of the fluid background mesh, including numerical examples to compared different approaches for smooth deformation. Finally, the separately tested components are coupled to solve FSI problems with large deformations. In a final benchmark problem, the monolithic coupling of the fluid ALE formulation with the solid formulation for hyperelastic material behavior is examined, along with the application of various time discretization methods including adaptive time stepping.

**Chapter 9** concludes the present work with a summary of the findings obtained. In addition, an outlook is given on possible future work in the fields considered.

It should be stated that all finite element implementations and computations have been done using the *AceGen* and *AceFEM* packages (version 7.203), see KORELC [240; 241; 242] and KORELC AND WRIGGERS [243] of *Mathematica* (version 13.0), see WOLFRAM RESEARCH INC. [422].

# 2 Basic aspects of continuum mechanics

To describe mechanical processes regarding fluids and structures, separately and coupled, the continuum mechanical approach is used in this work. In the continuum hypothesis, the description of physical phenomena is based on the assumption that nature is not composed of atoms, but consists of continuous masses. The present macroscopic approach to continuum mechanics is based, for example, on the work of RIVLIN [330], TRUESDELL AND NOLL [393], TRUESDELL AND TOUPIN [394] and NOLL [298]. Herein, a continuum body is assumed to consist of a set of material points and can be characterized by a certain number of field quantities. In order to explain mechanical processes mathematically, differential equations are used relating these physical field quantities. These equations are theoretical hypotheses whose validity has been verified by years of research. Thus, reliable statements can be derived from these differential equations within a certain range of validity. The application of continuum mechanics requires that, in addition to assumptions for mechanical processes, there are also assumptions to be made about material behavior. Further models are developed continuously in order to extend the overall range of validity.

Dealing with fluid-structure interaction problems involves the coupling of two domains in which independent field problems have to be solved. The objective of this chapter is to outline the mathematical derivation of basic equations for solving each field problem. The algorithmic implementation of the numerical solution of the coupled problem using the least-squares finite element method is explained in the subsequent chapters. In the following sections, the basic fields of the continuum mechanical concept, namely kinematics, the concept of stresses, the balance equations and constitutive relations are described in more detail. For more details regarding continuum mechanics, the interested reader is referred to related textbooks, such as e.g. ERINGEN [139], MALVERN [269], GURTIN [173], MARSDEN AND HUGHES [272], HOLZAPFEL [198], SHABANA [356], LAI ET AL. [252] and REDDY [326], and the references therein.

## 2.1 Kinematics

Kinematics or the theory of motion covers the analysis of motion and deformation of a continuum medium. The cause of the change in position, i.e. the acting forces and moments, are not considered. An infinitesimal volume element on a deformable body has 12 degrees of freedom describing the motion. More precisely, a body can be translated in three independent directions, rotated about three orthogonal axes, and can be subjected to six independent deformation states, three of which are elongations or compressions and three shear deformations. The objective of this section is to establish a correlation between the motion of a body and various strain measures. As will be shown, the deformation at a material point on a body in three dimensions can be described by six strain components. There are different representations of the strains, depending on the reference system used for their definition. The following notations are based on explanations in HOLZAPFEL [198], DONEA AND HUERTA [129] and WRIGGERS [424].

### 2.1.1 Configuration and motion

In order to describe the motion of a body $\mathcal{B}$, we consider the state of the material body in the geometric space at different times $t$, see Figure 2.1. In other words, the position of the body in three-dimensional Euclidean space $\mathbb{R}^3$ can be expressed by a mapping which assigns a unique position to each material point $P \in \mathcal{B}$. The spatial configuration at time $t = 0$, here described by the mapping $\boldsymbol{\chi}_0 : \mathcal{B} \rightarrow \Omega_0 \subset \mathbb{R}^3$, is also referred to as initial configuration. Assuming the body moves as time advances, the new position at time $t$, given as the mapping $\boldsymbol{\chi}_t : \mathcal{B} \rightarrow \Omega_t \subset \mathbb{R}^3$, is called the actual or deformed configuration.

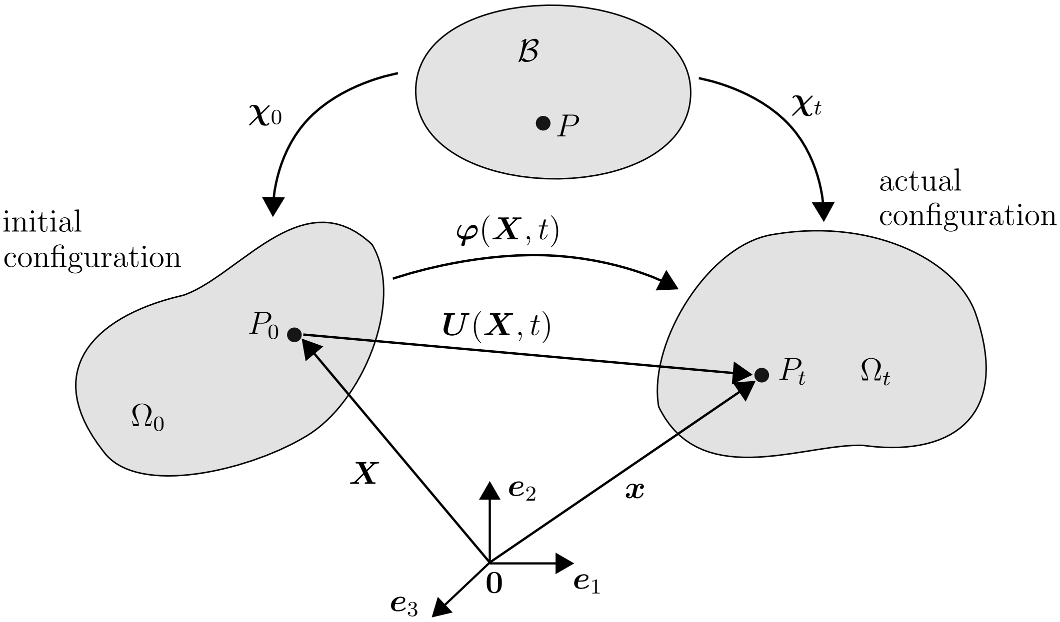

Figure 2.1: Configuration of a continuum body and displacement of a material point

For a better illustration of the motion description, one can focus on a material point $P \in \mathcal{B}$ of the moving body with position vector $\boldsymbol{X} = \boldsymbol{\chi}_0(P, 0) \in \Omega_0$ in the initial configuration and $\boldsymbol{x} = \boldsymbol{\chi}_t(P, t) \in \Omega_t$ in the actual configuration. $\boldsymbol{X}$ is also referred to as material coordinate, since this vector allows to identify the different material particles of the body. Based on the relation between both configurations the actual position can also be given by

$$\boldsymbol{x} = \boldsymbol{\chi}_t(\boldsymbol{\chi}_0(\boldsymbol{X}, t)) = \boldsymbol{\varphi}(\boldsymbol{X}, t), \tag{2.1}$$

where $\boldsymbol{\varphi}(\boldsymbol{X}, t) : \Omega_0 \rightarrow \Omega_t \subset \mathbb{R}^3$ denotes the motion. It is assumed that the latter has continuous derivatives in space and time and is uniquely invertible. Considering a cartesian, orthonormal base system denoted by $\boldsymbol{e}_i$ with $i = \{1, 2, 3\}$ in $\mathbb{R}^3$, respectively, the position vectors of all material and spatial points can be given in index notation as

$$\boldsymbol{X} = X_i \, \boldsymbol{e}_i \qquad \text{and} \qquad \boldsymbol{x} = x_i \, \boldsymbol{e}_i \qquad \text{with} \quad i = \{1, 2, 3\} \ . \tag{2.2}$$

Remark: For the representation of tensor and vector products, a single dot $(\cdot)$ and a colon $(:)$ are used as notation for a simple or a double contraction, respectively. Thus, a single multiplication between two second-order tensors, $\boldsymbol{A}$ and $\boldsymbol{B}$, or a tensor $\boldsymbol{A}$ and a vector $\boldsymbol{b}$ is written as

$$\begin{aligned} \boldsymbol{C} = \boldsymbol{A} \cdot \boldsymbol{B} \qquad & \text{with components} \quad C_{ik} = A_{ij} \, B_{jk} \\ \boldsymbol{c} = \boldsymbol{A} \cdot \boldsymbol{b} \qquad & \text{with components} \quad c_i = A_{ij} \, b_j \ . \end{aligned} \tag{2.3}$$

A double contraction between two second-order tensors or a fourth-order $\mathbb{A}$ and a second-order tensor is denoted as

$$\begin{aligned} C &= \boldsymbol{A} : \boldsymbol{B} \qquad \text{with components} \quad C = A_{ij}\, B_{ji} \\ \boldsymbol{C} &= \mathbb{A} : \boldsymbol{B} \qquad \text{with components} \quad C_{ik} = A_{ijkl}\, B_{lk} \ . \end{aligned} \tag{2.4}$$

### 2.1.2 Eulerian and Lagrangian description

When a continuum is in motion, its characteristic quantities, such as temperature, velocity, stress, can change with time. There are two different ways to express these changes and to describe the displacement and deformation of a medium in continuum mechanics, depending on the point of view. In the material or Lagrangian description of motion a particle is selected and one observes the change of quantities while following its movement in time. Whereas in the spatial or Eulerian description, the change of a quantity at a fixed position in space is considered, see e.g. Wriggers [424]. Taking weather forecasting as an example, one can say that a radiosonde carried by a balloon along with the airstream has a Lagrangian way of looking at, e.g., the flow velocity or temperature. An anemometer, on the other hand, located at a fixed weather station, measures wind speed in an Eulerian manner. A Lagrangian framework is typically used for modeling structural mechanics, and the Eulerian framework is more commonly used in fluid dynamics. Since both domains are relevant in the further course of this work, in the following the description of basic and derived quantities, such as displacement, velocity, acceleration, and strain measures, is considered from both points of view.

In the Lagrangian framework the displacement is described with respect to material coordinates $\boldsymbol{X}$ and time $t$, whereas in the Eulerian description the material coordinates $\boldsymbol{x}$ serve as a base system, leading to the representations

$$\boldsymbol{U}(\boldsymbol{X}, t) = \boldsymbol{x}(\boldsymbol{X}, t) - \boldsymbol{X} \qquad \text{and} \qquad \boldsymbol{u}(\boldsymbol{x}, t) = \boldsymbol{x} - \boldsymbol{X}(\boldsymbol{x}, t) \ . \tag{2.5}$$

Furthermore, it can be noted that there is a correlation between the two perspectives through the deformation map $\boldsymbol{\varphi}$ given by

$$\boldsymbol{U}(\boldsymbol{X}, t) = \boldsymbol{U}(\boldsymbol{\varphi}^{-1}(\boldsymbol{x}, t), t) = \boldsymbol{u}(\boldsymbol{x}, t). \tag{2.6}$$

This relationship can also be used to transform the velocities and accelerations, which are the first and second derivatives of displacement with respect to time, from one frame to another. The specific formulation and further characteristics are summarized in Table 2.1. The effect of the Lagrangian or Eulerian view on the time derivatives is explained in more detail below. Note that for better readability, the scalar and vector arguments are not always stated in the subsequent sections, if it is clear by the context to which configuration the quantities refer (e.g. $\boldsymbol{u}(\boldsymbol{x}, t) = \boldsymbol{u}$).

### 2.1.3 Material time derivative

In order to specify the velocity and acceleration, first of all we consider the material time derivative of a scalar field quantity $\theta(\boldsymbol{x}, t)$ at any position $\boldsymbol{x}$ at time $t$, which is derived using the chain rule

$$\dot{\theta}(\boldsymbol{x}, t) = \frac{\mathrm{D}\,\theta(\boldsymbol{x}, t)}{\mathrm{D}\,t} = \frac{\partial \theta(\boldsymbol{x}, t)}{\partial t} + \frac{\partial \theta(\boldsymbol{x}, t)}{\partial \boldsymbol{x}} \frac{\partial \boldsymbol{x}}{\partial t}. \tag{2.7}$$

This total derivative needs to be considered in the Eulerian representation. In the Lagrangian description, where the quantity depends on the fixed reference system with $\partial \boldsymbol{X}/\partial t = 0$ this reduces to the partial derivative

$$\dot{\theta}(\boldsymbol{X}, t) = \frac{\mathrm{D}\,\theta(\boldsymbol{X}, t)}{\mathrm{D}\,t} = \frac{\partial \theta(\boldsymbol{X}, t)}{\partial t} \; . \tag{2.8}$$

Using equation (2.8) the velocity and acceleration in the material description yield

$$\boldsymbol{V}(\boldsymbol{X}, t) = \frac{\partial \boldsymbol{U}(\boldsymbol{X}, t)}{\partial t} = \frac{\partial \boldsymbol{x}(\boldsymbol{X}, t) - \boldsymbol{X}}{\partial t} = \frac{\partial \boldsymbol{x}(\boldsymbol{X}, t)}{\partial t} = \dot{\boldsymbol{x}}(\boldsymbol{X}, t) \tag{2.9}$$

and

$$\boldsymbol{A}(\boldsymbol{X}, t) = \frac{\partial \boldsymbol{V}(\boldsymbol{X}, t)}{\partial t} = \frac{\partial^2 \boldsymbol{U}(\boldsymbol{X}, t)}{\partial t^2} = \ddot{\boldsymbol{x}}(\boldsymbol{X}, t) \; . \tag{2.10}$$

The spatial description of the velocity can be derived in analogy to equation (2.6) and using (2.9), which leads to

$$\boldsymbol{v}(\boldsymbol{x}, t) = \boldsymbol{V}(\boldsymbol{\varphi}^{-1}(\boldsymbol{x}, t), t) = \dot{\boldsymbol{x}}(\boldsymbol{X}, t). \tag{2.11}$$

The material time derivative, see equation (2.7), applied to the velocity field in Eulerian framework yields the spatial acceleration

$$\boldsymbol{a}(\boldsymbol{x}, t) = \dot{\boldsymbol{v}}(\boldsymbol{x}, t) = \underbrace{\frac{\partial \boldsymbol{v}(\boldsymbol{x}, t)}{\partial t}}_{\text{local acceleration}} + \underbrace{\frac{\partial \boldsymbol{v}(\boldsymbol{x}, t)}{\partial \boldsymbol{x}} \cdot \frac{\partial \boldsymbol{x}}{\partial t}}_{\text{convective acceleration}} = \frac{\partial \boldsymbol{v}}{\partial t} + \operatorname{grad} \boldsymbol{v} \cdot \boldsymbol{v} \; , \tag{2.12}$$

with $\operatorname{grad}(\bullet) = \nabla_x$ denoting the gradient with respect to the current configuration, i.e.

$$\frac{\partial \boldsymbol{v}}{\partial \boldsymbol{x}} = \frac{\partial v_i}{\partial x_j} \boldsymbol{e}_i \otimes \boldsymbol{e}_j \; . \tag{2.13}$$

Some relevant characteristics of both considered configurations and the time derived quantities in the Lagrangian and Eulerian framework are summarized in Table 2.1.

Table 2.1: Characteristics of Lagrangian and Eulerian description of motion

| description | Lagrangian (material) | Eulerian (spatial) |
|---|---|---|
| mostly used in: | structural mechanics | fluid mechanics |
| focus on: | moving material point | fixed point in space |
| base system: | material coordinates ($\boldsymbol{X}$) | spatial coordinates ($\boldsymbol{x}$) |
| displacement | $\boldsymbol{U}(\boldsymbol{X}, t) = \boldsymbol{x}(\boldsymbol{X}, t) - \boldsymbol{X}$ | $\boldsymbol{u}(\boldsymbol{x}, t) = \boldsymbol{x} - \boldsymbol{X}(\boldsymbol{x}, t)$ |
| velocity | $\boldsymbol{V}(\boldsymbol{X}, t) = \dot{\boldsymbol{x}}(\boldsymbol{X}, t)$ | $\boldsymbol{v}(\boldsymbol{x}, t) = \dot{\boldsymbol{x}}(\boldsymbol{X}, t)$ |
| acceleration | $\boldsymbol{A}(\boldsymbol{X}, t) = \ddot{\boldsymbol{x}}(\boldsymbol{X}, t)$ | $\boldsymbol{a}(\boldsymbol{x}, t) = \frac{\partial \boldsymbol{v}}{\partial t} + \operatorname{grad} \boldsymbol{v} \cdot \boldsymbol{v}$ |

REMARK: The material time derivative of the velocities (2.12), consisting of the local acceleration part and the convective part, is especially relevant in fluid dynamics, since it allows the calculation of the acceleration based on the spatial velocity field solely, without any knowledge on the motion. In many continuum mechanics problems, especially in fluid mechanics, the change in shape of a body is not of interest, but rather the rate at which the deformation occurs. For this purpose, the symmetric part of the strain rate tensor, also called symmetric velocity gradient, is often considered, which is defined as follows

$$\boldsymbol{D} = \frac{1}{2}\left(\nabla\boldsymbol{v} + (\nabla\boldsymbol{v})^T\right) = \nabla^s\boldsymbol{v} \quad \rightarrow \quad D_{ij} = \frac{1}{2}\left(\frac{\partial v_i}{\partial x_j} + \frac{\partial v_j}{\partial x_i}\right) \ . \tag{2.14}$$

Herein, the components $D_{ij}$ are referred to the base vectors $\boldsymbol{e}_i$ in the current configuration, such that the gradient is $\nabla(\bullet) = \nabla_x(\bullet)$. In the following, the subscript is omitted whenever it is clear from the context whether the derivation refers to the current or the initial configuration. The components of the velocity gradient for three dimensions can be written in matrix representation as

$$\nabla\boldsymbol{v} = \begin{pmatrix} \frac{\partial v_1}{\partial x_1} & \frac{\partial v_1}{\partial x_2} & \frac{\partial v_1}{\partial x_3} \\ \frac{\partial v_2}{\partial x_1} & \frac{\partial v_2}{\partial x_2} & \frac{\partial v_2}{\partial x_3} \\ \frac{\partial v_3}{\partial x_1} & \frac{\partial v_3}{\partial x_2} & \frac{\partial v_3}{\partial x_3} \end{pmatrix} \ . \tag{2.15}$$

### 2.1.4 Deformation gradient and strain measures

A relevant measure in continuum mechanics is the deformation gradient, which defines a relationship between the initial $\Omega_0$ and the current $\Omega_t$ configuration

$$\boldsymbol{F}(\boldsymbol{X},t) = \frac{\partial\boldsymbol{x}(\boldsymbol{X},t)}{\partial\boldsymbol{X}} = \operatorname{Grad}\boldsymbol{x}(\boldsymbol{X},t) = \nabla_X\boldsymbol{x} \ , \tag{2.16}$$

where Grad$(\bullet)$ or the Nabla operator $\nabla_X(\bullet)$ denote the gradient of a tensor with respect to the material coordinates $\boldsymbol{X}$. A component-wise notation considering the orthonormal bases as given in (2.2) yields

$$\boldsymbol{F} = \frac{\partial x_i}{\partial X_J}\boldsymbol{e}_i \otimes \boldsymbol{E}_J = F_{iJ}\ \boldsymbol{e}_i \otimes \boldsymbol{E}_J \ , \tag{2.17}$$

revealing that the deformation gradient is a two-field tensor with one base each in the initial and current configuration. Is is assumed that the deformation gradient is invertible and its determinant, defined as the Jacobian, is strictly positive $J = \det\boldsymbol{F} > 0$. Then the mappings of infinitesimal line, area and volume elements from the initial to the actual configuration using the deformation gradient are given as

$$\mathrm{d}\boldsymbol{x} = \boldsymbol{F}\cdot\mathrm{d}\boldsymbol{X} \ , \tag{2.18}$$

$$\mathrm{d}\boldsymbol{a} = (\det\boldsymbol{F})\boldsymbol{F}^{-T}\cdot\mathrm{d}\boldsymbol{A} \ , \tag{2.19}$$

$$\mathrm{d}v = (\det\boldsymbol{F})\ \mathrm{d}V \ , \tag{2.20}$$

with the area vectors $\mathrm{d}\boldsymbol{a} = \boldsymbol{n}\,\mathrm{d}a$ and $\mathrm{d}\boldsymbol{A} = \boldsymbol{N}\,\mathrm{d}A$ and unit outward normal vectors $\boldsymbol{n}$ and $\boldsymbol{N}$ to the surface of body $\mathcal{B}$. A combination of the deformation gradient and the displacement is provided by the displacement gradient tensor in the material or spatial description given as

$$\operatorname{Grad}\boldsymbol{U} = \boldsymbol{F}(\boldsymbol{X},t) - \boldsymbol{I} = \nabla_X \boldsymbol{U} \qquad \text{or} \qquad \operatorname{grad}\boldsymbol{u} = \boldsymbol{I} - \boldsymbol{F}^{-1}(\boldsymbol{x},t) = \nabla_x \boldsymbol{u}\ . \tag{2.21}$$

Here, $\operatorname{grad}(\bullet)$ or $\nabla_x(\bullet)$ is used to specify the gradient with respect to the position vector in the current configuration and $\boldsymbol{I}$ denoting the second-order identity tensor. Additionally the inverse of the deformation gradient can be determined by means of the displacement related to the actual state and is

$$\boldsymbol{F}^{-1} = \frac{\partial \boldsymbol{X}(\boldsymbol{x},t)}{\partial \boldsymbol{x}} = \boldsymbol{I} - \operatorname{grad}\boldsymbol{u}\ . \tag{2.22}$$

Due to the fact that the applied equations of continuum mechanics in the course of this work are related to the initial and to the current configuration, in the following some common strain tensors related to both configurations are given. Important measures regarding the Lagrangian description are the right Cauchy-Green deformation tensor $\boldsymbol{C}$ and the Green-Lagrange strain tensor $\boldsymbol{E}$ defined as

$$\boldsymbol{C} = \boldsymbol{F}^T \cdot \boldsymbol{F} \qquad \rightarrow \qquad C_{IJ} = F_{Jk} F_{kJ} \tag{2.23}$$

$$\text{and} \qquad \boldsymbol{E} = \frac{1}{2}(\boldsymbol{C} - \boldsymbol{I}) \quad \rightarrow \quad E_{IJ} = \frac{1}{2}(F_{Jk}F_{kJ} - \delta_{IJ})\ , \tag{2.24}$$

with components $C_{IJ}$ and $E_{IJ}$ referred to an orthonormal base system in the material configuration, and the Kronecker delta defined as

$$\delta_{ij} = \begin{cases} 1 \text{ if } i = j\,, \\ 0 \text{ else}\,. \end{cases} \tag{2.25}$$

An important property of the right Cauchy-Green deformation tensor is, that it is directly connected to the deformation and such to the strains within the body, and takes the value of the identity $\boldsymbol{I}$ throughout a rigid-body motion. Further important strain measures regarding the material and spatial description are summarized in Table 2.2.

Table 2.2: Definition and characteristics of common deformation and strain tensors

| | configuration | characteristics | definition |
|---|---|---|---|
| right Cauchy-Green tensor | initial | sym., pos. definite | $\boldsymbol{C} = \boldsymbol{F}^T \cdot \boldsymbol{F}$ |
| Green-Lagrange strain tensor | initial | symmetric | $\boldsymbol{E} = \frac{1}{2}(\boldsymbol{F}^T \cdot \boldsymbol{F} - \boldsymbol{I})$ |
| left Cauchy-Green tensor | actual | sym., pos. definite | $\boldsymbol{b} = \boldsymbol{F} \cdot \boldsymbol{F}^T$ |
| Almansi strain tensor | actual | symmetric | $\boldsymbol{e} = \frac{1}{2}(\boldsymbol{I} - \boldsymbol{F}^{-T} \cdot \boldsymbol{F}^{-1})$ |

REMARK: In structural mechanics, some materials undergo only small deformations when forces up to a certain magnitude are applied. In the calculation of such deformations, a great simplification can be obtained by approximating the exact strain tensors by an infinitesimal strain tensor, denoted as $\boldsymbol{\varepsilon}$. This approximation is based on the assumption that the components of the displacement gradient in such a case are comparatively small, i.e. $\partial U_I / \partial X_J \ll 1$, such that powers of those occurring for instance in the definition of the strain tensors $\boldsymbol{E}$ or $\boldsymbol{e}$ can be neglected. Consequently, it is indifferent whether the displacement gradients are obtained by differentiation according to material coordinates $\boldsymbol{X}$ or according to spatial coordinates $\boldsymbol{x}$, such that $\partial U_I / \partial X_J \approx \partial u_i / \partial x_j$. This leads to the infinitesimal strain tensor

$$\boldsymbol{\varepsilon} = \frac{1}{2} \left( \nabla \boldsymbol{u} + (\nabla \boldsymbol{u})^T \right) \ , \tag{2.26}$$

where in the limiting field of linear elasticity $\nabla(\bullet) = \nabla_X(\bullet) = \nabla_x(\bullet)$.

## 2.2 Concept of stresses

The motions and deformations considered so far result in stresses inside a material. In the following, the stress quantities which are of interest in this work are briefly introduced.

### 2.2.1 Surface traction

In order to illustrate the stress quantities, consider an arbitrary cut through a body under load in the initial configuration $\Omega_0$ and the actual deformed configuration $\Omega_t$, see Figure 2.2. Due to an external load acting on a boundary $\partial\Omega_{0/t}$, an infinitesimal resultant force vector

$$\mathrm{d}\boldsymbol{f} = \boldsymbol{T} \ \mathrm{d}A = \boldsymbol{t} \ \mathrm{d}a \tag{2.27}$$

acts inside the body on each surface element, where $\boldsymbol{T}$ denotes the first Piola-Kirchhoff traction vector and $\boldsymbol{t}$ the Cauchy traction vector defined in the initial and actual configuration, respectively.

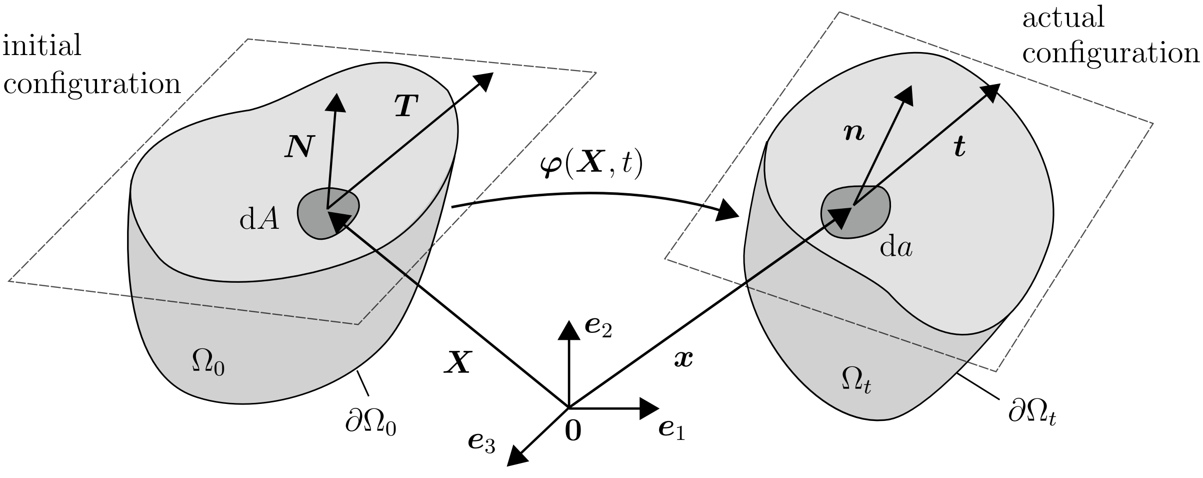

Figure 2.2: Concept of stresses - traction vectors acting on cut surface

According to Cauchy's stress theorem, there exist tensor fields, commonly called the Cauchy stress tensor $\boldsymbol{\sigma}$ and the first Piola-Kirchhof stress tensor $\boldsymbol{P}$, such that the traction vectors are linear in the unit outward normals $\boldsymbol{n}$ or $\boldsymbol{N}$ and

$$\boldsymbol{T} = \boldsymbol{P} \cdot \boldsymbol{N} \qquad \text{and} \qquad \boldsymbol{t} = \boldsymbol{\sigma} \cdot \boldsymbol{n} \ . \tag{2.28}$$

Note that the traction vectors generally do not coincide with the outward normals. The force applied across a surface does not necessarily act in the direction perpendicular to the surface. The Cauchy stress is a symmetric spatial tensor field and also referred to as true stress, since it defines the stress in the actual configuration acting on the actual boundary of $\Omega$, depending only on position $\boldsymbol{x}$ and time $t$.

### 2.2.2 Stress tensors

Based on equation (2.27), which defines the relation between both stress tensors as

$$\boldsymbol{P} \cdot \boldsymbol{N} \, \mathrm{d}A = \boldsymbol{\sigma} \cdot \boldsymbol{n} \, \mathrm{d}a \, , \tag{2.29}$$

and using the transport theorem of an area element, see (2.19), the Cauchy and the first Piola-Kirchhoff (PK) stress tensors can also be written as

$$\boldsymbol{\sigma} = J^{-1} \boldsymbol{P} \cdot \boldsymbol{F}^T \qquad \text{and} \qquad \boldsymbol{P} = J \boldsymbol{\sigma} \cdot \boldsymbol{F}^{-T} \, . \tag{2.30}$$

Further commonly used stress tensor are the second Piola-Kirchhoff stress tensor $\boldsymbol{S}$ and the Kirchhoff stress tensor, here denoted by $\boldsymbol{\tau}_K$, i.e.

$$\boldsymbol{S} = \boldsymbol{F}^{-1} \cdot \boldsymbol{P} = J \boldsymbol{F}^{-1} \cdot \boldsymbol{\sigma} \cdot \boldsymbol{F}^{-T} \qquad \text{and} \qquad \boldsymbol{\tau}_K = \boldsymbol{F} \cdot \boldsymbol{S} \cdot \boldsymbol{F}^T = J \boldsymbol{\sigma}. \tag{2.31}$$

The second Piola-Kirchhoff stress tensor is symmetric and formulated based on material coordinates and the Kirchhoff stress tensor represents the counterpart in the actual configuration. An overview of the stress quantities with some relevant characteristics and their relations is given in Table 2.3.

Table 2.3: Summary of relevant characteristics and relations of common stress tensors

| | configuration | symmetry | important relations |
|---|---|---|---|
| Cauchy stress | spatial | $\boldsymbol{\sigma} = \boldsymbol{\sigma}^T$ | $\boldsymbol{\sigma} = J^{-1} \boldsymbol{P} \cdot \boldsymbol{F}^T = J^{-1} \boldsymbol{F} \cdot \boldsymbol{S} \cdot \boldsymbol{F}^T$ |
| Kirchhoff stress | spatial | $\boldsymbol{\tau}_K = \boldsymbol{\tau}_K^T$ | $\boldsymbol{\tau}_K = J \boldsymbol{\sigma} = \boldsymbol{P} \cdot \boldsymbol{F}^T = \boldsymbol{F} \cdot \boldsymbol{S} \cdot \boldsymbol{F}^T$ |
| 1st Piola-Kirchhoff | two-field | $\boldsymbol{P} \neq \boldsymbol{P}^T$ | $\boldsymbol{P} = J \boldsymbol{\sigma} \cdot \boldsymbol{F}^{-T} = \boldsymbol{F} \cdot \boldsymbol{S}$ |
| 2nd Piola-Kirchhoff | material | $\boldsymbol{S} = \boldsymbol{S}^T$ | $\boldsymbol{S} = \boldsymbol{F}^{-1} \cdot \boldsymbol{P} = J \boldsymbol{F}^{-1} \cdot \boldsymbol{\sigma} \cdot \boldsymbol{F}^{-T}$ |

### 2.2.3 Stress deviator and hydrostatic pressure

It is often useful to decompose the Cauchy stress tensor $\boldsymbol{\sigma}$ in a deviatoric $\boldsymbol{\sigma}^D$ and spherical $\boldsymbol{\sigma}^S$ part as

$$\boldsymbol{\sigma} = \boldsymbol{\sigma}^D + \boldsymbol{\sigma}^S = \boldsymbol{\sigma}^D + \frac{1}{3} \operatorname{tr}(\boldsymbol{\sigma}) \boldsymbol{I} \, , \tag{2.32}$$

Therein, the deviatoric part is related to the shear components of the stress tensor $\sigma_{ij}$ with $i \neq j$, acting tangential to the surfaces, and the spherical part depends on the normal stress components $\sigma_{ii}$. If the shear stresses are zero, i.e. $\boldsymbol{\sigma}^D = \boldsymbol{0}$, then one obtains

$$\boldsymbol{\sigma} = -p \boldsymbol{I} \, , \tag{2.33}$$

or in index notation $\sigma_{ij} = -p\,\delta_{ij}$, with the Kronecker delta $\delta_{ij}$ defined in (2.25). This can be referred to as hydrostatic stress state with the scalar quantity $p = -\frac{1}{3}\,\mathrm{tr}\,\boldsymbol{\sigma}$ being the hydrostatic pressure, see HOLZAPFEL [198], SPENCER [368] or DONEA AND HUERTA [129], for instance.

REMARK: Related to the description of flow processes, equation (2.33) describes the state of a fluid at rest in which it cannot sustain shear stresses. The stress state in the static equilibrium is purely hydrostatic. The deviatoric stresses in fluid dynamics are often denoted as $\boldsymbol{\tau}$ and according to (2.32) taking into account the definition for the hydrostatic pressure, it follows that

$$\boldsymbol{\sigma} = \boldsymbol{\tau} - p\,\boldsymbol{I}\ . \tag{2.34}$$

## 2.3 Balance principles

In the following, the relevant physical principles that form the basis of both fluid dynamics and solid mechanics are considered. The balance of mass, the balance of momentum and the balance of moment of momentum describe the equilibrium of physical quantities in the body with consideration of an external load.

### 2.3.1 Conservation of mass

Assuming a closed system, the conservation of mass means, that the mass $m$ of a body remains constant and does not change with time and motion. It remains constant in time regardless of the configuration. In integral form over the entire region in the initial and actual configuration this reads

$$m = \int_{\Omega_0} \rho_0(\boldsymbol{X},t)\ \mathrm{d}V = \int_{\Omega_t} \rho(\boldsymbol{x},t)\ \mathrm{d}v \quad = \text{constant} > 0\ , \tag{2.35}$$

where $\rho_0$ and $\rho$ are the initial and actual density, which are related using the transport theorem (2.20) as $\rho_0 = \rho\,J$. A constant mass over time implies that the rate of mass change equals zero. Taking into account that the initial configuration is time independent and using the definition $\dot{J} = J\,\mathrm{div}\,\boldsymbol{v}$, the global statement can be written as

$$\begin{aligned} \dot{m} = \frac{\mathrm{D}\,m}{\mathrm{D}\,t} = \int_{\Omega_0} \frac{\mathrm{D}\,\rho_0(\boldsymbol{X},t)}{\mathrm{D}\,t}\ \mathrm{d}V &= \int_{\Omega_0} \frac{\mathrm{D}(\rho(\boldsymbol{x},t)\,J)}{\mathrm{D}\,t}\ \mathrm{d}V \\ = \int_{\Omega_0} \dot{\rho}(\boldsymbol{x},t)J + \rho(\boldsymbol{x},t)\dot{J}\ \mathrm{d}V & \\ = \int_{\Omega_0} J(\dot{\rho} + \rho\,\mathrm{div}\,\boldsymbol{v})\ \mathrm{d}V & \\ = \int_{\Omega_t} (\dot{\rho} + \rho\,\mathrm{div}\,\boldsymbol{v})\ \mathrm{d}v \quad &= 0\ . \end{aligned} \tag{2.36}$$

The local form in Eulerian description follows as

$$\dot{\rho} + \rho\,\mathrm{div}\,\boldsymbol{v} = 0\ , \tag{2.37}$$

where the material time derivative of the density is defined as $\dot{\rho} = \frac{\partial \rho}{\partial t} + \mathrm{grad}\,\rho \cdot \boldsymbol{v}$. Since only homogeneous materials are considered in the context of this work, the density is uniform over the entire region and thus the dependence on the coordinates $\boldsymbol{X}$ or $\boldsymbol{x}$ can be dropped, such that $(\operatorname{grad}\rho = \mathbf{0})$. Furthermore, when assuming incompressible materials the density is constant over time $(\dot{\rho} = 0)$ such that the mass continuity equation results in

$$\operatorname{div}\boldsymbol{v} = 0 \ . \tag{2.38}$$

Remark: This statement is a basic component of the Navier-Stokes equations for the flow description of incompressible fluids. The practical and commonly used representation in component notation reads as follows

$$\frac{\partial v_i}{\partial x_i} = 0 \qquad \text{with} \qquad i = \{1,2,3\} \ . \tag{2.39}$$

### 2.3.2 Balance of linear momentum

The balance of linear momentum states that the rate of change of momentum must be in equilibrium with all external forces acting on a body, i.e. $\dot{\boldsymbol{L}} = \boldsymbol{F}_{ext}$. Herein, the linear momentum in the initial and actual configuration is defined as the volume integral

$$\boldsymbol{L} = \int_{\Omega_0} \rho_0 \boldsymbol{V} \ \mathrm{d}V = \int_{\Omega_t} \rho \boldsymbol{v} \ \mathrm{d}v \ . \tag{2.40}$$

The resultant force can be split into a surface part, subjected to a traction vector, and a volume part, subjected to a body force $\boldsymbol{f}_b$ in the actual and $\boldsymbol{F}_b = J\boldsymbol{f}_b$ in the initial configuration, i.e.

$$\boldsymbol{F}_{ext} = \int_{\partial\Omega_t} \boldsymbol{t} \ \mathrm{d}a + \int_{\Omega_t} \boldsymbol{f}_b \ \mathrm{d}v = \int_{\partial\Omega_0} \boldsymbol{T} \ \mathrm{d}A + \int_{\Omega_0} \boldsymbol{F}_b \ \mathrm{d}V \ . \tag{2.41}$$

The traction vectors are the Cauchy traction $\boldsymbol{t}$ or the first Piola-Kirchhoff traction vector $\boldsymbol{T}$, depending on the configuration. The body force can include e.g. gravitational force per unit volume, i.e. $\boldsymbol{f}_b = \rho\boldsymbol{g}$ with the gravity acceleration $\boldsymbol{g}$.

With the material time derivative of the momentum, this gives the global form of the balance of linear momentum in Eulerian description as

$$\dot{\boldsymbol{L}} = \frac{\mathrm{D}}{\mathrm{D}t} \int_{\Omega_t} \rho\boldsymbol{v} \ \mathrm{d}v = \int_{\partial\Omega_t} \boldsymbol{t} \ \mathrm{d}a + \int_{\Omega_t} \boldsymbol{f}_b \ \mathrm{d}v \ . \tag{2.42}$$

By integrating Cauchy's stress theorem given in (2.28) and using the divergence theorem, which states for any tensor $\boldsymbol{A}$ that $\int_{\partial\Omega_t} \boldsymbol{A}\cdot\boldsymbol{n} \ \mathrm{d}a = \int_{\Omega_t} \operatorname{div}\boldsymbol{A} \ \mathrm{d}v$, the surface integral of the traction vector can be converted to a volume integral of the Cauchy stress tensor $\boldsymbol{\sigma}$

$$\int_{\partial\Omega_t} \boldsymbol{t} \ \mathrm{d}a = \int_{\partial\Omega_t} \boldsymbol{\sigma}\cdot\boldsymbol{n} \ \mathrm{d}a = \int_{\Omega_t} \operatorname{div}\boldsymbol{\sigma} \ \mathrm{d}v \ . \tag{2.43}$$

Substituting this equation into (2.42) and considering the material time derivative of the velocity $\dot{\boldsymbol{v}} = \frac{\partial\boldsymbol{v}}{\partial t} + \operatorname{grad}\boldsymbol{v}\cdot\boldsymbol{v}$, see equation (2.12), one obtains the global form of Cauchy's first equation of motion in the Eulerian description

$$\int_{\Omega_t} (\operatorname{div}\boldsymbol{\sigma} + \boldsymbol{f}_b - \rho\dot{\boldsymbol{v}}) \ \mathrm{d}v = \mathbf{0} \ , \tag{2.44}$$

and subsequently also the local form of this statement

$$\operatorname{div}\boldsymbol{\sigma} + \boldsymbol{f}_b - \rho\dot{\boldsymbol{v}} = \boldsymbol{0} \ . \tag{2.45}$$

For applications in the field of solid mechanics, it is often preferable to use a formulation in Lagrangian description. The material description of the global balance equation yields

$$\frac{\mathrm{D}}{\mathrm{D}\,t}\int_{\Omega_0} \rho_0 \boldsymbol{V}\ \mathrm{d}V = \int_{\partial\Omega_0} \boldsymbol{T}\ \mathrm{d}A + \int_{\Omega_0} \boldsymbol{F}_b\ \mathrm{d}V \ . \tag{2.46}$$

With further transformations using the divergence theorem and the mass continuity (**??**), the integral form of the balance of linear momentum in Lagrangian description is given as

$$\int_{\Omega_0} \left(\operatorname{Div}\boldsymbol{P} + \boldsymbol{F}_b - \rho_0\dot{\boldsymbol{V}}\right)\ \mathrm{d}V = \boldsymbol{0} \ , \tag{2.47}$$

with the first Piola-Kirchhoff stress tensor $\boldsymbol{P}$ and the initial density $\rho_0$. Analogously to the deliberations above, the local form of this expression can be formed and is

$$\operatorname{Div}\boldsymbol{P} + \boldsymbol{F}_b - \rho_0\dot{\boldsymbol{V}} = \boldsymbol{0} \ . \tag{2.48}$$

REMARK: The Eulerian description of the momentum balance is one of the governing equations for solving dynamic flows which are studied later. To ease the interpretation of these equations and for a straightforward implementation, it is often helpful to take a look at the index notation. Using component-wise representation and expanding the material time derivative of the velocities, see (2.12), the momentum balance in equation (2.45) can be represented as follows

$$\frac{\partial\sigma_{ij}}{\partial x_i} + f_j = \rho\left(\frac{\partial v_j}{\partial t} + v_k\frac{\partial v_j}{\partial x_k}\right) \ . \tag{2.49}$$

Regarding the physical meaning of these terms, one can see that the right side of the equation corresponds to the rate of change of the moment, and consists of the acceleration term and a convective part. The left side of the equation contains the forces which are in equilibrium with the accelerations. These include the gradient of the surface stresses and the volume forces, such as gravity acting on the mass of the volume under consideration. The surface stresses can be further divided into shear and normal stresses, as explained in more detail in Section 2.5.

### 2.3.3 Balance of angular momentum

The balance of angular momentum defines the equilibrium between the rate of change of angular momentum and all external moments acting on a body, i.e. $\dot{\boldsymbol{J}} = \boldsymbol{M}$. Herein, the angular momentum relative to a fixed point $\boldsymbol{x}_0$ is defined in the initial and actual configuration as the volume integral

$$\boldsymbol{J} = \int_{\Omega_0} \boldsymbol{r}\times\rho_0\boldsymbol{V}\ \mathrm{d}V = \int_{\Omega_t} \boldsymbol{r}\times\rho\boldsymbol{v}\ \mathrm{d}v \ , \tag{2.50}$$

with the position vector $\boldsymbol{r} = \boldsymbol{x} - \boldsymbol{x}_0$. The resultant moment can again be generated by volume and surface forces and reads

$$\boldsymbol{M} = \int_{\partial\Omega_t} \boldsymbol{r}\times\boldsymbol{t}\ \mathrm{d}a + \int_{\Omega_t} \boldsymbol{r}\times\boldsymbol{f}_b\ \mathrm{d}v = \int_{\partial\Omega_0} \boldsymbol{r}\times\boldsymbol{T}\ \mathrm{d}A + \int_{\Omega_0} \boldsymbol{r}\times\boldsymbol{F}_b\ \mathrm{d}V \ . \tag{2.51}$$

With the material time derivative of the angular momentum, this gives the global form of the balance of linear momentum in Eulerian description as

$$\dot{\boldsymbol{J}} = \frac{\mathrm{D}}{\mathrm{D}\,t} \int_{\Omega_t} \boldsymbol{r} \times \rho \boldsymbol{v} \ \mathrm{d}v = \int_{\partial\Omega_t} \boldsymbol{r} \times \boldsymbol{t} \ \mathrm{d}a + \int_{\Omega_t} \boldsymbol{r} \times \boldsymbol{f}_b \ \mathrm{d}v \ . \tag{2.52}$$

With further transformation, which will be omitted at this point, the final local statement of the balance of angular momentum in Eulerian description becomes

$$\boldsymbol{\sigma} = \boldsymbol{\sigma}^T \ , \tag{2.53}$$

which states the symmetry of the Cauchy stress tensor. Reformulation leads to the corresponding Lagrangian description

$$\boldsymbol{P} \cdot \boldsymbol{F}^T = \boldsymbol{F} \cdot \boldsymbol{P}^T \ , \tag{2.54}$$

which implies that the first Piola-Kirchhoff stress tensor is not necessarily symmetric.

An overview of the balance equations, which are relevant in the scope of this thesis can be found in Table 2.4, where the Eulerian and Lagrangian descriptions are given.

Table 2.4: Local statements of balance equations in Lagrangian and Eulerian description

| | Lagrangian description | Eulerian description |
|---|---|---|
| mass continuity | $\dot{\rho}_0 = 0$ | $\dot{\rho} + \rho \operatorname{div} \boldsymbol{v} = 0$ |
| balance of linear momentum | $\operatorname{Div} \boldsymbol{P} + \boldsymbol{F}_b - \rho_0 \dot{\boldsymbol{V}} = \boldsymbol{0}$ | $\operatorname{div} \boldsymbol{\sigma} + \boldsymbol{f}_b - \rho \dot{\boldsymbol{v}} = \boldsymbol{0}$ |
| balance of angular momentum | $\boldsymbol{F} \cdot \boldsymbol{P}^T = \boldsymbol{P} \cdot \boldsymbol{F}^T$ | $\boldsymbol{\sigma} = \boldsymbol{\sigma}^T$ |

## 2.4 Constitutive equations for elastic structures

So far in this work, the kinematics of deformations, the stress concept, the conservation equations and balance principles have been studied. Thereby, the Eulerian and Lagrangian approaches were derived for the different equations and descriptions, respectively. All these relations are valid for any kind of continuum, more precisely for any material. In order to distinguish between different materials, such as fluid and solid, or to be able to describe different material properties, such as elasticity or plasticity, further equations are required. In detail, terms are needed to relate the stresses inside the medium to the deformations causing these internal forces, taking into account various parameters characterizing the material properties, such as density and viscosity. The relationship is also known as the constitutive law and, in addition to being dependent on the material under consideration, it can also include dependence on, e.g., time, space, temperature.

In this section, the constitutive relations are established for elastic solids considering linear elastic and hyperelastic material behavior. The next section will deal with the material description and constitutive laws for Newtonian and generalized Newtonian fluids. In general, there are many ways in which a solid can respond to an external or internal load. Main properties are, e.g., elasticity, plasticity or viscosity, with the later describing a time-dependent material behavior. In addition, there are of course also mixed forms in which the material combines different properties in varying proportions, leading, for example, to elastoplastic, viscoelastic or viscoplastic behavior.

### 2.4.1 Description for hyperelastic material behavior

Within the scope of this work, only purely elastic deformation processes in the solid domain are considered. Materials are referred to as elastic if their constitutive behavior is a function of the current deformation state only and does not depend, for example, on time or the deformation rate. Additionally, all deformations are reversible such that a body returns to its initial state when the load is removed. Furthermore, only homogeneous and isotropic materials are considered for which it is assumed that on the one hand the constituents are uniformly distributed in the body, and on the other hand the material response under load is the same in all directions. During the deformation of such materials, referred to as hyperelastic, there is no energy generation or dissipation, the energy is conserved. For the constitutive relations in the framework of hyperelasticity or Green elasticity, the stresses can be derived from a stored energy function.

The behavior of hyperelastic materials depends on the choice of the free energy function. This work is restricted to materials of St. Venant-Kirchhoff (STVK) type, which are suitable for modeling large deformations at small strains. The energy function in this case reads

$$\psi(\boldsymbol{E}) := \frac{1}{2}\lambda_s(\operatorname{tr}\boldsymbol{E})^2 + \mu_s \operatorname{tr}(\boldsymbol{E}^2) = \frac{1}{2}\mathbb{C} : \boldsymbol{E}^2 \ , \tag{2.55}$$

where $\lambda_s$ and $\mu_s$ are the first and second Lamé material constants, respectively, which can be derived from the elasticity modulus $E_s$ and the Poisson ratio $\nu_s$ as

$$\lambda_s = \frac{E_s \nu_s}{(1+\nu_s)(1-2\nu_s)} \qquad \text{and} \qquad \mu_s = \frac{E_s}{2(1+\nu_s)} \ . \tag{2.56}$$

Furthermore, $\mathbb{C}$ denotes the constant elastic moduli defined as

$$\mathbb{C} = \lambda_s \boldsymbol{I} \otimes \boldsymbol{I} + 2\mu_s \mathbb{I} \ , \tag{2.57}$$

with the fourth order identity tensor $\mathbb{I} = (\boldsymbol{I} \otimes \boldsymbol{I})^{\overset{23}{T}}$ or in index notation $\mathbb{I}_{ijkl} = \delta_{ik}\delta_{jl}$ and the Kronecker delta $\delta_{ij}$ as in (2.25). The Green-Lagrange strain tensor $\boldsymbol{E}$ as defined in Section (2.1.4) is given by

$$\boldsymbol{E} = \frac{1}{2}(\boldsymbol{F}^T \cdot \boldsymbol{F} - \boldsymbol{I}) = \frac{1}{2}\left(\nabla_X \boldsymbol{u} + \nabla_X \boldsymbol{u}^T + \nabla_X \boldsymbol{u}^T \cdot \nabla_X \boldsymbol{u}\right) \ . \tag{2.58}$$

The relation between the stresses and strains can be derived from the second law of thermodynamics, considering that the internal dissipation is zero for perfectly elastic materials. For instance, based on the gradient of the energy function $\psi$ with respect to the Green-Lagrange strain tensor $\boldsymbol{E}$ the second Piola-Kirchhoff (PK) stress tensor $\boldsymbol{S}$ reads

$$\boldsymbol{S} = \frac{\partial \psi(\boldsymbol{E})}{\partial \boldsymbol{E}} = \lambda_s(\operatorname{tr}\boldsymbol{E})\,\boldsymbol{I} + 2\mu_s \boldsymbol{E} = \mathbb{C} : \boldsymbol{E} \ . \tag{2.59}$$

Note, that the St. Venant-Kirchhoff material model fulfills the principle of frame indifference, as it can easily be formulated in terms of the invariants of the right Cauchy-Green tensor $\boldsymbol{C}$. The relation (2.59) can be formulated in terms of the current configuration by transforming the second PK stress tensor into the Cauchy stress tensor via $\boldsymbol{\sigma} = J^{-1}\boldsymbol{F} \cdot \boldsymbol{S} \cdot \boldsymbol{F}^T$.

### 2.4.2 Description for linear elastic material behavior

In the case of linear elasticity, it is assumed that the gradient of the displacements is small, such that the quadratic term in (2.58) can be neglected and the Green-Lagrange strain reduces to the linear elastic strain measure as defined in (2.26). Then, the strain energy function for linear elastic solids with the first and second Lamé constants $\lambda_s$ and $\mu_s$ can be written as

$$\psi(\boldsymbol{\varepsilon}) := \frac{1}{2}\lambda_s(\operatorname{tr}\boldsymbol{\varepsilon})^2 + \mu_s \operatorname{tr}(\boldsymbol{\varepsilon}^2) \ , \tag{2.60}$$

and the constitutive law considering small deformations, which defines a linear relation between the Cauchy stresses and the strains, reads

$$\boldsymbol{\sigma} = \frac{\partial\psi(\boldsymbol{\varepsilon})}{\partial\boldsymbol{\varepsilon}} = \lambda_s(\operatorname{tr}\boldsymbol{\varepsilon})\boldsymbol{I} + 2\mu_s\boldsymbol{\varepsilon} = \mathbb{C} : \nabla^s\boldsymbol{u} \ . \tag{2.61}$$

Herein the symmetric gradient of the displacements is defined as $\nabla^s\boldsymbol{u} = \frac{1}{2}(\nabla\boldsymbol{u} + \nabla\boldsymbol{u}^T)$.

## 2.5 Constitutive equations for fluid dynamics

In the previous section, the characteristic equations describing the behavior of elastic solids were discussed. Since the focus of this work is rather on solving computational fluid flow and FSI problems, the properties of fluids and the basic equation necessary to describe their behavior will be explained in more detail in the following. The main difference between solid and fluid materials is the resistance to deformation when a traction is applied. Fluids are characterized by a high sliding ability of the particles at very low forces, while comparably high forces are often required to deform a solid. In general the origin of the deformation resistance of fluids lies in their inertia and viscosity. Besides the low resistance against deformation, many fluids exhibit a high resistance against volume change and can thus be treated as incompressible.

In general, the behavior of fluids is determined by a variety of material properties, such as viscosity and density, as well as flow properties, e.g. velocity and temperature. In turn, the properties of the fluid itself can also depend on the characteristics of the flow. Following, a brief overview of the most important properties is provided in order to facilitate the classification of the considered flow investigations and the imposed restrictions in this thesis. For more details about the rheology of fluids, reference is made to the detailed explanations in textbooks such as CURRIE [113], BIRD ET AL. [42], WHITE [414], DESHPANDE ET AL. [124] and SIGLOCH [363]. Different relevant flow and fluid characteristics as well as the required constitutive equations to model the flow of Newtonian and non-Newtonian fluids are outlined in the following.

### 2.5.1 Flow characteristics

A main property of flows is the characteristic velocity, which can be decisive for the type of flow that occurs. A distinction is made between steady and unsteady, and in the latter case between laminar and turbulent. Note, however, that the velocity is not exclusively responsible for the flow type which occurs, but that material properties also have an impact.

A **steady** flow is defined by the fact that all fluid variables, such as e.g. velocity, pressure and density, do not change over time at any fixed position in space. However, this does not mean that there is a uniform velocity field over the domain of consideration. That is, for steady-state flows, the velocity gradient is most likely not zero, but the derivative with respect to time must be. For the computation of steady-state flows, the balance equations are greatly simplified, since all time-dependent terms are omitted and thus no discretization with respect to time is necessary in the context of numerical computations.

A flow in which at least one quantity at a defined position in the domain changes with time is called **unsteady**. Thus, for unsteady flows, the partial derivatives of this quantity with respect to time must be considered. In the context of this work, unsteady flows are examined, in which the velocity does not remain constant over time. A temporal change of other quantities such as density or pressure is not taken into account.

A transient flow in which the fluid particles move on well-ordered paths is called **laminar**. Thereby, the individual developing layers can have different velocities and move past each other without crossing each other. A further increase in velocity can lead to a transition from a laminar state to a **turbulent** one. This happens when the originally stable laminar flow becomes unstable resulting in a disordered flow with many turbulences.

The point of this transition can be estimated quantitatively using the **Reynolds number**, which is one of the most important quantities in fluid mechanics. It characterizes the type of flow, taking into account the inertia and viscosity of a fluid. It can be calculated as

$$Re = \frac{v_0 \cdot L_0}{\nu_0} = \frac{\rho_0 \cdot v_0 \cdot L_0}{\eta_0} \ , \tag{2.62}$$

with characteristic values for length $L_0$, density $\rho_0$, kinematic viscosity $\nu_0$, dynamic viscosity $\eta_0$ and velocity $v_0$. In general, it holds that

$$Re < Re_{kr} \quad \rightarrow \quad \text{laminar flow} \tag{2.63}$$

$$Re > Re_{kr} \quad \rightarrow \quad \text{turbulent flow} \ , \tag{2.64}$$

where the critical Reynolds number $Re_{kr}$ depends on several influences such as the type of flow, initial turbulence or surface roughness and has to be determined experimentally. In the case of $Re \leq 1$, the special case of creeping flow is commonly assumed, which occurs when the viscous forces are very high compared to the inertial forces. Based on the Reynolds number, it becomes obvious that material properties are also very important for the characterization of flows.

### 2.5.2 Fluid properties

A relevant fluid property is the material density. Generally stated, this property determines the **compressibility**, i.e. whether the material can be compressed or not. For many types of flows, the change in density of the fluid can be ignored. This is especially the case when considering liquids, whereas in the case of gas flows, the compressibility must often be taken into account. If a fluid is called **incompressible**, this means that when considering a finite volume, not only the mass remains constant, but also the volume and thus the density. Although compressibility in itself is a property of the material, the assumption of incompressible behavior can also be made depending on the Mach number. This defines the relation between flow velocity, denoted as $v$, and speed of sound $c$ in the fluid as $Ma = v/c$. If the Mach number is very small ($Ma < 0.3$), the flow can be assumed to be incompressible. Note, that for the solution of incompressible flow problems, the energy equation is not required to solve the momentum and continuity equations. This can be seen, when considering the mathematical expression for the incompressibility

$$\frac{\partial \rho}{\partial t} = 0 \ , \tag{2.65}$$

which has already been used in equation (2.38) to simplify the balance of mass statement.

In addition to the compressibility of a fluid, its **viscosity** is also decisive for the flow and material behavior. The term viscosity refers to the resistance of a fluid to deformation when shear stress is applied. The capacity to withstand movement originates from internal friction that arises between layers of a liquid medium which move relative to one another. The greater the viscosity, the more the fluid resists motion. Generally, one can distinguish between viscous and inviscid materials, whereas the latter one is an idealization for fluids where the internal friction is negligible. For the modeling of inviscid flows, the governing equations simplify to the well-known Euler equation, which will not be discussed in more detail at this points.

Newton stated that the relation between the shear stress $\boldsymbol{\tau}$ and the shear rate $\dot{\gamma}$ of a fluid subjected to a mechanical force is linear and can be expressed by a viscosity coefficient. This can be illustrated considering a fluid layer between to plates as shown in Figure 2.3, where the lower plate is at rest and the upper plate moves with a velocity $v$ in $x$-direction. The distance between both plates in $z$-direction is given by $h$. If the velocity distribution between both plates is assumed to be constant, the shear rate is defined as $v/h$. But this holds only for thin fluid layers. Otherwise the shear rate must be expressed using the differential quotient $D = \mathrm{d}v/\mathrm{d}z = \dot{\gamma}$. Then the general form of **Newton's law of viscosity** reads

$$\tau_{xz} = \frac{F}{A} = \eta \, \frac{\mathrm{d}v}{\mathrm{d}z} = \eta \ D \ , \tag{2.66}$$

where $\tau_{xz}$ is the shear stress defined as the required force $F$ to move the plate with area $A$ in $x$-direction. The factor $\eta$ denotes the dynamic viscosity coefficient. Fluids that follow Newton's law of viscosity are called **Newtonian fluids**.

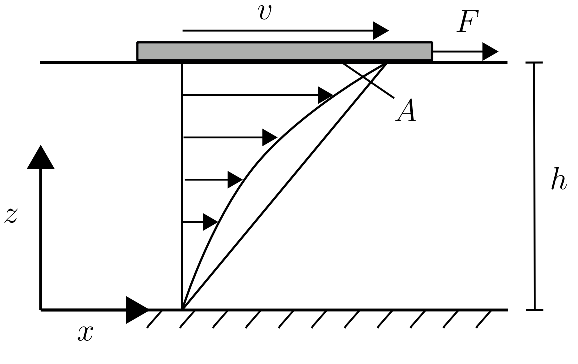

Figure 2.3: A viscous fluid sheared between two plates with apparent linear and non-linear velocity profiles, compare Sigloch [363]

Most organic and inorganic liquids with a low mass exhibit these properties. This means that at constant temperature and pressure, the shear stress is proportional to the shear rate. Many other fluids appearing for example in the field of chemistry, bioengineering and medical science exhibit a material behavior which can not be correctly modeled with the constitutive relation of Newtonian fluids. All fluids which do not follow Newton's law of viscosity are referred to as non-Newtonian. There is a practical way to further divide the group of **non-Newtonian fluids** into three categories according to their properties:

- Fluids for which the relation between the shear stress and shear rate shows a dependence on the duration of the shearing and the flow history. Such material behavior with kind of a memory effect is assigned to *time-dependent fluids*.
- Fluids in which the shear stress is only a function of the actual state, i.e. the viscosity at a fixed temperature and pressure depends purely on the shear rate $\eta = f(\dot{\gamma})$. This behavior does not differ much from Newtonian fluids, thus they are called *generalized Newtonian fluids*.
- Fluids which, in addition to viscous behavior, have elastic properties and can exhibit properties similar to those found in solids, such as recovery and creep, are called *viscoelastic fluids*.

The investigations within the scope of this work are limited to time-independent, purely viscous fluid behavior. For further information on the description of viscoelastic and time-dependent fluids, reference is made to the literature given at the beginning of this subsection. Below, the constitutive laws for Newtonian and generalized Newtonian fluids are outlined.

### 2.5.3 Description for Newtonian fluids

As mentioned above, in case of Newtonian fluids the viscosity $\eta$ is constant at a fixed temperature and pressure, such that the relation between the shear stress $\boldsymbol{\tau}$ and shear rate $\dot{\gamma}$ is linear. This correlation is also illustrated in Figure 2.4 (blue line). Considering three dimensions and with the restriction to incompressible fluids, the shear stress tensor can be written directly as

$$\boldsymbol{\tau} = 2\,\eta\,\nabla^s \boldsymbol{v}\ , \tag{2.67}$$

with the symmetric velocity gradient defined in (2.14). Inserting this into the term for the Cauchy stresses split into its deviatoric and spherical part in (2.34), yields the constitutive equation for the Cauchy stresses given as

$$\boldsymbol{\sigma} = 2\,\eta\,\nabla^s \boldsymbol{v} - p\boldsymbol{I} = 2\,\rho\,\nu\,\nabla^s \boldsymbol{v} - p\,\boldsymbol{I}\ . \tag{2.68}$$

Here, the dynamic viscosity is denoted by $\eta$ (or $\mu$) and the kinematic viscosity is denoted by $\nu = \eta/\rho$. For the description of unsteady flow of incompressible Newtonian fluids, the constitutive relation can be substituted into the balance of momentum principle (2.45), considering that

$$\operatorname{div}\boldsymbol{\sigma} = 2\,\mu\,\operatorname{div}(\nabla^s \boldsymbol{v}) + \nabla p\ . \tag{2.69}$$

In connection with the continuity equation (2.38), this results in the subsequent system of equations

$$\rho\ \boldsymbol{a} + \rho \nabla \boldsymbol{v} \cdot \boldsymbol{v} - 2\mu\ \operatorname{div}(\nabla^s \boldsymbol{v}) + \nabla p - \boldsymbol{f} = \boldsymbol{0}\ , \tag{2.70a}$$

$$\operatorname{div}\boldsymbol{v} = 0\ , \tag{2.70b}$$

with the acceleration vector $\boldsymbol{a} = \frac{\partial \boldsymbol{v}}{\partial t}$, the velocity vector $\boldsymbol{v}$, the pressure $p$ and the fluid density $\rho$. Equations (2.70) are known as the **Navier-Stokes equations** for incompressible fluids and can be written in more detail in index notation as

$$\rho \frac{\partial v_i}{\partial t} + \rho \frac{\partial v_i}{\partial x_k} v_k - \mu \frac{\partial^2 v_i}{\partial x_j \partial x_j} + \frac{\partial p}{\partial x_i} - f_i = 0 \ , \tag{2.71a}$$

$$\frac{\partial v_i}{\partial x_i} = 0 \, . \tag{2.71b}$$

### 2.5.4 Description for non-Newtonian fluids

A wide range of fluids can be described by the before mentioned approach for Newtonian fluids based on a linear relation between the shear stress and the shear rate. All fluids that do not follow Newton's viscosity law, but whose viscosity nevertheless depends only on the current state, i.e. which are not time-dependent, and which in addition do not exhibit elastic behavior, are referred to as generalized Newtonian fluids. For these fluids, the viscosity is a function of the shear rate at the time considered, but does not depend on the deformation history. Thus the shear stress tensor can be expressed as

$$\boldsymbol{\tau} = 2\,\eta(\dot{\gamma})\,\nabla^s \boldsymbol{v} \qquad \text{with} \qquad \dot{\gamma} = \sqrt{2(\nabla^s \boldsymbol{v} : \nabla^s \boldsymbol{v})} \ . \tag{2.72}$$

Utilizing this term, the expression for the Cauchy stresses in (2.34) becomes

$$\boldsymbol{\sigma} = 2\,\eta(\dot{\gamma})\,\nabla^s \boldsymbol{v} - p\boldsymbol{I} \ . \tag{2.73}$$

Analogous to the description of Newtonian fluids, these constitutive equations in combination with the balance principles yield the governing equations to model flows of incompressible generalized Newtonian fluids.

$$\rho\ \boldsymbol{a} + \rho \nabla \boldsymbol{v} \cdot \boldsymbol{v} - 2\mu(\dot{\gamma})\ \operatorname{div}(\nabla^s \boldsymbol{v}) + \nabla p - \boldsymbol{f} = \boldsymbol{0} \ , \tag{2.74a}$$

$$\operatorname{div} \boldsymbol{v} = 0 \ . \tag{2.74b}$$

However, one outstanding question is the determination of the exact dependence of $\eta$ on the shear rate $\dot{\gamma}$. And for this it is fundamental to know the characteristics of the fluid under consideration. The behavior of several non-Newtonian fluids is sketched as an example in Figure 2.4, which illustrates the shear stress - shear rate correlation and the viscosity - shear rate relation. A possible behavior for a generalized Newtonian fluid is shear thinning (green line), where a rearrangement of particles leads to a decreasing viscosity with increasing shear rate. Such fluids, which are also known as pseudoplastic, are e.g. polymers, paint or blood. The opposite behavior is shown by shear thickening fluids, see Figure 2.4 (orange line), such as corn starch in water, where the particles stick together and the viscosity increases with rise in shear rate. These materials are usually also called dilatant fluids. Another generalized Newtonian fluid characteristic is Bingham plastic (purple line). In this case, a certain yield stress is required to initiate the flow.

A variety of different models have been developed in the past to simulate generalized Newtonian fluids, such as the Power-Law model, the Carreau and Carreau-Yasuda model,

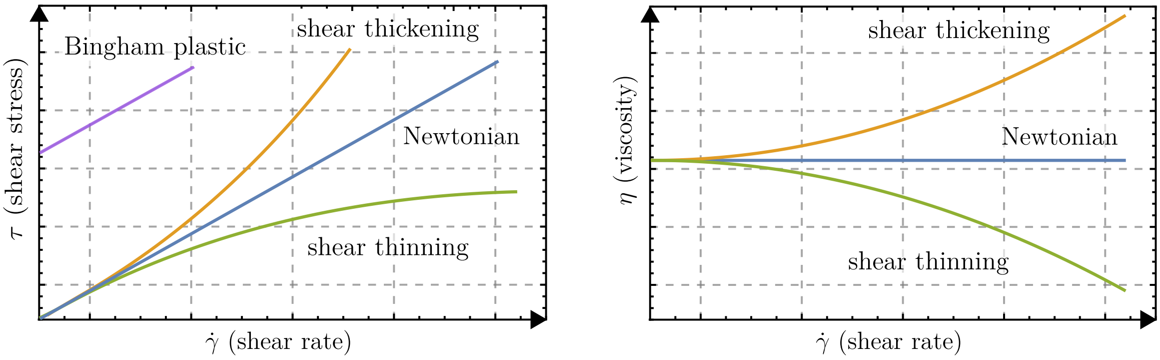

Figure 2.4: Characteristic behavior of different generalized Newtonian fluids: relation between shear rate $\dot{\gamma}$ and shear stress $\tau$ (left) or viscosity $\eta$ (right)

the Prandl-Eyring, the Bingham-Plastic model, and the Cross model. In the framework of this thesis, the **Carreau-Yasuda model** is implemented, in which the relation between the viscosity $\eta$ and the shear rate $\dot{\gamma}$ takes the form

$$\eta(\dot{\gamma}) = \eta_\infty + (\eta_0 - \eta_\infty)\,(1 + (\lambda\,\dot{\gamma})^a)^{\frac{n-1}{a}}\ . \tag{2.75}$$

Herein, $\eta_0$ and $\eta_\infty$ are material constants to define the upper and lower viscosity bounds and $n$, $\lambda$ and $a$ are further model parameters such as e.g. the power law index and the Carreau time constant to describe the fluid rheology. Setting the parameter $n < 1$ or $n > 1$ allows to model shear-thinning or shear-thickening behavior. The constitutive model reduces to a Newtonian fluid for $n = 1$. A wide range of generalized Newtonian fluids can be modeled using this Carreau-Yasuda model as presented in Yasuda et al. [427] and Bird et al. [42], which is an extension of the the Carreau model, see Carreau [91].

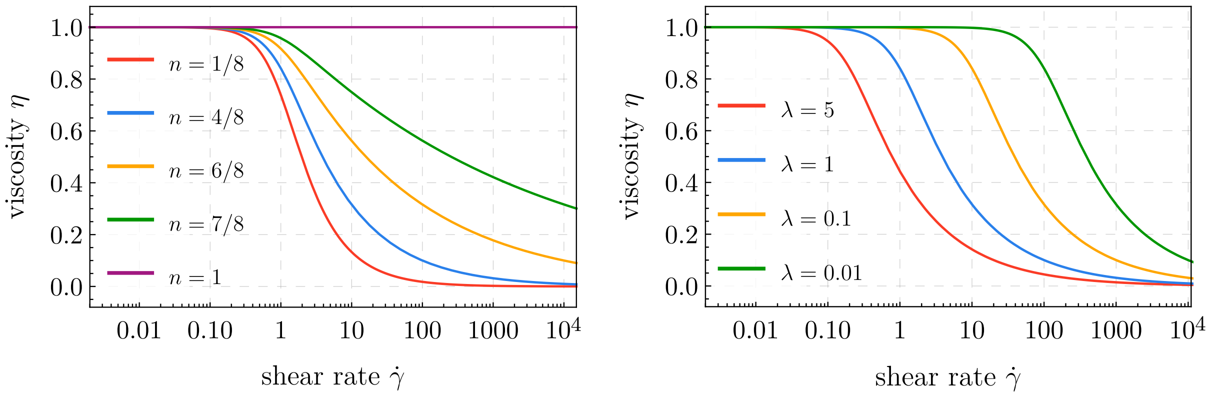

Figure 2.5: Viscosity function for different values of the parameters $n$ (left) and $\lambda$ (right) with the Carreau-Yasuda model

The graphs in Figure 2.5 show exemplarily the curves of the viscosity as a function of the shear rate for different values of the parameters $n$ and $\lambda$. For these plots, the remaining unvaried parameters of the Carreau-Yasuda model are chosen to be $a = 2$, $\eta_0 = 0$, $\eta_\infty = 1$, $n = 0.5$ and $\lambda = 1$. It is visible that $n$ defines the slope of the decline (left) within the power law region and by the parameter $\lambda$ the position of the decline is varied (right). The power law region is defined as the range of shear rate in which the viscosity lies between the upper viscosity limit $\eta_\infty$ and the lower bound $\eta_0$.

# 3 Spatial discretization using least-squares finite elements

There are several numerical methods for solving partial differential equations in the context of mechanics, the best known being the finite difference method, the finite volume method and the finite element method (FEM). The former, which is the oldest of the three methods, is based on a regular mesh and the local application of a Taylor expansion, which can cause problems when dealing with complex structures in multiple dimensions. The finite volume method is very popular, especially for solving flow problems. In this work, the FEM is applied to the spatial discretization, an approach that offers a number of positive properties, being very robust for a wide range of problems (see VALLALA ET AL. [402]) and, moreover, allowing the analysis of complex geometries using arbitrary unstructured meshes. First publications on the finite element method and its immediate preliminaries were released in the 1960th by e.g. TURNER ET AL. [400], ARGYRIS AND KELSEY [5] and ZIENKIEWICZ AND CHEUNG [434], whereas the expression "finite element" was initiated in 1960 by CLOUGH [106]. A detailed historical overview of the background and evolution of model-based simulation methods is given in FELIPPA [146].

## 3.1 The finite element discretization

This section focuses on a spatial discretization based on the least-squares finite element method. Therefore, first the basic components of the finite element method in general like the domain triangulation, the interpolation of the field quantities and the integration over the domain are briefly introduced in the following. This includes also some rules for the construction of the used shape functions based on coordinates in the parameter or physical space. Detailed explanations of the procedure using finite element discretization can be found in the standard works of HUGHES [206], BOFFI ET AL. [59], ZIENKIEWICZ AND TAYLOR [431] and WRIGGERS [424], among others. Following the general principles of the FEM, the procedure for the application of the least-squares finite element method is explained. This is done by discussing some special features of the method, followed by the procedure to generate the LS functionals and completed by the definition of corresponding boundary conditions. Furthermore, the process of incorporating data into numerical calculations based on the LSFEM is described for use in the later course of this work.

**Triangulation**

The main idea of FEM is to calculate an approximate solution of a continuous problem by transforming it into a number of discrete problems. Thus, discretization describes the conversion of the continuous model into a discrete model by means of two main steps. On the one hand, the computational domain $\Omega$ is divided into a finite number $n_{\text{ele}}$ of non-overlapping elements $\Omega^e$ such that

$$\Omega \approx \Omega^h = \bigcup_{e=1}^{n_{\text{ele}}} \Omega^e \ , \tag{3.1}$$

where $\Omega^h$ denotes an admissible triangulation of the domain, see Figure 3.1. On the other hand the fields of the primary variables, such as stresses, velocities and pressure, are approximated by appropriate interpolation functions on each element and globally assembled to a system of algebraic equations. Depending on whether the problem is two-dimensional or three-dimensional, the domain $\Omega_h$ is an area or a volume. The elements are joined by nodes lying on the corners or additionally on the edges, depending on their approximation degree. In this work, triangular and tetrahedral elements are used, with which a suitable discretization of an arbitrary domain is often simpler than with rectangular elements, according to Zienkiewicz and Cheung [434]. For a quantitative measure of the mesh resolution, the parameter $h$ is introduced related to the element size, such that for $h \to 0$ the solution of the continuous problem should be obtained.

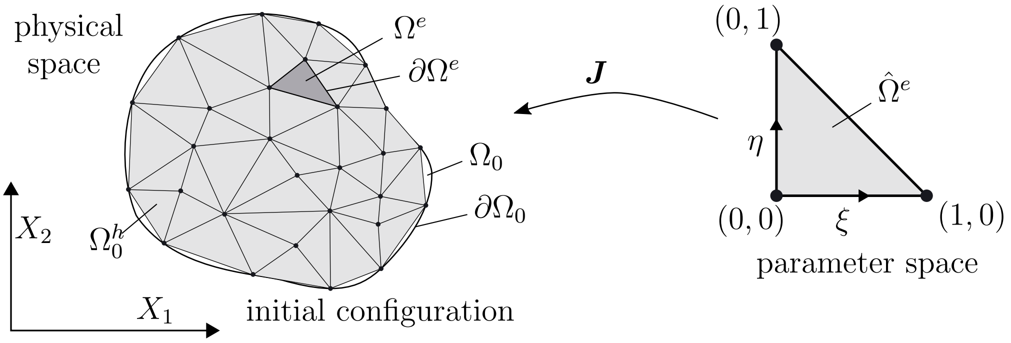

Figure 3.1: Triangulation $\Omega_h$ of an arbitrary domain $\Omega$ in 2D using triangular elements with element domain $\Omega^e$ and mapping from parameter space $\hat{\Omega}_e$ to physical space

**Interpolation**

Within finite element discretization, the main concept is to approximate the primary variables by means of interpolation or shape functions. Hence, considering any field quantity, such as e.g. displacements or velocities, the quantity can be approximated within each element as

$$\boldsymbol{v} \approx \boldsymbol{v}_h = \sum_{I=1}^{n_{v,e}} N^I \boldsymbol{v}^I \,, \tag{3.2}$$

with $N^I$ denoting the shape functions, $\boldsymbol{v}^I$ are the nodal values and $n_{v,e}$ the number of e.g. velocity nodes. When using the classical isoparametric concept, the same interpolation functions are used for the interpolation of the geometry and the fields. The interpolation of the position vectors in the initial and actual configuration can be expressed by

$$\boldsymbol{X} \approx \boldsymbol{X}_h = \sum_{I=1}^{n_e} N^I \boldsymbol{X}^I \qquad \text{and} \qquad \boldsymbol{x} \approx \boldsymbol{x}_h = \sum_{I=1}^{n_e} N^I \boldsymbol{x}^I \,, \tag{3.3}$$

with the material or spatial element nodal coordinates $\boldsymbol{X}^I$ or $\boldsymbol{x}^I$ and the number of geometric nodes $n_e$. The shape functions can be defined in terms of material coordinates in the reference configuration or directly in terms of spatial coordinates in the actual configuration. In the second case, it is important to note that the shape functions in a Lagrange formulation change with the deformation of the body. A common way is to define the interpolation functions in terms of natural coordinates $\boldsymbol{\xi} = \{\xi, \eta, \zeta\}$ in the parameter space. Then an element $\Omega^e$ is typically generated in the two or three dimensional space by an isoparametric mapping from the reference element $\hat{\Omega}^e$ parameterized in $\boldsymbol{\xi}$. The reference element has often an edge length of one, as e.g. a unit triangle with $\hat{\Omega}^e = (0,1)^2$ as illustrated in Figure 3.1.

Based on a reference element in the parameter space, the transformation to the physical space, i.e. to the initial or actual configuration, can be performed using the transformation matrices

$$\boldsymbol{J} = \frac{\partial \boldsymbol{X}}{\partial \boldsymbol{\xi}} \qquad \text{and} \qquad \boldsymbol{j} = \frac{\partial \boldsymbol{x}}{\partial \boldsymbol{\xi}} \; . \tag{3.4}$$

As outlined in Chapter 2, a mapping between the actual and initial configuration can be conducted by means of the deformation gradient $\boldsymbol{F} = \frac{\partial \boldsymbol{x}}{\partial \boldsymbol{X}} = \boldsymbol{j}\boldsymbol{J}^{-1}$. An exemplary transformation of an element $\hat{\Omega}^e$ from the parameter space to the initial configuration with the discretized domain $\Omega_0^h$ is displayed in Figure 3.1.

In the considered least-squares formulation, also the gradient terms of velocities and displacements are required. These can be approximated using the derivatives of the shape functions with respect to the initial or actual configuration, such that

$$\operatorname{Grad} \boldsymbol{v} = \sum_{I=1}^{n_{v,e}} \boldsymbol{v}^I \otimes \nabla_X N^I \tag{3.5}$$

$$\operatorname{grad} \boldsymbol{v} = \sum_{I=1}^{n_{v,e}} \boldsymbol{v}^I \otimes \nabla_x N^I \tag{3.6}$$

with $\nabla_x$ and $\nabla_X$ as defined in Section 2. In case of interpolation functions constructed in the parameter space and defined in terms of natural coordinates, i.e. $N^I(\boldsymbol{\xi})$, the derivatives in the physical space with respect to the initial and actual configuration are defined using the transformation matrices (3.4) as

$$\nabla_X N^I = \boldsymbol{J}^{-T} \nabla_\xi N^I \qquad \text{and} \qquad \nabla_x N^I = \boldsymbol{j}^{-T} \nabla_\xi N^I \tag{3.7}$$

In the context of this work, the displacements, velocities, and pressure are approximated using Lagrange polynomials. Depending on the particular case, the interpolation functions are constructed with the help of a reference element in the parameter space or directly in the current deformed configuration.

For the approximation of the stresses vector-valued Raviart-Thomas interpolation functions are applied. The degrees of freedom of the stresses are denoted by $\boldsymbol{\beta}^J$ with $J$ being the interpolation site. Then the approximation of the primary variable and its divergence read

$$\boldsymbol{\sigma} \approx \boldsymbol{\sigma}_h = \sum_{J=1}^{m} \boldsymbol{\beta}^J \otimes \boldsymbol{\psi}^J \qquad \text{and} \qquad \operatorname{div} \boldsymbol{\sigma} \approx \operatorname{div} \boldsymbol{\sigma}_h = \sum_{J=1}^{m} \operatorname{div} \boldsymbol{\psi}^J \boldsymbol{\beta}^J \; . \tag{3.8}$$

If the Raviart-Thomas shape functions are defined in terms of natural coordinates, again an additional mapping from parameter to physical space is required. Considering vector-valued basis functions $\hat{\boldsymbol{\psi}}^J(\boldsymbol{\xi})$ given in parameter space, the transformations of the functions and its divergence to the physical space are given by

$$\boldsymbol{\psi}^J = \frac{1}{\det \boldsymbol{J}} \boldsymbol{J} \hat{\boldsymbol{\psi}}^J \qquad \text{and} \qquad \operatorname{div} \boldsymbol{\psi}^J = \frac{1}{\det \boldsymbol{J}} \operatorname{div} \hat{\boldsymbol{\psi}}^J \; . \tag{3.9}$$

REMARK: In Section 3.2, some construction rules for the used shape functions and further aspects for the implementation are given. These descriptions are limited to the construction of functions directly based on the current configuration, avoiding the transformation from parameter to physical space. Further information on the construction of basis functions using reference elements and the corresponding mappings can be found in, e.g., RAVIART AND THOMAS [324], BREZZI AND FORTIN [69], ZIENKIEWICZ AND TAYLOR [431], WRIGGERS [424] and BOFFI ET AL. [59].

**Integration**
For the application of the finite element method a numerical integration scheme is required to evaluate the integrals of functions $f$ on each element domain $\Omega_e$. This is performed by means of the Gauss quadrature, which involves evaluating the function at various integration points on the domain, multiplying by corresponding Gauss weights $w_{GP}$, and then summing them up, as

$$\begin{aligned} \int_{\Omega_e} f(\boldsymbol{X})\,\mathrm{d}V &= \int_{\Omega_\triangle} f(\boldsymbol{\xi})\det(\boldsymbol{J}(\boldsymbol{\xi}))\,\mathrm{d}V_\triangle \\ &\approx \sum_{GP=1}^{n_{GP}} f(\boldsymbol{\xi}_{GP})\det(\boldsymbol{J}(\boldsymbol{\xi}_{GP}))\;w_{GP}\,. \end{aligned} \tag{3.10}$$

Herein, the function can be evaluated using the isoparametric concept on the unit reference element at positions $\boldsymbol{\xi}_{GP}$ or directly on the element in the physical space (in the initial configuration at $\boldsymbol{X}$ or the actual configuration at $\boldsymbol{x}$). Depending on the choice of the configuration an appropriate mapping must be considered. To ensure the accuracy of the solution, a sufficiently high number of Gaussian points $n_{GP}$ and suitable integration positions must be chosen. For more information on the appropriate selection, reference is made, for example, to ZIENKIEWICZ AND TAYLOR [431] and WRIGGERS [424] and the references therein.

## 3.2 Interpolation functions

As mentioned above, for the approximation of field quantities in the framework of the finite element method, suitable interpolation functions are required. The choice of appropriate functions depends on the interpolation spaces, which are explained subsequently. Thereafter, the interpolation functions used in this work for the approximation of stresses, velocities and pressure in the different LS formulations are presented. This includes standard Lagrangian interpolation polynomials for conformal discretization in $W^{1,p}(\Omega)$, and vector-valued Raviart-Thomas interpolation functions which ensure conformal discretization in $W^q(\mathrm{div},\Omega)$.

### 3.2.1 Function spaces and norms

In this contribution, the mixed least-squares formulations for fluid and solid dynamics are based on the stresses and velocities and some also include the pressure. For a suitable choice of interpolation functions for these unknowns the standard Sobolev $\mathcal{W}^{k,p}(\Omega)$ and Hilbert spaces are considered. The Sobolev spaces are defined based on the Lebesgue space $L^p(\Omega)$ for $1 \leq p < \infty$, which is the space of all measurable functions $y : \Omega \rightarrow \mathbb{R}$ which are $p$-integrable on a domain $\Omega$, such that

$$L^p(\Omega) := \left\{ y : \int_\Omega |\,y\,|^p\;\mathrm{d}V \quad < \infty \right\}\,. \tag{3.11}$$

The corresponding norm is defined by

$$\|y\|_{L^p(\Omega)} := \left( \int_\Omega |\, y \,|^p \, \mathrm{d}V \right)^{1/p} . \tag{3.12}$$

The Sobolev spaces $\mathcal{W}^{k,p}(\Omega)$ with $1 \leq p < \infty$ and $k \in \mathbb{N}_0$ consist of functions where not only the functions, but also their weak derivatives $D^\alpha y$ are in $L^p(\Omega)$. With the weak derivatives given by

$$D^\alpha \, y = \frac{\partial^{|\alpha|} y}{\partial x_1^{\alpha_1} \cdots \partial x_d^{\alpha_d}} , \tag{3.13}$$

where the index $\alpha \in \mathbb{N}_0^d$ and $|\alpha| = \alpha_1 + \cdots + \alpha_d$, the Sobolev spaces are defined as

$$\mathcal{W}^{k,p}(\Omega) := \{ y \in L^p(\Omega) : D^\alpha y \in L^p(\Omega) \quad \text{for all} \quad |\alpha| \leq k \} . \tag{3.14}$$

Therein, $k$ denotes the differentiation index and $p$ defines the norm. The Sobolev space is equipped with the norm

$$\|y\|_{\mathcal{W}^{k,p}(\Omega)} := \left( \|y\|^p_{L^p(\Omega)} + \sum_{\alpha=1}^{k} \|D^\alpha y\|^p_{L^p(\Omega)} \right)^{1/p} , \tag{3.15}$$

containing also constraints for the derivatives of the functions. Therein, the norm for vector functions $\boldsymbol{u} \in L^p(\Omega)$ and second-order tensor functions $\boldsymbol{B} \in L^p(\Omega)$ is defined based on (3.11) as

$$||\boldsymbol{b}||_{L^2(\Omega)} := \left( \int_\Omega \boldsymbol{b} \cdot \boldsymbol{b} \, \mathrm{d}V \right)^{1/2} \quad \text{and} \quad ||\boldsymbol{B}||_{L^2(\Omega)} := \left( \int_\Omega \boldsymbol{B} : \boldsymbol{B} \, \mathrm{d}V \right)^{1/2} . \tag{3.16}$$

Considering the particular case $p = 2$ the Lebesgue and Sobolev spaces are Hilbert spaces, which can be expressed as

$$H^k(\Omega) = \mathcal{W}^{k,2}(\Omega) \quad \text{for} \quad k \in \mathbb{N}_0 . \tag{3.17}$$

and per definition $H^0(\Omega) = L^2(\Omega)$. Suitable function spaces in case of linear elasticity or Stokes flow for unknown field variables, such as velocities, stresses and pressure, are e.g. the spaces $\mathcal{W}^{1,2}(\Omega)$, $\mathcal{W}^2(\mathrm{div}, \Omega)$ and $L^2(\Omega)$, respectively, with

$$\mathcal{W}^{1,2}(\Omega) = H^1(\Omega) = \big\{ y \in L^2(\Omega) : \nabla y \in L^2(\Omega) \ \big\} \tag{3.18}$$

and

$$\mathcal{W}^2(\mathrm{div}, \Omega) = H(\mathrm{div}, \Omega) = \{ y \in L^2(\Omega) : \mathrm{div}\, y \in L^2(\Omega) \} . \tag{3.19}$$

However, the mentioned function spaces are also used in the context of this work in the case of nonlinear formulations, compare e.g. Müller et al. [284].

### 3.2.2 Lagrange interpolating polynomials for triangles

For conforming approximations in $\mathcal{W}^{1,2}(\Omega)$, where primary variables as well as their derivatives have to satisfy the $L^2(\Omega)$-norm, see (3.18), standard Lagrange interpolation functions are used. Functions of Lagrange type are constructed as products of polynomials in one to three coordinates depending on the considered dimension. These polynomials are build in such a way that they have a value of unity at the considered node and zero at all other coordinates. With a restriction to two dimensions and the spatial coordinates denoted as $\boldsymbol{x} = \{x, y\}$ in this chapter, this can be expressed as

$$N^I(\boldsymbol{x}_J) = \begin{cases} 1 & \text{if} \quad I = J \\ 0 & \text{if} \quad I \neq J \end{cases} \quad . \tag{3.20}$$

Therein, indices $I$ and $J$ denote the number of the considered node or shape function. A Lagrange polynomial of order $n-1$ in one dimension can be written as

$$N^I(x) = \prod_{\substack{J=1 \\ J \neq I}}^{n} \frac{x - x_J}{x_I - x_J} \ . \tag{3.21}$$

An extension to two or three dimensions is simply obtained by taking the product of these polynomials given in two or three coordinates, such that e.g.

$$N^I(x, y) = N^J(x)\, N^K(y) \qquad \text{or} \qquad N^I(x, y, z) = N^J(x)\, N^K(y)\, N^L(z) \ . \tag{3.22}$$

In the following, the construction rules are exemplarily given for shape functions on triangles in two dimensions as illustrated in Figure 3.2. These elements are referred to as $P_k$ in this work, with $k \in \mathbb{R}^2$ denoting the polynomial order. The resulting number of nodes in each element is given by $n = (k+1)(k+2)/2$ and the order for linear, quadratic and cubic elements is depicted in Figure 3.2.

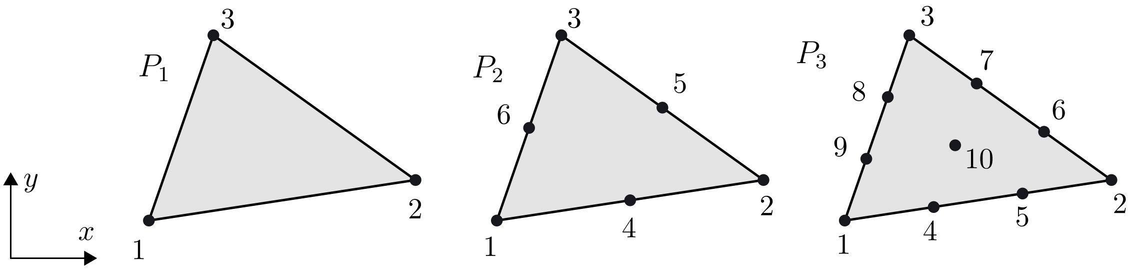

Figure 3.2: Order of corner, edge and inner nodes in triangular elements $P_k$ with $k = \{1, 2, 3\}$ for linear, quadratic and cubic Lagrange polynomials (left to right)

According to Zienkiewicz and Taylor [431], several normalized coordinates for triangles are introduced at this points. So-called area coordinates of an arbitrary point $B$ in a triangle, see Figure 3.3, are defined as the ratio of areas, such that

$$L_i = \frac{A_i}{A_\triangle} \quad \text{for} \quad i = \{1, 2, 3\} \ , \tag{3.23}$$

where $A_i$ are subareas of the considered triangle and $A_\triangle$ is the total element area. In terms of nodal coordinates using the element vertices $\boldsymbol{x}_I = (x_I, y_I)$ with $I = \{1, 2, 3\}$, these area coordinates are given as

$$L_i(x, y) = \frac{1}{2A_\triangle}(a_i + b_i x + c_i y) \quad \text{for} \quad i = \{1, 2, 3\} \tag{3.24}$$

with

$$A_{\triangle} = \frac{1}{2} \det \begin{bmatrix} 1 & x_1 & y_1 \\ 1 & x_2 & y_2 \\ 1 & x_3 & y_3 \end{bmatrix} \ , \tag{3.25}$$

and

$$\begin{aligned} a_1 &= x_2 y_3 - x_3 y_2 \\ b_1 &= y_2 - y_3 \\ c_1 &= x_3 - x_2 \ . \end{aligned} \tag{3.26}$$

For a linear triangle, the Lagrange shape functions are identical to the area coordinates, i.e. $N^I = L_i$ for $I = i = \{1, 2, 3\}$. The resulting functions in the actual configuration with spatial coordinates $\boldsymbol{x} = \{x, y\}$ are given by

$$\begin{aligned} N^1(x,y) = L_1(x,y) &= \frac{1}{2A_{\triangle}}(x_2y_3 - x_3y_2 + (y_2 - y_3)x + (x_3 - x_2)y) \\ N^2(x,y) = L_2(x,y) &= \frac{1}{2A_{\triangle}}(x_3y_1 - x_1y_3 + (y_3 - y_1)x + (x_1 - x_3)y) \\ N^3(x,y) = L_3(x,y) &= \frac{1}{2A_{\triangle}}(x_1y_2 - x_2y_1 + (y_1 - y_2)x + (x_2 - x_1)y) \ , \end{aligned} \tag{3.27}$$

where $x_I$ and $y_I$ with $I = \{1, 2, 3\}$ are the coordinates of the corner nodes $P^j$ as specified in Figure 3.3.

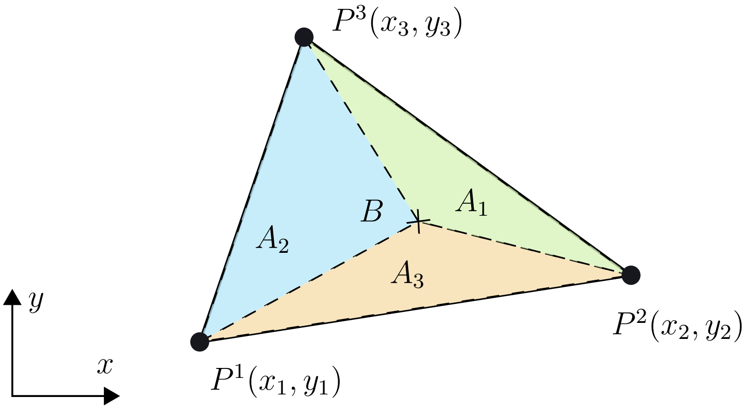

Figure 3.3: Area coordinates for construction of Lagrange shape functions on triangles, according to Zienkiewicz and Taylor [431]

High-order approximation functions, e.g., for quadratic and cubic triangles, with restriction to straight-edged elements, can be constructed using products of the defined area coordinates. Depending on the regarded type or position of the node (corner, edge or interior) the construction rules, following Zienkiewicz and Taylor [431], read for elements $P_2$ with quadratic polynomials

$$\begin{aligned} N^i(x,y) &= (2L_i - 1)L_i \quad \text{for} \quad i = \{1,2,3\} \\ N^4(x,y) &= 4L_1L_2 \\ N^5(x,y) &= 4L_2L_3 \\ N^6(x,y) &= 4L_3L_1 \end{aligned} \tag{3.28}$$

Further Lagrange type shape functions for cubic triangular elements in two dimensions are listed in Appendix A.1. These formulations for the construction of high-order interpolation functions are based on early publications by Argyris et al. [4]. Further details can be found, for example, in Silvester [365] and Taylor [385].

### 3.2.3 Raviart-Thomas interpolation functions for triangles

For a conforming approximation in $\mathcal{W}^2(\text{div}, \Omega)$, where primary variables as well as their divergence have to satisfy the $L^2(\Omega)$-norm, see (3.19), vector-valued Raviart-Thomas functions are selected. In the context of this work, these properties apply to the Cauchy stresses in the mixed LS formulations for solid and fluid. The application of Raviart-Thomas interpolation functions for the stresses leads to a continuous approximation of the normal components of these quantities, but without restrictions on the tangential components, see e.g. Raviart and Thomas [324] or Ervin [140]. In the following, the construction of Raviart-Thomas functions for triangular elements in two dimensions is discussed. These elements are referred to as $RT_m$ with the number and position of interpolation sites as depicted exemplarily for $m = \{0, 1, 2\}$ in Figure 3.4.

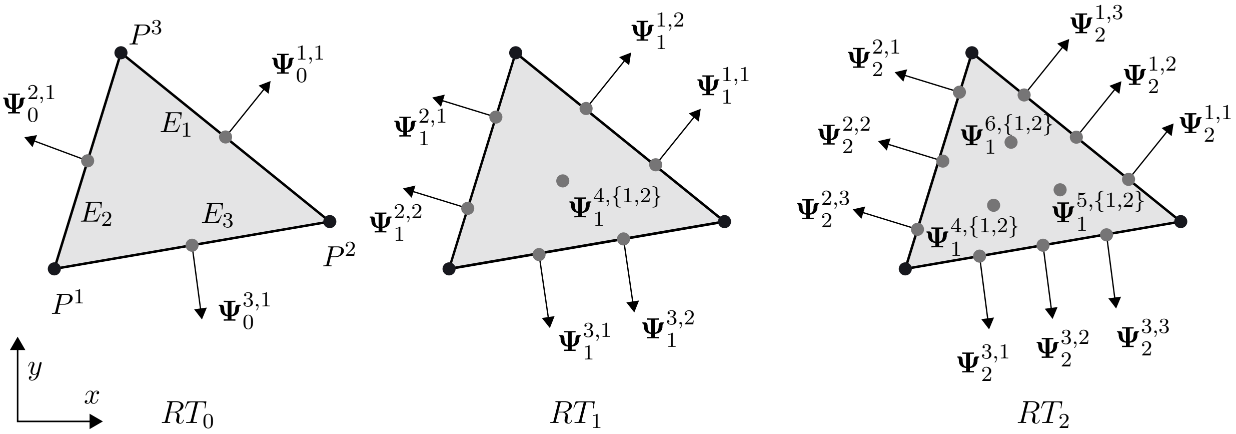

Figure 3.4: Order of interpolation sites and naming of Raviart-Thomas shape functions for elements $RT_0$, $RT_1$ and $RT_2$

The vector-valued functions are denoted $\boldsymbol{\Psi}_m^{j,i}$, with $j \leq 3$ indicating the number of the associated edge $E_j$, $i$ the respective node on this edge, and $m$ the approximation order. The edges are numbered such that the indices always match those of the opposite vertex, e.g. $E_1$ is the edge opposing $P^1$. All functions with $j > 3$ are related to internal interpolation points, with two nodes $i = \{1, 2\}$ at the same position. Several procedures exist to build vector-valued $RT_m$ functions. A common way is the solution of equation systems based on the evaluation of inner and outer moments, cf. Brezzi and Fortin [69], Boffi et al. [59], Schwarz [345], Steeger [371] or Igelbücher [211], for instance.

Here, the approach of Bahriawati and Carstensen [14] for so-called edge-basis functions is applied. Therein, the local definition of the lowest-order Raviart-Thomas functions $\boldsymbol{\Psi}_0^{j,i}$ for a triangle $T$ with one node per edge, i.e. $i = 1$, in terms of actual coordinates $\boldsymbol{x} \in T$ is given as

$$\boldsymbol{\Psi}_0^{j,1} = a_j \frac{|E_j|}{2A_\triangle}(\boldsymbol{x} - P^j) \qquad \text{for} \quad j = \{1, 2, 3\} \ . \tag{3.29}$$

This definition contains the lengths of the element edges $E_j$, which are opposite to the vertices $P^j$ and the area of the triangle $A_\triangle$ as defined in (3.25). Furthermore, a scalar value $a_j$ is included, which contains information on the edge orientation and is defined as

$$a_j = \boldsymbol{n}_j \cdot \boldsymbol{n}_{Ej} = \begin{cases} 1 & \text{if } \boldsymbol{n}_{Ej} \text{ points outward} \\ -1 & \text{otherwise}\ , \end{cases} \tag{3.30}$$

with outer unit normal vectors $\boldsymbol{n}_j$ on the element edges and unit normal vectors $\boldsymbol{n}_{Ej}$, having a globally defined orientation pointing outward or inward of the element.

High-order shape functions of Raviart-Thomas type can be constructed based on the low-order functions $\boldsymbol{\Psi}_0^{j,1}$ and Lagrange functions as defined in (3.27) or (3.28). But therefore, Lagrange polynomials are not formed with respect to the vertices of the element under consideration. Instead, new triangles are generated within the base element. These inner triangles are created based on additional interpolation sites which are located on the edges and inside the element. For the element $RT_1$, for example, two nodes per edge denoted by $P^{j,i}$ and one internal node $P^{I,1}$ on the centroid are added. The placement of the supplementary interpolation points and the construction of the inner triangles for the definition of the Lagrange basis functions is illustrated in Figure 3.5 for elements $RT_1$ and $RT_2$.

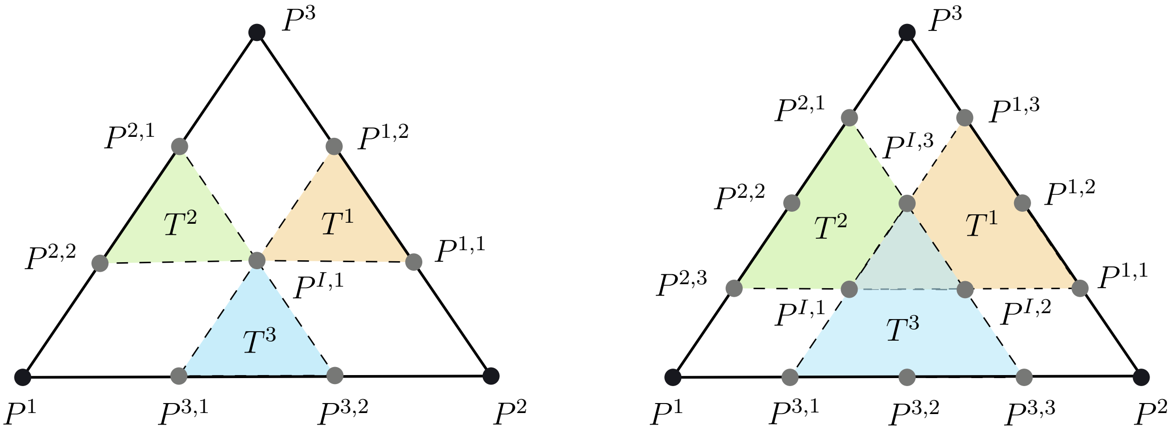

$RT_1$ $RT_2$

Figure 3.5: Construction of Raviart-Thomas functions for $RT_1$ and $RT_2$ based on $\boldsymbol{\Psi}_0^{j,1}$ and Lagrange functions defined on subtriangles

In case of $m > 0$ the vector-valued shape functions on the edges in terms of physical coordinates $\boldsymbol{x} \in T$ can be formed as

$$\boldsymbol{\Psi}_m^{j,i}(\boldsymbol{x}) = \boldsymbol{\Psi}_0^{j,1}(\boldsymbol{x})\ N_m^{j,P^{j,i}}(\boldsymbol{x}) \qquad \text{for} \quad j = \{1,2,3\}\ , \tag{3.31}$$

again with index $i$ identifying the respective nodes on each edge $j$ and the interpolation order $m$. The additional shape functions for internal nodes, i.e. $j > 3$, can be constructed as

$$\boldsymbol{\Psi}_m^{j,i}(\boldsymbol{x}) = \boldsymbol{\Psi}_0^{i+1,1}(\boldsymbol{x})\ N_m^{i+1,P^{I,j-3}}(\boldsymbol{x}) \tag{3.32}$$

The Lagrange shape functions are build as specified in Section 3.2.2 for each individual sub-triangle $T^i$ with $i = \{1,2,3\}$ in the base element as depicted in Figure 3.5, under consideration of added edge nodes $P^{j,i}$ and inner nodes $P^{I,k}$. For the evaluation of the element $RT_1$, for example, three sets of linear Lagrange polynomials are needed and the calculation of element $RT_2$ requires three sets of quadratic Lagrange polynomials.

## 3.3 The least-squares finite element method

In this part, some aspects of the FEM based on the mixed least-squares method are considered. Among other things, the positive characteristics as well as the disadvantages of the least-squares finite element method are briefly described. Furthermore, the fundamentals consisting in the construction of a least-squares functional and its variations to solve the minimization problem are outlined. This is completed with some remarks on the boundary conditions. In addition, the strategy for assembling data into numerical simulations based on the LSFEM is described. The implementation of this technique is demonstrated in Section 5 using various examples dealing with the calculation of non-Newtonian fluid flow. For more detailed information concerning the LSFEM in general, reference is made to the literature of e.g. EASON [136], JIANG [219], KAYSER-HEROLD AND MATTHIES [229] and BOCHEV AND GUNZBURGER [54].

### 3.3.1 Advantages and disadvantages

The purpose of this section is to briefly present the properties of the mixed least-squares finite element method focussing on most relevant advantages and disadvantages. Over the past decades, the LSFEM has gained popularity especially for the simulation of flow problems. A justification for this lies in some numerical advantages over, e.g., the mixed Galerkin method. The application of the LSFEM results in minimization problems with positive (semi-)definite coefficient matrices even in the case of differential equations with non self-adjoint operators, see for example BOCHEV AND GUNZBURGER [54]. This is of interest, e.g., for the applicability of different iterative solution strategies. Therefore, it is promising in particular for the solution of the Navier-Stokes equations. Such second-order systems can be transformed to first-order systems by introducing new variables, which allows to apply $\mathcal{C}^0-$continuous approximation functions. Therein, further arises the advantage of the possibility to choose physically meaningful solution variables of interest. This is particularly relevant for the present work, since it enables the construction of formulations for fluid and solid dynamics based on the same quantities. The formulations proposed in the following are expressed, e.g., in terms of stresses and velocities, which are directly related to the coupling conditions when dealing with fluid-structure interaction problems. With conforming discretization of the velocities and stresses this leads to an automatic fulfillment of the coupling constraints avoiding an explicit treatment along the interface as explained in Section 8.

Moreover, since the LSFEM as a minimization approach circumvents the so-called Ladyzhenskaya-Babuška-Brezzi (LBB) condition, based on LADYZHENSKAYA [249], BABUŠKA [13] and BREZZI [67], there are no restrictions on the choice of polynomial order to interpolate the field quantities considering the stability. This can be regarded as one of the main advantages over the mixed Galerkin method, the application of which demands the fulfillment of the LBB condition, whose proof is usually nontrivial, see e.g. BRAESS [66] or BOCHEV AND GUNZBURGER [54]. Several approaches are based on stabilization techniques to circumvent this requirement and therefore enable the use of standard finite elements. Examples can be found in Brooks and Hughes [71], Hughes et al. [208] and Brezzi and Douglas [68].

A further advantage of the mixed LSFEM is the availability of an a posteriori error estimator without additional costs, because the LS functional itself can be used as such an error measure. This may be very useful for the application of adaptive mesh refinement algorithms as investigated for various fluid and solid formulations, for example, by Starke [369], Münzenmaier and Starke [286], Müller et al. [284], Münzenmaier [285], Müller [282], Bringmann and Carstensen [70] and Nisters [294]. Another feature exploited in this thesis, is the straightforward possibility, with the help of the LSFEM, to include data without additional computational effort into numerical simulations. Thus, experimental measurements and numerical simulations can be combined very easily to achieve results as realistic as possible. Further details on the implementation of data assimilation are given in Section 3.4 and the application in two and three dimensional problems is presented in Section 5.

Despite these advantages, the least-squares FEM plays only a minor role compared to, e.g., the mixed Galerkin method. Although the research of both methods started at about the same time, see Lynn and Arya [263], Zienkiewicz et al. [433] and for an overview Eason [136], LSFEMs could not prevail. One major cause for this is presumably that least-squares elements with shape functions based on low-order polynomials have only a moderate approximation quality, cf. e.g. Pontaza [309], Pontaza and Reddy [312] and Schwarz et al. [348]. Consequently, in the last decades preference was given to other methods that achieve accurate results even with low interpolation orders, and little attention was paid to the LSFEM. Besides the possibility of improvement by increasing the approximations order using e.g. spectral high-order finite elements, different approaches were investigated, such as modifying the LS functional or choosing different weighting terms. The modification are often based on extending the functional by additional terms that are mathematically redundant but lead to an improvement in finite element performance.

In the context of poor approximation quality, a well-known problem of LSFEM applied to fluid dynamics is that mass conservation is not always automatically fulfilled, see e.g. Chang and Nelson [97], Deang and Gunzburger [119] and Bolton and Thatcher [61]. This issue has been investigated extensively, with the result that mass loss can be significantly limited by the use of weighting terms, as for example in Deang and Gunzburger [119], Bolton and Thatcher [61] and Lee and Chen [260]. Another possibility to improve the conservation of mass is to apply high-order interpolation functions, see e.g. Pontaza and Reddy [313], Proot and Gerritsma [315] and Kayser-Herold and Matthies [230]. Further investigations on this subject have been carried out by, e.g. Chang and Nelson [97], Heys et al. [191; 192] and Nickaeen et al. [293], to name but a few. The listed works include not only the approaches already mentioned, but also the application of Lagrange multipliers to enforce continuity. Thus, of course, it is possible to obtain accurate results, but generally more degrees of freedom are needed than with other methods. This limits competitiveness of the LSFEM due to the additional computing costs.

Due to the general construction of the LSFEM based on the minimization of the sums of several residuals related to the partial differential equations (PDEs), arises the possibility, but in some cases also necessity, to introduce weightings. The influence of the individual residual terms on the solution can be determined by different weighting factors. These weightings can be chosen independently and freely for each of the considered differential equations. The choice may have a significant impact on the quality of the solution, and this can be considered both an advantage and disadvantage of the method. A problem can occur due to the fact that appropriate weights depend on many factors, such as the LS formulation, the problem considered and parameters used, and a precise determination of the best terms is difficult when the exact solution is often unknown. A number of different approaches to determine weighting factors have been presented in the literature in the past years. SALONEN AND FREUND [334] and KAYSER-HEROLD [227] apply matrix weights computed from the analytical solution of the diffusion problem under consideration. As a result, a significant increase in solution accuracy can be observed. But for complex problems such matrices are complicated or impossible to find. Other approaches by BOCHEV AND GUNZBURGER [54], DEANG AND GUNZBURGER [119] and BOCHEV [46], for example, are based on mesh-dependent weights or equivalent norms. Furthermore, JIANG [218; 219], RASMUSSEN [321], RASMUSSEN ET AL. [323], LEE AND CHEN [260] and JEONG AND LEE [215] analyze different weights taking into account, among others, nonlinear factors, weighted norm LSFEM and local error estimates based on the LS residuals. The choice of weights depending on the respective differential equations and their units leads to an approach with physically motivated weightings. This is considered, e.g., by BELL AND SURANA [35; 36], WINTERSCHEIDT AND SURANA [421] and HEYS ET AL. [189], when solving fluid flow problems based on the Navier-Stokes equations. In KAYSER-HEROLD [227], KAYSER-HEROLD AND MATTHIES [231], NISTERS [294] and AVERWEG ET AL. [9], for instance, physical weights are used in LS formulations for coupled FSI problems.

### 3.3.2 Construction aspects of the LSFEM for nonlinear systems

The general idea of the LSFEM is the construction of a functional $\mathcal{F}(\boldsymbol{b})$ by applying, for example, the quadratic $L^2$-norm to a first-order system of differential equations consisting of at least one residual term $\mathcal{R}(\boldsymbol{b})$ defined on a domain $\Omega$. Then, a function $\boldsymbol{b}$ in a suitable space $\boldsymbol{V}(\Omega)$ must be found, that minimizes the constructed functional $\mathcal{F}(\boldsymbol{b})$ defined by

$$\mathcal{F}(\boldsymbol{b}) := \frac{1}{2}\sum_i ||\omega_i \; \mathcal{R}_i(\boldsymbol{b})||^2_{L^2(\Omega)} \; . \tag{3.33}$$

Herein, $\omega_i$ denote residual weighting functions of each residual term $\mathcal{R}_i(\boldsymbol{b})$, which must be appropriately selected due to their essential contribution to the efficiency of the least-squares approach. Furthermore,

$$||\bullet||^2_{L^2(\Omega)} = (\bullet,\bullet)_\Omega = \int_\Omega |\bullet|^2 \mathrm{d}V \tag{3.34}$$

is the quadratic $L^2$-norm on the domain $\Omega \subset \mathbb{R}^3$ with its boundary $\partial\Omega$ and the $L^2(\Omega)$ scalar product $(\bullet,\bullet)_\Omega$.

This minimization problem can be solved under the condition that the first variation of the least-squares functional $\mathcal{F}$ with respect to the unknowns $\boldsymbol{b}$ vanishes, i.e.

$$\delta_{\boldsymbol{b}}\mathcal{F}(\boldsymbol{b};\delta\boldsymbol{b}) = \lim_{\epsilon\rightarrow 0}\frac{\mathcal{F}(\boldsymbol{b}+\epsilon\;\delta\boldsymbol{b}) - \mathcal{F}(\boldsymbol{b})}{\epsilon} = 0 \qquad \forall\; \delta\boldsymbol{b} \in \boldsymbol{V}. \tag{3.35}$$

Note that in the case of, e.g. the Navier-Stokes equations or a hyperelastic material law, the underlying governing equations are nonlinear. Such a system, consisting of nonlinear PDEs, can be solved by first constructing the least-squares functional based on (3.33) leading to

$$\mathcal{F}(\boldsymbol{b}) = \frac{1}{2}(\mathcal{R}(\boldsymbol{b}), \mathcal{R}(\boldsymbol{b}))_\Omega \;, \tag{3.36}$$

where the weighting factor has been omitted at this point for clarity. Then Newton's scheme is employed to find the root of the first variation of that functional, see (3.35). The first variations of the nonlinear functional in (3.36) read

$$\delta_{\boldsymbol{b}}\mathcal{F}(\boldsymbol{b}; \delta\boldsymbol{b}) = (\mathcal{R}(\boldsymbol{b}), \mathcal{D}\mathcal{R}(\boldsymbol{b}) \cdot \delta\boldsymbol{b})_\Omega \;, \tag{3.37}$$

with the Gâteaux derivative $\mathcal{D}$. The required linearization to apply Newton's method, results in the second variations

$$\Delta_{\boldsymbol{b}}\delta_{\boldsymbol{b}}\mathcal{F}(\boldsymbol{b}; \delta\boldsymbol{b}, \Delta\boldsymbol{b}) = (\mathcal{D}\mathcal{R}(\boldsymbol{b}) \cdot \Delta\boldsymbol{b}, \mathcal{D}\mathcal{R}(\boldsymbol{b}) \cdot \delta\boldsymbol{b})_\Omega + (\mathcal{R}(\boldsymbol{b}), \mathcal{D}^2\mathcal{R}(\boldsymbol{b}) \cdot \Delta\delta\boldsymbol{b})_\Omega \;. \tag{3.38}$$

The resulting system can then be solved using the iterative algorithm of Newton's method, which reads

$$\delta_{\boldsymbol{b}}\mathcal{F}(\boldsymbol{b}; \delta\boldsymbol{b}) + \Delta_{\boldsymbol{b}}\delta_{\boldsymbol{b}}\mathcal{F}(\boldsymbol{b}; \delta\boldsymbol{b}, \Delta\boldsymbol{b}) = 0 \qquad \forall\; \delta\boldsymbol{b} \in \boldsymbol{V}, \tag{3.39}$$

where (3.37) and (3.38) are applied. Note, that another approach to the one presented above is also possible by first linearizing the residuals and then constructing the functional from these linearized equations. In this case the term $(\mathcal{R}(\boldsymbol{b}), \mathcal{D}^2\mathcal{R}(\boldsymbol{b}) \cdot \Delta\delta\boldsymbol{b})_\Omega$ in the second variation (3.38) is not present.

### 3.3.3 Boundary and initial conditions

To solve an initial boundary value problem, besides the governing equations, the definition of boundary conditions is required. Typically, Dirichlet and Neumann type boundaries are applied, such that the boundary $\partial\Omega$ of an area $\Omega$ can be divided into

$$\partial\Omega = \partial\Omega_N \cup \partial\Omega_D \qquad \text{and} \qquad \partial\Omega_N \cap \partial\Omega_D = \emptyset \;. \tag{3.40}$$

Dirichlet boundary conditions are also referred to as essential boundary conditions and related to the primary variables, whereas Neumann also denoted as natural boundary conditions are related to the derivatives of primary variables. Considering the mixed LS formulations in terms of velocities $\boldsymbol{v}$, stresses $\boldsymbol{\sigma}$, and possibly pressure $p$, all boundary conditions can be considered essential, and whenever the definition of boundary conditions is provided throughout this thesis, they will be imposed in a strong sense. The corresponding boundary conditions, depending on the formulation used and the primary variables included, read as follows

$$\boldsymbol{v} = \boldsymbol{v}_D \qquad \text{on } \partial\Omega_{Dv} \times (0,T] \qquad \text{with} \qquad \partial\Omega_{Dv} \subseteq \partial\Omega \;, \tag{3.41a}$$

$$\boldsymbol{\sigma} \cdot \boldsymbol{n} = \boldsymbol{t}_D \qquad \text{on } \partial\Omega_{Ds} \times (0,T] \qquad \text{with} \qquad \partial\Omega_{Ds} \subseteq \partial\Omega \;, \tag{3.41b}$$

$$p = p_D \qquad \text{on } \partial\Omega_{Dp} \times (0,T] \qquad \text{with} \qquad \partial\Omega_{Dp} \subseteq \partial\Omega \;. \tag{3.41c}$$

For time-dependent problems, additional initial conditions at time $t = t_0$ are required which, in the case of the formulations used here, specify the velocities and, depending on the time discretization applied, possibly also the accelerations $\boldsymbol{a}$ or displacements $\boldsymbol{u}$. According initial conditions, depending on the applied formulation and time integration scheme, are denoted as

$$\boldsymbol{v}(t_0) = \boldsymbol{v}_0 \qquad \text{on } \Omega \quad \text{at} \quad t = t_0 \ , \tag{3.42a}$$

$$\boldsymbol{a}(t_0) = \boldsymbol{a}_0 \qquad \text{on } \Omega \quad \text{at} \quad t = t_0 \ , \tag{3.42b}$$

$$\boldsymbol{u}(t_0) = \boldsymbol{u}_0 \qquad \text{on } \Omega \quad \text{at} \quad t = t_0 \ . \tag{3.42c}$$

### 3.3.4 Interpolation spaces for mixed least-squares formulations

The choice of the approximation spaces for the LS stress-velocity formulations for solid and fluid dynamics presented in the following chapters is based on a conforming spatial discretization of the stresses in $H(\text{div})$ and the velocities in $H^1$. Thus, in the dimension $d$ the following finite element spaces are selected

$$\boldsymbol{V}_k^h = \{\boldsymbol{v} \in H^1(\Omega)^d : \boldsymbol{v}|_{\Omega_e} \in P_k(\Omega_e)^d \ \ \forall\, \Omega_e\} \subseteq \boldsymbol{V} \ , \tag{3.43}$$

$$\boldsymbol{W}_m^h = \{\boldsymbol{\sigma} \in H(\text{div}, \Omega)^d : \boldsymbol{\sigma}|_{\Omega_e} \in RT_m(\Omega_e)^d \ \ \forall\, \Omega_e\} \subseteq \boldsymbol{W} \, , \tag{3.44}$$

where $P_k(\Omega_e)$ are Lagrange interpolation polynomials of order $k$, and $RT_m(\Omega_e)$ represent vector-valued Raviart-Thomas interpolation functions of order $m$, see e.g. RAVIART AND THOMAS [324] or BREZZI AND FORTIN [69].

Additionally to the mixed LS stress-velocity formulations, a stress-velocity-pressure formulation for non-Newtonian fluid flow in 3D is applied in this thesis. Therefore, standard finite element interpolations for the velocities, stresses and pressure are chosen in the element spaces

$$\boldsymbol{W}_k^h = \{\boldsymbol{\sigma} \in H^1(\Omega)^3 : \boldsymbol{\sigma}|_{\Omega_e} \in P_k(\Omega_e)^3 \ \ \forall\, \Omega_e\} \subseteq \boldsymbol{W} \, , \tag{3.45}$$

$$\boldsymbol{V}_m^h = \{\boldsymbol{v} \in H^1(\Omega)^3 : \boldsymbol{v}|_{\Omega_e} \in P_m(\Omega_e)^3 \ \ \forall\, \Omega_e\} \subseteq \boldsymbol{V} \ , \tag{3.46}$$

$$\boldsymbol{Q}_n^h = \{p \in L^2(\Omega)^3 : p|_{\Omega_e} \in P_n(\Omega_e)^3 \ \ \forall\, \Omega_e\} \subseteq \boldsymbol{Q} \, , \tag{3.47}$$

with $P_i(\Omega_e)^3$ denoting Lagrangian interpolation polynomials of order $i$.

## 3.4 Assimilation of data to numerical simulations

Assimilating data from experiments into numerical simulations offers a way to reduce inaccuracies and uncertainties in numerical models. This can be particularly helpful in the field of fluid dynamics when considering very complex problems and can lead to improved and more realistic results. A variety of reasons exist for data assimilation into numerical modeling, from both experimental and numerical perspectives. For example, numerics can be used to complete results from experiments. It enables to fill gaps caused by the fact that certain quantities are difficult or impossible to measure, or because the measurement intervals cannot be reduced in time or space. Experiments, in turn, can also be a tool to advance numerical calculations. By adding experimental data, discretization or model errors can be decreased and the solution can be adjusted to get closer to reality. Of course, reducing discretization errors requires very accurate experimental data or large discretization errors. In the last decades there have been several efforts in the field of fluid dynamics regarding the subject of data assimilation. To give just a small selection of existing works, consider TALAGRAND AND COURTIER [380], BLUM ET AL. [45], VAN LEEUWEN [404], D'ELIA AND VENEZIANI [122], BERTAGNA ET AL. [38], BURMAN AND OKSANEN [74] and BOULAKIA ET AL. [65] or for some basic information on data assimilation see RAYNER ET AL. [325].

In the course of this work, the assimilation of numerical and experimental data is tested in combination with the LSFEM. For this purpose, firstly, the preparation of experimental data prior to the implementation by means of the Kriging interpolation method and, secondly, the direct integration of these data by means of the LSFEM are briefly discussed below.

### 3.4.1 Data preparation using the Kriging interpolation method

When implementing data assimilation into numerical calculations, the first challenge is to find a suitable set of experimental data. Experimental data can be measured, for example, using particle image velocimetry (PIV) on several cross-sections of a flow, see e.g. KIM ET AL. [232], WESTERDALE ET AL. [413] and AGATI ET AL. [2]. For a straightforward data implementation in the FEM code, it is required that values are available at the locations of the grid nodes. Since this is usually not the case, the collected data must be pre-processed. A convenient option to determine the data at the required positions is the Kriging interpolation method. This tool, whose first approaches were developed by MATHERON [273] based on the work of KRIGE [244], is very popular especially in the field of geophysics. The term Kriging covers various interpolation approaches. One of the most widely used is ordinary Kriging, which will be applied in the following. With this method a value is estimated based on a linear combination of weighted given data in the neighborhood of the interpolation site. Assuming a given set of values $z_i = z(x_i)$ at locations $x_i$, the estimation at an unmeasured position $x_0$ is given by

$$\hat{z}(x_0) = \sum_{i=1}^{n} \lambda_i \; z_i \; , \tag{3.48}$$

where $\lambda_i$ denotes the Kriging weights and $n$ is the number of sample values. In order to ensure unbiasedness, the weights have to sum up to one, i.e. $\sum_{i=1}^{n} \lambda_i = 1$. The determination of the weights is based on the condition that the best estimate has to minimize the variance of the prediction error. With the estimation error given by

$$e(x_0) = \hat{z}(x_0) - z(x_0) \; , \tag{3.49}$$

the estimation variance is defined as the expected quadratic difference and reads

$$\begin{aligned} \operatorname{var}[\hat{z}(x_0) - z(x_0)] &= E\big[\,(\hat{z}(x_0) - z(x_0))^2\,\big] = E\left[\left(\sum_{i=1}^{n} \lambda_i \; z(x_i) - z(x_0)\right)^2\right] \\ &= 2\sum_{i=1}^{n} \lambda_i \; \gamma(x_i - x_0) - \sum_{i=1}^{n}\sum_{j=1}^{n} \lambda_i \lambda_j \; \gamma(x_i - x_j) \; , \end{aligned} \tag{3.50}$$

where $\gamma(h)$ is the semivariance between the specified points. The semivariance is determined using the theoretical semivariogram model. The choice of the model depends on the experimental semivariogram $\hat{\gamma}$, which can be determined by grouping the sample data regarding their distances and plotting the semivariance as a function of the distance $h$ using

$$\hat{\gamma}(h) = \frac{1}{2n} \sum_{i=1}^{n} \left[ z(x_i) - z(x_i + h) \right]^2 \ . \tag{3.51}$$

Typical theoretical variogram models are e.g. the spherical, exponential and gaussian variogram model. The last one, which is used in the context of this work, reads

$$\gamma(h) = s \left( 1 - exp \left( \frac{-h^2}{r^2} \right) \right) \ , \tag{3.52}$$

where parameters $s$ and $r$ can be used to fit the function to the experimental variogram. By minimizing the estimation variance in (3.50) and considering that the weights $\lambda_i$ sum up to one, the resulting system of equations takes the form

$$\begin{bmatrix} \gamma(x_1 - x_1) & \cdots & \gamma(x_1 - x_n) & 1 \\ \vdots & \ddots & \vdots & \vdots \\ \gamma(x_n - x_1) & \cdots & \gamma(x_n - x_n) & 1 \\ 1 & \cdots & 1 & 0 \end{bmatrix} \begin{bmatrix} \gamma_1 \\ \vdots \\ \gamma_n \\ \mu \end{bmatrix} = \begin{bmatrix} \gamma(x_1 - x_0) \\ \vdots \\ \gamma(x_n - x_0) \\ 1 \end{bmatrix} \ , \tag{3.53}$$

where $\mu$ is the Lagrange multiplier for ordinary Kriging. By solving the system of equations, one obtains the corresponding weights, which yield the integration at point $x_0$ by substitution in (3.48). For more details on the implementation and the historical background of the Kriging method see for example Chilès and Delfiner [102], Cressie [110], Stein [373], Wackernagel [407], Oliver and Webster [300] and Chilès and Desassis [103]. Once the data is formatted, it can directly be implemented using the LSFEM.

### 3.4.2 Data assimilation using the LSFEM

The mixed least-squares FEM provides a straightforward possibility to include data without additional computational effort. Studies on data integration to the solution of the steady and unsteady Navier-Stokes equations using weighted LSFEM are presented e.g. in Heys et al. [193], Wei et al. [412], Rajaraman et al. [316]. The focus of these papers is, among others, on the weighting of the assimilated data which is determined depending on the accuracy of the data itself. The authors investigate the influence of noise in assimilated data and evaluate the impact of strongly or weakly constrained internal and external boundary conditions. Another approach presented by Rajaraman et al. [317] enables combining an arbitrary numerical method for solving the underlying problem with the weighted LSFEM for data assimilation.

In this thesis, the same approach as presented by Dwight [135], Schwarz and Dwight [346] and Averweg et al. [12] is applied. Therein, the assimilation of data to the solution of the Navier-Stokes equations to simulate Newtonian flow with the LSFEM was investigated. Since the discrete observations $\boldsymbol{d} \in \mathbb{R}^M$ are not in the same space as the numerical quantities $\boldsymbol{v}$, an operator $\boldsymbol{H} : \boldsymbol{V} \rightarrow \mathbb{R}^M$ is introduced for the mapping with a suitable Sobolev space $\boldsymbol{V}$. Assuming that $\boldsymbol{d} \approx \boldsymbol{H} \cdot \boldsymbol{v}$, a functional of the form

$$\mathcal{F}^{data}(\boldsymbol{v}) = \frac{1}{2} \sum_{i=1}^{M} \zeta^{i} (\boldsymbol{d}^{i} - \boldsymbol{H}^{i} \cdot \boldsymbol{v})^{2} \tag{3.54}$$

is constructed. Herein, $\zeta_i$ are the weights associated to the measured values $\boldsymbol{d}_i$. The total mixed least-squares functional with data assimilation is then compost as

$$\mathcal{F}^{*}(\mathcal{U}) = \mathcal{F}(\mathcal{U}) + \mathcal{F}^{data}(\boldsymbol{v}) \ , \tag{3.55}$$

with the unknowns $\mathcal{U}$ depending on the chosen formulation. Within the scope of this work, data assimilation is applied to solve flow of non-Newtonian fluids with mixed LS formulations based on the stresses and velocities in 2D and using a stress-velocity-pressure formulation in 3D, i.e. $\mathcal{U} = (\boldsymbol{\sigma}, \boldsymbol{v})$ in 2D and $\mathcal{U} = (\boldsymbol{\sigma}, \boldsymbol{v}, p)$ in 3D, respectively.

# 4 LSFEM for Newtonian fluids

The flow of incompressible Newtonian fluids is governed by the incompressible Navier-Stokes equations (2.70) derived in Section 2.5. For a straightforward application of the least-squares FEM this equation system is transformed into a first-order system in order to use $\mathcal{C}^0$-continuous functions. A common procedure for reformulating a second-order partial differential equation system is to introduce a new variable. Among the most studied versions in fluid mechanics are velocity-vorticity-pressure LS formulations or stress-velocity-pressure formulations. The definition of new variables based on the velocity flux, stream functions or a pressure gradient is a further established way of reformulating the Navier-Stokes equations. For a detailed overview of the various least-squares formulations and the associated literature references, see Section 1.2.1. Since both, a stress-velocity-pressure (SVP) formulation and a reduced stress-velocity (SV) formulation are investigated in this work, the derivation of the former formulation is assumed first, and then this is further reformulated to obtain the SV formulation.

## 4.1 Stress-velocity-pressure formulation for fluid dynamics

In order to transform the Navier-Stokes equations (2.70) into a first-order system, the constitutive law for the Cauchy stresses $\boldsymbol{\sigma} = 2\rho_f\nu_f\nabla^s\boldsymbol{v} - p\boldsymbol{I}$, relating the stresses to the velocities and the pressure is considered. The corresponding residuals in terms of stresses, velocities and pressure can be written in the following form

$$\mathcal{R}_1^F := \rho_f\boldsymbol{a} - \operatorname{div}\boldsymbol{\sigma} + \rho_f\nabla\boldsymbol{v}\cdot\boldsymbol{v} - \boldsymbol{f}, \quad \mathcal{R}_2^F := \boldsymbol{\sigma} - 2\rho_f\nu_f\nabla^s\boldsymbol{v} + p\boldsymbol{I}, \quad \mathcal{R}_3^F := \operatorname{div}\boldsymbol{v}, \tag{4.1}$$

compare Schwarz et al. [353] and Nisters and Schwarz [295], for instance. The least-squares functional is then constructed by applying the quadratic $L^2$-norm to the residual terms and approximating the accelerations depending on the velocities by means of a time discretization scheme. Then the functional for the SVP formulation reads

$$\begin{aligned}\mathcal{F}^F(\boldsymbol{\sigma},\boldsymbol{v},p) = \frac{1}{2}\Big(&||\omega_{f1}(\rho_f\boldsymbol{a}(\boldsymbol{v}) - \operatorname{div}\boldsymbol{\sigma} + \rho_f\nabla\boldsymbol{v}\cdot\boldsymbol{v} - \boldsymbol{f})||^2_{L^2(\Omega_f)} \\ &+ ||\omega_{f2}(\boldsymbol{\sigma} - 2\rho_f\nu_f\nabla^s\boldsymbol{v} + p\boldsymbol{I})||^2_{L^2(\Omega_f)} + ||\omega_{f3}(\operatorname{div}\boldsymbol{v})||^2_{L^2(\Omega_f)}\Big) \ ,\end{aligned} \tag{4.2}$$

with appropriate positive weightings factors $\omega_{f1}, \omega_{f2}$ and $\omega_{f3}$. For solving the minimization problem with Newton's method, the first and second variations of the functional with respect to all unknowns are needed. For the presented SVP formulation the required variations, omitting the body force term, are given by

$$\begin{aligned}\delta_{\boldsymbol{\sigma}}\mathcal{F}^F(\mathcal{U};\delta\boldsymbol{\sigma}) = \int_{\Omega_f} \big[ &-\omega_{f1}^2\,(\rho_f\boldsymbol{a} - \operatorname{div}\boldsymbol{\sigma} + \rho_f\nabla\boldsymbol{v}\cdot\boldsymbol{v})\cdot\operatorname{div}\delta\boldsymbol{\sigma} \\ &+ \omega_{f2}^2\,(\boldsymbol{\sigma} - 2\rho_f\nu_f\nabla^s\boldsymbol{v} + p\boldsymbol{I}) : \delta\boldsymbol{\sigma}\ \big]\ \mathrm{d}V \ ,\end{aligned} \tag{4.3}$$

$$\begin{aligned}\delta_{\boldsymbol{v}}\mathcal{F}^F(\mathcal{U};\delta\boldsymbol{v}) = \int_{\Omega_f} \Big[&\omega_{f1}^2(\rho_f\boldsymbol{a}(\boldsymbol{v}) - \operatorname{div}\boldsymbol{\sigma} + \rho_f\nabla\boldsymbol{v}\cdot\boldsymbol{v})\cdot\rho_f(\delta\boldsymbol{a} + \nabla\delta\boldsymbol{v}\cdot\boldsymbol{v} + \nabla\boldsymbol{v}\cdot\delta\boldsymbol{v}) \\ &- \omega_{f2}^2\,(\boldsymbol{\sigma} - 2\rho_f\nu_f\nabla^s\boldsymbol{v} + p\boldsymbol{I}) : (\rho_f\nu_f\nabla^s\delta\boldsymbol{v}) \\ &+ \omega_{f3}^2\,(\operatorname{div}\boldsymbol{v}\ \operatorname{div}\delta\boldsymbol{v})\ \Big]\ \mathrm{d}V \ ,\end{aligned} \tag{4.4}$$

$$\delta_p \mathcal{F}^F(\mathcal{U};\delta p) = \int\limits_{\Omega_f} \left[\, \omega_{f2}^2\,(\boldsymbol{\sigma} - 2\rho_f \nu_f \nabla^s \boldsymbol{v} + p\boldsymbol{I}) : \delta p\, \boldsymbol{I} \,\right] \mathrm{d}V \;, \tag{4.5}$$

with $\mathcal{U} = (\boldsymbol{\sigma}, \boldsymbol{v}, p)$. Note, that the variation of the accelerations $\delta\boldsymbol{a} := \frac{\partial \boldsymbol{a}(\boldsymbol{v})}{\partial \boldsymbol{v}} \delta\boldsymbol{v}$ depends on the chosen time discretization method. For the application of Newton's method the linearizations of (4.3)-(4.5) are required. The linearizations with respect to the stresses are given with

$$\Delta_{\boldsymbol{\sigma}}\delta_{\boldsymbol{\sigma}}\mathcal{F}^F = \int\limits_{\Omega_f} \left[ -\,\omega_{f1}^2\,(\operatorname{div}\Delta\boldsymbol{\sigma} \cdot \operatorname{div}\delta\boldsymbol{\sigma}) + \omega_{f2}^2\,(\Delta\boldsymbol{\sigma} : \delta\boldsymbol{\sigma}) \,\right] \mathrm{d}V \;, \tag{4.6}$$

$$\begin{aligned}\Delta_{\boldsymbol{\sigma}}\delta_{\boldsymbol{v}}\mathcal{F}^F = \int\limits_{\Omega_f} \Big[ & -\,\omega_{f1}^2\operatorname{div}\Delta\boldsymbol{\sigma} \cdot \rho_f(\delta\boldsymbol{a} + \nabla\delta\boldsymbol{v}\cdot\boldsymbol{v} + \nabla\boldsymbol{v}\cdot\delta\boldsymbol{v}) \\ & -\;\omega_{f2}^2\,(\Delta\boldsymbol{\sigma} : \rho_f\nu_f\nabla^s\delta\boldsymbol{v}) \Big] \mathrm{d}V \;,\end{aligned} \tag{4.7}$$

$$\Delta_{\boldsymbol{\sigma}}\delta_p\mathcal{F}^F = \int\limits_{\Omega_f} \left[\, \omega_{f2}^2\,\Delta\boldsymbol{\sigma} : \delta p\,\boldsymbol{I} \,\right] \mathrm{d}V \;, \tag{4.8}$$

and the linearizations with respect to the velocities read

$$\begin{aligned}\Delta_{\boldsymbol{v}}\delta_{\boldsymbol{\sigma}}\mathcal{F}^F = \int\limits_{\Omega_f} \Big[ & -\,\omega_{f1}^2\,(\rho_f\Delta\boldsymbol{a} + \rho_f\nabla\Delta\boldsymbol{v}\cdot\boldsymbol{v} + \rho_f\nabla\boldsymbol{v}\cdot\Delta\boldsymbol{v})\cdot\operatorname{div}\delta\boldsymbol{\sigma} \\ & -\;\omega_{f2}^2\,(2\rho_f\nu_f\nabla^s\Delta\boldsymbol{v} : \delta\boldsymbol{\sigma}) \Big] \mathrm{d}V \;,\end{aligned} \tag{4.9}$$

$$\begin{aligned}\Delta_{\boldsymbol{v}}\delta_{\boldsymbol{v}}\mathcal{F}^F = \int\limits_{\Omega_f} \Big[ & \omega_{f1}^2{\rho_f}^2(\Delta\boldsymbol{a} + \nabla\Delta\boldsymbol{v}\cdot\boldsymbol{v} + \nabla\boldsymbol{v}\cdot\Delta\boldsymbol{v})\cdot(\delta\boldsymbol{a} + \nabla\delta\boldsymbol{v}\cdot\boldsymbol{v} + \nabla\boldsymbol{v}\cdot\delta\boldsymbol{v}) \\ & + \omega_{f1}^2(\rho_f\boldsymbol{a}(\boldsymbol{v}) - \operatorname{div}\boldsymbol{\sigma} + \rho_f\nabla\boldsymbol{v}\cdot\boldsymbol{v})\cdot\rho_f(\nabla\delta\boldsymbol{v}\cdot\Delta\boldsymbol{v} + \Delta\nabla\boldsymbol{v}\cdot\delta\boldsymbol{v}) \\ & +\;\omega_{f2}^2\,(2{\rho_f}^2{\nu_f}^2\nabla^s\Delta\boldsymbol{v} : \nabla^s\delta\boldsymbol{v}) +\; \omega_{f3}^2\,(\operatorname{div}\Delta\boldsymbol{v}\;\operatorname{div}\delta\boldsymbol{v}) \Big] \mathrm{d}V \;,\end{aligned} \tag{4.10}$$

$$\Delta_{\boldsymbol{v}}\delta_p\mathcal{F}^F = \int\limits_{\Omega_f} \left[ -\;\omega_{f2}^2\,(2\rho_f\nu_f\nabla^s\Delta\boldsymbol{v} : \delta p\,\boldsymbol{I}) \,\right] \mathrm{d}V \;. \tag{4.11}$$

Furthermore, the terms for the linearizations with respect to the pressure are given with

$$\Delta_p\delta_{\boldsymbol{\sigma}}\mathcal{F}^F = \int\limits_{\Omega_f} \left[ \omega_{f2}^2\,(\Delta p\boldsymbol{I} : \delta\boldsymbol{\sigma}) \,\right] \mathrm{d}V \;, \tag{4.12}$$

$$\Delta_p\delta_{\boldsymbol{v}}\mathcal{F}^F = \int\limits_{\Omega_f} \left[ -\,\omega_{f2}^2\,(\Delta p\boldsymbol{I} : \rho_f\nu_f\nabla^s\delta\boldsymbol{v}) \,\right] \mathrm{d}V \;, \tag{4.13}$$

$$\Delta_p\delta_p\mathcal{F}^F = \int\limits_{\Omega_f} \left[ \omega_{f2}^2\,\Delta p\boldsymbol{I} : \delta\boldsymbol{\sigma} \,\right] \mathrm{d}V \;. \tag{4.14}$$

In the context of this work, the presented mixed SVP formulation is applied in an extended form for the solution of flows of non-Newtonian fluids in Section 5. Further information regarding the discretization and the resulting system of equations are thus provided in later sections.

## 4.2 Stress-velocity formulation for fluid dynamics

In addition to the SVP formulation, a least-squares approach in terms of stresses and velocities is considered in this study, with the main motivation of the inherent fulfillment of the coupling conditions in FSI calculations. Furthermore, the elimination of the pressure field leads to a reduction of the size of the equation system. For this purpose, the formulation presented in Nisters and Schwarz [295] and Averweg et al. [9] is adopted, in which a term for the pressure is derived, by evaluating the trace of the constitutive equation and considering the continuity equation, i.e. $\operatorname{div} \boldsymbol{v} = 0$, which reads

$$p = -\frac{1}{3}\operatorname{tr}(\boldsymbol{\sigma}) + \frac{2}{3}\nu_f \rho_f \operatorname{div} \boldsymbol{v} = -\frac{1}{3}\operatorname{tr}(\boldsymbol{\sigma}) \ . \tag{4.15}$$

By additionally using the definition of the deviatoric part of the Cauchy stresses written as $\operatorname{dev} \boldsymbol{\sigma} = \boldsymbol{\sigma} - \frac{1}{3}\operatorname{tr}(\boldsymbol{\sigma})$, and adding the mass balance again as an additional residual, one obtains the stress-velocity formulation for incompressible fluid flow, which consists of the following three residuals

$$\mathcal{R}_1^F := \rho_f \boldsymbol{a} - \operatorname{div} \boldsymbol{\sigma} + \rho_f \nabla \boldsymbol{v} \cdot \boldsymbol{v} - \boldsymbol{f} \ , \quad \mathcal{R}_2^F := \operatorname{dev} \boldsymbol{\sigma} - 2\rho_f \nu_f \nabla^s \boldsymbol{v} \ , \quad \mathcal{R}_3^F := \operatorname{div} \boldsymbol{v} \ . \tag{4.16}$$

The application of the squared $L^2$-norm and the introduction of a time discretization scheme, relating the accelerations $\boldsymbol{a}$ to the velocity field $\boldsymbol{v}$ (see Section 7.3), leads to the resulting least-squares functional as

$$\begin{aligned} \mathcal{F}^F(\boldsymbol{\sigma}, \boldsymbol{v}) = \frac{1}{2} \Big( & ||\omega_{f1} \left(\rho_f \boldsymbol{a}(\boldsymbol{v}) - \operatorname{div} \boldsymbol{\sigma} + \rho_f \nabla \boldsymbol{v} \cdot \boldsymbol{v} - \boldsymbol{f}\right)||^2_{L^2(\Omega_f)} \\ & + ||\omega_{f2} \left(\operatorname{dev} \boldsymbol{\sigma} - 2\rho_f \nu_f \nabla^s \boldsymbol{v}\right)||^2_{L^2(\Omega_f)} + \ ||\omega_{f3} \left(\operatorname{div} \boldsymbol{v}\right)||^2_{L^2(\Omega_f)} \Big) \ , \end{aligned} \tag{4.17}$$

with appropriate positive weighting factors $\omega_{f1}$, $\omega_{f2}$ and $\omega_{f3}$. The required first variations of the functional with respect to the unknowns $\mathcal{U} = (\boldsymbol{\sigma}, \boldsymbol{v})$ for the solution of the minimization problem, omitting the body force term, are given by

$$\begin{aligned} \delta_{\boldsymbol{\sigma}} \mathcal{F}^F(\mathcal{U}; \delta\boldsymbol{\sigma}) = \int_{\Omega_f} \big[ & - \omega_{f1}^2 \ \left(\rho_f \boldsymbol{a}(\boldsymbol{v}) - \operatorname{div} \boldsymbol{\sigma} + \rho_f \nabla \boldsymbol{v} \cdot \boldsymbol{v}\right) \cdot \operatorname{div} \delta\boldsymbol{\sigma} \\ & + \ \omega_{f2}^2 \ \left(\operatorname{dev} \boldsymbol{\sigma} - 2\rho_f \nu_f \nabla^s \boldsymbol{v}\right) : \operatorname{dev} \delta\boldsymbol{\sigma} \big] \, \mathrm{d}V \ , \end{aligned} \tag{4.18}$$

$$\begin{aligned} \delta_{\boldsymbol{v}} \mathcal{F}^F(\mathcal{U}; \delta\boldsymbol{v}) = \int_{\Omega_f} \big[ & \omega_{f1}^2 \ \left(\rho_f \boldsymbol{a}(\boldsymbol{v}) - \operatorname{div} \boldsymbol{\sigma} + \rho_f \nabla \boldsymbol{v} \cdot \boldsymbol{v}\right) \cdot \rho_f (\delta \boldsymbol{a} + \nabla \delta\boldsymbol{v} \cdot \boldsymbol{v} + \nabla \boldsymbol{v} \cdot \delta\boldsymbol{v}) \\ & - \omega_{f2}^2 \ \left(\operatorname{dev} \boldsymbol{\sigma} - 2\rho_f \nu_f \nabla^s \boldsymbol{v}\right) : 2\rho_f \nu_f \nabla^s \delta\boldsymbol{v} \\ & + \omega_{f3}^2 \ \left(\operatorname{div} \boldsymbol{v} \cdot \operatorname{div} \delta\boldsymbol{v}\right) \ \big] \, \mathrm{d}V \ . \end{aligned} \tag{4.19}$$

Again, the variation of the acceleration $\delta \boldsymbol{a} := \frac{\partial \boldsymbol{a}(\boldsymbol{v})}{\partial \boldsymbol{v}} \delta \boldsymbol{v}$ depends on the applied time discretization method. Here as well, the construction of the variations is carried out on the assumption that the body force is zero. Moreover, the linearization required to solve the system using Newton's method leads to the following linearizations $\Delta\delta\mathcal{F}$ of the functional in the case of the SV Fluid formulation

$$\Delta_{\boldsymbol{\sigma}}\delta_{\boldsymbol{\sigma}}\mathcal{F}^F = \int\limits_{\Omega_f} \left[\omega_{f1}^2 \, (\operatorname{div}\delta\boldsymbol{\sigma}\cdot\operatorname{div}\Delta\boldsymbol{\sigma}) + \omega_{f2}^2 \, (\operatorname{dev}\delta\boldsymbol{\sigma} : \operatorname{dev}\Delta\boldsymbol{\sigma}) \,\right] \mathrm{d}V \ , \tag{4.20}$$

$$\begin{aligned} \Delta_{\boldsymbol{\sigma}}\delta_{\boldsymbol{v}}\mathcal{F}^F = -\int\limits_{\Omega_f} \big[&\omega_{f1}^2 \ \operatorname{div}\delta\boldsymbol{\sigma}\cdot(\rho_f\Delta\boldsymbol{a} + \rho_f\nabla\Delta\boldsymbol{v}\cdot\boldsymbol{v} + \rho_f\nabla\boldsymbol{v}\cdot\Delta\boldsymbol{v}) \\ &- \omega_{f2}^2 \, (2\rho_f\nu_f \ \operatorname{dev}\delta\boldsymbol{\sigma} : \nabla^s\Delta\boldsymbol{v}) \,\big] \mathrm{d}V \ , \end{aligned} \tag{4.21}$$

$$\begin{aligned} \Delta_{\boldsymbol{v}}\delta_{\boldsymbol{\sigma}}\mathcal{F}^F = -\int\limits_{\Omega_f} \big[&\omega_{f1}^2 \, (\rho_f\delta\boldsymbol{a} + \rho_f\nabla\delta\boldsymbol{v}\cdot\boldsymbol{v} + \rho_f\nabla\boldsymbol{v}\cdot\delta\boldsymbol{v})\cdot\operatorname{div}\Delta\boldsymbol{\sigma} \\ &- \omega_{f2}^2 \, (2\rho_f\nu_f\nabla^s\delta\boldsymbol{v} : \operatorname{dev}\Delta\boldsymbol{\sigma}) \,\big] \mathrm{d}V \ , \end{aligned} \tag{4.22}$$

$$\begin{aligned} \Delta_{\boldsymbol{v}}\delta_{\boldsymbol{v}}\mathcal{F}^F = \int\limits_{\Omega_f} \big[&\omega_{f1}^2 \ {\rho_f}^2 \, (\delta\boldsymbol{a} + \nabla\delta\boldsymbol{v}\cdot\boldsymbol{v} + \nabla\boldsymbol{v}\cdot\delta\boldsymbol{v})\cdot(\Delta\boldsymbol{a} + \nabla\Delta\boldsymbol{v}\cdot\boldsymbol{v} + \nabla\boldsymbol{v}\cdot\Delta\boldsymbol{v}) \\ &- \omega_{f1}^2 \, (\rho_f\boldsymbol{a}(\boldsymbol{v}) - \operatorname{div}\boldsymbol{\sigma} + \rho_f\nabla\boldsymbol{v}\cdot\boldsymbol{v})\cdot\rho_f\,(\nabla\delta\boldsymbol{v}\cdot\Delta\boldsymbol{v} + \nabla\Delta\boldsymbol{v}\cdot\delta\boldsymbol{v}) \\ &- \omega_{f2}^2 \, (4{\rho_f}^2{\nu_f}^2 \ \nabla^s\delta\boldsymbol{v} : \nabla^s\Delta\boldsymbol{v}) + \omega_{f3}^2 \, (\operatorname{div}\delta\boldsymbol{v}\cdot\operatorname{div}\Delta\boldsymbol{v}) \,\big] \mathrm{d}V \ . \end{aligned} \tag{4.23}$$

### 4.2.1 Discretization and assembly aspects

For a conforming spatial discretization of the stresses in $H(\mathrm{div})$ and the velocities in $H^1$, vector-valued Raviart-Thomas functions of order $m$ and Lagrange interpolation functions of order $k$ are selected as specified in Section 3.3.4. The resulting element is referred to as $RT_mP_k$. For a typical element $e$, the discretized linear system of equations in matrix notation reads

$$\boldsymbol{K}^e\cdot\Delta\boldsymbol{D}^e = -\boldsymbol{P}^e \quad \Rightarrow \quad \begin{bmatrix} \boldsymbol{k}_{vv}^e & \boldsymbol{k}_{v\sigma}^e \\ \boldsymbol{k}_{\sigma v}^e & \boldsymbol{k}_{\sigma\sigma}^e \end{bmatrix} \begin{bmatrix} \Delta\boldsymbol{w} \\ \Delta\boldsymbol{\beta} \end{bmatrix} = -\begin{bmatrix} \boldsymbol{r}_v^e \\ \boldsymbol{r}_\sigma^e \end{bmatrix} , \tag{4.24}$$

where $\boldsymbol{w}^I$ and $\boldsymbol{\beta}^J$ are the degrees of freedom of the velocities and stresses at nodes $I$ and $J$, which are defined in the 2D case as

$$\boldsymbol{w}^I = \begin{bmatrix} w_1^I \\ w_2^I \end{bmatrix} \qquad \text{and} \qquad \boldsymbol{\beta}^J = \begin{bmatrix} \beta_1^J \\ \beta_2^J \end{bmatrix} \ . \tag{4.25}$$

These are approximated in terms of Lagrangian interpolation functions denoted with $N^I$ and Raviart-Thomas shape functions denoted with $\psi^J$. This yields in index notation for the components of the unknowns and corresponding derivatives

$$v_i^h = \sum_I N^I w_i^I \ , \qquad v_{i,j}^h = \sum_I N_{,j}^I \ w_i^I \qquad \text{and} \qquad v_{i,i}^h = \sum_I N_{,i}^I \ w_i^I \tag{4.26}$$

and

$$\sigma_{ij}^h = \sum_J \psi_j^J \beta_i^J \qquad \text{and} \qquad \sigma_{ij,j}^h = \sum_J \psi_{j,j}^J \ \beta_i^J \ . \tag{4.27}$$

# 5 LSFEM for non-Newtonian fluids

Modeling of fluids with non-Newtonian behavior is an important issue for many industrial and scientific applications, for example in the field of chemistry, bioengineering and medical science. These fluids are characterized by a viscosity that is not constant at a fixed pressure and temperature, in contrast to Newtonian fluids which exhibit a linear relation between the shear stress and the shear rate. As discussed in more detail in Section 2.5, non-Newtonian fluids can be divided into viscoelastic fluids, time-dependent fluids, and generalized Newtonian fluids. For each category, various material models exist to approximate the material behavior. Common models which include a partly elastic behavior and thus are suitable for the modeling of viscoelastic fluids are, e.g., the Maxwell (MAXWELL [276]), Giesekus (GIESEKUS [168]), Oldroyd-B (OLDROYD [299]) and the Phan-Thien-Tanner model (PHAN-THIEN AND TANNER [307]). The property of viscoelasticity often appears in polymers, which in fact can be either a liquid or a solid, depending on the time scale or the rate at which deformation occurs. Generalized Newtonian fluids, for which the shear stress is a function of the shear rate at the considered time, can be shear-thinning, shear-thickening, and plastic. Some typical models to simulate primarily shear-thinning material behavior are e.g. the power-law equation of Ostwald and de Waele (OSTWALD [301]), the Cross model (CROSS [112]), the Carreau model (CARREAU ET AL. [90]), and the Carreau-Yasuda model (YASUDA ET AL. [427]). Viscoplastic fluids, characterized by the presence of an apparent yield stress which must be exceeded for the fluid to flow, are commonly modeled using the Herschel-Bulkley (HERSCHEL AND BULKLEY [182]), for instance. For a deeper understanding of the origin, use, and study of rheological material models for complex fluids, reference is made to textbooks such as BIRD ET AL. [42], CHHABRA AND RICHARDSON [101], KRISHNAN ET AL. [245], CROCHET ET AL. [111] and SARAMITO [336], for example.

In the following, least-squares formulations for solving flows of generalized Newtonian fluids in 2D and 3D are presented, using the Carreau-Yasuda model to describe the relation between dynamic viscosity $\eta$ and shear rate $\dot{\gamma}$. The model has already been introduced in Section 2.5 and reads

$$\eta(\dot{\gamma}) = \eta_\infty + (\eta_0 - \eta_\infty)\,(1 + (\lambda\,\dot{\gamma})^a)^{\frac{n-1}{a}} \qquad \text{with} \qquad \dot{\gamma} = \sqrt{2(\nabla^s \boldsymbol{v} : \nabla^s \boldsymbol{v})} \tag{5.1}$$

with $\nabla^s \boldsymbol{v}$ denoting the symmetric velocity gradient (2.14). The parameters $\eta_0$ and $\eta_\infty$ define the upper and lower viscosity bounds, $\lambda$ the relaxation time, and $n$ and $a$ are further model parameters to adapt the model to the specific material behavior. The mixed LS formulations are implemented and investigated by computing different numerical examples in two and three dimensions.

Another aspect of this chapter is the assimilation of numerical and experimental data into the simulation of flow problems based on the mixed LSFEM. For this purpose, given data are directly assimilated by adding an additional term to the LS functional, as explained in Section 3.4. The implementation of this approach is presented in the next sections, first for the computation of non-Newtonian flows through a narrowing channel in two dimensions. Subsequently, experimental as well as numerical data are included in the simulation of a blood flow through a carotid bifurcation in three dimensions. The numerical calculations and studies presented in this chapter appear to some extent in the publications AVERWEG ET AL. [10; 11; 12].

## 5.1 SV formulation for incompressible non-Newtonian fluids in 2D

For the computation of flow problems involving generalized Newtonian fluids in two dimensions, the SV formulation derived in (4.16) is extended to consider the nonlinear dependence of the dynamic viscosity $\eta$ on the shear rate $\dot{\gamma}$. Furthermore, only steady-state flows are considered in the context of the mixed LSFEM analysis for generalized Newtonian fluids, hence the time-dependent term, i. e. the accelerations, can be omitted. Consequently, the LS functional for the simulation of generalized Newtonian fluids based on stresses and velocities reads as follows

$$\begin{aligned}\mathcal{F}^F(\boldsymbol{\sigma}, \boldsymbol{v}) = \frac{1}{2} \Big( &||\omega_{f1} \left(\operatorname{div} \boldsymbol{\sigma} - \rho_f \nabla \boldsymbol{v} \cdot \boldsymbol{v} + \boldsymbol{f}\right)||^2_{L^2(\Omega_f)} \\ &+ ||\omega_{f2} \left(\operatorname{dev} \boldsymbol{\sigma} - 2\eta(\dot{\gamma}) \nabla^s \boldsymbol{v}\right)||^2_{L^2(\Omega_f)} + \ ||\omega_{f3} \left(\operatorname{div} \boldsymbol{v}\right)||^2_{L^2(\Omega_f)} \Big) ,\end{aligned} \tag{5.2}$$

with the Cauchy stresses $\boldsymbol{\sigma}$, the velocities $\boldsymbol{v}$, the symmetric velocity gradient defined as $\nabla^s \boldsymbol{v} = 1/2(\nabla \boldsymbol{v} + (\nabla \boldsymbol{v})^T)$, the fluid density $\rho_f$, and the positive weighting factors $\omega_{f1}$, $\omega_{f2}$ and $\omega_{f3}$. The dynamic viscosity is determined based on the Carreau-Yasuda viscosity model given in (5.1). The required first and second variations of the functional with respect to all unknowns to solve the minimization problem with Newton's method, are obtained in a similar way as explained in 4.2. It should be noted that the viscosity is a function of the velocity and, in addition, the time-dependent terms can be dropped. For the spatial discretization of the mixed LS stress-velocity formulation, conformal approximation functions for the stresses and velocities in the solution spaces $H(\operatorname{div}, \Omega) \times H^1(\Omega)$ are selected based on Lagrange interpolation functions of order $k$ and vector-valued Raviart-Thomas functions of order $m$ leading to finite elements denoted by $RT_m P_k$, see Section 3.3.4. The resulting discretized system of equations is then equivalent the one for the SV formulation for Newtonian fluids, which is given in equation (5.11) with the corresponding discretization.

## 5.2 Numerical examples: Steady flow of non-Newtonian fluids in 2D

Several studies are performed to validate, verify and investigate the presented LS SV formulation including the Carreau-Yasuda model. First, a benchmark problem with an exact solution is analyzed to validate and verify the implementation of the formulation and to perform a convergence study. For this purpose, interpolation functions with different orders are applied and the order of convergence in space is determined. Next, two numerical benchmark examples, namely the flow in a driven cavity and the flow over a backward facing step, are evaluated. Thereby, the parameters of the Carreau-Yasuda model are varied and the influence of these model parameters is investigated. In the last part of this section, the assimilation of data into a numerical simulation of a flow through a smooth contraction based on the LSFEM is implemented. Therefore, data points generated by a numerical solution produced on a fine mesh are embedded in this numerical example. In all numerical examples in this section, the physical weighting factors in (5.2) are selected as

$$\omega_{f1} = \sqrt{\frac{1}{\rho_f}} \ , \qquad \omega_{f2} = \sqrt{\frac{1}{\rho_f \nu_f}} \qquad \text{and} \qquad \omega_{f3} = 1 \ . \tag{5.3}$$

### 5.2.1 Flow in a square domain with analytical solution

As a first numerical example, in this section a two-dimensional flow through a square domain (SD) with an analytical solution from Fortin et al. [154] is considered to validate the presented LS stress-velocity formulation for non-Newtonian fluids. The geometry of the domain $\Omega_f = [0,1] \times [0,1]$ and the according boundary conditions on $\partial\Omega_f$ for the velocities and stresses are illustrated in Figure 5.1 (left). Additionally, the exact solution for the velocities over the domain is plotted, see Figure 5.1 (right).

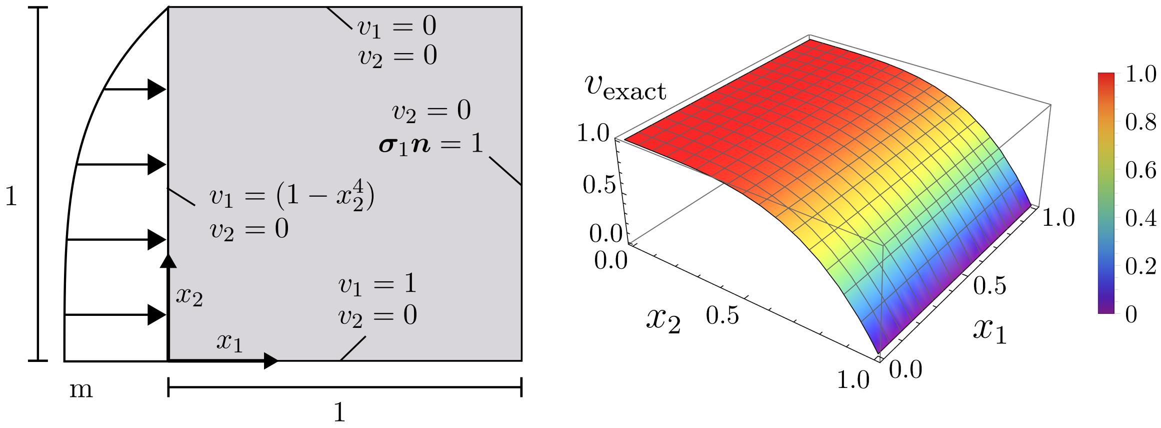

Figure 5.1: SD - geometry and boundary conditions for flow in a square domain (left) and exact solution for total velocity field (right, in m/s)

The terms for the exact solution of the velocity and pressure are given by

$$\boldsymbol{v}_{\text{exact}} = \begin{bmatrix} 1 - x_2^4 \\ 0 \end{bmatrix} \qquad \text{and} \qquad p_{\text{exact}} = -x_1^2 \,, \tag{5.4}$$

provided that a forcing function for the body force is added to the momentum equation, which is chosen as

$$\boldsymbol{f} = \begin{bmatrix} 12\, x_2^2 \; (1 + 16\, n \; \lambda^2 \; (x_2)^6) \; (1 + 16\, \lambda^2 \; (x_2)^6)^{\frac{n-3}{2}} - 2x_1 \\ 0 \end{bmatrix} \,, \tag{5.5}$$

see Chen et al. [98]. Based on (5.4), the resulting exact solution for the stresses can be computed using the constitutive equation (2.73) for non-Newtonian fluids and the Carreau-Yasuda viscosity model (5.1), yielding

$$\boldsymbol{\sigma}_{\text{exact}} = \begin{pmatrix} x_1^2 & -4x_2^3\,(\eta_0(1 - 16x_2^6\lambda^2))^{\frac{n-1}{a}} \\ -4x_2^3\,(\eta_0(1 - 16x_2^6\lambda^2))^{\frac{n-1}{a}} & x_1^2 \end{pmatrix} \,. \tag{5.6}$$

Therein, the lower viscosity bound is directly set to zero, i.e. $\eta_\infty = 0$, according to the chosen model parameters in this example. For the calculations the remaining parameters for the Carreau-Yasuda viscosity function are selected as $\eta_0 = 1\,\text{kg/(ms)}$, $n = 0.2$, $\lambda = 1\,\text{s}$ and $a = 2$, resulting in a shear-thinning fluid behavior. For the material properties the fluid density is set to $\rho_f = 1\,\text{kg/m}^3$. By choosing the model parameter $a = 2$ this is also referred to as the Carreau model in the literature, see Carreau [91].

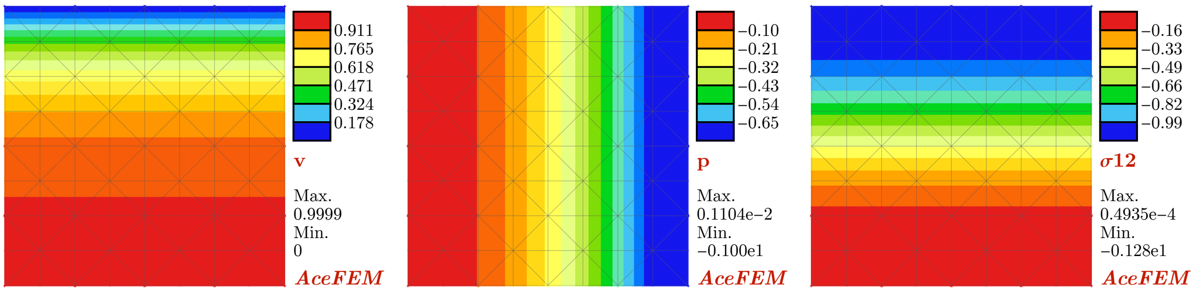

Figure 5.2: SD - solution for total velocity field (left, in m/s), pressure (center, in $\mathrm{N/m^2}$) and stresses $\sigma_{12}$ (right, in $\mathrm{N/m^2}$) for a mesh size of 128 triangles using element $RT_2P_3$

The solution for the resulting total velocity $|\boldsymbol{v}|$, pressure $p$, and stress field $\sigma_{12}$ are exemplified in Figure 5.2. These results are obtained with the element $RT_2P_3$ and an element length of $h = 1/8\,\mathrm{m}$, and agree with the exact solutions.

The convergence properties using different element orders for the stresses and velocities are evaluated based on the discretization error compared to the exact solution. Therefore, the error in the velocities and stresses is computed using the $L^2$-norm as

$$e_{\boldsymbol{v}} = ||\boldsymbol{v}_{\text{exact}} - \boldsymbol{v}_{\text{h}}||_{L^2(\Omega_f)} \qquad \text{and} \qquad e_{\boldsymbol{\sigma}} = ||\boldsymbol{\sigma}_{\text{exact}} - \boldsymbol{\sigma}_{\text{h}}||_{L^2(\Omega_f)}\ , \tag{5.7}$$

where $\boldsymbol{v}_{\text{exact}}$ and $\boldsymbol{\sigma}_{\text{exact}}$ refer to the analytical solutions of the problem and $\boldsymbol{v}_{\text{h}}$ and $\boldsymbol{\sigma}_{\text{h}}$ denote the approximated quantities. An error analysis for elements $RT_1P_2$ and $RT_2P_3$ has been performed for a regular mesh refinement. Table 5.1 contains mesh information such as number of elements and degrees of freedom of the meshes used in the numerical simulations.

Table 5.1: SD - mesh level, number of elements ($n_{\text{ele}}$) and degrees of freedom ($n_{\text{dof}}$) for different element types

|  |  | $n_{\text{dof}}$ |  |
|---|---|---|---|
| level | $n_{\text{ele}}$ | $RT_1P_2$ | $RT_2P_3$ |
| 1 | 8 | 113 | 241 |
| 2 | 32 | 449 | 961 |
| 3 | 128 | 1,793 | 3,841 |
| 4 | 512 | 7,169 | 15,361 |
| 5 | 2,048 | 28,673 | 61,441 |
| 6 | 8,192 | 114,689 | 245,761 |
| 7 | 32,768 | 458,753 | 983,041 |

To evaluate the spatial convergence order, Figure 5.3 displays the discretization errors over the element length $h$ in a logarithmic scale. The slopes of the fitted linear regression lines for the velocities with quadratic and cubic interpolation orders take the form $\mathcal{O}(h^3)$ and $\mathcal{O}(h^4)$, while the error convergence of the stresses discretized with $RT_1$ and $RT_2$ takes the form $\mathcal{O}(h^2)$ and $\mathcal{O}(h^3)$, respectively. Thus, the graphs show that the error decrease in the $L^2$-norm is consistent with the expected values of order $\mathcal{O}(h^{n+1})$ for polynomials $P_n$ and of order $\mathcal{O}(h^{m+1})$ for Raviart-Thomas functions $RT_m$.

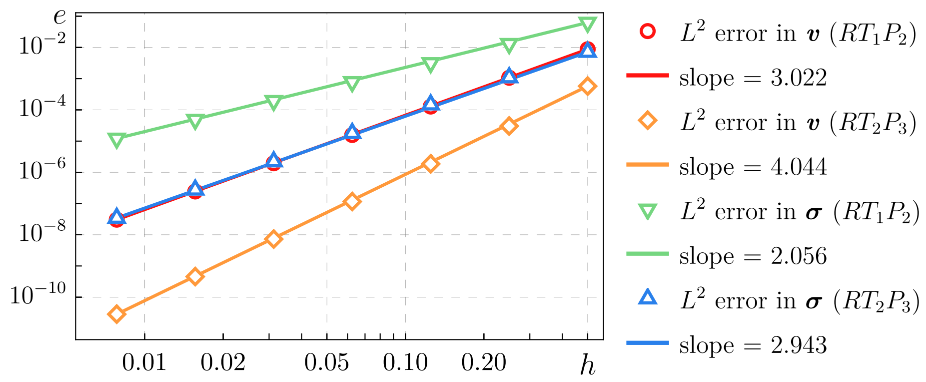

Figure 5.3: SD - $L^2$-norm of the discretization error in approximation of velocities $\boldsymbol{v}$ and stresses $\boldsymbol{\sigma}$ for different element orders and mesh sizes

### 5.2.2 Lid driven cavity flow of non-Newtonian fluid

Next, a parameter study of the constitutive Carreau-Yasuda model is performed for the lid-driven cavity (LDC) flow to investigate the effects of the model parameters on the flow kinematics. This benchmark problem is among the most studied problems in computational fluid dynamics, since it consists of a simple geometry, but it shows complex flow phenomena such as recirculation. The geometry of the computational square domain $\Omega_f = [0,1]^2$ and the boundary conditions for the problem are equivalent to those in SURANA ET AL. [377] and KIM AND REDDY [234], and illustrated in Figure 5.4. The calculations for this numerical example are performed using the element denoted as $RT_2P_3$.

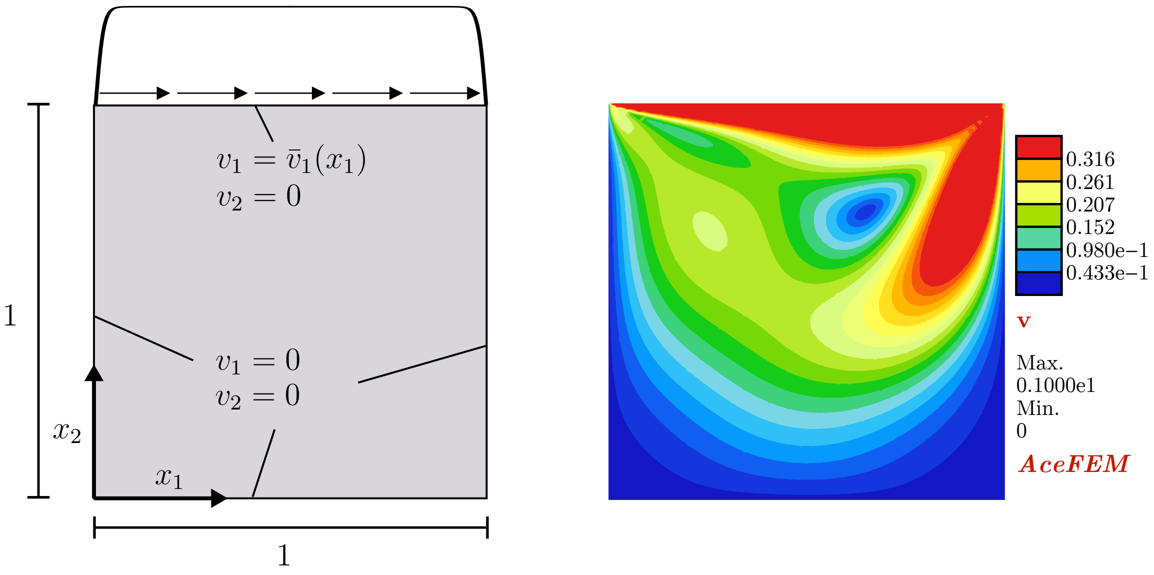

Figure 5.4: LDC - geometry and boundary conditions (left, in m) and solution for the total velocity field (right, in m/s)

The simulation area is bounded at the sides and bottom by fixed walls with no-slip boundary conditions. At the top, a horizontal velocity is applied which is described by the function

$$\bar{v}_1(x_1) = \begin{cases} \tanh(50x_1)\ , & \text{if } 0 \le x_1 \le 0.5\ , \\ -\tanh(50x_1 - 50)\ , & \text{if } 0.5 \le x_1 \le 1\ . \end{cases} \tag{5.8}$$

The use of a tangent function allows a smooth increase of the velocity at the corners. Therefore, corner singularities caused by impulsively assigned horizontal velocities at the corners can be avoided. The occurrence of these discontinuities and the resulting difficulties in accuracy analysis have been the subject of several studies, see e.g. Botella and Peyret [64] and Auteri et al. [7]. Additionally, for the degrees of freedom assigned to the stresses, the boundary conditions are specified at one point in the center on the bottom edge as $\boldsymbol{\sigma}_2 \cdot \boldsymbol{n} = 0$.

In a first step, the results for the velocity field are validated by comparison with the reference solution of Kim and Reddy [234]. For this purpose, the values in Table 5.2 are adopted for the material and model parameters. These coefficients correspond to a Reynolds number of $Re = 100$, identical to that in the reference literature.

Table 5.2: LDC - material and viscosity model parameters

| $\rho_f$ | $\eta_0$ | $\eta_\infty$ | $n$ | $a$ | $\lambda$ |
|---|---|---|---|---|---|
| kg/m$^3$ | kg/(ms) | kg/(ms) | - | - | s |
| 45 | 0.45 | 0 | 0.756 | 2.0 | 1.85 |

The horizontal and vertical velocity components at the centerlines ($x_1 = 0.5\,\mathrm{m}$ and $x_2 = 0.5\,\mathrm{m}$) are evaluated and compared with the reference values. Figure 5.5 shows the results for different uniform meshes with $h$ denoting the element length. It can be observed that the calculated velocity profiles show mesh convergence and correspond well with those of Kim and Reddy [234], as soon as a number of 512 elements is exceeded. The result for the total velocity on the domain $\Omega_f$ is shown in Figure 5.4 (right) for a mesh with 8192 elements, where the formation of the inner vortex is visible.

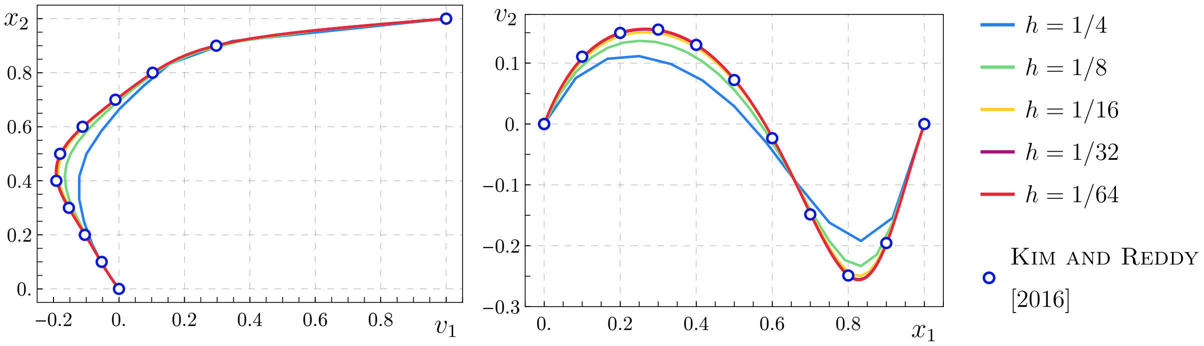

Figure 5.5: LDC - velocity profiles at centerlines in $x_1$- and $x_2$-direction obtained with element $RT_2P_3$ and different mesh sizes compared to reference solution from Kim and Reddy [234] (units [$h$]=[$x$]=m and [$v$]=m/s)

Furthermore, the influence of the various parameters of the Carreau-Yasuda viscosity model (5.1) is investigated. More precisely, a parameter study for the parameters $\lambda$ and $n$ is performed at this point. For this purpose, the change of the horizontal and vertical velocity profiles at the vertical and horizontal centerline of the cavity, respectively, are observed depending on the change of individual parameters. These calculations are performed using a mesh with element length $h = 1/64\,\mathrm{m}$ and the remaining model parameters, except for $\lambda$ and $n$, are set as indicated in Table 5.2.

Figure 5.6 shows how the cavity flows are affected by changing $n$, while the relaxation time is set to $\lambda = 1\,\mathrm{s}$. As can be seen, $v_1$ and $v_2$ deviate increasingly from the Newtonian fluid obtained with $n = 1$ as the value for the parameter decreases. This can be explained with reference to Figure 2.5 (left), where the viscosity curve is plotted as a function of shear rate for various values of $n$. For smaller parameter values, the slope of the viscosity curve in the power-law region becomes continuously steeper.

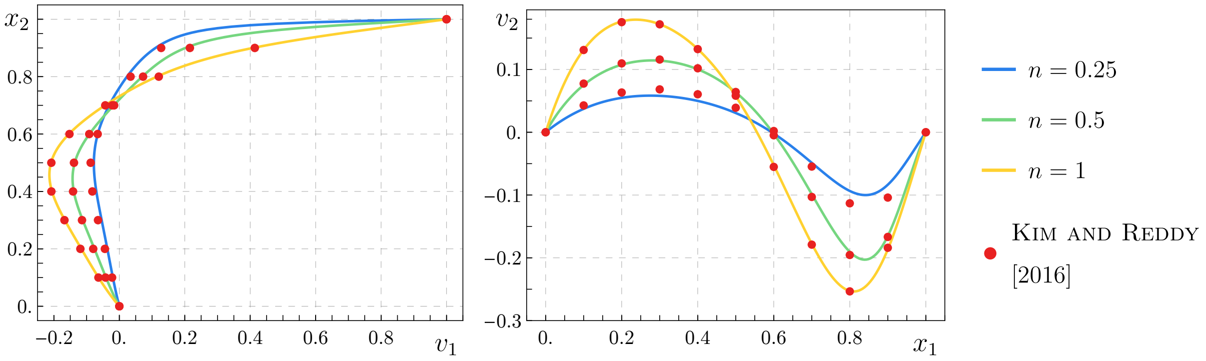

Figure 5.6: LDC - influence of parameter $n$ on velocity profiles (units $[x]$=m and $[v]$=m/s))

Varying the relaxation parameter $\lambda$ leads to a shift in the power-law region in Figure 2.5 (right) such that the change from the upper to the lower viscosity limit occurs at higher shear rates $\dot{\gamma}$ for decreasing values $\lambda$. The effect of this can be seen in the change in velocity profiles in Figures 5.7. For these calculations, the values for $\lambda$ were varied while $n = 0.5$ was fixed.

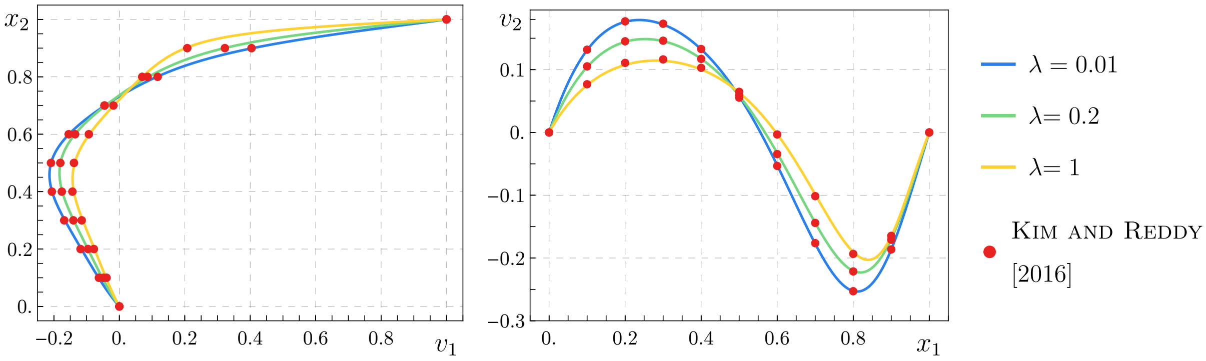

Figure 5.7: LDC - influence of parameter $\lambda$ on velocity profiles (units $[x]$=m and $[v]$=m/s))

### 5.2.3 Flow over a backward facing step with parameter study

Another commonly used benchmark problem in computational fluid dynamics is the flow over a backward-facing step (BFS), characterized by the presence of a recirculation zone downstream of the step. The length of this recirculation zone depends on the flow and fluid properties. These can also be described by the typical Reynolds number, which depends on the flow velocity, viscosity and geometry. In the following, this typical problem is solved for the flow of a generalized Newtonian fluid approximating the material behavior with the Carreau-Yasuda model given in (5.1).

The effect on the recirculation zone when varying the model parameters is examined. The geometry was chosen equivalent to the specifications in Gartling [162] and Kim and Reddy [234] and is depicted in Figure 5.8. On the left side of the channel an inflow is applied at $H \leq x_2 \leq 2H$ with $H = 0.5\,\mathrm{m}$ the vertical velocity component is $v_2 = 0$ and the horizontal component is defined as

$$\bar{v}_1(x_2) = \begin{cases} -24(x_2-1)(x_2-0.5), & \text{if } H \leq x_2 \leq 2H \ , \\ 0 \ , & \text{if } 0 \leq x_2 \leq H \ . \end{cases} \tag{5.9}$$

On the upper and lower walls, the velocities are set to zero according to the no-slip conditions. At the outflow the velocity in $x_2$-direction is set to $v_2 = 0$ and the stress related degrees of freedom are prescribed as $\boldsymbol{\sigma}_1 \cdot \boldsymbol{n} = 0$.

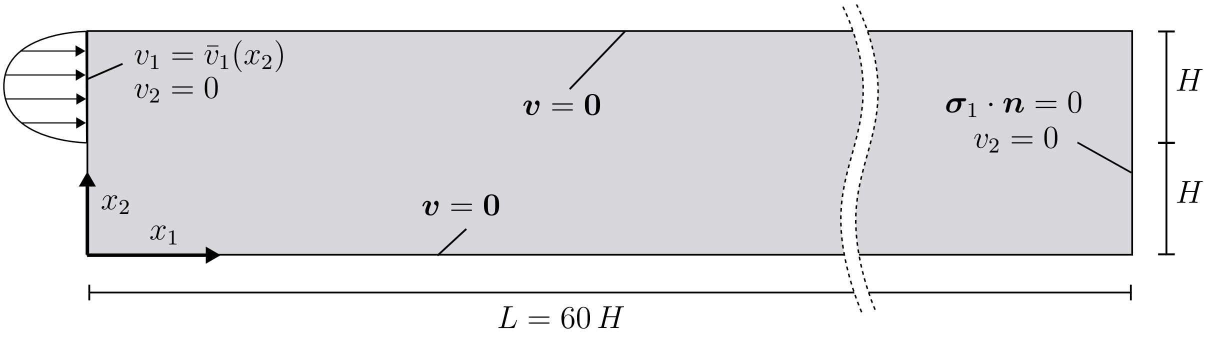

Figure 5.8: BFS - geometry and boundary conditions with length $h = 0.5\,\mathrm{m}$

The domain is discretized using element $RT_2P_3$ with a structured mesh, see Figure 5.9, where the element length $h$ is smaller in the front region and larger towards the outflow. This ensures that the recirculation zone behind the step is resolved well enough to correctly represent the flow behavior.

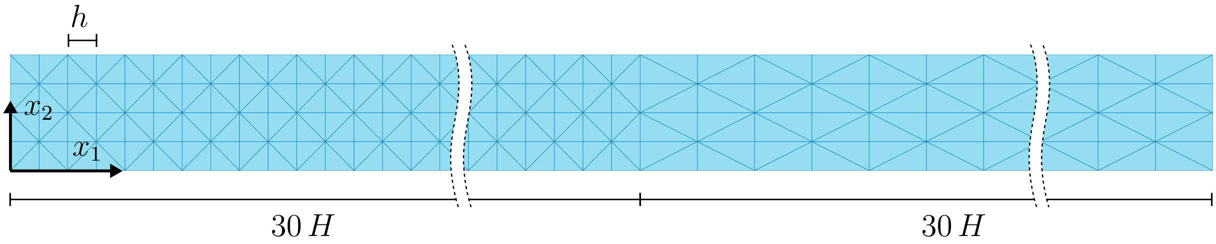

Figure 5.9: BFS - structured mesh exemplary for element length $h = 1/4\,\mathrm{m}$

**Validation**

First, the formulation is validated by comparing the solution of the velocity profiles at the locations $x_1 = 7\,\mathrm{m}$ and $x_1 = 15\,\mathrm{m}$ with the reference values in Gartling [162], see Figure 5.11. For this purpose, the material parameters for the first calculations are selected according to the specifications in the referenced literature as follows:

$$\rho_f = 1.0\,\mathrm{kg/m^3}, \quad \eta_0 = 1.25 \times 10^{-3}\,\mathrm{kg/(ms)}, \quad \eta_\infty = 0, \quad n = 1.0, \quad a = 2.0, \quad \lambda = 1.0\,\mathrm{s} \ .$$

This choice corresponds to modeling a Newtonian fluid at a Reynolds number of $Re = 800$. The characteristic values for this boundary value problem, which are used to calculate the

Reynold number (2.62), are the bulk velocity, which is two-thirds of the maximum inflow velocity, i.e. $v_B = 2/3\,\bar{v}_1^{\max} = 1\,\mathrm{m/s}$, and the characteristic length, which is twice the inflow height $L_{ch} = 2H = 1\,\mathrm{m}$. The resulting total velocity field $|\boldsymbol{v}|$ for this parameter set is shown in Figure 5.10. The entire domain is displayed unscaled divided into two plots, where on the upper image the flow separation as a consequence of the backward facing step can be identified. Further downstream it is visible that a parallel flow develops.

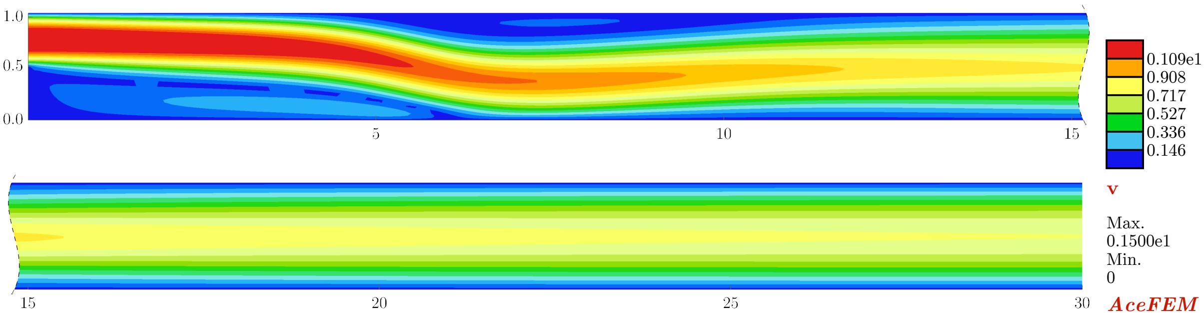

Figure 5.10: BFS - distribution of total velocity field $|\boldsymbol{v}|$ obtained with mesh level 3

The velocity profiles versus the height of the channel for the horizontal and vertical components of the velocity at the two selected cuts are shown in Figure 5.11. Different mesh levels are considered for the calculations where $h$ denotes the edge length of the elements in the fine grid region on the left side of the domain. Information such as the number of elements used and the number of resulting degrees of freedom at each mesh level are given in Table 5.3.

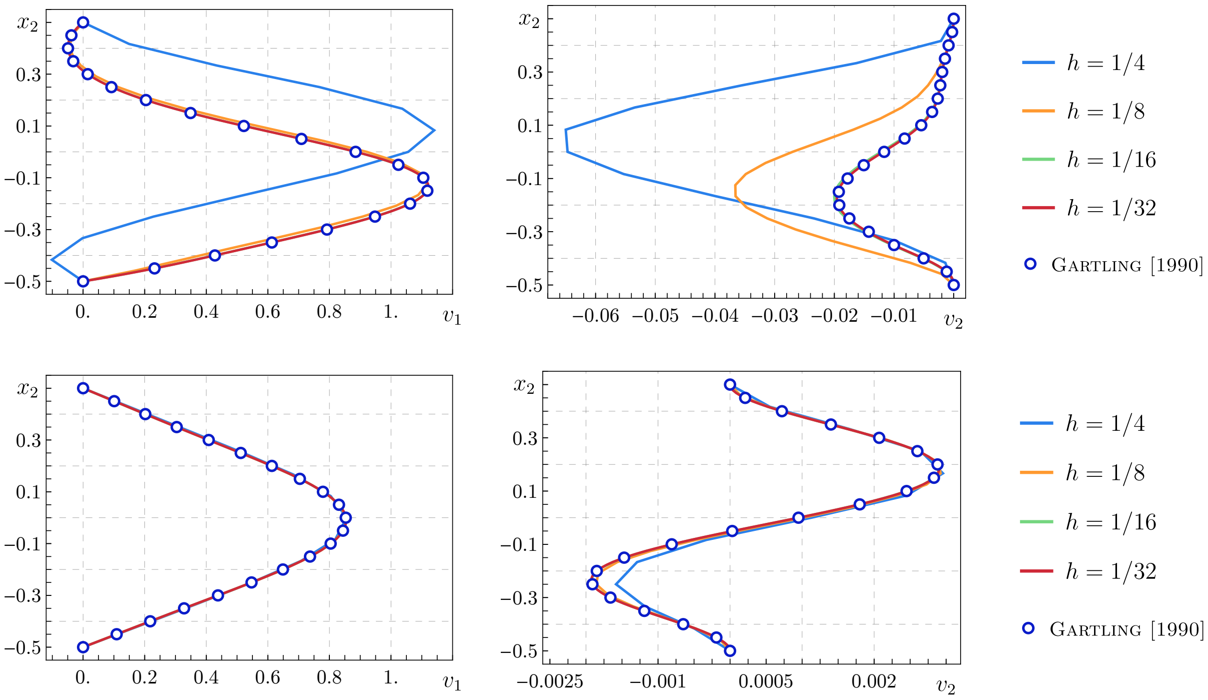

Figure 5.11: BFS - velocity profiles for different mesh levels at $x_1 = 7\,\mathrm{m}$ (top) and $x_2 = 15\,\mathrm{m}$ (bottom) compared to reference solution from GARTLING [162] for $Re = 800$

Table 5.3: BFS - mesh level, minimum element length $h$, number of elements ($n_{\text{ele}}$) and degrees of freedom ($n_{\text{dof}}$) for discretizations with element $RT_2P_3$

| level | length $h$ | $n_{\text{ele}}$ | $n_{\text{dof}}$ |
|---|---|---|---|
| 1 | 1/4 | 720 | 21,601 |
| 2 | 1/8 | 2,880 | 86,401 |
| 3 | 1/16 | 11,520 | 345,601 |
| 4 | 1/32 | 46,080 | 1,382,401 |

The graphs show that from the third mesh level onwards with $h = 1/16\,\text{m}$ a convergent solution is obtained, which is in agreement with the results obtained in the work of GARTLING [162]. Furthermore, it is visible that especially in the cut at $x_1 = 7\,\text{m}$ the deviations using coarse meshes are very large. The reason therefore is, that in this region the velocity gradients are very high and these flow kinematics cannot be modeled correctly with a low resolution.

**Effect of Reynolds number**

In a next step, the influence of the viscosity on the flow kinematic is studied. More precisely, the reattachment length $x_R$ is evaluated for different Reynolds numbers, which is in fact varied by changing the viscosity. The reattachment point is the length of the recirculation zone and can be evaluated considering the position on the lower wall, at which the shear stress is zero downstream of the large recirculation eddy, i.e. $\boldsymbol{\sigma}_1 \cdot \boldsymbol{n} = 0$. The material and model parameters for the second study of the BFS benchmark problem are specified just as in the previous calculations, except that the dynamic viscosity $\eta_0$ is varied. The different values for the viscosity, the corresponding Reynolds numbers and the resulting reattachment points are listed in Table 5.4.

Table 5.4: BFS - reattachment length $x_R$ for different Reynolds numbers by changing the dynamic viscosity

| *Re* | - | 100 | 150 | 400 | 800 |
|---|---|---|---|---|---|
| $\eta_0$ | kg/(ms) | $10^{-2}$ | $6.6\times10^{-3}$ | $2.5\times10^{-3}$ | $1.25\times10^{-3}$ |
| $x_R$ | m | 1.64 | 2.17 | 4.33 | 6.12 |

The curve of the shear stress at the lower wall in $x1$-direction is depicted in Figure 5.12 for different flow properties. Only the first part of the region in which the zero shear stress occurs is shown.

**Effect of model parameters**

The final investigation on the flow over the backward-facing step is a parameter study, in which the effect of the different coefficients of the Carreau-Yasuda viscosity model is examined. For this purpose, the reattachment length is again evaluated while the power-law index $n$ and the relaxation parameter $\lambda$ are varied. In this case, the material and model parameters are defined as

$$\rho_f = 1.0\,\text{kg/m}^3, \quad \eta_0 = 10^{-2}\,\text{kg/(ms)}, \quad \eta_\infty = 0, \quad a = 2.0 \quad ,$$

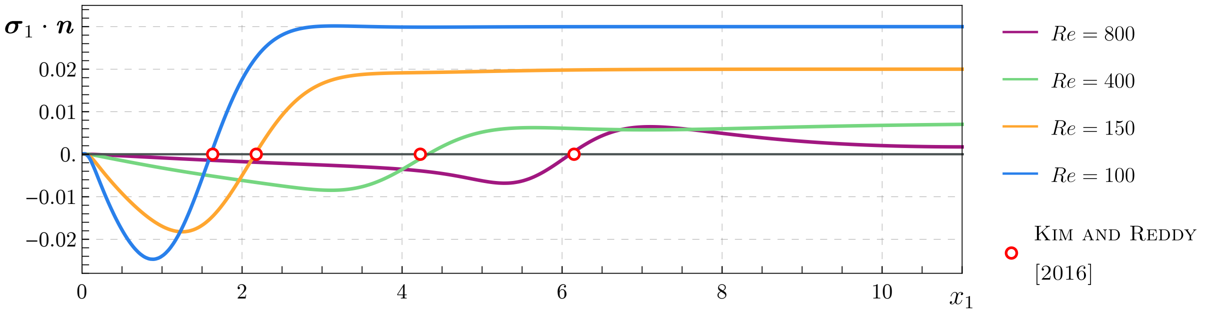

Figure 5.12: BFS - shear stress $\boldsymbol{\sigma}_1 \cdot \boldsymbol{n}$ at bottom wall and points of reattachment compared to reference solution from Kim and Reddy [234] for different Reynolds numbers

leading to a Reynolds number of $Re = 100$. The values for $n$ and $\lambda$ are changed as specified in the tabular in Figure 5.13 (right). This table also contains the resulting values of the reattachment points $x_R$ when varying the parameters. Furthermore, the relation between the reattachment length and the model parameters is illustrated in Figure 5.13 (left). An increase of the parameter $n$ leads to an extension of the recirculation zone, whereas an increase in $\lambda$ results in a shorter recirculation zone.

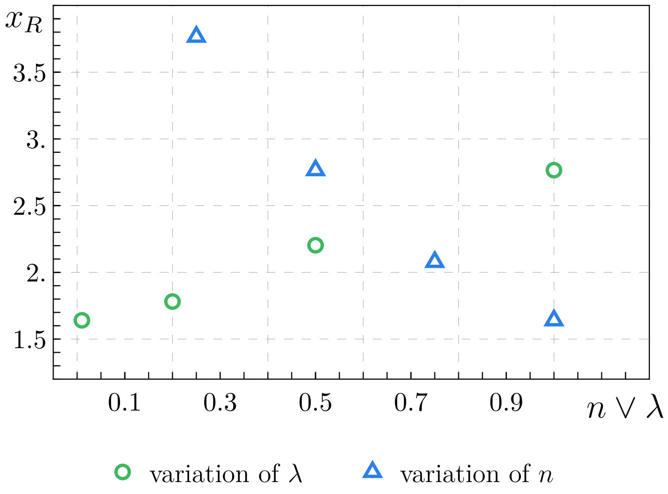

| $n$ | 0.25 | 0.5 | 0.75 | 1.0 |
|---|---|---|---|---|
| $x_R$ | 3.766 | 2.766 | 2.078 | 1.641 |

| $\lambda$ | 0.01 | 0.2 | 0.5 | 1.0 |
|---|---|---|---|---|
| $x_R$ | 1.641 | 1.781 | 2.203 | 2.766 |

Figure 5.13: BFS - reattachment point $x_R$ depending on different values for $\lambda$ and $n$

It can be seen that the reattachment length reduces with increasing power index $n$ ranging from 0.25 to 1.0 while the other parameters remain constant. This is due to the fact that the viscosity decreases relative to the parameter $n$, since the viscosity approaches the lower limit $\eta_\infty$ with lower values for the power index already at smaller shear rates, see Figure 2.5 (left). Thus, the reattachment length for simulations with a low power index increases. An increase in relaxation time parameter $\lambda$ leads to a decrease in viscosity as the transition zone from the upper to the lower viscosity bound is shifted, see Figure 2.5 (right). As a result, a fluid with higher value $\lambda$ exhibits a more extended recirculation zone. Additionally, the effect on the wall shear stress can be seen in Figures 5.14 and 5.15, which are consistent with the properties described.

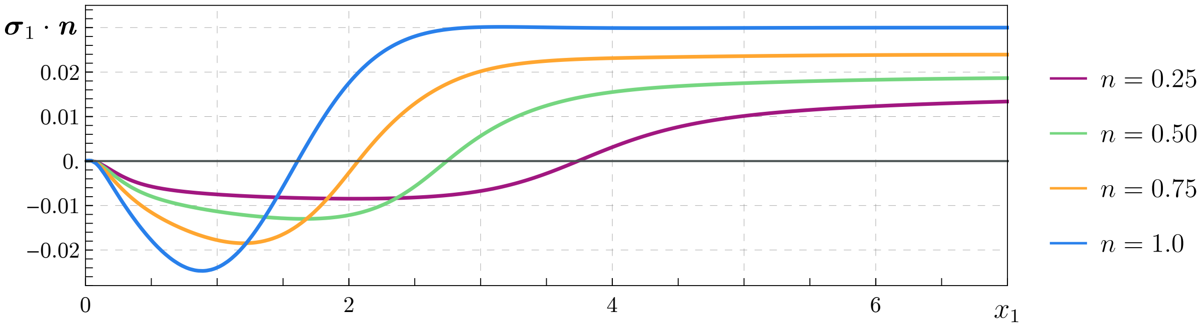

Figure 5.14: BFS - shear stress $\boldsymbol{\sigma}_1 \cdot \boldsymbol{n}$ at bottom wall for different values $n$

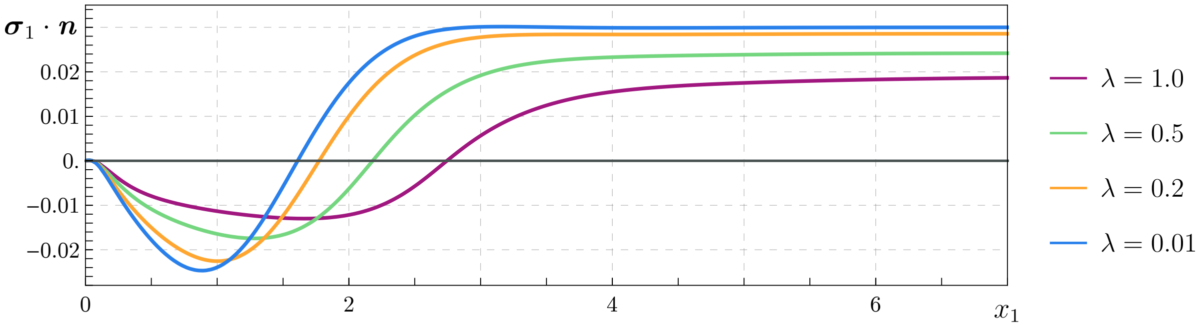

Figure 5.15: BFS - shear stress $\boldsymbol{\sigma}_1 \cdot \boldsymbol{n}$ at bottom wall for different values $\lambda$

### 5.2.4 Channel flow with smooth contraction 4:1 and data assimilation

In the last example regarded for the numerical calculation of non-Newtonian fluids in 2D, the assimilation of data into the analysis with the LSFEM is described. Therefore, the mixed least-squares formulation in terms of stresses and velocities for flow of non-Newtonian fluids defined in (5.2) is extended with (3.54). The total LS functional with data assimilation reads then

$$\mathcal{F}^*(\boldsymbol{\sigma}, \boldsymbol{v}) = \mathcal{F}^F(\boldsymbol{\sigma}, \boldsymbol{v}) + \mathcal{F}^{data}(\boldsymbol{v}) \ . \tag{5.10}$$

For a typical element $e$, the discretized linear system of equations in matrix notation reads

$$\boldsymbol{K}^e \cdot \Delta \boldsymbol{D}^e = -\boldsymbol{P}^e \quad \Rightarrow \quad \begin{bmatrix} \boldsymbol{k}^e_{vv} & \boldsymbol{k}^e_{v\sigma} \\ \boldsymbol{k}^e_{\sigma v} & \boldsymbol{k}^e_{\sigma\sigma} \end{bmatrix} \begin{bmatrix} \Delta \boldsymbol{w} \\ \Delta \boldsymbol{\beta} \end{bmatrix} = - \begin{bmatrix} \boldsymbol{r}^e_v \\ \boldsymbol{r}^e_\sigma \end{bmatrix} , \tag{5.11}$$

where $\boldsymbol{w}^I$ and $\boldsymbol{\beta}^J$ are the degrees of freedom of the velocities and stresses at nodes $I$ and $J$. Both the element matrix $\boldsymbol{K}^e$ and the right-hand-side vector $\boldsymbol{P}^e$ contain entries related to the standard functional $\mathcal{F}(\boldsymbol{\sigma}, \boldsymbol{v})$ and, at the corresponding degrees of freedom, of the functional $\mathcal{F}^{data}(\boldsymbol{v})$. The algorithmic implementation of the SV formulation in 2D including data assimilation is described in Appendix B.1. In order to test the assimilation of data, flow through a smoothly narrowing channel (NC), see Figure 5.16, is simulated. The tightening with a ratio of 4:1 leads to a strong necking and to an increase of the flow velocity, which can easily lead to the well-known problem of mass loss using the least-squares FEM.

For the straightforward implementation of data assimilation and the investigation of the effect on the LSFEM solution, a numerical reference solution is applied. This is obtained

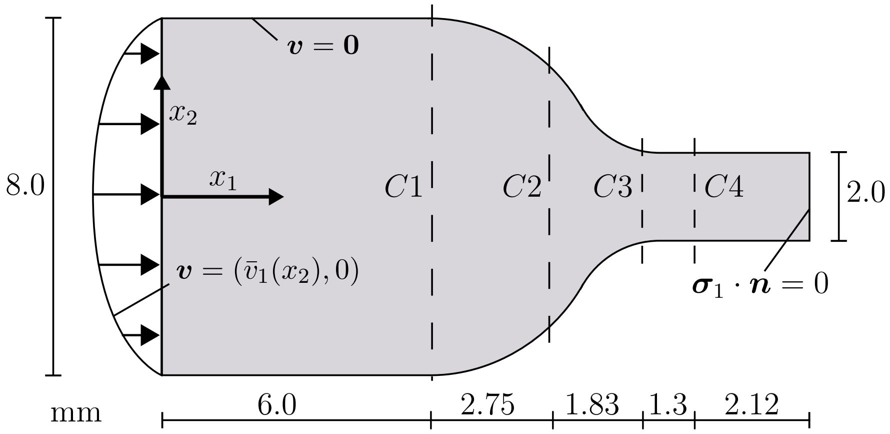

Figure 5.16: NC - geometry for channel with smooth 4:1 narrowing

in this example by using a mixed Taylor-Hood Galerkin triangle element on a fine grid. The inflow is assumed to be parallel with $v_2 = 0$ and the horizontal velocity component is prescribed with

$$\bar{v}_1(x_2) = 0.15 - \frac{0.6}{0.008^2}(x_2)^2 \text{ m/s} . \tag{5.12}$$

Furthermore, the channel has no-slip boundary conditions and at the outflow the degrees of freedom related to the stresses are defined as $\boldsymbol{\sigma}_1 \cdot \boldsymbol{n} = 0$. The material and model parameters are selected as

$$\eta_0 = 22 \cdot 10^{-3}\,\text{Pa s}, \qquad \eta_\infty = 2.2 \cdot 10^{-3}\,\text{Pa s}, \qquad \rho_f = 1410\,\text{kg/m}^3$$
$$n = 0.392, \qquad \lambda = 0.11\,\text{s}, \qquad a = 0.644 \quad .$$

This choice results in a shear-thinning fluid and, according to Gijsen et al. [169], is suitable for modeling blood flow. The resulting velocity distribution is shown in Figure 5.17 (right). The strong increase in velocities in the area of the necking is visible. First, a grid convergence without data assimilation is performed for the element $RT_2P_3$. Different structured meshes are applied with a regular refinement. The arrangement of the elements for a mesh with 896 triangles is shown as an example in Figure 5.17 (left). The information on the different meshes, the corresponding number of elements and degrees of freedom are listed in Table 5.5.

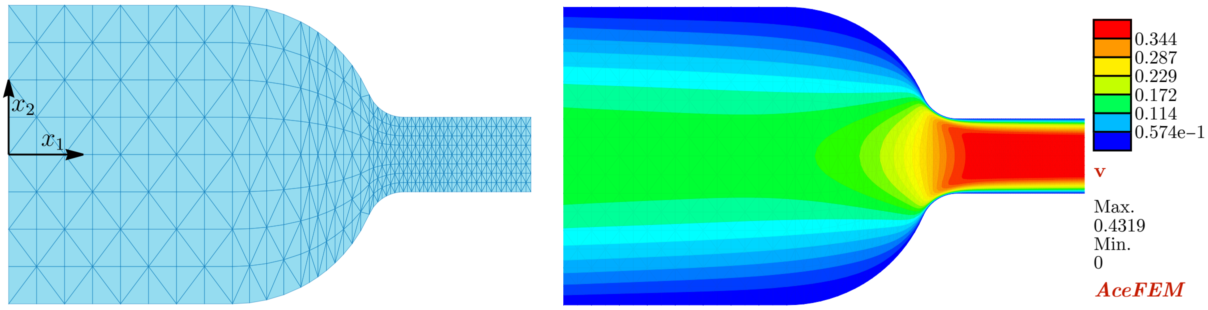

Figure 5.17: NC - mesh structure (left) and total velocity field for mesh level M3 with element $RT_2P_3$ (right, in m/s)

To quantify the quality of the numerical solution, the mass loss and the absolute velocity error $e_v$ are evaluated. The mass loss is calculated by simply analyzing the difference between the inflow and outflow. The error in the velocities is assessed by comparing the solution for the horizontal and vertical velocity components at different positions in $x_1$-direction to a fine-grid solution obtained with a mixed Taylor-Hood Galerkin element. Thus the error is defined as

$$e_v = \frac{1}{N} \sum_{i=1}^{N} ||\boldsymbol{v}^i - \hat{\boldsymbol{v}}^i|| = \frac{1}{N} \sum_{i=1}^{N} \sqrt{(v_1^i - \hat{v}_1^i)^2 + (v_2^i - \hat{v}_2^i)^2} \ , \tag{5.13}$$

where the reference values are denoted with the hat symbol and $N$ is the number of data points. For the calculation of the error the cuts $C1$, $C2$ and $C4$, see Figure 5.16, are considered. The results for the mass loss and the velocity error are additionally included in Table 5.5. From this it is visible that a very fine mesh with a high number of degrees of freedom is needed to reduce the mass loss by using the presented mixed least-squares stress-velocity formulation.

Table 5.5: NC - mesh level, number of elements ($n_{\text{ele}}$), number of degrees of freedom ($n_{\text{dof}}$) and results for mass loss (difference of inflow and outflow in %) and absolute velocity error (in cuts $C1$, $C2$, $C4$) compared to numerical reference solution

| mesh level | M1 | M2 | M3 | M4 | M2 + data assimilation |
|---|---|---|---|---|---|
| $n_{\text{ele}}$ | 224 | 896 | 3,584 | 14,336 | 896 |
| $n_{\text{dof}}$ | 6,732 | 26,904 | 107,568 | 430,176 | 26,904 |
| mass loss | 68.8 | 45.4 | 15.4 | 1.4 | 1.04 |
| error $e_v$ | $3.80 \cdot 10^{-1}$ | $2.62 \cdot 10^{-1}$ | $9.07 \cdot 10^{-2}$ | $8.60 \cdot 10^{-3}$ | $1.21 \cdot 10^{-2}$ |

In a next step, the effect of data assimilation is evaluated by including the fine-grid reference data at cut $C3$ into the numerical least-squares FEM computation. For this purpose, the second mesh level M2 is selected, which yields a very high mass loss of almost 50% in the previous simulation without data assimilation. The new result for the mass loss and velocity error considering data assimilation at cut $C3$ is given in the last column of Table 5.5. The comparison of the results shows the significant improvement of the numerical least-squares solution.

The improvement can also be observed in Figure 5.18, which shows the velocity profiles of component $v_1$ over the height of the channel at cuts $C1$, $C2$ and $C4$. The figure presents the profiles of the velocity for three different grids without assimilation of data and additionally the velocity distribution when data is assimilated into the solution with a coarse grid (dashed line). A comparison of these graphs reveals a significant enhancement, because in all considered cuts, no matter if upstream or downstream, the numerical solution with data assimilation is basically equal to the reference solution. Thus, the numerical accuracy can be greatly improved by data integration, such that even coarse meshes with low computational cost lead to accurate solutions.

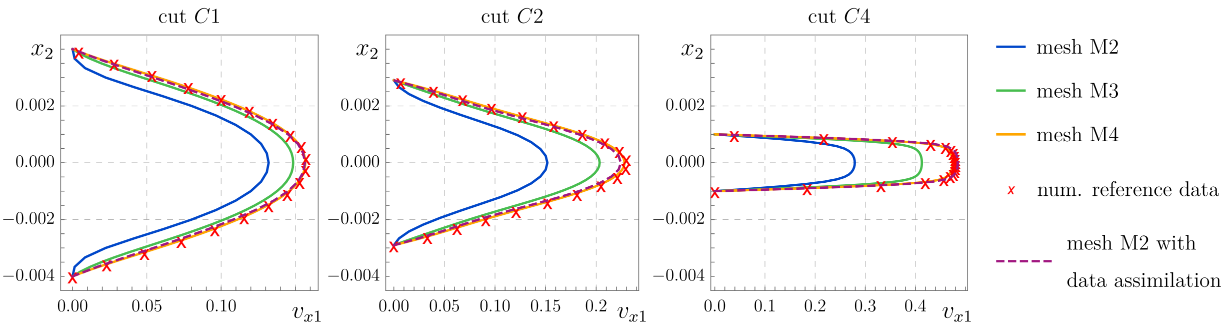

Figure 5.18: NC - velocity profiles (in m/s) without data assimilation (mesh levels M2, M3, M4) and with data assimilation at cut $C3$ (for mesh M2)

## 5.3 SVP formulation for incompressible non-Newtonian fluids in 3D

For the computation of flow problems involving generalized Newtonian fluids in three dimensions, a mixed LS stress-velocity-pressure formulation is applied in the following. Therefore, the SVP formulation given in (4.2) is modified to take into account the non-linear dependence of the dynamic viscosity $\eta$ on the shear rate $\dot{\gamma}$. Steady-state flows of generalized Newtonian fluids are considered at this point, so the time-dependent term, i.e. the accelerations, are dropped in the following notation. This leads to the LS functional in terms of stresses, velocities and pressure written as

$$\begin{aligned}\mathcal{F}^F(\boldsymbol{\sigma},\boldsymbol{v},p) = \frac{1}{2}\Big(&||\omega_{f1}(\operatorname{div}\boldsymbol{\sigma}-\rho_f\nabla\boldsymbol{v}\cdot\boldsymbol{v}+\boldsymbol{f})||^2_{L^2(\Omega_f)}\\&+||\omega_{f2}(\boldsymbol{\sigma}-2\eta(\dot{\gamma})\nabla^s\boldsymbol{v}+p\boldsymbol{I})||^2_{L^2(\Omega_f)}+||\omega_{f3}(\operatorname{div}\boldsymbol{v})||^2_{L^2(\Omega_f)}\Big)\ ,\end{aligned} \tag{5.14}$$

with appropriate positive weighting factors $\omega_{f1}, \omega_{f2}$ and $\omega_{f3}$. For solving the minimization problem with Newton's method, the first and second variations of the functional with respect to all unknowns are required again. The derivation of these variations for the general mixed least-squares SVP formulation for unsteady flow of Newtonian fluids is explained in (4.3)-(4.5). Further explanations are omitted here, since the procedure is similar. It should only be noted that the viscosity is a function of the velocity and, in addition, the time-dependent terms can be dropped.

For the discretization of the presented variational formula with $\mathcal{F}(\boldsymbol{\sigma},\boldsymbol{v},p)\ :\ \boldsymbol{W}\times\boldsymbol{V}\times\boldsymbol{Q}\ \rightarrow\ \mathbb{R}^3$, standard finite element interpolations for the velocities, stresses and pressure are chosen as specified in Section 3.3.4. Therein, the interpolation orders are set to $k = n = m-1$, leading to mixed finite element descriptions $P_kP_{k+1}P_k$. Similar approaches based on p-version LS formulations for non-Newtonian fluids were studied e.g. by Bell and Surana [36], Edgar and Surana [137], Surana et al. [377] and Kim and Reddy [234; 235] for two-dimensional problems and by Kim and Reddy [236] also for three-dimensional problems.

Based on the first variations and linearization of the SVP formulation, the resulting discretized linear system of equations for a typical element $e$ in matrix notation reads

$$\boldsymbol{K}^e\cdot\Delta\boldsymbol{D}^e = -\boldsymbol{P}^e \quad\Rightarrow\quad \begin{bmatrix}\boldsymbol{k}^e_{vv} & \boldsymbol{k}^e_{v\sigma} & \boldsymbol{k}^e_{vp}\\ \boldsymbol{k}^e_{\sigma v} & \boldsymbol{k}^e_{\sigma\sigma} & \boldsymbol{k}^e_{\sigma p}\\ \boldsymbol{k}^e_{pv} & \boldsymbol{k}^e_{p\sigma} & \boldsymbol{k}^e_{pp}\end{bmatrix}\begin{bmatrix}\Delta\boldsymbol{w}\\ \Delta\boldsymbol{\beta}\\ \Delta q\end{bmatrix} = -\begin{bmatrix}\boldsymbol{r}^e_v\\ \boldsymbol{r}^e_\sigma\\ \boldsymbol{r}^e_p\end{bmatrix}\ , \tag{5.15}$$

where $\boldsymbol{w}^I$, $\boldsymbol{\beta}^J$ and $q^L$ are the degrees of freedom of the velocities, stresses and pressure at nodes $I, J$ and $L$, respectively. These can be approximated as defined in Appendix B.2.

In this section, the assimilation of numerical as well as experimental data into the simulation of three dimensional non-Newtonian fluid flow is investigated. Therefore, the total mixed least-squares functional is constructed based on the SVP formulation given in (5.14) and the LS data functional (3.54), and reads

$$\mathcal{F}^*(\boldsymbol{\sigma}, \boldsymbol{v}, p) = \mathcal{F}^F(\boldsymbol{\sigma}, \boldsymbol{v}, p) + \mathcal{F}^{data}(\boldsymbol{v}) \ . \tag{5.16}$$

In case of data assimilation, both the element matrix $\boldsymbol{K}^e$ and the right-hand-side vector $\boldsymbol{P}^e$ in (5.15) contain entries related to the standard functional $\mathcal{F}(\boldsymbol{\sigma}, \boldsymbol{v}, p)$ and, at the corresponding degrees of freedom, of the functional $\mathcal{F}^{data}(\boldsymbol{v})$. Further details regarding the implementation are provided in Appendix B.2.

## 5.4 Numerical examples: Steady flow of non-Newtonian fluids in 3D

The following section contains several numerical examples to model generalized Newtonian fluids in three dimensions. These serve on one hand to validate and verify the presented mixed LS SVP formulation and on the other hand to investigate the effect of data assimilation in the simulation of three dimensional flow problems with the LSFEM. For validation, a steady-state flow in a cubic domain containing an analytical solution is calculated. Then, the assimilation of data is investigated by simulating the flow of blood through a carotid bifurcation. The physically motivated least-squares weights are chosen for the following numerical examples as

$$\omega_1 = \frac{1}{\sqrt{\rho_f}}, \quad \omega_2 = \frac{1}{\sqrt{\eta_{ch}}} \qquad \text{and} \quad \omega_3 = 1 \ . \tag{5.17}$$

The parameter $\eta_{ch}$ denotes the characteristic viscosity, which is obtained by substituting $\dot{\gamma} = v_B/L$ into Eq. (5.1), where $v_B$ is the bulk velocity and $L$ the characteristic length of the considered boundary value problem.

### 5.4.1 Flow in a cubical domain with analytical solution

To validate the presented least-squares stress-velocity-pressure formulation for flow of non-Newtonian fluids in three dimensions, the numerical example presented by Kwack and Masud [248] is solved. This consists of a flow in a cubical domain defined by $\Omega_f = [-0.5, 0.5]^3$ with an analytical solution for the velocities and the pressure as

$$\boldsymbol{v} = \begin{bmatrix} -2x_3 \cos(\pi x_1) \cos(\pi x_2) \ e^{\pi(-(x_3)^2+0.25)} \\ -2x_3 \cos(\pi x_1) \cos(\pi x_2) \ e^{\pi(-(x_3)^2+0.25)} \\ \sin(\pi(x_1 + x_2)) \ (e^{\pi(-x_3^2+0.25)} - 1) \end{bmatrix} , \tag{5.18}$$

$$\text{and} \qquad p = \sin(2\pi x_1) \ \sin(2\pi x_2) \ \sin(2\pi x_3) \ . \tag{5.19}$$

The associated body force $\boldsymbol{f}$ is generated by substituting the terms for the velocities (5.18) and the pressure (5.19) into the balance of momentum. The resulting term for the body force considering a non-Newtonian fluid is given in Appendix B.3. The selected material and model parameters for the Carreau-Yasuda viscosity model are given in Table 5.6.

Table 5.6: Cube - material and model parameters

| $\rho_f$<br>kg m$^{-3}$ | $\eta_0$<br>Pa s | $\eta_\infty$<br>Pa s | $n$<br>- | $a$<br>- | $\lambda$<br>s |
|---|---|---|---|---|---|
| 1 | $5.0 \cdot 10^{-2}$ | $3.0 \cdot 10^{-3}$ | 0.5 | 2 | 2 |

The boundary conditions for the velocities and the pressure are defined on the outer faces by equations (5.18) and (5.19). To investigate the convergence properties when using interpolation functions of different orders for the field quantities, the deviation between the calculated LS solution and the exact solution is calculated. The error is evaluated for the velocities and the pressure based on the $L_2$ norm and denoted as $\varepsilon_v$ and $\varepsilon_p$, respectively.

The deviation in the quantities is assessed over the entire domain and plotted on a logarithmic scale over the inverse of the element length $h$, see Figure 5.19. Furthermore, for a quantitative comparison, the slope in the last mesh refinement step is given. This also reflects qualitatively the development of the individual convergence curves. The values reveal the increase of the convergence order with increasing element order. However, a statement about the expected order of convergence is hardly possible due to the high nonlinearity of the problem.

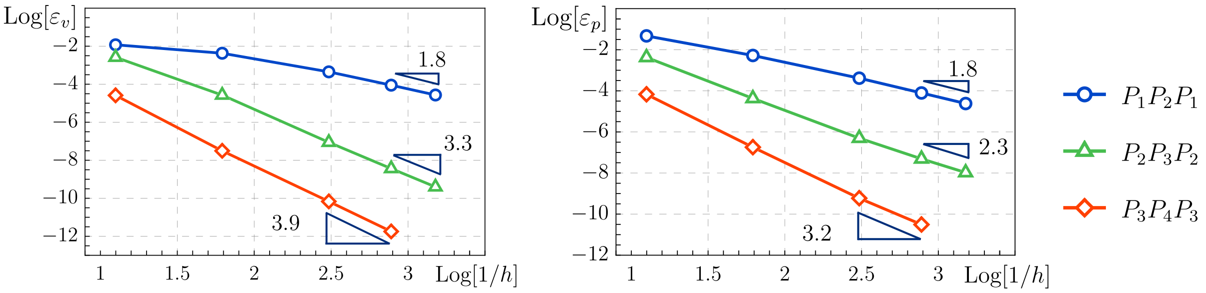

Figure 5.19: Cube - error of total velocity $\varepsilon_v$ and pressure $\varepsilon_p$ compared to exact solution over element length in logarithmic scale for different element orders

The solution for the velocity field is illustrated exemplarily in the symmetry planes at $x_1 = 0$, $x_2 = 0$ and $x_3 = 0$ in Figure 5.20. The results are obtained with the element $P_2P_3P_2$ and a mesh level corresponding to 180,962 degrees of freedom. The velocity plots are consistent with the exact solution. Furthermore, Figure 5.21 shows the pressure field and the viscosity in the cube.

### 5.4.2 Steady blood flow in a carotid artery bifurcation

The following sections demonstrates the assimilation of data into the simulation of blood flow through a carotid bifurcation model using the least-squares FEM. The applied geometry is a model of a typical Y-shaped carotid bifurcation of a human adult, consisting of the common carotid artery (CCA) that divides into the internal (ICA) and external carotid artery (ECA). The development of the initial model is attributed to Bharadvaj et al. [39; 40] and Ku et al. [246], who studied the shape of the carotid artery of 57 patients and constructed a geometric template based on mean values. For

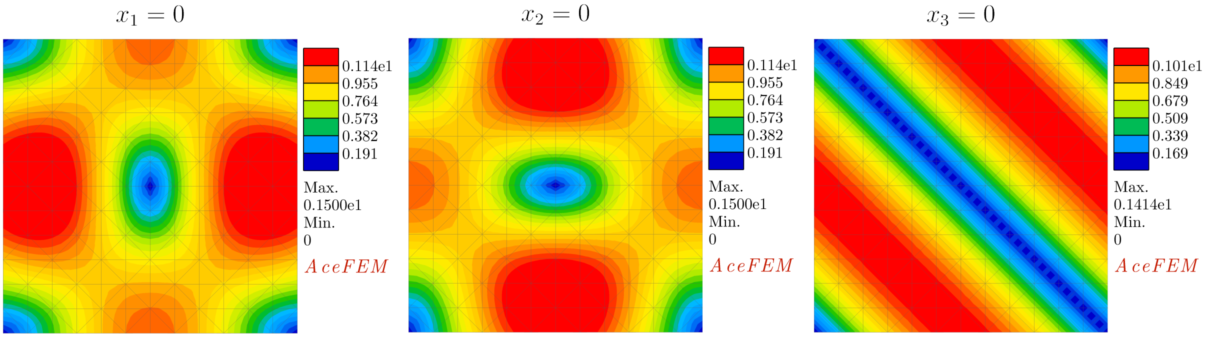

Figure 5.20: Cube - velocity field $|\boldsymbol{v}|$ in planes $x_1 = 0$, $x_2 = 0$ and $x_3 = 0$ (in m/s)

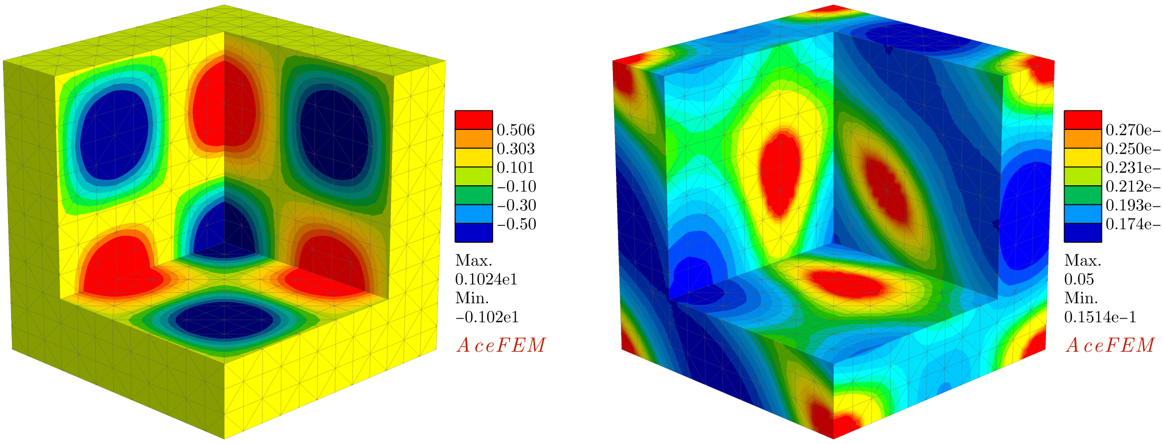

Figure 5.21: Carotid - pressure field (left, in N/m$^2$) and viscosity (right, in kg/(m s)) on a mesh with element length $h = 1/12$m

the experimental flow investigation these authors used an aqueous solution of glycerine to model Newtonian flow behavior.

The geometric dimensions used in this example are shown in Figure 5.22. The common carotid artery with an inflow radius of 4 mm splits with an angle $\alpha = 25°$ into the ECA and ICA with different diameters as illustrated. The used flow conditions and material parameters are the same as in GIJSEN ET AL. [169], see Table 5.7, resulting at the inlet in a Reynolds number of $Re = (\rho\; d\; v_B)/\eta_N = 270$, where $d$ is the inflow diameter and $\eta_N$ is the dynamic viscosity of the Newtonian control fluid $\eta_N$. Given the corresponding bulk velocity of $v_B = 0.069415\,\text{m/s}$, the parabolic velocity profile at the inlet reads

$$\boldsymbol{v}(x_2, x_3) = \begin{bmatrix} 0.1388 - 8676.86(x_2^2 + x_3^2) \\ 0.0 \end{bmatrix} \tag{5.20}$$

with the coordinate origin at the center of the circular cross-sectional area. The coefficients for the Carreau-Yasuda model as presented in Table 5.7, correspond to those of a mixture of a solution of potassium thiocyanate in water as Newtonian control fluid with 250 ppm Xanthan gum. This aqueous Xanthan gum solution, which has shear-thinning and viscoelastic properties, is a typical material used in experiments for imitating the behavior of blood. By applying the Carreau-Yasuda model, as in GIJSEN ET AL. [169], only the shear-thinning properties are considered. Here, the authors found that the viscoelasticity does not have a significant effect on the velocity in this steady-state example.

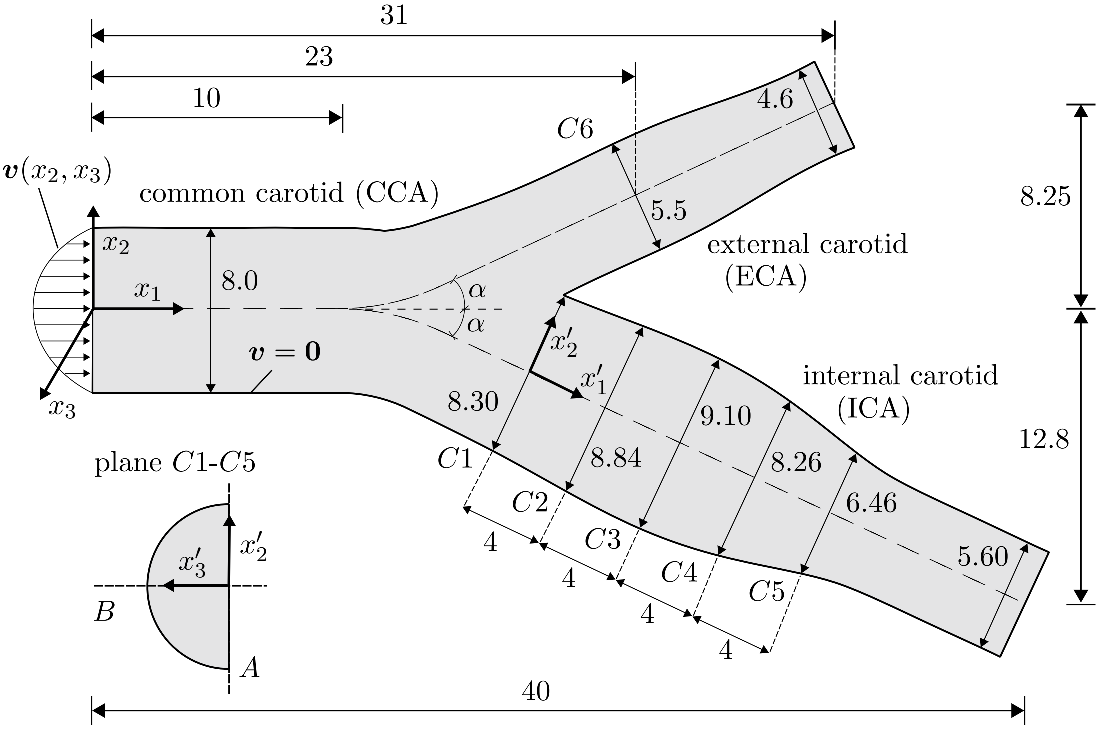

Figure 5.22: Carotid - geometry and boundary conditions artery bifurcation (in mm)

Table 5.7: Carotid - material and model parameters

| $\rho_f$<br>kg m$^{-3}$ | $\eta_N$<br>Pa s | $\eta_0$<br>Pa s | $\eta_\infty$<br>Pa s | $n$<br>- | $a$<br>- | $\lambda$<br>s |
|---|---|---|---|---|---|---|
| 1410 | $2.9 \cdot 10^{-3}$ | $22 \cdot 10^{-3}$ | $2.2 \cdot 10^{-3}$ | 0.392 | 0.644 | 0.11 |

The artery walls have no-slip boundary conditions, i.e. $\boldsymbol{v} = \mathbf{0}$, and at the outlet of the external and internal carotid artery, the pressure $p$ and the stress components $\sigma_{11}, \sigma_{22}, \sigma_{33}$ are set to zero. To reduce calculation costs, only half of the geometry is simulated. Thus additional constraints are set on the symmetry plane for the velocities $v_3 = 0$ and the stresses $\boldsymbol{\sigma}_1 \cdot \boldsymbol{n} = (\sigma_{11}, \sigma_{12}, \sigma_{13}) \cdot (0, 0, 1)^T = 0$ and $\boldsymbol{\sigma}_2 \cdot \boldsymbol{n} = (\sigma_{21}, \sigma_{22}, \sigma_{23}) \cdot (0, 0, 1)^T = 0$, i.e. $\sigma_{13} = 0$ and $\sigma_{23} = 0$.

### Model verification

In a first step, the problem is solved with different element orders and mesh sizes as specified in Table 5.8. The table contains the mesh information of the successively refined finite element meshes used in the numerical simulations. The grids are constructed using Gmsh, cf. GEUZAINE AND REMACLE [165].

In Figure 5.23, the total velocity distribution and the pressure field on the symmetry plane $x_3 = 0$ are visualized, which are calculated with mesh level M4, corresponding to 64,444 tetrahedral elements of type $P_2P_3P_2$. At the beginning of the bifurcation, high velocities can be observed especially near the inner/divider wall of the ICA. This high velocity region results from the flow splitting with a simultaneous bending of the ICA and leads to a recirculation region at the outer wall with very low velocities. Another factor besides the bifurcation and bending, which strongly influences the flow behavior, is the changing

Table 5.8: Carotid - mesh level, number of elements ($n_{\text{ele}}$) and number of degrees of freedom ($n_{\text{dof}}$) for different element types

| | | $n_{\text{dof}}$ | | |
|---|---|---|---|---|
| level | $n_{\text{ele}}$ | $P_1P_2P_1$ | $P_2P_3P_2$ | $P_3P_4P_3$ |
| M1 | 2,063 | 10,825 | 49,322 | 136,882 |
| M2 | 7,432 | 38,403 | 176,731 | 491,880 |
| M3 | 22,204 | 116,577 | 523,749 | 1,448,518 |
| M4 | 64,444 | 333,820 | 1,497,322 | 4,196,380 |
| M5 | 119,255 | 618,973 | 2,782,227 | |
| M6 | 531,893 | 2,748,538 | | |

cross-sectional area of the internal vessel. The widening and later narrowing leads first to a deceleration of the fluid and then to a strong acceleration.

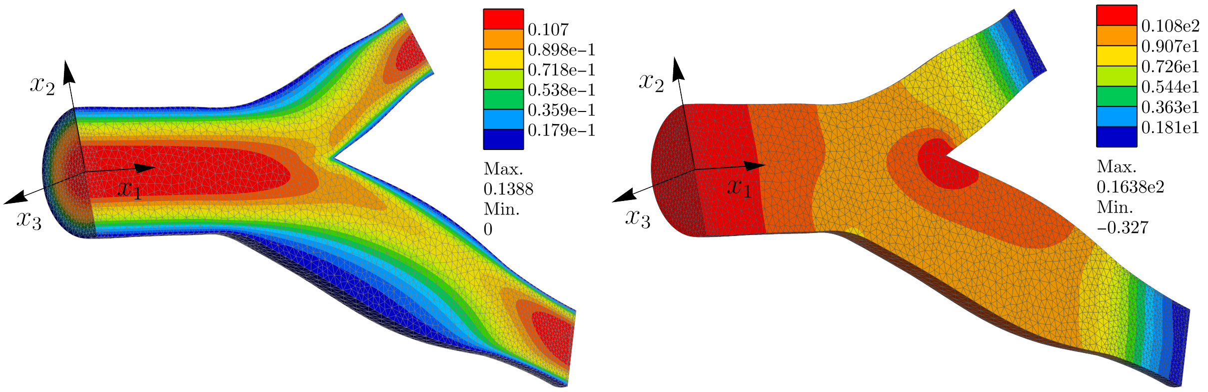

Figure 5.23: Carotid - velocity field $|\boldsymbol{v}|$ (left, in m/s) and pressure field $p$ (right, in N/m$^2$)

Next, Figure 5.24 presents the velocity and pressure distribution directly after the bifurcation point in the ICA (at cut plane $C1$ see Figure 5.22). The left contour plot shows the total velocity field $|\boldsymbol{v}|$ with a high velocity located in the upper middle region of the cut surface and a regular velocity gradient towards the boundary walls. The second contour plot illustrates the pressure field depicting a radial pressure gradient from the outer (bottom) to the divider (top) wall. This distribution matches the observation in the last image, which shows a secondary flow in the cross-sectional area. The fluid moves vertically along the symmetry plane towards the upper wall and back along the outer wall, which results in a vortex as shown in Figure 5.24 (right).

In order to study the convergence behavior and the scale of the discretization error the error compared to a fine-grid solution obtained with a mixed Taylor-Hood Galerkin tetrahedral element (quadratic velocity and linear pressure approximation) is evaluated. More precisely, the error based on the mean of the normed differences between the LS solution $\boldsymbol{v}$ and the Galerkin reference solution $\hat{\boldsymbol{v}}$ at a number of $N$ compared nodes in all spatial directions is computed as

$$\varepsilon_v = \frac{1}{N}\sum_{i=1}^{N} \left|\left|\boldsymbol{v}^i - \hat{\boldsymbol{v}}^i\right|\right| = \frac{1}{N}\sum_{i=1}^{N} \sqrt{(v_1^i - \hat{v}_1^i)^2 + (v_2^i - \hat{v}_2^i)^2 + (v_3^i - \hat{v}_3^i)^2} \, . \tag{5.21}$$

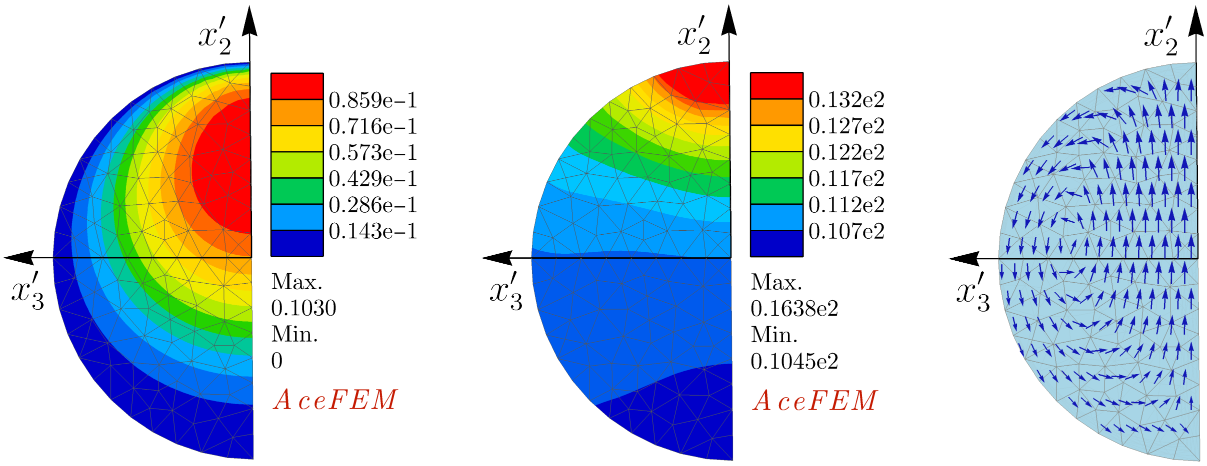

Figure 5.24: Carotid - velocity field (left, in m/s), pressure field $p$ (center, in N/m$^2$) and vector plot showing secondary flow (right) in cut plane $C1$

The error is evaluated using the nodal data on the centerlines $A$ and $B$ (see Figure 5.22) in the cut planes ($C1$-$C5$) and plotted in a logarithmic scale over the degrees of freedom ($n_{\mathrm{dof}}$), see Figure 5.25 (left). As expected, the error decreases with increasing polynomial degree. Whereby the convergence order for the low-order element is lowest and the elements $P_2P_3P_2$ and $P_3P_4P_3$ show similar convergence rates.

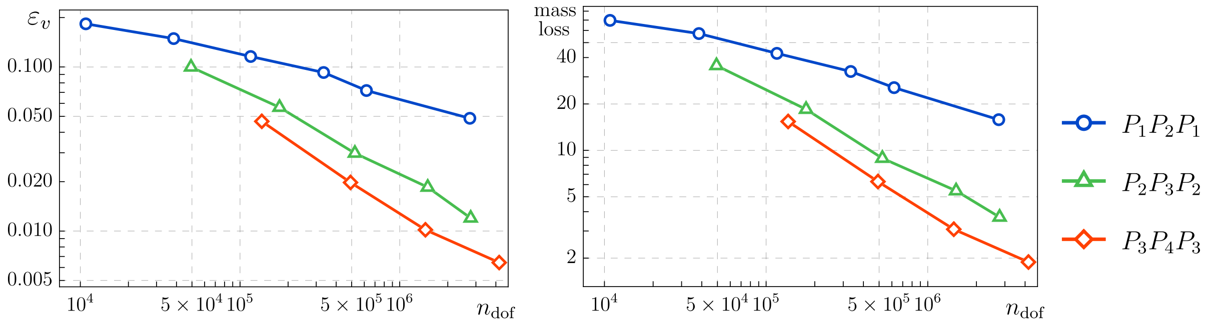

Figure 5.25: Carotid - absolute error in velocity compared to Galerkin reference solution (left) and mass loss (right) with different mesh levels and element orders

Since a common problem with least-squares FEM approaches is the poor conservation of mass, this is evaluated as well and presented in Figure 5.25 (right). The graphs confirm the poor performance of the low-order element, but concurrently clearly show that better convergence behavior can be achieved with higher polynomial degrees. Nevertheless, a high number of degrees of freedom is required to compensate for the mass loss and obtain satisfying results.

When comparing the velocity evolution (exemplarily in the sections $C1, C3, C5$) with the numerical fine-grid Galerkin FEM reference solution and the experimental results, see Figure 5.26, it can be seen that there are deviations between the measured data and the numerical reference solution. This difference, which was similarly reported by GIJSEN ET AL. [169], can have various causes. In numerical solutions, not only discretization errors are involved, but also possible inaccuracies in the assumption of the material model and the model parameters, e.g., for the non-Newtonian fluid, or uncertainties in defining the boundary conditions. In the next section, the assimilation of experimental data into the numerical calculation of flow through a carotid bifurcation is implemented to evaluate the effect on the performance.

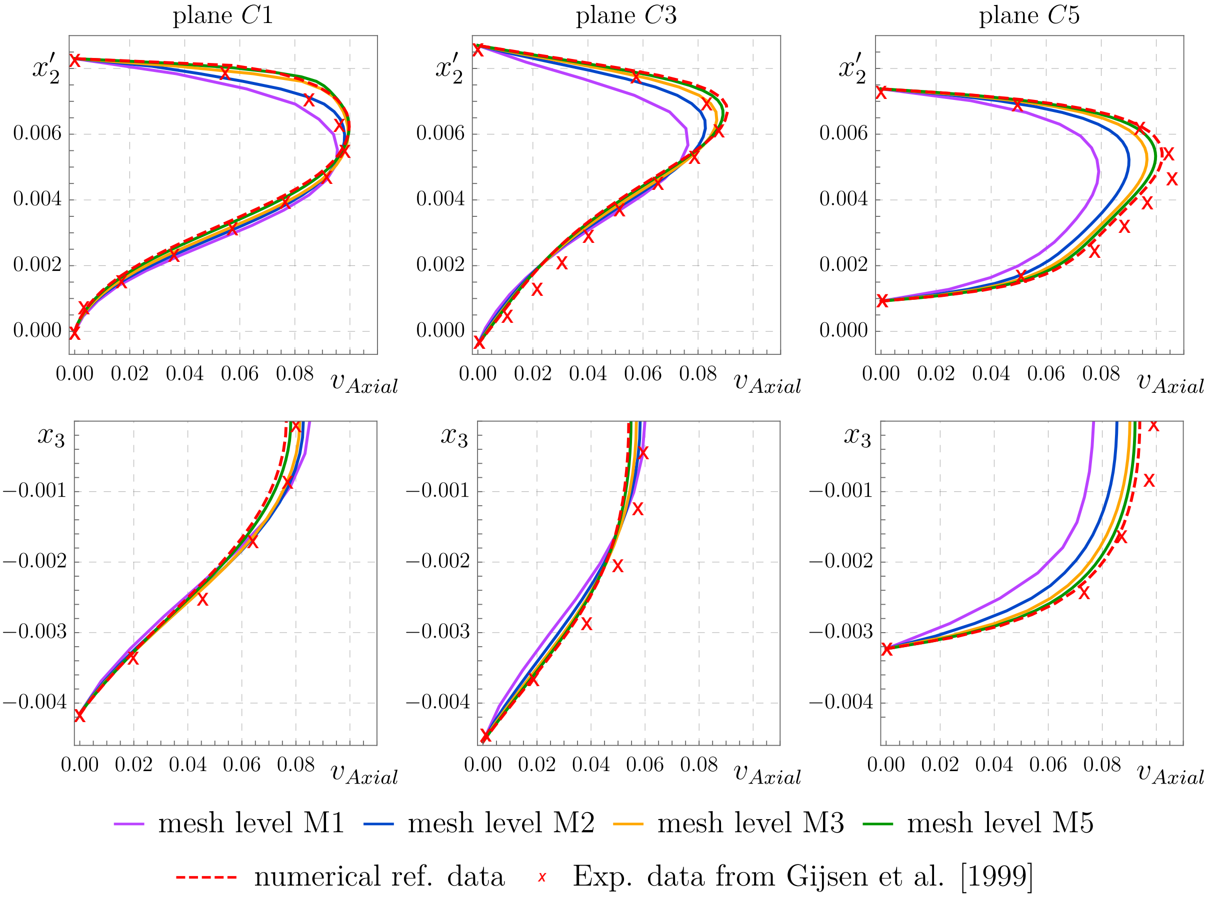

Figure 5.26: Carotid - velocity profiles (in m/s) along centerlines $A$ (top) and $B$ (bottom) in planes $C1, C3, C5$, obtained with element $P_2P_3P_2$ and different mesh levels (axis in m)

### 5.4.3 Carotid bifurcation model - assimilation of experimental data

As a first step the integration of experimental data using measured velocities given in Gijsen et al. [169] is investigated. The authors present axial velocity profiles at different planes in the internal carotid artery along the symmetry plane and perpendicular thereto (centerlines $A$ and $B$ in Figure 5.22). The given axial velocity data is transformed to the $x_1$- and $x_2$-component as follows

$$v_1 = v_{Axial} \cdot \cos(\alpha), \quad v_2 = -v_{Axial} \cdot \sin(\alpha). \tag{5.22}$$

The implementation of the data assimilation is carried out exemplarily with element $P_2P_3P_2$ and mesh level M2 at the centerlines of the planes $C2$ and $C4$. The axial velocity profiles in the remaining planes, where no data is integrated, are illustrated in Figure 5.27. The graphs display the velocity profiles obtained without and with assimilation of data, as well as the experimental data taken from Gijsen et al. [169]. Comparing the profiles of the calculation without data assimilation (blue line) to those with data assimilation on the centerlines (green line), we see that the solution in the neighboring cross sections to those with data assimilation is closer to the real data. But the correction is still rather poor. A similar statement can be made by evaluating the mass loss, as the difference between the applied inflow function and the outflow at the ICA and ECA, see Table 5.9. The mass loss can be reduced, but the effect is quite small. The numerical solution of a three dimensional problem is hardly influenced, when data is integrated only along certain lines, which seems to be rather obvious.

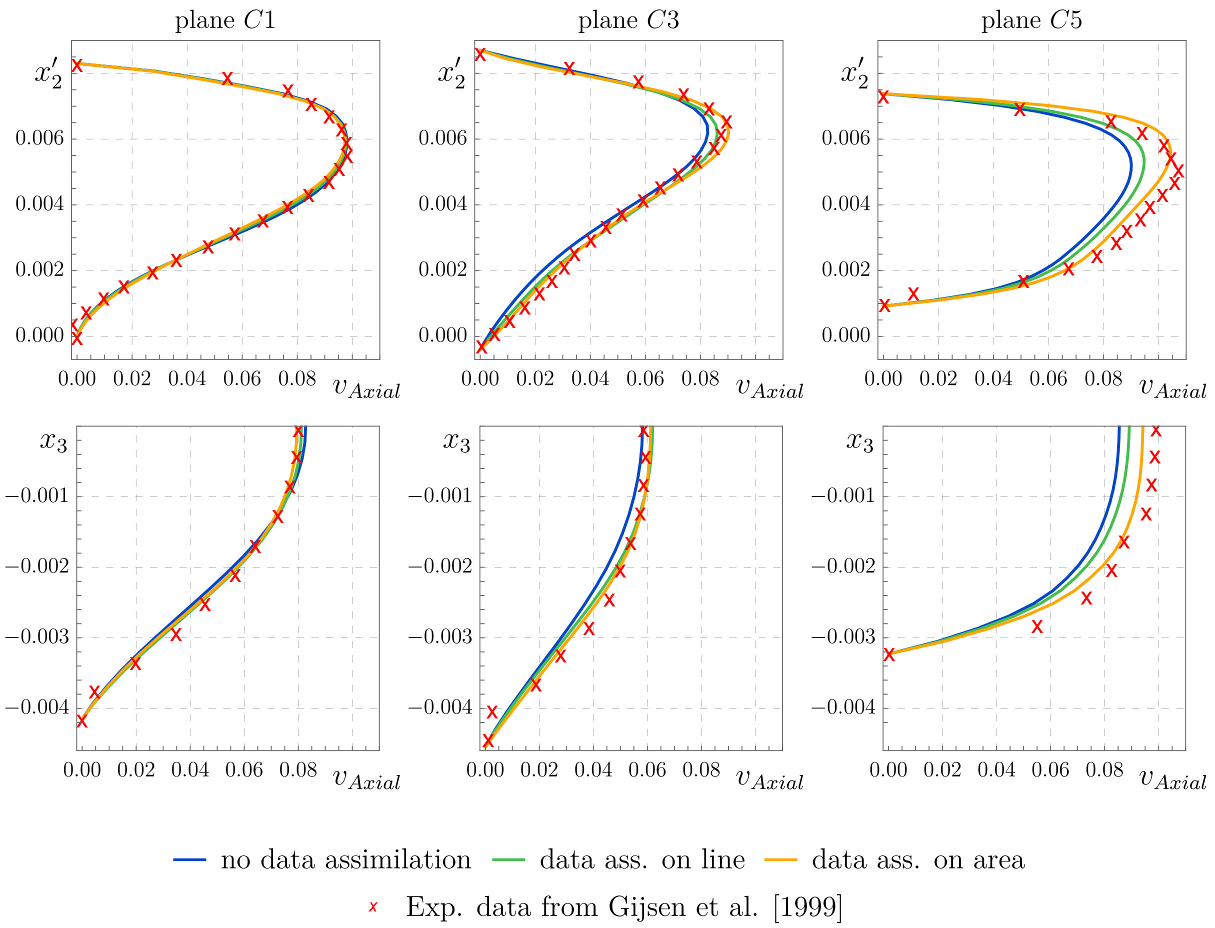

Figure 5.27: Carotid - velocity profiles (in m/s) along centerlines $A$ (top) and $B$ (bottom) in planes $C1, C3, C5$, results without data assimilation and with experimental data assimilation on line and on whole plane (axis in m)

Table 5.9: Carotid - effect of experimental data assimilation on mass loss (in %), obtained with element $P_2P_3P_2$ and mesh level M2

| no data assimilation | data on line | data on area |
|---|---|---|
| 18.46 | 15.44 | 6.30 |

Based on this finding, the assimilation of data on a plane is examined in the following. Due to the lack of measurement data on an entire cut surface, the existing data is interpolated using the Kriging method to generate two-dimensional data based on the available values on the lines in two directions. It should be noted that this approach is used only to demonstrate the general implementation and impact of experimental data assimilation into non-Newtonian fluid flow simulations. For a reasonable final application of data assimilation, it is of course advisable to use measurement data directly obtained on a surface. The result of the Kriging interpolation for the cut planes $C2$ and $C4$ is illustrated in Figure 5.28. It is visible, that the interpolated data match the input velocities and become zero at the boundaries of the artery.

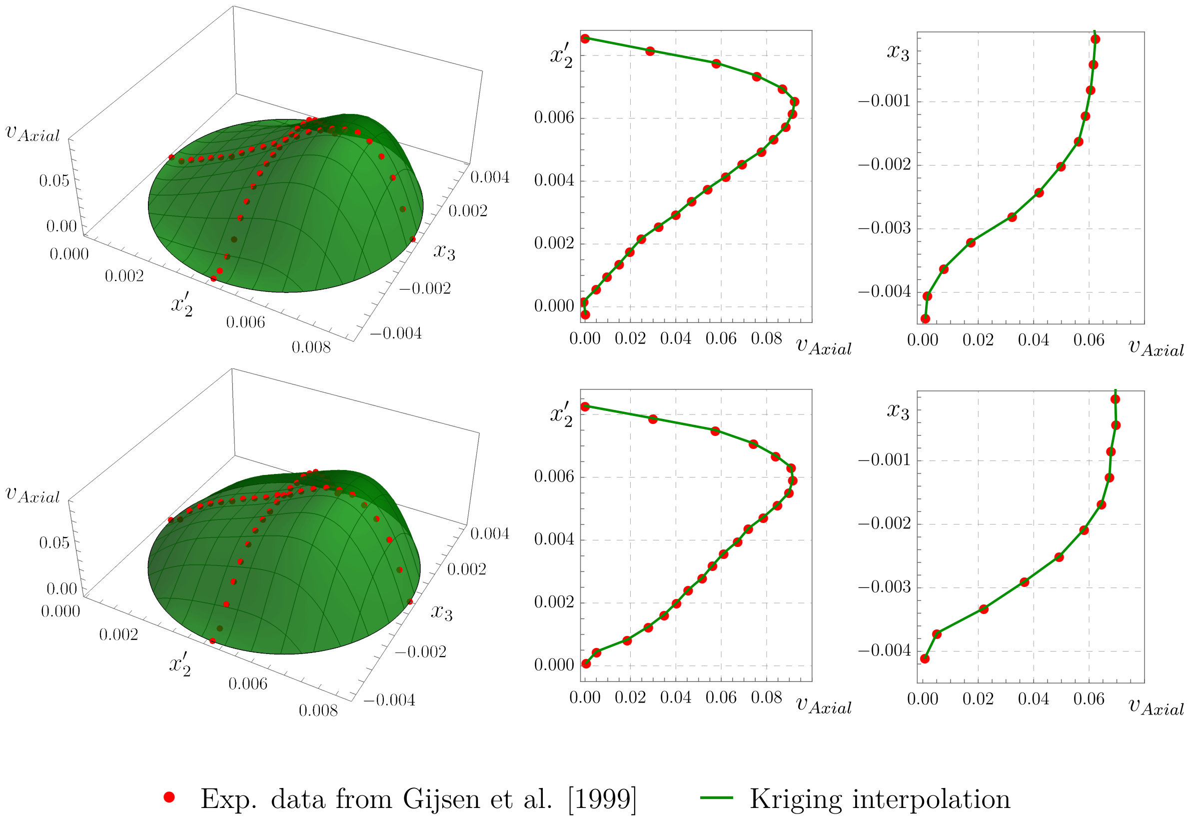

Figure 5.28: Carotid - interpolation of experimental velocity data (in m/s) on planes $C2$ (top) and $C4$ (bottom) in internal carotid artery (axis in m)

The generated velocity data in axial direction is again split into the $x_1$- and $x_2$-components and then implemented into the numerical calculation. The outcome of the data assimilation on all nodes in planes $C2$ and $C4$, is additionally plotted in Figure 5.27 (orange lines), besides the results of data inclusion on the lines (green lines). The presented velocity profiles in the cross sections $C1, C3, C5$ indicate that the accuracy in solving the velocity is increased considerably as compared to the previous approach, when data is assimilated only along lines. The data integration on all nodes on the cross-sectional areas also leads to an improved mass conservation as present in Table 5.9.

Because of the present geometry, which consists of one artery splitting into two branches, the proposed data integration loses some effectiveness, since the flow field in the external carotid artery is rarely affected by data integrated in the internal carotid artery. Therefore, the mass loss in the ECA remains rather high. Due to a lack of experimental data in the ECA of this considered problem, to numerical data is used in the following to assimilate data in the internal and external carotid artery.

### 5.4.4 Carotid bifurcation model - assimilation of numerical data

The integration of data into the internal and external carotid artery is studied by applying a generated fine-grid solution obtained with a Taylor-Hood Galerkin tetrahedral element. It should be noted that by including numerical data, only the influence on the discretization error can be investigated, but not possible model errors, e.g., due to the material model or the boundary conditions, since these also exist in the numerical reference solution. The fine-grid Galerkin solution from Section 5.4.2 is assimilated once at planes $C1$ and $C5$ in the ICA and then additionally at plane $C6$ in the ECA. Therefore, the velocity components in all three spatial directions at all nodal coordinates in the cut planes are extracted. For the LSFEM solution with data assimilation, the element $P_2P_3P_2$ and mesh level $M2$ are used. The axial velocity profiles along the centerlines of the planes $C2$-$C4$, where no data is integrated, are shown in Figure 5.29 with the numerical reference solution.

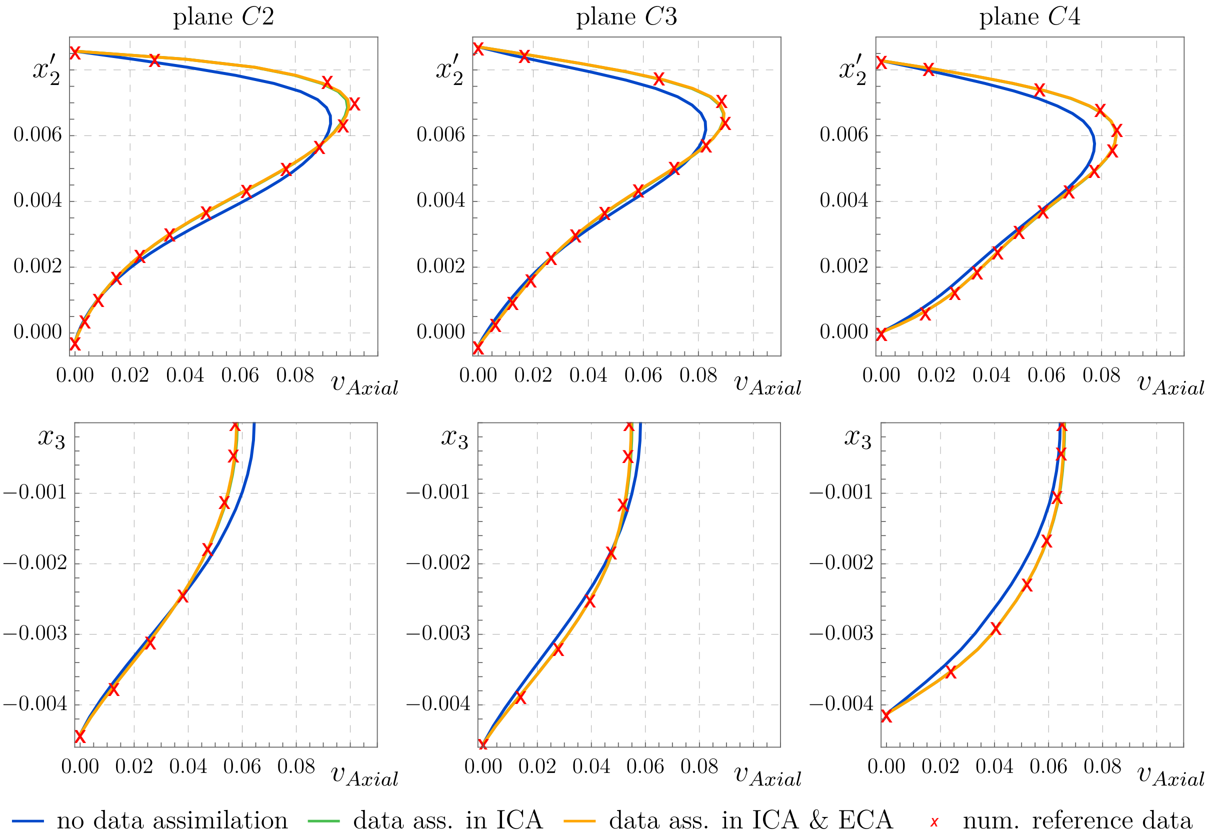

Figure 5.29: Carotid - velocity profiles (in m/s) along centerlines $A$ (top) and $B$ (bottom) in planes $C2$-$C4$, results without data assimilation and with numerical data assimilation on planes only in ICA ($C1, C5$) and on planes in ICA & ECA ($C1, C5, C6$) (axis in m)

It is visible that it does not matter for the velocity in the presented cuts in the ICA whether data is only included in the ICA or also in the ECA. Moreover, the plots show that it is sufficient to include the data in one cut downstream and upstream to almost completely eliminate the discretization error in between. In addition, for a quantitative evaluation of the effect on the performance of the numerical analysis the mass loss based on the in-and outflow and the error in the planes $C2$-$C4$ are calculated once more according to (5.21), see Table 5.10. The significant reduction of mass loss, i.e. from $>$ 18% to <6% and <2%, as well as the decrease in the velocity error show the efficiency of the data assimilation. It becomes even more apparent if one considers how many unknowns would be required to achieve values that are comparably low. Even the use of mesh level M5 with 119,255 tetrahedral elements of order $P_2P_3P_2$ leads, despite considerably more degrees of freedom, to a slightly lower accuracy than numerical calculations including data assimilation with mesh level M2. As Figure 5.29 has already demonstrated, the velocity error $\varepsilon_v$ in the ICA (cuts $C2$-$C4$) can hardly be improved further by additional data inclusion in the ECA, since it already agrees very well with the reference solution when assimilating data exclusively into the ICA. However, the numerical solution in the ECA can be further improved leading to a reduction of total mass loss from more than 18% to less than 2%.

Table 5.10: Carotid - effect of data assimilation in ICA ($C1, C5$) or ICA & ECA ($C1, C5, C6$) with element $P_2P_3P_2$ and mesh level M2 or M5, mass loss (difference of in- and outflow in %) and velocity error ($C2$-$C4$)

|  | no data assim. | $C1, C5$ | $C1, C5, C6$ | ⋮ | no data assim. |
|---|---|---|---|---|---|
| mass loss | 18.46 | 5.78 | 1.70 | ⋮ | 3.69 |
| error $\varepsilon_v$ | $2.56 \times 10^{-2}$ | $4.98 \times 10^{-3}$ | $4.26 \times 10^{-3}$ | ⋮ | $4.95 \times 10^{-3}$ |
| $n_{\text{dof}}$ (mesh) | 176,731 (M2) | 176,731 (M2) | 176,731 (M2) | ⋮ | 2,782,227 (M5) |

# 6 LSFEM for elastic solid dynamics

In this section least-squares formulations for linear as well as hyperelastic solid material behavior are presented. For both approaches the final terms are given depending on stresses and velocities to enable a straightforward monolithic coupling to the least-squares formulation for the fluid domain likewise written in terms of stresses and velocities. The presented LS solid formulation for linear elasticity is used to investigate the implementation and performance of different time discretization schemes for solving dynamic structural behavior, with the overall goal of simulating time-dependent FSI problems. The formulation for hyperelastic material behavior is required to correctly solve coupled problems in which the solid undergoes large deformations, when the assumption of linear elasticity loses its validity. Both presented formulations for linear and hyperelastic materials are based on conforming approximations for the velocities with $\boldsymbol{v} \in H^1(\Omega)$ and the stresses with $\boldsymbol{\sigma} \in H(\mathrm{div}, \Omega)$. For the implementation, different polynomial Lagrangian and vector-valued Raviart-Thomas approximation functions are chosen for this purpose, as defined in (3.43) and (3.44).

## 6.1 Stress-velocity formulation for linear elastic materials

The least-squares functional for the description of linear elastic materials undergoing small strains can be constructed based on the balance of momentum (2.45) and the constitutive relation (2.61) for linear elasticity. The corresponding residuals in terms of stresses and displacements can take the following form

$$\mathcal{R}_1^{LE} := \mathrm{div}\,\boldsymbol{\sigma} + \boldsymbol{f} - \rho_s\, \boldsymbol{a}(\boldsymbol{u}) \quad \text{and} \quad \mathcal{R}_2^{LE} := \mathbb{C}^{-1} : \boldsymbol{\sigma} - \nabla^s \boldsymbol{u} \ , \tag{6.1}$$

with the Cauchy stresses $\boldsymbol{\sigma}$, the vectors $\boldsymbol{f}$, $\boldsymbol{a}$ and $\boldsymbol{u}$ denoting the body force, acceleration and displacement, respectively, the solid density $\rho_s$, and the inverse of the forth-order material tensor $\mathbb{C}$. The tensor $\mathbb{C}^{-1}$ assuming plane strain conditions is given in matrix notation with Lamé constants $\mu_s$ and $\lambda_s$, and setting $\alpha = 4(\lambda_s\mu_s + \mu_s^2)$, as

$$\mathbb{C}^{-1}_{ijkl} = \begin{bmatrix} \mathbb{C}^{-1}_{1111} & \mathbb{C}^{-1}_{1112} & \mathbb{C}^{-1}_{1121} & \mathbb{C}^{-1}_{1122} \\ \mathbb{C}^{-1}_{1211} & \mathbb{C}^{-1}_{1212} & \mathbb{C}^{-1}_{1221} & \mathbb{C}^{-1}_{1222} \\ \mathbb{C}^{-1}_{2111} & \mathbb{C}^{-1}_{2112} & \mathbb{C}^{-1}_{2121} & \mathbb{C}^{-1}_{2122} \\ \mathbb{C}^{-1}_{2211} & \mathbb{C}^{-1}_{2212} & \mathbb{C}^{-1}_{2221} & \mathbb{C}^{-1}_{2222} \end{bmatrix} = \begin{bmatrix} \dfrac{-\lambda_s}{\alpha} + \dfrac{1}{2\mu_s} & 0 & 0 & \dfrac{-\lambda_s}{\alpha} \\ 0 & \dfrac{1}{2\mu_s} & 0 & 0 \\ 0 & 0 & \dfrac{1}{2\mu_s} & 0 \\ \dfrac{-\lambda_s}{\alpha} & 0 & 0 & \dfrac{-\lambda_s}{\alpha} + \dfrac{1}{2\mu_s} \end{bmatrix} . \tag{6.2}$$

There are several least-squares approaches in the literature regarding the solution of linear elastic materials. An important aspect of investigation in these studies is, among other things, the fulfillment of the symmetry of the Cauchy stress tensor resulting from the balance of angular momentum (2.53). Compliance with this condition can be considered in several manners that result in a strong or weak enforcement. For instance, a possibility to control the stress symmetry directly but still in a weak sense is to add a further residual containing the condition $\boldsymbol{\sigma} = \boldsymbol{\sigma}^T$, as studied e.g. in Cai and Starke [78], Schwarz et al. [351] and Igelbüscher et al. [212]. Further publications investigating a LS stress-displacement formulation for linear elasticity are, for instance, Cai and Starke [79], Cai et al. [84; 87], Schwarz et al. [347]. In the context of this work, the focus is not on studying the performance of the LS solid formulation in detail and it is assumed sufficient at this point that the stress symmetry is satisfied by the constitutive equation in a weak sense.

The main objective is rather the direct coupling of the fluid and solid formulation, for which the given equations for both domains are written in the same unknowns. For the restatement of (6.1), the displacements $\boldsymbol{u}$ and accelerations $\boldsymbol{a}$ have to be described as a function of the velocities $\boldsymbol{v}$. This is accomplished in the course of this thesis with the help of various time discretization methods, yielding the final residuals as follows

$$\mathcal{R}_1^{LE} := \operatorname{div} \boldsymbol{\sigma} + \boldsymbol{f} - \rho_s \, \boldsymbol{a}(\boldsymbol{v}) \quad \text{and} \quad \mathcal{R}_2^{LE} := \mathbb{C}^{-1} : \boldsymbol{\sigma} - \nabla^s \boldsymbol{u}(\boldsymbol{v}) \; . \tag{6.3}$$

Refer to, e.g., Nisters et al. [296] and Nisters [294] for the implementation and study on this formulation considering the Newmark and Houbolt methods for time discretization. The application of the quadratic $L^2$-norm leads to the LS functional for linear elasticity in terms of stresses and velocities

$$\mathcal{F}^{LE}(\boldsymbol{\sigma}, \boldsymbol{v}) = \frac{1}{2} \Big( ||\omega_{s1} \; (\operatorname{div} \boldsymbol{\sigma} + \boldsymbol{f} - \rho_s \, \boldsymbol{a}(\boldsymbol{v}))||^2_{L^2(\Omega_s)} + ||\omega_{s2} \; (\mathbb{C}^{-1} : \boldsymbol{\sigma} - \nabla^s \boldsymbol{u}(\boldsymbol{v}))||^2_{L^2(\Omega_s)} \Big) \, , \tag{6.4}$$

with positive weighting factors $\omega_{s1}$ and $\omega_{s2}$. The first variations of the presented first-order system, which are required for minimizing the least-squares functional, are given with respect to the unknowns by

$$\delta_{\boldsymbol{v}} \mathcal{F}^{LE} = - \int\limits_{\Omega_s} \big[ \omega_{s1}^2 \; (\operatorname{div} \boldsymbol{\sigma} - \rho_s \boldsymbol{a}) \cdot \rho_s \delta \boldsymbol{a} + \omega_{s2}^2 \; (\mathbb{C}^{-1} : \boldsymbol{\sigma} - \nabla^s \boldsymbol{u}) : \nabla^s \delta \boldsymbol{u} \big] \mathrm{d}V \; , \tag{6.5}$$

$$\delta_{\boldsymbol{\sigma}} \mathcal{F}^{LE} = \int\limits_{\Omega_s} \big[ \omega_{s1}^2 \; (\operatorname{div} \boldsymbol{\sigma} - \rho_s \boldsymbol{a}) \cdot \operatorname{div} \delta \boldsymbol{\sigma} + \omega_{s2}^2 (\mathbb{C}^{-1} : \boldsymbol{\sigma} - \nabla^s \boldsymbol{u}) : \mathbb{C}^{-1} : \delta \boldsymbol{\sigma} \big] \mathrm{d}V \; , \tag{6.6}$$

where $\delta \boldsymbol{a} := \frac{\partial \boldsymbol{a}(\boldsymbol{v})}{\partial \boldsymbol{v}} \delta \boldsymbol{v}$ and $\nabla^s \delta \boldsymbol{u} := \frac{\partial \boldsymbol{u}(\boldsymbol{v})}{\partial \boldsymbol{v}} \nabla^s \delta \boldsymbol{v}$ are defined based on the chosen time discretization scheme. Furthermore, the body force is omitted in the derivation of the variations. The linearizations $\Delta \delta \mathcal{F}$ of the least-squares functional for linear elastic material are given as

$$\Delta_{\boldsymbol{v}} \delta_{\boldsymbol{v}} \mathcal{F}^{LE} = \int\limits_{\Omega_s} \big[ \omega_{s1}^2 \; \rho_s^2 \; \delta \boldsymbol{a} \cdot \Delta \boldsymbol{a} + \omega_{s2}^2 \; \nabla^s \delta \boldsymbol{u} : \nabla^s \Delta \boldsymbol{u} \big] \mathrm{d}V \; , \tag{6.7}$$

$$\Delta_{\boldsymbol{v}} \delta_{\boldsymbol{\sigma}} \mathcal{F}^{LE} = - \int\limits_{\Omega_s} \big[ \omega_{s1}^2 \; \rho_s \; \operatorname{div} \delta \boldsymbol{\sigma} \cdot \Delta \boldsymbol{a} + \omega_{s2}^2 \; (\mathbb{C}^{-1} : \delta \boldsymbol{\sigma}) : \nabla^s \Delta \boldsymbol{u} \big] \mathrm{d}V \; , \tag{6.8}$$

$$\Delta_{\boldsymbol{\sigma}} \delta_{\boldsymbol{v}} \mathcal{F}^{LE} = - \int\limits_{\Omega_s} \big[ \omega_{s1}^2 \; \rho_s \delta \boldsymbol{a} \cdot \operatorname{div} \Delta \boldsymbol{\sigma} + \omega_{s2}^2 \; \nabla^s \delta \boldsymbol{u} : (\mathbb{C}^{-1} : \Delta \boldsymbol{\sigma}) \big] \mathrm{d}V \; , \tag{6.9}$$

$$\Delta_{\boldsymbol{\sigma}} \delta_{\boldsymbol{\sigma}} \mathcal{F}^{LE} = \int\limits_{\Omega_s} \big[ \omega_{s1}^2 \; \operatorname{div} \delta \boldsymbol{\sigma} \cdot \operatorname{div} \Delta \boldsymbol{\sigma} + \omega_{s2}^2 \; (\mathbb{C}^{-1} : \delta \boldsymbol{\sigma}) : (\mathbb{C}^{-1} : \Delta \boldsymbol{\sigma}) \big] \mathrm{d}V \; . \tag{6.10}$$

## 6.2 Stress-velocity formulation for hyperelastic materials

The least-squares functional for the description of hyperelastic materials can be constructed based on the balance of momentum (2.45) and the constitutive relation (2.59) for hyperelasticity, in which the relation of the stresses and strains is defined based on a free energy function. Furthermore, the symmetry of the Cauchy stress tensor resulting from the balance of angular momentum (2.53) is considered. Using additonally the relation between the second Piola-Kirchhoff stress tensor $\boldsymbol{S}$ and the Cauchy stress tensor $\boldsymbol{\sigma}$, see (2.31), the corresponding residuals in terms of Cauchy stresses and displacements can be defined as

$$\mathcal{R}_1^{HE} := \operatorname{div}\boldsymbol{\sigma} + \boldsymbol{f} - \rho_s\,\boldsymbol{a}\ , \quad \mathcal{R}_2^{HE} := \boldsymbol{\sigma} - \boldsymbol{F}\cdot\boldsymbol{S}\cdot\boldsymbol{F}^T J^{-1} \quad \text{and} \quad \mathcal{R}_3^{HE} := \boldsymbol{\sigma} - \boldsymbol{\sigma}^T\ . \tag{6.11}$$

Therein, the second Piola-Kirchhoff stress tensor $\boldsymbol{S}$ is defined depending on a free energy function. The free energy function used in this work is based on the St. Venant-Kirchhoff material model defined in (2.55), which is valid for boundary value problems with large displacements and rather small strains. Thus, the second PK stress tensor is given by

$$\boldsymbol{S} = \partial_{\boldsymbol{E}}\psi(\boldsymbol{E}) = \lambda_s(\operatorname{tr}\boldsymbol{E})\,\boldsymbol{I} + 2\mu_s\boldsymbol{E} = \mathbb{C} : \boldsymbol{E}\ , \tag{6.12}$$

with the Green-Lagrange strain tensor $\boldsymbol{E}$ and the right Cauchy-Green deformation tensor $\boldsymbol{C}$ defined as

$$\boldsymbol{E} = \frac{1}{2}(\boldsymbol{C} - \boldsymbol{I}) = \frac{1}{2}(\boldsymbol{F}^T\cdot\boldsymbol{F} - \boldsymbol{I}) \quad \text{and} \quad \boldsymbol{C} = \boldsymbol{F}^T\cdot\boldsymbol{F}\ , \tag{6.13}$$

while the deformation gradient can be calculated with (2.21) in terms of the actual configuration as

$$\boldsymbol{F}(\boldsymbol{x}) = (\boldsymbol{I} - \operatorname{grad}\boldsymbol{u})^{-1}\ . \tag{6.14}$$

Furthermore, the fourth-order material tensor $\mathbb{C}$ in terms of the Lamé constants is given by

$$\mathbb{C} = \begin{pmatrix} \begin{pmatrix} \lambda\mathrm{s} + 2\mu & 0 & 0 \\ 0 & \lambda\mathrm{s} & 0 \\ 0 & 0 & \lambda\mathrm{s} \end{pmatrix} & \begin{pmatrix} 0 & 0 & 0 \\ 2\mu & 0 & 0 \\ 0 & 0 & 0 \end{pmatrix} & \begin{pmatrix} 0 & 0 & 0 \\ 0 & 0 & 0 \\ 2\mu & 0 & 0 \end{pmatrix} \\ \begin{pmatrix} 0 & 2\mu_s & 0 \\ 0 & 0 & 0 \\ 0 & 0 & 0 \end{pmatrix} & \begin{pmatrix} \lambda_s & 0 & 0 \\ 0 & \lambda_s + 2\mu_s & 0 \\ 0 & 0 & \lambda_s \end{pmatrix} & \begin{pmatrix} 0 & 0 & 0 \\ 0 & 0 & 0 \\ 0 & 2\mu_s & 0 \end{pmatrix} \\ \begin{pmatrix} 0 & 0 & 2\mu_s \\ 0 & 0 & 0 \\ 0 & 0 & 0 \end{pmatrix} & \begin{pmatrix} 0 & 0 & 0 \\ 0 & 0 & 2\mu_s \\ 0 & 0 & 0 \end{pmatrix} & \begin{pmatrix} \lambda_s & 0 & 0 \\ 0 & \lambda_s & 0 \\ 0 & 0 & \lambda_s + 2\mu_s \end{pmatrix} \end{pmatrix}\ . \tag{6.15}$$

To provide a straightforward monolithic coupling of the solid and fluid domains, the formulation in (6.11) is converted into a stress-velocity formulation by means of a time discretization scheme. Following the construction rules in (3.33) and by applying a time discretization scheme to define the accelerations $\boldsymbol{a}(\boldsymbol{v})$ and displacements $\boldsymbol{u}(\boldsymbol{v})$, the mixed LS functional is obtained in terms of stresses and velocities as

$$\begin{aligned} \mathcal{F}^{HE}(\boldsymbol{\sigma},\boldsymbol{v}) = \frac{1}{2}\Big( &||\omega_{s1}(\operatorname{div}\boldsymbol{\sigma} + \boldsymbol{f} - \rho_s\,\boldsymbol{a}(\boldsymbol{v}))||^2_{L^2(\Omega_s)} \\ &+ ||\omega_{s2}\left(\boldsymbol{\sigma} - \boldsymbol{F}\cdot(\mathbb{C}:\boldsymbol{E})\cdot\boldsymbol{F}^T J^{-1}\right)||^2_{L^2(\Omega_s)} \\ &+ ||\omega_{s3}\left(\boldsymbol{\sigma} - \boldsymbol{\sigma}^T\right)||^2_{L^2(\Omega_s)}\Big)\ , \end{aligned} \tag{6.16}$$

with the weighting factors $\omega_{s1}$, $\omega_{s2}$ and $\omega_{s3}$, the determinant of the deformation gradient $J = \det(\boldsymbol{F})$ and the deformation gradient as well as the Green-Lagrange strain tensor as an indirect function of the velocities with $\boldsymbol{F}(\boldsymbol{u}(\boldsymbol{v}))$ and $\boldsymbol{E}(\boldsymbol{u}(\boldsymbol{v}))$, respectively.

Remark: In this thesis, the formulation for hyperelasticity in terms of stresses and velocities is discretized with shape functions directly constructed in the actual configuration. Thus, also the stress interpolation depends on the displacements and hence on the velocities. For the construction of the first and second variations, which are needed to solve the minimization problem, this dependency is not presented for more clarity. Hence, the first variations of the given LS functional, omitting the body force, are given by

$$\begin{aligned}\delta_{\boldsymbol{\sigma}}\mathcal{F}^{HE} = \int\limits_{\Omega_s} \big[&\omega_{s1}^2(\operatorname{div}\boldsymbol{\sigma} - \rho_s\boldsymbol{a}) \cdot \operatorname{div}\delta\boldsymbol{\sigma} + \omega_{s2}^2\left(\boldsymbol{\sigma} - \boldsymbol{F}\cdot\mathbb{C} : \boldsymbol{E}\cdot\boldsymbol{F}^T J^{-1}\right) : \delta\boldsymbol{\sigma} \\ &+ \omega_{s3}^2(\boldsymbol{\sigma} - \boldsymbol{\sigma}^T) : (\delta\boldsymbol{\sigma} - \delta\boldsymbol{\sigma}^T)\big]\ \mathrm{d}V\ ,\end{aligned} \tag{6.17}$$

$$\delta_{\boldsymbol{v}}\mathcal{F}^{HE} = \int\limits_{\Omega_s} \big[\omega_{s1}^2(\operatorname{div}\boldsymbol{\sigma} - \rho_s\boldsymbol{a}) \cdot \rho_s\delta\boldsymbol{a} + \omega_{s2}^2\left(\boldsymbol{\sigma} - \boldsymbol{F}\cdot\mathbb{C} : \boldsymbol{E}\cdot\boldsymbol{F}^T J^{-1}\right) : \boldsymbol{T}\big]\ \mathrm{d}V\ , \tag{6.18}$$

where $\boldsymbol{T} = -J^{-1}(\delta\boldsymbol{F}\cdot\mathbb{C} : \boldsymbol{E}\cdot\boldsymbol{F}^T + \boldsymbol{F}\cdot\mathbb{C} : \delta\boldsymbol{E}\cdot\boldsymbol{F}^T + \boldsymbol{F}\cdot\mathbb{C} : \boldsymbol{E}\cdot\delta\boldsymbol{F}^T) + \boldsymbol{F}\cdot\mathbb{C} : \boldsymbol{E}\cdot\boldsymbol{F}^T\delta J^{-1}$ is introduced for abbreviation. The second variations with respect to the stresses are then obtained as

$$\begin{aligned}\Delta_{\boldsymbol{\sigma}}\delta_{\boldsymbol{\sigma}}\mathcal{F}^{HE} = \int\limits_{\Omega_s} \big[&\omega_{s1}^2(\operatorname{div}\Delta\boldsymbol{\sigma}\cdot\operatorname{div}\delta\boldsymbol{\sigma}) + \omega_{s2}^2\,(\Delta\boldsymbol{\sigma} : \delta\boldsymbol{\sigma}) \\ &+ \omega_{s3}^2(\Delta\boldsymbol{\sigma} - \Delta\boldsymbol{\sigma}^T) : (\delta\boldsymbol{\sigma} - \delta\boldsymbol{\sigma}^T)\big]\ \mathrm{d}V\ ,\end{aligned} \tag{6.19}$$

$$\Delta_{\boldsymbol{\sigma}}\delta_{\boldsymbol{v}}\mathcal{F}^{HE} = \int\limits_{\Omega_s} \big[\omega_{s1}^2(\operatorname{div}\Delta\boldsymbol{\sigma}\cdot\rho_s\delta\boldsymbol{a} + \omega_{s2}^2\ \Delta\boldsymbol{\sigma} : \boldsymbol{T}\big]\ \mathrm{d}V\ , \tag{6.20}$$

and with respect to the velocities as

$$\begin{aligned}\Delta_{\boldsymbol{v}}\delta_{\boldsymbol{\sigma}}\mathcal{F}^{HE} = \int\limits_{\Omega_s} \big[&\omega_{s1}^2(-\rho_s\Delta\boldsymbol{a}\cdot\operatorname{div}\delta\boldsymbol{\sigma}) \\ &+ \omega_{s2}^2\left(\Delta\boldsymbol{F}\cdot\mathbb{C} : \boldsymbol{E}\cdot\boldsymbol{F}^T J^{-1} + \boldsymbol{F}\cdot\mathbb{C} : \Delta\boldsymbol{E}\cdot\boldsymbol{F}^T J^{-1}\right. \\ &\left.\quad + \boldsymbol{F}\cdot\mathbb{C} : \boldsymbol{E}\cdot\Delta\boldsymbol{F}^T J^{-1} + \boldsymbol{F}\cdot\mathbb{C} : \boldsymbol{E}\cdot\boldsymbol{F}^T\Delta J^{-1}\right) : \delta\boldsymbol{\sigma}\big]\ \mathrm{d}V\ ,\end{aligned} \tag{6.21}$$

$$\begin{aligned}\Delta_{\boldsymbol{v}}\delta_{\boldsymbol{v}}\mathcal{F}^{HE} = \int\limits_{\Omega_s} \big[&\omega_{s1}^2(-\rho_s\Delta\boldsymbol{a}\cdot\rho_s\delta\boldsymbol{a}) + \omega_{s2}^2\left(\boldsymbol{\sigma} - \boldsymbol{F}\cdot\mathbb{C} : \boldsymbol{E}\cdot\boldsymbol{F}^T J^{-1}\right) : \\ &\big((-\delta\boldsymbol{F}\cdot(\mathbb{C} : \Delta\boldsymbol{E}\cdot\boldsymbol{F}^T J^{-1} + \mathbb{C} : \boldsymbol{E}\cdot\Delta\boldsymbol{F}^T J^{-1} + \mathbb{C} : \boldsymbol{E}\cdot\boldsymbol{F}^T\Delta J^{-1}) \\ &- \Delta\boldsymbol{F}\cdot\mathbb{C} : \delta\boldsymbol{E}\cdot\boldsymbol{F}^T J^{-1} - \boldsymbol{F}\cdot\mathbb{C} : \Delta\delta\boldsymbol{E}\cdot\boldsymbol{F}^T J^{-1} \\ &- \boldsymbol{F}\cdot\mathbb{C} : \delta\boldsymbol{E}\cdot\Delta\boldsymbol{F}^T J^{-1} - \boldsymbol{F}\cdot\mathbb{C} : \delta\boldsymbol{E}\cdot\boldsymbol{F}^T\Delta J^{-1} \\ &- (\Delta\boldsymbol{F}\cdot\mathbb{C} : \boldsymbol{E}J^{-1} + \boldsymbol{F}\cdot\mathbb{C} : \Delta\boldsymbol{E}J^{-1} + \boldsymbol{F}\cdot\mathbb{C} : \boldsymbol{E}\Delta J^{-1})\cdot\delta\boldsymbol{F}^T \\ &- (\Delta\boldsymbol{F}\cdot\mathbb{C} : \boldsymbol{E}\cdot\boldsymbol{F}^T + \boldsymbol{F}\cdot\mathbb{C} : \Delta\boldsymbol{E}\cdot\boldsymbol{F}^T + \boldsymbol{F}\cdot\mathbb{C} : \boldsymbol{E}\cdot\Delta\boldsymbol{F}^T)\delta J^{-1}\big) \\ &- \omega_{s2}^2\big(\Delta\boldsymbol{F}\cdot\mathbb{C} : \boldsymbol{E}\cdot\boldsymbol{F}^T J^{-1} + \boldsymbol{F}\cdot\mathbb{C} : \Delta\boldsymbol{E}\cdot\boldsymbol{F}^T J^{-1} \\ &+ \boldsymbol{F}\cdot\mathbb{C} : \boldsymbol{E}\cdot\Delta\boldsymbol{F}^T J^{-1} + \boldsymbol{F}\cdot\mathbb{C} : \boldsymbol{E}\cdot\boldsymbol{F}^T\Delta J^{-1}\big) : \boldsymbol{T}\big]\ \mathrm{d}V\ .\end{aligned} \tag{6.22}$$

The derived variations contain several varied variables, which are given by

$$\begin{aligned}
&\delta \boldsymbol{E} = \frac{1}{2}\left(\delta \boldsymbol{F}^T \cdot \boldsymbol{F} + \boldsymbol{F}^T \cdot \delta \boldsymbol{F}\right) \ , \qquad && \delta J = J \boldsymbol{F}^{-T} \cdot \delta \boldsymbol{F} \ , \\
&\Delta \boldsymbol{E} = \frac{1}{2}\left(\Delta \boldsymbol{F}^T \cdot \boldsymbol{F} + \boldsymbol{F}^T \cdot \Delta \boldsymbol{F}\right) \ , \qquad && \Delta J = J \boldsymbol{F}^{-T} \cdot \Delta \boldsymbol{F} \ , \\
&\Delta\delta \boldsymbol{E} = \frac{1}{2}\left(\delta \boldsymbol{F}^T \cdot \Delta \boldsymbol{F} + \Delta \boldsymbol{F}^T \cdot \delta \boldsymbol{F}\right)
\end{aligned} \tag{6.23}$$

with $\delta \boldsymbol{F} = \nabla(\delta \boldsymbol{u})$ and $\Delta \boldsymbol{F} = \nabla(\Delta \boldsymbol{u})$. Furthermore, the terms

$$\begin{aligned}
&\delta \boldsymbol{a} := \frac{\partial \boldsymbol{a}(\boldsymbol{v})}{\partial \boldsymbol{v}} \delta \boldsymbol{v} \qquad && \text{and} \qquad && \Delta \boldsymbol{a} := \frac{\partial \boldsymbol{a}(\boldsymbol{v})}{\partial \boldsymbol{v}} \Delta \boldsymbol{v} \ , \\
&\nabla \delta \boldsymbol{u} := \frac{\partial \boldsymbol{u}(\boldsymbol{v})}{\partial \boldsymbol{v}} \nabla \delta \boldsymbol{v} \qquad && \text{and} \qquad && \nabla \Delta \boldsymbol{u} := \frac{\partial \boldsymbol{u}(\boldsymbol{v})}{\partial \boldsymbol{v}} \nabla \Delta \boldsymbol{v} \ ,
\end{aligned} \tag{6.24}$$

are defined based on the chosen time discretization scheme.

REMARK: Note that the mixed LS formulations for solids in terms of stresses and velocities always require discretization in time, even when stationary problems are considered where the acceleration term can be omitted. Therefore, numerical examples to validate the formulations presented will be given once the schemes for the discretization in time are discussed.

# 7 Time discretization schemes for fluid and solid dynamics

In order to simulate unsteady flow problems or dynamic deformations as prescribed by the formulations in Sections 4 and 6, not only the spatial directions, but also the time component has to be discretized. The difference between the spatial and temporal domain is that quantities, such as a force or velocity, acting at one spatial point have influence on the solution in the entire spatial domain. In contrast, a force that acts at a certain point in time, for example, only affects the solution in the subsequent time interval. There are different solution methods for unsteady and dynamic problems depending on the order of discretization in space and time. One can roughly divide the procedures into two categories. Either space and time are discretized simultaneously (space-time discretization) or separately. Then one can conduct first the space then the time discretization (method of lines) or vice versa (Rothe's method). When uniform discretizations are used, the method of lines and the Rothe's method are considered equivalent.

Several works are available in which the application of space-time methods in combination with the least-squares FEM for solving unsteady problems is described. Among others the authors Nguyen and Reynen [291], Donea and Quartapelle [130] as well as Perrochet and Azérad [305] consider space-time LSFEM approaches for the solution of the transient advection or advection-diffusion equations. In Bell and Surana [35; 37], Kayser-Herold and Matthies [228], Pontaza [310] and Pontaza and Reddy [313; 314] the coupled space-time discretization is dealt with to solve the Navier-Stokes equations. Moreover, the application of space-time LSFEM to parabolic equations is investigated in, e.g., Majidi and Starke [265; 266] and Führer and Karkulik [158]. In this thesis, a separate discretization of space and time domain is considered. In the context of LSFEM, as used for the spatial discretization in this work, it is necessary to first discretize in time. Then the least-squares variation can be applied to the semi-discrete system, see Donea and Huerta [129] and Kayser-Herold [227], for instance. Further applications of time discretization schemes in combination with least-squares FEM can be found in Chen [99; 100], Tang and Tsang [381] and Tang et al. [382]. For more general information on time discretization in the context of numerical methods, cf. Donea and Huerta [129], Bathe [19], Ferziger and Perić [149] and Richter [329], for instance.

The objective of this chapter is to explain and investigate the application of different time integration methods to discretize the mixed LS stress-velocity formulations for solid and fluid dynamics. For this purpose, first some general aspects regarding time integration methods are provided. For getting started, the implicit Euler method and the family of Runge-Kutta methods are presented for the integration of first-order ordinary differential equations. In this context, basic properties of the methods used in this thesis as well as some implementation aspects are explained. The computation of a simple 1D advection example serves for a better understanding of the implementation. This is followed by the description of the various methods used in connection with the least-squares SV fluid and solid formulations. All relevant terms for the application of the Euler, Houbolt, Newmark, Crank-Nicolson and different Runge-Kutta methods are defined. Furthermore, various numerical fluid and solid examples are calculated to investigate the accuracy and convergence behavior of the implemented methods in combination with the stress-velocity formulations.

## 7.1 Brief introduction to the basic concept

According to the nature of time, all solution methods are based on stepping methods where the regarded time interval $I = [t_0, T]$ is divided into $N$ discrete subintervals with the time step size $\Delta t$ as

$$[t_0, T] = \bigcup_{n=0}^{N-1} [t_n, t_{n+1}] \quad \text{with} \quad \Delta t = t_{n+1} - t_n \ . \tag{7.1}$$

Herein, the subscripts $n+1$ and $n$ denote the actual and previous time steps, respectively, and the time steps are given by $t_n = t_0 + n\Delta t$ with $n = 0, ..., N$. Many time discretization methods can be easily explained by solving an initial value problem of ordinary differential equations (ODE). Therefore, a simplified notation is first used in the following, where an approximate solution for the variable $\phi(t)$ of an initial value problem of the form

$$\dot{\phi}(t) = \frac{\mathrm{d}\phi(t)}{\mathrm{d}t} = f(t, \phi(t)), \quad \phi(t_0) = \phi^0 \ , \tag{7.2}$$

is searched. The discrete solution at every time step $t_n$ is then denoted by $\phi(t_n) = \phi^n$. See Figure 7.1 for a graphical representation of the time discretization of an initial value problem.

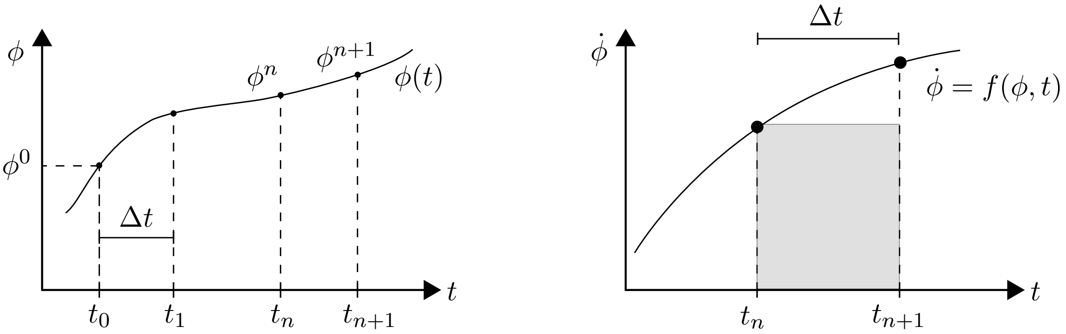

Figure 7.1: Schematic visualization of the solution of initial value problems, division in subintervals (left) and explicit function integration (right)

The solutions at the individual time steps are now calculated step by step, starting e.g. in the first step with the solution for $\phi^1 = \phi(t_1)$ at $t_1 = t_0 + \Delta t$. The obtained solution can then be considered as initial condition for the next time step. Assuming that the value $\phi^n$ is known, e.g. as initial condition $\phi^0$, the next value $\phi^{n+1}$ can be obtained by integrating (7.2). Integration of both sides over the interval $\Delta t$ leads to

$$\begin{aligned} \int_{t_n}^{t_{n+1}} \frac{\mathrm{d}\phi(t)}{\mathrm{d}t} \ \mathrm{d}t &= \int_{t_n}^{t_{n+1}} f(t, \phi(t)) \ \mathrm{d}t \\ \leftrightarrow \quad \phi^{n+1} &= \phi^n + \int_{t_n}^{t_{n+1}} f(t, \phi(t)) \ \mathrm{d}t \ . \end{aligned} \tag{7.3}$$

The primitive function of the left side can be easily formed, but since the function on the right side is unknown, the integral has to be approximated. The various time integration methods differ basically in the manner in which this integral is approximated. A main difference is the position at which the function $f(t, \phi(t))$ is evaluated. If only positions $t_i$

with $i \leq n$ are considered for the evaluation, this yields an **explicit time integration** scheme. For example, the simplest approximation is the explicit Euler method, where the function value is assumed to be constant over an interval, with the value equal to the solution at the lower limit of the interval, i.e., the solution of the last time step. Fully explicit algorithms, where the time derivatives depend only on the values of previous time steps, can be numerically unstable, especially for stiff systems. This limits the time step size, see e.g. JOHN ET AL. [223], WRIGGERS [424], or GHABOUSSI AND WU [167]. Even though the computation of a single time step using an explicit scheme is comparatively fast, the need for very small time increments can lead to high overall computational costs.

In the following, only **implicit time integration** methods are considered, where the evaluation of the function always involves the current time step, although not necessarily exclusively. Especially for complex simulations with a large number of unknowns, as in the case of many FSI problems, or stiff formulations, the demand on stable and efficient time integration schemes is tremendous. An implicit treatment of the time-dependent terms offers the possibility of unconditional stability, see, e.g., WRIGGERS [424] and the references therein. In this work, time integration methods with different approximation orders will be investigated and compared. Many recent approaches consider time integration schemes, which are up to second-order accurate for fluid, solid and interaction problems. These include, for example, the backward-difference scheme, see e.g. CURTISS AND HIRSCHFELDER [114] and HU ET AL. [204], the Newmark method as in NEWMARK [290], SUBBARAJ AND DOKAINISH [375] and WOOD ET AL. [423], for instance, the generalized-$\alpha$ method, see for example CHUNG AND HULBERT [105] and DETTMER AND PERIĆ [126], and the Crank-Nicolson method as in CRANK AND NICOLSON [109], NAMKOONG ET AL. [287] and JOHN ET AL. [223]. However, also the investigation of algorithms with higher order than two could be reasonable. This is motivated by the successful application of integration schemes such as continuous Galerkin, discontinuous Galerkin or implicit Runge-Kutta (IRK) for fluid dynamical problems, e.g. see BUTCHER [76], BIJL ET AL. [41], CARSTENS AND KUHL [92] and HUSSAIN ET AL. [210]. Additionally, different IRK methods have already been implemented and investigated for coupled problems by, e.g., VAN ZUIJLEN AND BIJL [405] and YANG AND MAVRIPLIS [426].

Several methods which are implemented in this thesis to solve fluid, solid and FSI problems are explained in more detail in the following. It should be noted that the least-squares formulations used are formulated in terms of stresses and velocities for both the fluid domain and the solid domain. This means for the time discretization methods that in the end a formulation for the time-dependent quantities in dependence of the velocities is required. In the fluid formulation, the equations are first-order differential equations in time, such that only the approximation for one time-dependent quantity, in this case the accelerations, is needed. However, in the formulation for the solid, the time discretization must provide besides an expression for the accelerations also an approximation for the displacements.

In the following notation, a distinction is made between one-step and multi-step methods, depending on whether the solution of one or more preceding time steps is taken into account for the calculation of the next time step. However, one-step methods can also include methods with several stages, in which one or more intermediate stages are solved within one time step.

## 7.2 Overview on some time integration methods for first-order ODEs

As mentioned above, many time integration methods can be explained relatively straightforward by solving a simple ordinary differential equation. Therefore, this subsection is restricted to the application of integration methods for solving first-order ODEs. In this way, general implementation aspects for Runge-Kutta methods used in this thesis will be explained first. For better understanding, a simple introductory example in 1D is presented. For this purpose, an advection equation is discretized in space with the finite difference method and solved with the implicit Euler method and a two-stage RK algorithm. The explanation regarding the application of different time integration methods within the context of the LSFEM follows in the next section.

### 7.2.1 Implicit Euler

The implicit Euler (or backward Euler) method is probably one of the simplest and best known integration methods. It has a convergence order of one and is A-stable, thus there are no restrictions on the time step size due to stability, see Hairer et al. [179]. For a comprehensible description we consider again equation (7.3) with the aim to approximate the integral in the right side. When applying the implicit Euler, the function value is assumed to be constant over each interval, with the value equal to the solution at the upper limit of the interval, i.e., the solution of the actual time step. This results in the term

$$\phi^{n+1} = \phi^n + f(t_{n+1}, \phi^{n+1})\Delta t \ . \tag{7.4}$$

Considering equation (7.2), the function evaluated at the time step $t_{n+1}$ is equal to the slope at this position. More precisely, it is the discrete time derivative such that $f(t_{n+1}) = \dot{\phi}^{n+1}$. Thus, the implicit Euler can also be written as

$$\dot{\phi}^{n+1} = \frac{\phi^{n+1} - \phi^n}{\Delta t} \ , \tag{7.5}$$

which describes the time derivative at the actual time step in terms of the actual unknown variable and its value of the last time step.

### 7.2.2 Crank-Nicolson method

The second-order Crank-Nicolson time integration scheme as presented by Crank and Nicolson [109] is a one-step method, which can be considered as a combination of the explicit and implicit Euler method. In contrast to the implicit Euler scheme, the Crank-Nicolson method assumes a linear function in each interval, such that

$$\phi^{n+1} = \phi^n + \frac{1}{2}(f(t_{n+1}, \phi^{n+1}) + f(t_n, \phi^n))\Delta t \ . \tag{7.6}$$

The Crank-Nicolson method is often also known as trapezoidal rule or a simple case of the Runge-Kutta methods which are presented in the following.

### 7.2.3 The family of Runge-Kutta methods

The above mentioned methods are all one-stage methods, where one equation system has to be solved per time step, with a maximum convergence order of two. The family of

Runge-Kutta (RK) methods are very popular high-order time integration methods. These combine good stability properties with the possibility of applying adaptive time-stepping algorithms, see e.g. Ellsiepen and Hartmann [138] and Montlaur et al. [281].

In general, when implementing RK methods, the integral in (7.3) is approximated by means of quadrature points $\gamma_j$ and weights $\beta_j$. This leads to the approximate solution

$$\phi^{n+1} = \phi^n + \Delta t \sum_{j=1}^{s} \beta_j k_j \tag{7.7a}$$

$$\text{with} \quad k_j = f\left(t_n + \gamma_j \Delta t, \phi^n + \Delta t \sum_{l=1}^{s} \alpha_{jl} k_l\right) \ , \quad \text{for } j = 1, ..., s \ , \tag{7.7b}$$

where $\Delta t$ is the time step-size and $s$ is the number of stages. Furthermore, the coefficients are constructed in such a way that $\gamma_j = \sum_{l=1}^{s} \alpha_{jl}$ for all stages $j = 1, ..., s$ with $\alpha_{jl}$ denoting the weights within the stages. The coefficients can be presented in form of a general Butcher tableau, see Table 7.1.

Table 7.1: General Butcher tableau for fully implicit RK with $s$ stages (left) and for SDIRK with $s = 4$ stages (right)

$$\begin{array}{c|cccc}
\gamma_1 & \alpha_{11} & \cdots & \cdots & \alpha_{1s} \\
\vdots & \vdots & \ddots & & \vdots \\
\vdots & \vdots & & \ddots & \vdots \\
\gamma_s & \alpha_{s1} & \cdots & \cdots & \alpha_{ss} \\
\hline
 & \beta_1 & \cdots & \cdots & \beta_s
\end{array}
\qquad\qquad
\begin{array}{c|cccc}
\gamma_1 & \alpha_{11} & 0 & 0 & 0 \\
\gamma_2 & \alpha_{21} & \alpha_{11} & 0 & 0 \\
\gamma_3 & \alpha_{31} & \alpha_{32} & \alpha_{11} & 0 \\
1 & \alpha_{41} & \alpha_{42} & \alpha_{43} & \alpha_{11} \\
\hline
 & \beta_1 & \beta_2 & \beta_3 & \beta_4
\end{array}$$

Depending on the entries of the tableau, the Runge-Kutta methods can have different properties, such as being explicit or implicit. In the case of $\alpha_{jl} = 0$ for $j \leq l$, the solution in the current time step for $\phi_{n+1}$ can be computed explicitly from the values of the last time step and the previous stages. As mentioned before, explicit solution methods are often unstable due to the stiffness of many realistic problems and therefore not practical, see e.g. Montlaur et al. [281] or John et al. [223]. By using a coefficient matrix in which the upper triangular matrix contains non-zero values, stable methods can be achieved. A completely filled tableau, for example, leads to a fully implicit Runge-Kutta method, in which, the size of the system of equations to be solved at each time step, increases to $s$ times the number of degrees of freedom $n_{\text{dof}}$. This can lead to huge systems of equations, especially for mixed FEM.

This drawback can be avoided by taking a reduced coefficient matrix where $\alpha_{jl} = 0$ for $j < l$, leading to a diagonally implicit method. In this case, the large system of equations ($s \times n_{\text{dof}}$) is divided into a number of $s$ systems of equations of size $n_{\text{dof}}$, which are solved sequentially at each time step. A further classification called singly diagonally implicit Runge-Kutta (SDIRK) is obtained when all diagonal entries in the coefficient matrix $\alpha_{ii}$ are equal, see Alexander [3]. Another subgroup of implicit RK methods with $\beta_j = \alpha_{sj}$ for $j = 1, ..., s$ and $\gamma_s = 1$ has the property of being stiffly accurate. This condition implies that the projection step given by (7.7a) can be omitted, because the result of the last stage corresponds already to the solution of the considered actual time step. In the following, we also consider schemes with an explicit first stage, denoted

ESDIRK. In this case, no system of equations has to be solved for the first stage, since the solutions correspond to the values of the last time step. The different types of RK methods according to the coefficients in the Butcher tables are summarized in Table 7.2. For a more detailed overview of the properties of the various classes of Runge-Kutta methods and a deeper insight into the mathematical investigations thereof, the reader is referred to, e.g., Hairer et al. [178; 179] and Hairer and Wanner [177].

Table 7.2: Characteristics of Runge-Kutta methods

| | |
|---|---|
| $\alpha_{jl} = 0$ for $l \geq j$ | explicit Runge-Kutta |
| $\alpha_{jl} \neq 0$ for $l \geq j$ | fully implicit Runge-Kutta |
| $\alpha_{jl} = 0$ for $l > j$ | diagonally implicit Runge-Kutta (DIRK) |
| $\alpha_{jj}$ equal | singly diagonally implicit Runge-Kutta (SDIRK) |
| $\alpha_{11} = 0$ | explicit, singly diagonally implicit RK (ESDIRK) |
| $\beta_j = \alpha_{sj}$, $\gamma_s = 1$ | stiffly accurate, result of last stage yields solution at $t_{n+1}$ |

### 7.2.4 Simple example: Advection equation in 1D

The application of the different presented time discretization methods in the field of numerics is explained in the following by a short example in 1D. Therefore, the instationary linear advection equation in one dimension is used, given by

$$\begin{aligned} \frac{\partial z(x,t)}{\partial t} &= -c\frac{\partial z(x,t)}{\partial x} \\ \Leftrightarrow \quad \dot{z}(x,t) &= f(z(x,t)) \; . \end{aligned} \tag{7.8}$$

It is a simple example of an hyperbolic PDE, which describes the advection of a property of a fluid particle, here denoted by $z(x,t)$, through a medium with a constant velocity $c$ in $x$-direction. If the speed of the advection is $c > 0$, then the solution moves along the positive direction of $x$. The initial value problem is completed by the definition of initial values

$$z(x,0) = z_0 = g(x). \tag{7.9}$$

The equation can be solved analytically and it holds in general that

$$z(x,t) = g(x - c\;t) \; , \tag{7.10}$$

with $g(x)$ being an arbitrary function, see Donea and Huerta [129](Chapter 3) for more details. For the numerical solution of this initial boundary value problem a double discretization process is required, namely the discretization in space and in time. For this simple example the advection equation is discretized in space using a finite difference (FD) scheme. The main idea of using FD is to approximate derivatives using difference quotients. Although there are better methods than finite differences for spatial discretizations, in this section FD are used because they are very straightforward to understand and implement. Therefore, the domain with a length $L$ is divided into grid points $i = \{1, ..., M\}$ with a distance $h = L/(M-1)$ as depicted in Figure 7.3.

In the following, the upwind difference scheme is applied, such that the right side of (7.8) with the partial derivative of $z(x,t)$ with respect to $x$ results for a positive constant

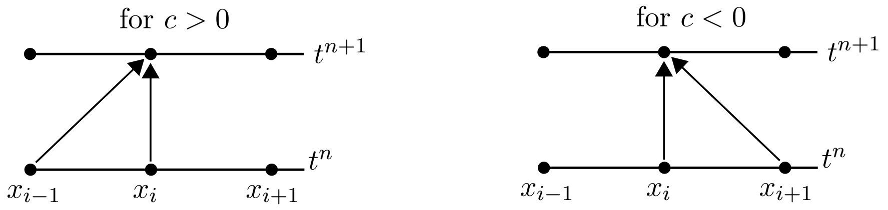

Figure 7.2: Schematic visualization of the upwind finite difference scheme

velocity $c > 0$ in

$$-c\frac{\partial z(x,t)}{\partial x} \approx -c\frac{z_i - z_{i-1}}{x_i - x_{i-1}} = -c\frac{z_i - z_{i-1}}{h} = f(z_i)\ , \tag{7.11}$$

omitting at this point the time dependence of $z_i(t)$ for more clarity. Herein, the solution is always determined based on data at the considered position and at upstream positions and the information travels downstream. First approaches to the upwind scheme are given in the work of Courant et al. [108].

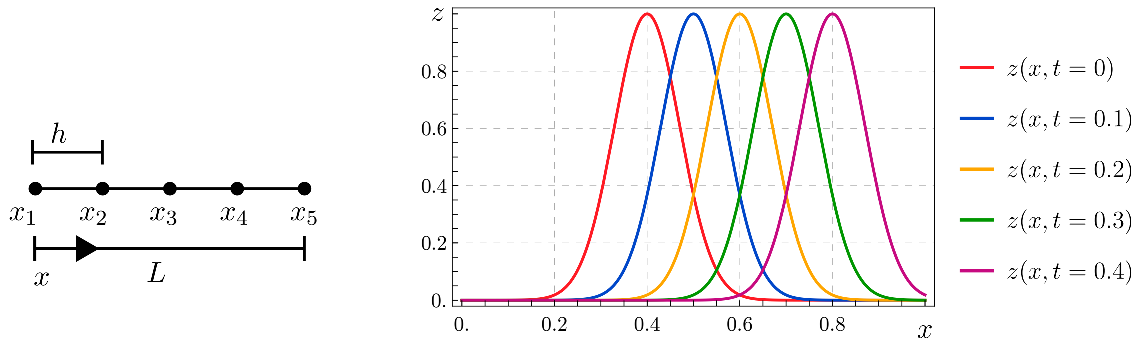

Figure 7.3: Spatial discretization using FD scheme for advection equation in 1D (left) and analytical solution at different times (right)

In the following, the one-dimensional Gauß-pulse with the initial state

$$z(x, 0) = z_0 = \exp(-100(x - 0.4)^2) \tag{7.12}$$

is considered on a spatial domain $x \in [0, 1]$ over a time period $t \in [0, 1]$ with the constant velocity $c = 1\,\mathrm{m/s}$. According to equation (7.10) the analytical solution of the initial value problem reads

$$\hat{z}(x, t) = \exp(-100(x - c\,t - 0.4)^2)\ . \tag{7.13}$$

The boundary conditions are set at $x = 0$ and $x = 1$ to

$$z(0, t) = \hat{z}(0, t) \quad \text{and} \quad z(1, t) = \hat{z}(1, t). \tag{7.14}$$

With the spatial discretization in hand, the next step is to trace the evolution of the solution in time. Therefore, the time interval is divided into discrete time steps $t_n = t_0 + n\Delta t$ with $n = 0, ..., N$ with a step size $\Delta t$.

**Implicit Euler**

For a better understanding of the individual steps of the multi-stage Runge-Kutta methods, the solution of the problem is first shown with a simple discretization, namely the implicit Euler. Considering the approximation in time as presented in (7.4) and the approximation in space defined in equation (7.11), the fully discretized form of (7.8) reads

$$\begin{aligned} & \frac{z_i^{n+1} - z_i^n}{\Delta t} = f\left(t_{n+1}, z_i^{n+1}\right) \\ \Leftrightarrow \quad & \frac{z_i^{n+1} - z_i^n}{\Delta t} = -\frac{z_i^{n+1} - z_{i-1}^{n+1}}{h} \ , \end{aligned} \tag{7.15}$$

with $n+1$ and $n$ denoting the actual and previous time steps. The initial conditions are defined at all grid points based on equation (7.12). The resulting values are given in the first row of Table 7.3.

Table 7.3: Solution $z(x_i, t_n)$ with implicit Euler and FD upwind scheme at discrete grid points $x_i$ at different time steps $t_n$

| $t$ | $z_1$ | $z_2$ | $z_3$ | $z_4$ | $z_5$ |
|---|---|---|---|---|---|
| 0.0 | 0. | $1.054\times10^{-1}$ | $3.679\times10^{-1}$ | $4.790\times10^{-6}$ | 0. |
| 0.1 | 0. | $7.529\times10^{-2}$ | $2.843\times10^{-1}$ | $8.123\times10^{-2}$ | 0. |
| 0.2 | 0. | $5.378\times10^{-2}$ | $2.184\times10^{-1}$ | $1.204\times10^{-1}$ | 0. |
| 0.3 | 0. | $3.841\times10^{-2}$ | $1.670\times10^{-1}$ | $1.337\times10^{-1}$ | $1.234\times10^{-4}$ |
| 0.4 | 0. | $2.744\times10^{-2}$ | $1.271\times10^{-1}$ | $1.318\times10^{-1}$ | $1.832\times10^{-2}$ |

For a discretization with $M = 5$ grid points and a time step size of $\Delta t = 0.1$ the temporal evaluation of the solution at locations $x_i$ with $i = \{2, 3, 4\}$ can be calculated with

$$\begin{aligned} z_2^{n+1} &= -\frac{\Delta t}{h}(z_2^{n+1} - z_1^{n+1}) + z_2^n \\ z_3^{n+1} &= -\frac{\Delta t}{h}(z_3^{n+1} - z_2^{n+1}) + z_3^n \\ z_4^{n+1} &= -\frac{\Delta t}{h}(z_4^{n+1} - z_3^{n+1}) + z_4^n \ . \end{aligned}$$

The first time step is solved by first inserting the known values for the initial conditions $z_i^0$ with $i = \{2, 3, 4\}$ and for the boundary conditions $z_1^{n+1}$ and $z_5^{n+1}$ , and then solving the resulting system of equations for $z_i^{n+1}$ with $i = \{2, 3, 4\}$. This procedure is repeated for each time step. The final values are listed in Table 7.3.

**Version 1: Runge-Kutta method with two stages in standard form**

For the purpose of clarifying the application of the RK methods, a 2-stage Runge-Kutta procedure with an explicit first stage is implemented at this point. The corresponding parameters which are shown in Table 7.4 fulfill all characteristics of an ESDIRK. The use of these parameters leads to the Crank-Nicolson method.

Applying equation (7.7) to the advection formula in (7.8), under consideration of the integration parameters given in Table 7.4 with $s = 2$ stages, results in the semi-discretized

Table 7.4: General Butcher tableau for 2-stage ESDIRK-2 (Crank-Nicolson)

$$\begin{array}{c|cc} 0 & 0 & 0 \\ 1 & \frac{1}{2} & \frac{1}{2} \\ \hline & \frac{1}{2} & \frac{1}{2} \end{array}$$

formulation

$$z^{n+1} = z^n + \Delta t \sum_{j=1}^{2} \beta_j k_j = z^n + \Delta t(\beta_1 k_1 + \beta_2 k_2) = z^n + \frac{\Delta t}{2}(k_1 + k_2) \ , \tag{7.16}$$

$$\text{with} \quad k_1 = f\left(t_n + \gamma_1 \Delta t, z^n + \Delta t \sum_{l=1}^{2} \alpha_{1l} k_l\right) = f\left(z^n\right) \ , \tag{7.17a}$$

$$k_2 = f\left(t_n + \gamma_2 \Delta t, z^n + \Delta t \sum_{l=1}^{2} \alpha_{2l} k_l\right) = f\left(z^n + \frac{\Delta t}{2}(k_1 + k_2)\right) \ , \tag{7.17b}$$

where at this point the space dependence of $z$ and $k$ is omitted for better readability. In addition, it has been taken into account that $f$ is not a function of time $t$ in this case. It is visible that the solution in the first stage for $k_1$ depends only on the solution of the previous time step, as is always the case in RK methods with a first explicit stage.

Considering the spatial discretization by the upwind difference scheme given in (7.11), the RK formulations in (7.16) and (7.17) read in the fully discretized form

$$z_i^{n+1} = z_i^n + \frac{\Delta t}{2}(k_{1,i} + k_{2,i}) \ , \tag{7.18}$$

$$\text{with} \quad k_{1,i} = f(z_i^n) = -\frac{z_i^n - z_{i-1}^n}{h} \ , \tag{7.19a}$$

$$\begin{aligned} k_{2,i} &= f\left(z_i^n + \frac{\Delta t}{2}(k_{1,i} + k_{2,i})\right) = f\left(z_i^n\right) + \frac{\Delta t}{2} f(k_{1,i}) + \frac{\Delta t}{2} f(k_{2,i}) \\ &= -\frac{z_i^n - z_{i-1}^n}{h} - \frac{\Delta t(k_{1,i} - k_{1,i-1})}{2h} - \frac{\Delta t(k_{2,i} - k_{2,i-1})}{2h} \ . \end{aligned} \tag{7.19b}$$

With a spatial division of the domain into $M = 5$ segments as shown in Figure 7.3, the discrete terms at positions $x_i$ with $i = \{2, 3, 4\}$ yield

$$\begin{aligned} z_2^{n+1} &= z_2^n + \frac{\Delta t}{2}(k_{1,2} + k_{2,2}) \ , \\ z_3^{n+1} &= z_3^n + \frac{\Delta t}{2}(k_{1,3} + k_{2,3}) \ , \\ z_4^{n+1} &= z_4^n + \frac{\Delta t}{2}(k_{1,4} + k_{2,4}) \ , \end{aligned} \tag{7.20}$$

with

$$\begin{aligned}
\text{at } x_2: \quad k_{1,2} &= -\frac{z_2^n - z_1^n}{h}\,, \\
k_{2,2} &= -\frac{z_2^n - z_1^n}{h} - \frac{\Delta t(k_{1,2} - k_{1,1})}{2h} - \frac{\Delta t(k_{2,2} - k_{2,1})}{2h}\,, \\
\text{at } x_3: \quad k_{1,3} &= -\frac{z_3^n - z_2^n}{h}\,, \\
k_{2,3} &= -\frac{z_3^n - z_2^n}{h} - \frac{\Delta t(k_{1,3} - k_{1,2})}{2h} - \frac{\Delta t(k_{2,3} - k_{2,2})}{2h}\,, \\
\text{at } x_4: \quad k_{1,4} &= -\frac{z_4^n - z_3^n}{h}\,, \\
k_{2,4} &= -\frac{z_4^n - z_3^n}{h} - \frac{\Delta t(k_{1,4} - k_{1,3})}{2h} - \frac{\Delta t(k_{2,4} - k_{2,3})}{2h}\,,
\end{aligned} \tag{7.21}$$

and $k_{1,1} = k_{2,1} = 0$. The final result in each time step is obtained by solving the system of equations (7.21) for $k_{2,i}$ with $i = \{2, 3, 4\}$ and substituting the values into (7.20). The results for the first four time steps are given in Table 7.5.

Table 7.5: Solution $z(x_i, t_n)$ with implicit Runge-Kutta (s=2) and FD upwind scheme at discrete grid points $x_i$ at different time steps $t_n$

| $t$ | $z_1$ | $z_2$ | $z_3$ | $z_4$ | $z_5$ |
|---|---|---|---|---|---|
| 0.0 | 0. | $1.054\times10^{-1}$ | $3.679\times10^{-1}$ | $4.790\times10^{-6}$ | 0. |
| 0.1 | 0. | $7.027\times10^{-2}$ | $2.745\times10^{-1}$ | $1.071\times10^{-1}$ | 0. |
| 0.2 | 0. | $4.684\times10^{-2}$ | $2.025\times10^{-1}$ | $1.509\times10^{-1}$ | 0. |
| 0.3 | 0. | $3.123\times10^{-2}$ | $1.480\times10^{-1}$ | $1.590\times10^{-1}$ | $1.234\times10^{-4}$ |
| 0.4 | 0. | $2.082\times10^{-2}$ | $1.074\times10^{-1}$ | $1.486\times10^{-1}$ | $1.832\times10^{-2}$ |

It should be noted that the spatial discretization with the upwind finite difference method of first-order with five grid points leads to a very large deviation from the exact result. The graphical representation of the approximations in Figure 7.4 is based on a discretization with 100 grid points. The graphs illustrate the solutions obtained with the implicit Euler method and the RK methods with a time step size of $\Delta t = 0.1$. It is visible that the outcome obtained with the second-order Runge-Kutta method is closer to the exact solution than the approximation with the implicit Euler, which has only a first-order accuracy. More detailed studies on the convergence and further comparisons are discussed in later chapters, for the direct application of the methods in the context of the LSFEM.

REMARK: The approach on the Runge-Kutta method described above leads to a system of equations formulated as a function of the stage quantity $k_2$, which corresponds to the time derivative of the solution variable $z(x, t)$. For the later application of the RK methods to solve the Navier-Stokes equations using the least-squares stress-velocity formulation, an approach for the time-derived quantity depending on the solution variable is needed. More precisely, the accelerations have to be described dependent on the velocities, in order to solve the whole system of equations for stresses and velocities. To provide a simpler understanding of the use of this approach in the context of the least-squares FEM, the transformed formulation is explained below for solving the advection equation.

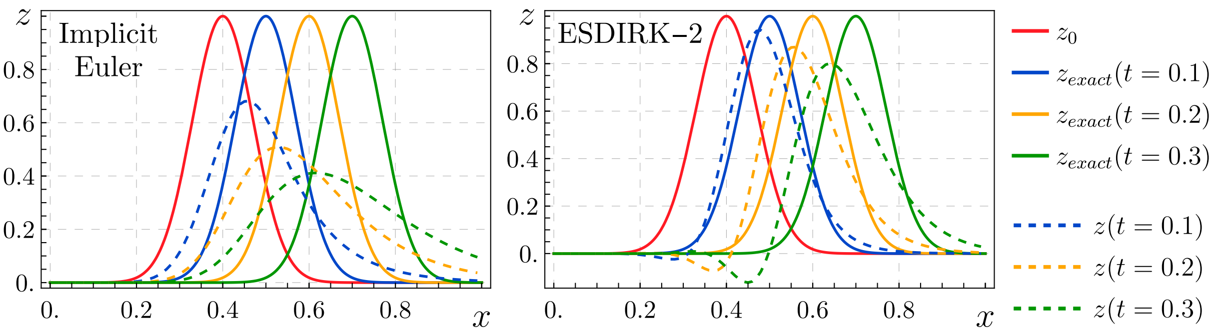

Figure 7.4: Approximation at different times steps (dashed line) compared to exact solution (solid line) obtained with implicit Euler (left) and RK method with parameters corresponding to Crank-Nicolson method (right) with 100 grid points

### Version 2: Runge-Kutta method reformulated

When considering the semi-discretized Eqs.(7.16) and (7.17) one can see a correlation between $z$ and $k_2$, that is

$$k_1 = f\left(z^n\right) \tag{7.22a}$$

$$k_2 = f\Big(\underbrace{z^n + \frac{\Delta t}{2}(k_1 + k_2)}_{z^{n+1}}\Big) = \dot{z}^{n+1} \ , \tag{7.22b}$$

such that

$$k_2 = 2\frac{z^{n+1} - z^n}{\Delta t} - f\left(z^n\right) \ = f(z^{n+1}). \tag{7.23}$$

In this case, for an ESDIRK with two stages with stiff accuracy, i.e. $\beta_j = \alpha_{sj}$ and $\gamma_s = 1$, this relation can also be seen by considering equation (7.16). The derivation for methods with more than one implicit stage is slightly different, since the solution of the current time step $z^{n+1}$ can not be calculated directly, but the intermediate solutions for $z$ in the individual stages must be determined beforehand. However, the procedure is similar and will be explained in more detail, when applying RK methods for least-squares SV formulations in Section 7.3.5.

Considering equation (7.23) and the spatial discretization by the upwind difference scheme stated in (7.11), the fully discretized form of the advection equation reads

$$\begin{aligned} & 2\frac{z_i^{n+1} - z_i^n}{\Delta t} - f\left(z_i^n\right) && = f(z_i^{n+1}) \\ \Leftrightarrow \quad & \frac{z_i^{n+1} - z_i^n}{\Delta t} && = \frac{1}{2}\left(f(z_i^{n+1}) + f\left(z_i^n\right)\right) \\ \Leftrightarrow \quad & \frac{z_i^{n+1} - z_i^n}{\Delta t} && = \frac{1}{2}\left(-\frac{z_i^{n+1} - z_{i-1}^{n+1}}{h} - \frac{z_i^n - z_{i-1}^n}{h}\right) \ , \end{aligned} \tag{7.24}$$

whereby in the second step the equality to the Crank-Nicolson method, see (7.6), is visible. As in the previous sections, the solution for a discretization with $M = 5$ grid points at locations $x_i$ with $i = \{2, 3, 4\}$ can be calculated as follows

$$\begin{aligned}
\frac{z_2^{n+1} - z_2^n}{\Delta t} &= \frac{1}{2}\left(-\frac{z_2^{n+1} - z_1^{n+1}}{h} - \frac{z_2^n - z_1^n}{h}\right) \\
\frac{z_3^{n+1} - z_3^n}{\Delta t} &= \frac{1}{2}\left(-\frac{z_3^{n+1} - z_2^{n+1}}{h} - \frac{z_3^n - z_2^n}{h}\right) \\
\frac{z_4^{n+1} - z_4^n}{\Delta t} &= \frac{1}{2}\left(-\frac{z_4^{n+1} - z_3^{n+1}}{h} - \frac{z_4^n - z_3^n}{h}\right) \; .
\end{aligned} \tag{7.25}$$

The final result in each time step is again obtained by solving this system of equations for $z_i^{n+1}$ with $i = \{2, 3, 4\}$ taking into account the known values for the initial conditions $z_i^0$ with $i = \{2, 3, 4\}$ and for the boundary conditions $z_1^{n+1}$ and $z_5^{n+1}$. The resulting values are identical with those given in Table 7.5.

## 7.3 Time integration methods for least-squares SV formulations

After this general introduction of the time discretization methods for the solution of ordinary differential equations, the specific application in the framework of the FEM shall now be discussed. As mentioned earlier, least-squares formulations in terms of stresses and velocities are used in this work for both the fluid and the solid domain. Hence in this section, the necessary terms are given for all time discretization methods as a function of the velocities. As in the previous chapters, $\boldsymbol{a}$, $\boldsymbol{v}$ and $\boldsymbol{u}$ are used as notation for the accelerations, velocities and displacements. Furthermore, the index $n+1$ denotes the current time step and $n, n-1$ and $n-2$ indicate previous time steps. These indices can appear as either superscripts or subscripts, depending on how the notation is clearest. To be precise, the objective is to approximate the time dependent quantities $\boldsymbol{a}(\boldsymbol{v})$ and $\boldsymbol{u}(\boldsymbol{v})$ with any time discretization scheme. First the general steps of the time discretization are explained and then the approximation specifications of the individual methods follow.

The general procedure for all integration schemes considered can be summarized in the following steps:

1. Division of the regarded time interval from $t_0$ to $T$ into $N$ subintervals with the time step size $\Delta t$: $[t_0, T] = \bigcup_{n=0}^{N-1} [t_n, t_{n+1}]$ with $\Delta t = t_{n+1} - t_n$, where the subscripts $n+1$ and $n$ denote the actual and previous time steps.

2. Approximation of the time dependent quantities $\boldsymbol{a}^{n+1}(\boldsymbol{v})$ and $\boldsymbol{u}^{n+1}(\boldsymbol{v})$ based on the known field quantities of one or more previous time steps $(t_n, t_{n-1}, ...)$ and the unknowns of the actual time step $(t_{n+1})$, see next sections.

3. Iterative solution of the nonlinear equation system including all residual terms with the Newton-Raphson method.

   Fluid domain:
   Evaluation of the functional $\mathcal{F}^F(\boldsymbol{\sigma}^{n+1}, \boldsymbol{v}^{n+1}, \boldsymbol{a}^{n+1})$ with $\boldsymbol{a}^{n+1}$ as defined by the chosen time discretization method.

   Solid domain:
   Evaluation of the functional $\mathcal{F}^S(\boldsymbol{\sigma}^{n+1}, \boldsymbol{a}^{n+1}, \boldsymbol{u}^{n+1})$ with $\boldsymbol{a}^{n+1}$ and $\boldsymbol{u}^{n+1}$ as defined by the chosen time discretization method.

4. Updating of all actual quantities: e.g. $\boldsymbol{v}^{n+1} \rightarrow \boldsymbol{v}_n$

5. Repetition of steps two to four up to final time $T$.

Note, that the procedure is modified if adaptive time step control is applied. A more detailed description of the third step including the required formulas for the approximation of the time dependent quantities and information on the implementation of all schemes is given in the following.

### 7.3.1 Implicit Euler method for least-squares SV formulations

The implicit Euler method is implemented only for comparison, because at the same computational cost the accuracy is lower compared to other methods like, e.g., Crank-Nicolson. Considering equation (7.5), it can be used directly to describe the accelerations, defined as $\boldsymbol{a} = \dot{\boldsymbol{v}}$, as a function of the velocities, which yields

$$\boldsymbol{a}_{n+1} = \frac{\boldsymbol{v}_{n+1} - \boldsymbol{v}_n}{\Delta t} \ . \tag{7.26}$$

A transformation of (7.5) to obtain a dependence on the time-derived quantity leads to a description for the displacements depending on the velocities, which reads

$$\boldsymbol{u}_{n+1} = \boldsymbol{u}_n + \boldsymbol{v}_{n+1}\,\Delta t \ . \tag{7.27}$$

### 7.3.2 Newmark method for least-squares SV formulations

The Newmark method is a well-known one-step method, which is commonly used especially to solve dynamical structure problems as it is suitable to discretize second-order systems in time. The method was developed by NEWMARK [290] and in its original form it leads to a term for the actual velocities and displacements depending on the accelerations of the actual and last time step given as

$$\boldsymbol{u}_{n+1} = \boldsymbol{u}_n + \boldsymbol{v}_n \Delta t + \Delta t^2 \left[ \left( \frac{1}{2} - \beta \right) \boldsymbol{a}_n + \beta \ \boldsymbol{a}_{n+1} \right] \ , \tag{7.28}$$

$$\boldsymbol{v}_{n+1} = \boldsymbol{v}_n + \Delta t \left[ (1-\gamma)\, \boldsymbol{a}_n + \gamma \ \boldsymbol{a}_{n+1} \right] . \tag{7.29}$$

The Newmark parameters $\gamma$ and $\beta$ specify the behavior of the discretization method and for linear structural dynamics these parameters are mathematically limited to $0 \leq \beta \leq \frac{1}{2}$ and $0 \leq \gamma \leq 1$. Furthermore, the choice of $\gamma = \frac{1}{2}$ results in an optimal and second-order accurate method when applied to linear dynamics. Different parameter combinations have been investigated in the past. Most commonly used selections are $\beta = \frac{1}{4}$ and $\gamma = \frac{1}{2}$ which leads to the constant acceleration method and $\beta = \frac{1}{6}$ and $\gamma = \frac{1}{2}$ which yields the linear acceleration method. Besides, the Newmark method is equal to the explicit central difference scheme for a parameter choice of $\beta = 0$ and $\gamma = \frac{1}{2}$. For further information on the Newmark method and its characteristics see, for instance, HUGHES [206], BATHE [19], ZIENKIEWICZ AND TAYLOR [431], BATHE [20] and WRIGGERS [424].

For the application to the previously presented least-squares formulations for the solid and fluid domain in terms of stresses and velocities, the Newmark method is reformulated such that

$$\boldsymbol{a}_{n+1} = \frac{1}{\gamma \Delta t}\boldsymbol{v}_{n+1} - \frac{1}{\gamma \Delta t}\left(\boldsymbol{v}_n + (1-\gamma)\boldsymbol{a}_n \Delta t\right) \ , \tag{7.30}$$

$$\boldsymbol{u}_{n+1} = \boldsymbol{u}_n + \boldsymbol{v}_n \Delta t + \Delta t^2 \left(\frac{1}{2} - \beta\right)\boldsymbol{a}_n + \frac{\beta \Delta t}{\gamma}\left(\boldsymbol{v}_{n+1} - \boldsymbol{v}_n - (1-\gamma)\boldsymbol{a}_n \Delta t\right) \ . \tag{7.31}$$

These expressions define the actual displacements $\boldsymbol{u}_{n+1}$ and accelerations $\boldsymbol{a}_{n+1}$ depending on the actual velocities $\boldsymbol{v}_{n+1}$ and on values of the last time step $\boldsymbol{a}_n, \boldsymbol{v}_n, \boldsymbol{u}_n$.

Remark: With a choice of the parameters $\beta = \frac{1}{4}$ and $\gamma = \frac{1}{2}$ the Newmark method in the formulation depending on the velocities, results in equivalent terms as the Runge-Kutta method denoted as ESDIRK-2 and explained in Section 7.3.5.

### 7.3.3 Houbolt method for least-squares SV formulations

The Houbolt method, first presented in Houbolt [201], is based on a standard finite difference approach for the accelerations and velocities and assumes a cubic displacement function. The velocities and accelerations are approximated in terms of the displacements applying backward differences which are second-order accurate, see e.g. Subbaraj and Dokainish [375]. This leads to the initial formulation as follows

$$\boldsymbol{a}_{n+1} = \frac{1}{\Delta t^2}(2\boldsymbol{u}_{n+1} - 5\boldsymbol{u}_n + 4\boldsymbol{u}_{n-1} - \boldsymbol{u}_{n-2}) \ , \tag{7.32}$$

$$\boldsymbol{v}_{n+1} = \frac{1}{6\Delta t}(11\boldsymbol{u}_{n+1} - 18\boldsymbol{u}_n + 9\boldsymbol{u}_{n-1} - 2\boldsymbol{u}_{n-2}) \ , \tag{7.33}$$

where the values at $t_{n+1} = t_n + \Delta t$ are calculated based on the data at the time steps $t_n$, $t_{n-1} = t_n - \Delta t$ and $t_{n-2} = t_n - 2\Delta t$. This procedure in general requires a special starting procedure to approximate the values at $t = t_0 - \Delta t$ and $t = t_0 - 2\Delta t$ as e.g. the explicit central difference scheme. The method has unconditional stability, such that the time step size is not limited by stability constraints, but it implies also an inherent algorithmic damping, especially when large time steps are used, see Subbaraj and Dokainish [375].

A reformulation to approximate the actual displacements $\boldsymbol{u}_{n+1}$ and accelerations $\boldsymbol{a}_{n+1}$ depending on the actual velocities $\boldsymbol{v}_{n+1}$ and known field quantities from previous time steps leads to

$$\boldsymbol{u}_{n+1} = \frac{6}{11}\boldsymbol{v}_{n+1}\Delta t + \frac{18}{11}\boldsymbol{u}_n - \frac{9}{11}\boldsymbol{u}_{n-1} + \frac{2}{11}\boldsymbol{u}_{n-2} \ , \tag{7.34}$$

$$\boldsymbol{a}_{n+1} = \frac{1}{\Delta t^2}\left[\frac{12}{11}\boldsymbol{v}_{n+1}\Delta t - \frac{19}{11}\boldsymbol{u}_n + \frac{26}{11}\boldsymbol{u}_{n-1} - \frac{7}{11}\boldsymbol{u}_{n-2}\right] . \tag{7.35}$$

### 7.3.4 Crank-Nicolson method for least-squares SV formulations

As already mentioned in Section 7.2.2, the Crank-Nicolson method is a one step method with second-order accuracy. The approach can be derived from the basic $\theta$-scheme as presented for the first time within the LSFEM by, e.g., Carey and Jiang [88] with $\theta = \frac{1}{2}$. A number of applications of the Crank-Nicolson method exists in the context of FEM for the solution of the unsteady Navier-Stokes equations, see Turek [395], Rannacher [320], Cho and Kim [104], for instance.

The accelerations are approximated based on the backward difference scheme and given as

$$\boldsymbol{a}_{n+1} = \frac{\boldsymbol{v}_{n+1} - \boldsymbol{v}_n}{\Delta t} \ , \tag{7.36}$$

and the remaining part of the equation is evaluated based on the unknowns of the current and possibly last time step. Such that in general, using the notation of the $\theta$-scheme, the equation system yields

$$\boldsymbol{a}_{n+1} = \theta \, \boldsymbol{G}(\mathcal{U}^{n+1}) + (1-\theta) \, \boldsymbol{G}(\mathcal{U}^{n}) \ , \tag{7.37}$$

where $\mathcal{U}$ denotes the unknowns in the actual time step $t_{n+1}$ or $t_n$. In the scope of this thesis, the method will be applied to semi-discretize the mixed least-squares fluid formulation in terms of stresses and velocities (4.17), such that $\mathcal{U} = (\boldsymbol{\sigma}, \boldsymbol{v})$. According to TUREK [395], there are different ways to handle the time-independent quantities, such as the pressure or the stresses. The authors mention, that the procedure has the same accuracy, regardless of the fact if for the pressure in the Navier-Stokes equations only the current value or also the value from the last time step is considered. When applied in the context of the LSFEM for fluid dynamics, for example, there is also the question of whether the averaged calculation based on the evaluation at the current and previous time is applied only to the residual with the time-derived quantity, i.e. the accelerations, or to all residual terms.

In the context of this work, different variants are examined and compared for the solution of unsteady flow based on the incompressible Navier-Stokes equations. For a convenient presentation, the notation of the $\theta$-method is used in the following to specify the semi-discrete form of the stress-velocity fluid formulation. Therefore, the least-squares functional discretized in time reads

$$\mathcal{F}^F_{n+1} = \frac{1}{2}\left( ||\mathcal{R}_1^{n+1}||^2_{L^2(\Omega_f)} + ||\mathcal{R}_2^{n+1}||^2_{L^2(\Omega_f)} + \ ||\mathcal{R}_3^{n+1}||^2_{L^2(\Omega_f)} \right) , \tag{7.38}$$

with the residuals, omitting the weighting terms and body force, given by

$$\begin{aligned} \mathcal{R}_1^{n+1} &= \rho_f \boldsymbol{a}^{n+1} - \theta_{\sigma 1} \operatorname{div} \boldsymbol{\sigma}^{n+1} - (1-\theta_{\sigma 1}) \operatorname{div} \boldsymbol{\sigma}^{n} \\ &\quad + \rho_f \, \theta_{v1} \nabla \boldsymbol{v}^{n+1} \cdot \boldsymbol{v}^{n+1} + \rho_f (1-\theta_{v1}) \nabla \boldsymbol{v}^{n} \cdot \boldsymbol{v}^{n} \ , \end{aligned} \tag{7.39a}$$

$$\begin{aligned} \mathcal{R}_2^{n+1} &= \theta_{\sigma 2} \operatorname{dev} \boldsymbol{\sigma}^{n+1} + (1-\theta_{\sigma 2}) \operatorname{dev} \boldsymbol{\sigma}^{n} \\ &\quad - 2\rho_f \nu_f \left( \theta_{v2} \ \nabla^s \boldsymbol{v}^{n+1} + (1-\theta_{v2}) \ \nabla^s \boldsymbol{v}^{n} \right) \ , \end{aligned} \tag{7.39b}$$

$$\mathcal{R}_3^{n+1} = \theta_{v3} \operatorname{div} \boldsymbol{v}^{n+1} + (1-\theta_{v3}) \operatorname{div} \boldsymbol{v}^{n} \ . \tag{7.39c}$$

Depending on the choice of the parameters $\theta_{\sigma_1}, \theta_{\sigma_2}, \theta_{v1}, \theta_{v2}, \theta_{v3}$, this description provides a different approach with regard to time discretization. For the case that all parameters are set to one or zero, one obtains e.g. either the implicit or explicit Euler method. In Section 7.4, various combinations of the parameters are examined in terms of temporal accuracy.

REMARK: Another notation often used for the Crank-Nicolson method is to represent it as a Runge-Kutta procedure, with the corresponding Butcher parameters as given in Table 7.4. The procedure for implementing singly-diagonally Runge-Kutta methods for discretizing the mixed stress-velocity formulations is explained next.

### 7.3.5 SDIRK methods for least-squares SV formulations

As stated in Section 7.2.3, the family of Runge-Kutta methods belongs to the group of multi-stage integration schemes, in which a certain number of stages is evaluated in each time step. In the context of this work, only singular diagonal implicit Runge-Kutta methods (SDIRK) are investigated, where the stages can be evaluated sequentially one after the other. Each stage is based on the results of previously solved stages and time steps. Under this condition, and adding the relation $\dot{\phi} = f(\phi)$ as given in the initial value problem in (7.2), the equations (7.7) can be transformed into

$$\phi^{n+1} = \phi^n + \Delta t \sum_{j=1}^{s} \beta_j k_j \tag{7.40}$$

$$\begin{aligned} \text{with} \qquad k_j &= f\Big(t_n + \gamma_j \Delta t, \;\; \phi^n + \Delta t \sum_{l=1}^{j} \alpha_{jl} k_l\Big) = \dot{\phi}_j \\ &= f\Big(t_n + \gamma_j \Delta t, \;\; \underbrace{\phi^n + \Delta t \sum_{l=1}^{j} \alpha_{jl} \; \dot{\phi}_l}_{\phi_j}\Big) \;, \qquad \text{for } j = 1, ..., s \;. \end{aligned} \tag{7.41}$$

Remark: The upper limit of the summation in (7.41) changed from $s$ to $j$ and the solutions at stages $j = 1...s$ are denoted by $\phi_j$.

Then, the correlation in (7.41) can be used to construct the approximation of the time-derived quantity for each stage as a function of the unknown stage quantity $\phi_j$, as follows

$$\begin{aligned} \phi_j &= \phi^n + \Delta t \sum_{l=1}^{j} \alpha_{jl} \; \dot{\phi}_l \qquad (7.42) \\ &= \phi^n + \Delta t \; \Big(\alpha_{j1} \; \dot{\phi}_1 + \alpha_{j2} \; \dot{\phi}_2 + ... + \alpha_{jj} \; \dot{\phi}_j\Big) \end{aligned}$$

$$\Leftrightarrow \qquad \dot{\phi}_j = \frac{1}{\Delta t \; \alpha_{jj}} \left( \phi_j - \phi^n - \sum_{l=1}^{j-1} \alpha_{jl} \; \dot{\phi}_l \right) \;, \quad \text{for} \quad j = 1, ..., s \;. \tag{7.43}$$

Transferring this to the least-squares formulations, the following expression is obtained for the velocities at the actual time step $\boldsymbol{v}^{n+1}$ from equations (7.40)

$$\boldsymbol{v}^{n+1} = \boldsymbol{v}^n + \Delta t \sum_{j=1}^{s} \beta_j \, \boldsymbol{a}_j \;. \tag{7.44}$$

And with (7.43) a term for the accelerations at all stage levels is given as

$$\boldsymbol{a}_j = \frac{1}{\Delta t \; \alpha_{jj}} \left( \boldsymbol{v}_j - \boldsymbol{v}^n - \sum_{l=1}^{j-1} \alpha_{jl} \; \boldsymbol{a}_l \right) \;, \quad \text{for} \quad j = 1, ..., s \;. \tag{7.45}$$

However, using SDIRK methods with an explicit first stage, referred to as ESDIRK, the first parameter is $\alpha_{11} = 0$, and therefore the accelerations are approximated as follows

$$\boldsymbol{a}_j = \begin{cases} \boldsymbol{a}^n & \text{for } j = 1 \\ \dfrac{1}{\Delta t \; \alpha_{jj}} \Big( \boldsymbol{v}_j - \boldsymbol{v}^n - \Delta t \sum\limits_{l=1}^{j-1} \alpha_{jl} \; \boldsymbol{a}_l \Big) & \text{for } j = 2, ..., s \;. \end{cases} \tag{7.46}$$

Furthermore, for the solution of the least-squares SV solid formulation, an approximation for the displacements depending on the velocities is needed. Considering the relation $\dot{\boldsymbol{u}} = \boldsymbol{v}$ and inserting this into equation (7.42), the displacements in the individual stages can be calculated with

$$\boldsymbol{u}_j = \boldsymbol{u}^n + \Delta t \sum_{l=1}^{j} \alpha_{jl} \, \boldsymbol{v}_l \ , \quad \text{for} \quad j = 1, ..., s \ . \tag{7.47}$$

Remark: Due to the stiff accuracy of the applied Runge-Kutta schemes in this work, i.e. $\beta_j = \alpha_{sj}$ and $\gamma_s = 1$, the result of the last stage corresponds to the solution of the associated time step. Therefore, the projection step which is given by (7.40) can be omitted. For more general and detailed information on the family of Runge-Kutta methods, the reader is referred to Alexander [3], Cash [93], Hairer and Wanner [177] and Hairer et al. [179], for instance.

In this thesis, several singly diagonally implicit Runge-Kutta methods with and without an explicit first stage are implemented and investigated to solve unsteady flow and dynamic structure problems. Several information on the applied schemes are summarized in Table 7.6. This includes the order of the methods, the number of stages, the used acronyms and the source literature for the parameter sets.

Table 7.6: List of used RK methods with number of all stages $s$, number of implicitly evaluated stages, order $p$, order of embedded method $q$, and source literature

| name | stages $s$ | implicit stages | order $p$ | order $q$ | reference |
|---|---|---|---|---|---|
| ESDIRK-2 | 2 | 1 | 2 | - | Williams et al. [420] |
| ESDIRK-2(1) | 2 | 1 | 2 | 1 | Rang [318] |
| SDIRK-2(1) | 2 | 2 | 2 | 1 | Ellsiepen and Hartmann [138] |
| ESDIRK-3 | 4 | 3 | 3 | - | Montlaur et al. [281] |
| ESDIRK-3(2) | 4 | 3 | 3 | 2 | Bijl et al. [41] |
| SDIRK-4(3) | 5 | 5 | 4 | 3 | Hairer and Wanner [177] |
| ESDIRK-4(3) | 6 | 5 | 4 | 3 | Bijl et al. [41] |

When naming the individual Runge-Kutta methods, in this thesis the order of the method is appended to the abbreviation. Furthermore, in the names of some methods, a number in parentheses is added. This is the case for embedded RK methods, where two methods of different orders exist with the same coefficients $\alpha_{jl}$. The number in parentheses stands for the order $q$ of the embedded procedure. These embedded methods are very useful for adaptive control of time step sizes. Further details are given in Chapter 7.6. The coefficients of all implemented methods are given in Appendix C.1.

## 7.4 Numerical examples: Unsteady flow of Newtonian fluids

In this section, the application of the different time discretization schemes to solve unsteady flow based on the incompressible Navier-Stokes equations is investigated. This is done using two different benchmark problems in two dimensions, namely a Taylor-Green vortex flow and a flow around a cylinder at a Reynolds number of $Re = 100$. The problems are solved based on the mixed LS stress velocity formulation as presented in (4.17) with according physical weighting factors chosen as

$$\omega_{f1} = \sqrt{\frac{\Delta t}{\rho_f}}, \quad \omega_{f2} = \sqrt{\frac{1}{\rho_f \nu_f}} \qquad \text{and} \quad \omega_{f3} = 1 \; . \tag{7.48}$$

### 7.4.1 Unsteady Taylor-Green vortex

As a first numerical example in this section, two-dimensional Taylor-Green vortex (TGV) flow is considered to study the convergence of several presented time discretization methods. This flow problem was originally developed in the context of studying turbulent flows with the purpose of analyzing the formation of small vortices from larger vortices, see Taylor and Green [384]. In this work, the same definition of the problem is used as in Sanderse and Koren [335]. The flow is initialized with a smooth two-dimensional velocity field

$$\boldsymbol{v}^0(x_1, x_2) = \begin{bmatrix} -\sin(\pi x_1)\cos(\pi x_2) \\ \cos(\pi x_1)\sin(\pi x_2) \end{bmatrix} \; . \tag{7.49}$$

The Taylor-Green vortex flow is an exact solution of the Navier-Stokes equations without any forcing term ($\boldsymbol{f} = \boldsymbol{0}$), where the flow decreases exponentially with time and satisfies equations

$$\boldsymbol{v}(x_1, x_2, t) = \begin{bmatrix} -\sin(\pi x_1)\cos(\pi x_2) \\ \cos(\pi x_1)\sin(\pi x_2) \end{bmatrix} \; \exp(-2\nu_f \pi^2 t) \; , \tag{7.50a}$$

$$p(x_1, x_2, t) = \frac{1}{4}(\cos(2\pi x_1) + \cos(2\pi x_2)) \; \exp(-4\nu_f \pi^2 t) \; . \tag{7.50b}$$

The computations are restricted to the spatial square domain $\Omega_f = \left[\frac{1}{4}, \frac{1}{2}\right]^2$ and the evolution of the flow is simulated from $t_0 = 0\,\text{s}$ to $t = 1\,\text{s}$. In all simulations the fluid viscosity and density are set to $\nu_f = 0.01\,\text{m}^2/\text{s}$ and $\rho_f = 1\,\text{kg/m}^3$, resulting in a Reynolds number of $Re = 100$. Time dependent boundary conditions for the velocities are prescribed according to (7.50a) on the entire boundary. For the degrees of freedom assigned to the stresses, the boundary conditions are specified at one point in the center on the top edge as $\boldsymbol{\beta} = \boldsymbol{\sigma} \cdot \boldsymbol{n} = [\sigma_{12}, \sigma_{22}]^T$. The exact solution for the stresses is therefore calculated by inserting definitions (7.50) into $\boldsymbol{\sigma} = 2\rho_f \nu_f \nabla^s \boldsymbol{v} - p\boldsymbol{I}$. This yields the following stress components

$$\begin{aligned} \sigma_{11}(x_1, x_2, t) = &-2\pi\nu_f\rho_f \cos(\pi x_1)\cos(\pi x_2) \; \exp\left(-2\pi^2 \nu_f t\right) \\ &- \frac{1}{4}(\cos(2\pi x_1) + \cos(2\pi x_2)) \; \exp\left(-4\pi^2 \nu_f t\right) \; , \end{aligned} \tag{7.51a}$$

$$\sigma_{12}(x_1, x_2, t) = \sigma_{21}(x_1, x_2, t) = 0 \; , \tag{7.51b}$$

$$
\begin{aligned}
\sigma_{22}(x_1,x_2,t) = {} & 2\pi\nu_f\rho_f\cos(\pi x_1)\cos(\pi x_2)\exp(-2\pi^2\nu_f t) \\
& -\frac{1}{4}(\cos(2\pi x_1)+\cos(2\pi x_2))\exp(-4\pi^2\nu_f t)\ .
\end{aligned}
\tag{7.51c}
$$

As for the initial conditions, the velocities on the entire domain are set as given in (7.65). For the methods under consideration, the solution does not depend on the pressure, or in case of the SV formulation on the stresses, at the start of a time step. Therefore, the initial conditions for the stresses are not required. However, according to the time discretization scheme, initial conditions for the accelerations (i.e. for all ESDIRK methods) or displacements (for the Houbolt method) must be specified. The corresponding history fields can be prescribed as a function of the initial velocity as follows

$$
\boldsymbol{a}(x_1,x_2,t) = \boldsymbol{v}(x_1,x_2,t)\cdot(-2\pi^2\nu_f) \quad \Rightarrow \quad \boldsymbol{a}^0(x_1,x_2) = \boldsymbol{v}^0(x_1,x_2)\cdot(-2\pi^2\nu_f)\ , \tag{7.52}
$$

and

$$
\boldsymbol{u}(x_1,x_2,t) = \boldsymbol{v}(x_1,x_2,t)\cdot(-2\pi^2\nu_f)^{-1}
$$

$$
\Rightarrow \quad \begin{cases}
\boldsymbol{u}^0(x_1,x_2) & = \boldsymbol{v}^0(x_1,x_2)\cdot(-2\pi^2\nu_f)^{-1}\ , \\
\boldsymbol{u}^{-1}(x_1,x_2) & = \boldsymbol{v}^0(x_1,x_2)\cdot\exp(2\pi^2\nu_f\Delta t)\cdot(-2\pi^2\nu_f)^{-1}\ , \\
\boldsymbol{u}^{-2}(x_1,x_2) & = \boldsymbol{v}^0(x_1,x_2)\cdot\exp(4\pi^2\nu_f\Delta t)\cdot(-2\pi^2\nu_f)^{-1}\ .
\end{cases}
\tag{7.53}
$$

Figures 7.5 and 7.6 present the solution at the final time $t = 1\,\mathrm{s}$, which is obtained with the time discretization method ESDIRK-2 using a time step size of $\Delta t = 10^{-3}\,\mathrm{s}$ and with a spatial discretization of $32 \times 32$ elements of order $RT_3P_4$. It can be seen that the area under consideration represents a quarter of a vortex. In addition, the shear stresses are basically equal to zero, which is consistent with the exact solution (7.51b).

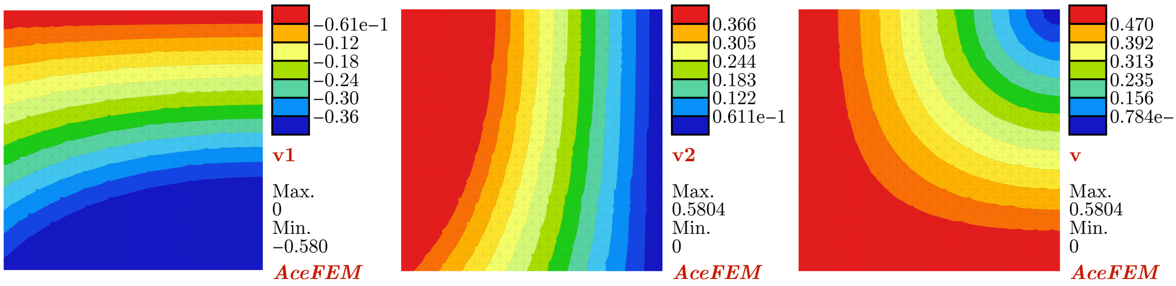

Figure 7.5: TGV - distribution of the velocity components $v_1$ (left), $v_2$ (center) and the total velocity $|\boldsymbol{v}|$ (right) at time $t = 1\,\mathrm{s}$, obtained with ESDIRK-2 and $RT_3P_4$ (in m/s)

In order to evaluate the convergence of the constructed LS SV formulation regarding the discretization in space and time, the approximated solution is compared to the exact solution for the velocities (7.50) and the stresses (7.51). For the spatial convergence, the global error for the velocity and the stress is evaluated at the final time $t = 1\,\mathrm{s}$ on the entire domain using the $L_2$-norm as

$$
e_v = ||\boldsymbol{v}^h - \boldsymbol{v}^{\mathrm{exact}}||_{L^2(\Omega)} \tag{7.54}
$$

and

$$
e_\sigma = ||\boldsymbol{\sigma}^h - \boldsymbol{\sigma}^{\mathrm{exact}}||_{L^2(\Omega)}\ . \tag{7.55}
$$

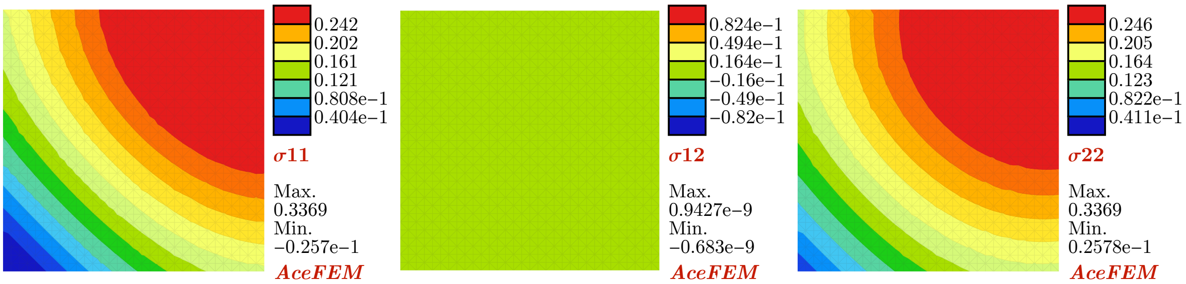

Figure 7.6: TGV - distribution of the stress components $\sigma_{11}$ (left), $\sigma_{12}$ (center) and $\sigma_{22}$ (right) at time $t = 1\,\text{s}$, obtained with ESDIRK-2 and $RT_3P_4$ (in N/m$^2$)

For the temporal convergence the norm of the global error in the velocities is evaluated at every time step on the time interval $T = [0, 1]\,\text{s}$. Assembling all error measures leads to $e_v^{all} = [e_v^1, e_v^2, ..., e_v^{n+1}]$ and for the numerical estimation of the convergence order the mean value is calculated, such that

$$e_v = \text{mean}(e^{all}) = \text{mean}([e_v^1, e_v^2, ..., e_v^{n+1}]) \; . \tag{7.56}$$

**Analysis of spatial accuracy**

In order to evaluate the spatial accuracy, the simulations are advanced with a very small time step $\Delta t = 10^{-3}\,\text{s}$ using the time discretization ESDIRK-2, in such a way that the time discretization errors can be considered as negligible with respect to the spatial ones. The calculations were performed with three different element orders, namely $RT_1P_2$, $RT_2P_3$ and $RT_3P_4$, and four mesh levels. Table 7.7 contains mesh information such as number of elements and degrees of freedom of the meshes used in the numerical simulations.

Table 7.7: TGV - mesh level, number of elements ($n_{\text{ele}}$) and degrees of freedom ($n_{\text{dof}}$) for different element types

| | | $n_{\text{dof}}$ | | |
|---|---|---|---|---|
| level | $n_{\text{ele}}$ | $RT_1P_2$ | $RT_2P_3$ | $RT_3P_4$ |
| 1 | 32 | 514 | 1058 | 1794 |
| 2 | 128 | 1922 | 4034 | 6914 |
| 3 | 512 | 7426 | 15746 | 27138 |
| 4 | 2048 | 29186 | 62210 | 107522 |

To study the spatial convergence order, the error in the velocities and stresses is plotted using a logarithmic scale over the inverse of the element length $h$, see Figure 7.7. The graphs show that the error decrease in the $L^2$-norm is approximately of order $\mathcal{O}(h^{n+1})$ for polynomials $P_n$ for the velocity and of order $\mathcal{O}(h^{m+1})$ for Raviart-Thomas functions $RT_m$ for the stresses.

**Analysis of temporal accuracy**

To further test the application of the different time integration methods to solve the mixed LS SV fluid formulation, the TGV flow is solved with a fine mesh ($n_{\text{ele}} = 8192$) and the element $RT_3P_4$. In this manner, the spatial discretization error can be assumed to be

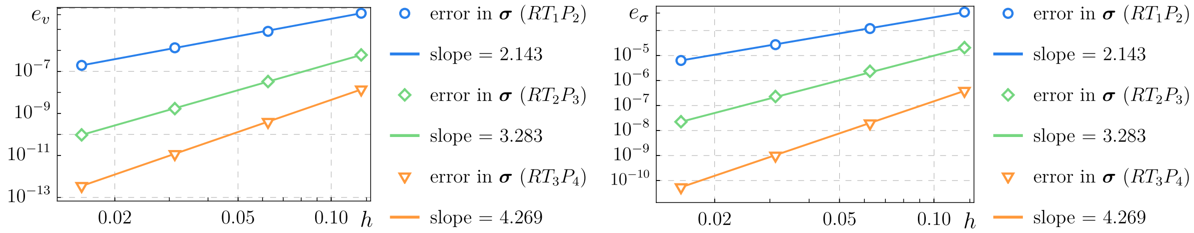

Figure 7.7: TGV - $L^2$-norm of the error in velocities and stresses obtained with ESDIRK-2 for different element orders and mesh levels

much smaller than the temporal discretization error and thus the convergence behavior in time is not affected. The time step size is varied for all schemes from $\Delta t = 0.1\,\mathrm{s}$ to $\Delta t = 0.0125\,\mathrm{s}$ by division by two. In this examination, the evolution of the error in the time-dependent quantity, i.e. velocity, is plotted in a logarithmic scale over the time step size, see Figure 7.8.

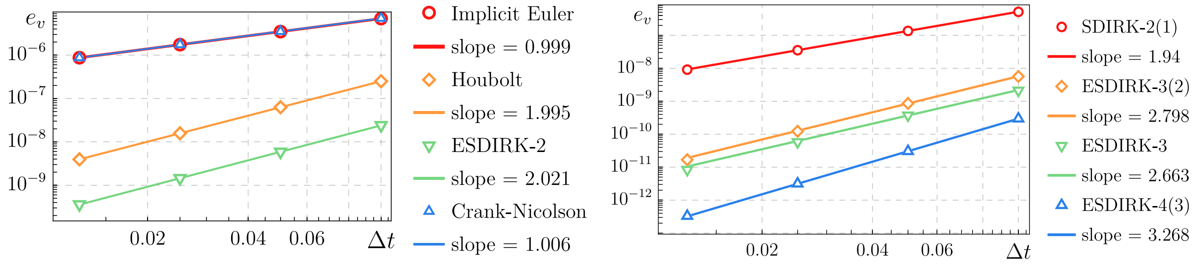

Figure 7.8: TGV - $L^2$-norm of the error in velocities obtained with $n_{\text{ele}} = 8192$ elements of order $RT_3P_4$ for different time discretization methods and time step sizes $\Delta t$

The methods studied include the implicit Euler, Houbolt, and Crank-Nicolson methods, the former having a theoretical accuracy of first-order and the others being theoretically second-order accurate. In addition, some Runge-Kutta methods with theoretical orders of convergence from two to four are considered. It can be clearly seen that for each case, the error follows a linear decrease in the logarithmic scale. The slopes of the lines are specified in the diagrams and in most cases correspond approximately to the expected order of convergence.

REMARK 1: For the high-order ESDIRK methods, an order reduction of roughly 10-20% can be observed. There can be several possible reasons for these problems. Order reduction phenomena that occur in connection with higher-order RK methods have been studied frequently in the literature. Established reasons for this loss of accuracy that have been investigated are, for example, stiff systems or the application of time-dependent boundary conditions in the intermediate stages of the RK procedures. In the context of this work, the occurrence of order reduction will not be investigated further, but detailed studies on this can be found in HAIRER ET AL. [178], BURRAGE AND PETZOLD [75], CARPENTER ET AL. [89], HAIRER AND WANNER [177], ABARBANEL ET AL. [1], PATHRIA [303], among others.

REMARK 2: In a first approach, the parameters for the Crank-Nicolson method described in (7.39) are chosen so that $\theta_{v1} = \frac{1}{2}$ and all others $\theta_{\sigma 1} = \theta_{\sigma 2} = \theta_{v2} = \theta_{v3} = 1$. This leads to a time discretization where the first residual is evaluated based on the velocities of the current and the previous time step and where, moreover, only the current quantities are considered for the stresses in all three residuals. As can be seen in Figure 7.8, this is not an optimal choice, since this variant only leads to a first-order temporal accuracy in contrast to the expected theoretical order $\mathcal{O}(\Delta t^2)$.

Based on this finding, further parameter combinations are analyzed and compared. The naming of the variations and the associated parameters are briefly given in Table 7.8. The outcome of the convergence study is shown in Figure 7.9. The comparison shows that even the version in which the current stresses are taken into account in addition to the velocities when evaluating the first residual, referred to as CN2, does not show improved convergence behavior. On the contrary, the error in the velocities is even slightly larger. To achieve the expected convergence order of $\mathcal{O}(\Delta t^2)$, it is essential that in the second residual the velocities of the previous time step are also taken into account. However, it is irrelevant how the third residual is evaluated.

Table 7.8: TGV - Parameters for Crank-Nicolson method presented in (7.39)

| | parameters | | | | |
|---|---|---|---|---|---|
| name | $\theta_{v1}$ | $\theta_{v2}$ | $\theta_{v3}$ | $\theta_{\sigma 1}$ | $\theta_{\sigma 2}$ |
| CN1 | $\frac{1}{2}$ | 1 | 1 | 1 | 1 |
| CN2 | $\frac{1}{2}$ | 1 | 1 | $\frac{1}{2}$ | 1 |
| CN3 | $\frac{1}{2}$ | $\frac{1}{2}$ | 1 | 1 | 1 |
| CN4 | $\frac{1}{2}$ | $\frac{1}{2}$ | $\frac{1}{2}$ | $\frac{1}{2}$ | $\frac{1}{2}$ |

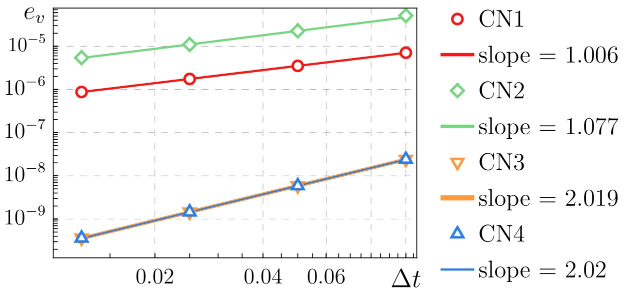

Figure 7.9: TGV - $L^2$-norm of error in velocities for different $\Delta t$ ($n_{\text{ele}} = 512$, $RT_3P_4$)

### 7.4.2 Unsteady flow around a cylinder

In a next example, the fluid benchmark problem flow around a cylinder (FAC) from Schäfer et al. [338], see Figure 7.10, is used to further investigate the application of several presented time discretization schemes to solve the incompressible Navier-Stokes equations. In order to solve the time-dependent flow problem in this section, the least-squares SV fluid formulation (4.17) is discretized in time using the Houbolt, Crank-Nicolson and ESDIRK-3 and ESDIRK-4(3) methods. The Runge-Kutta parameters for the latter two are given in Appendix C.1.

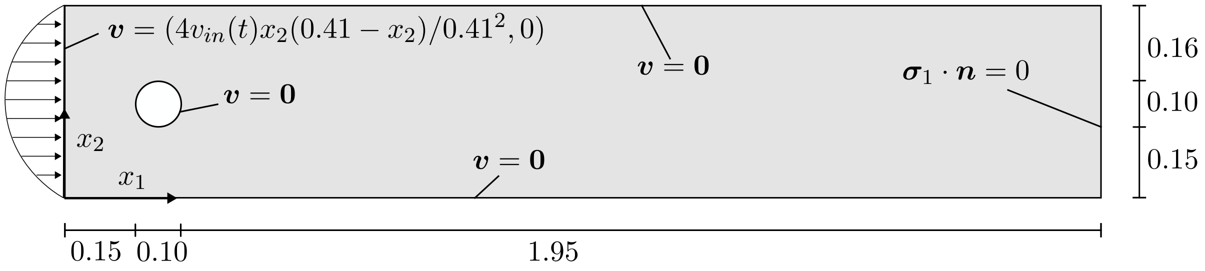

Figure 7.10: FAC - geometry and boundary conditions (unit m)

For the spatial discretization vector-valued Raviart-Thomas functions are implemented for the stresses and Lagrange polynomials are used for the velocities with different polynomial orders. The geometry and the boundary conditions of the problem are illustrated in Figure 7.10. An inflow on the left side, pressure-related stress boundary conditions for an outflow on the right side and no-slip boundary conditions on the top and bottom sides and on the cylinder are defined. In case of the stress-velocity formulation, the suitable stress boundary conditions imposed to the outflow are $\boldsymbol{\sigma}_1 \cdot \boldsymbol{n} = 0$, with $\boldsymbol{\sigma}_1 = [\sigma_{11}\ \sigma_{12}]$.

The fluid material parameters are chosen such that the fluid density $\rho_f = 1.0\,\mathrm{kg/m^3}$ and the kinematic viscosity $\nu = 0.001\,\mathrm{m^2/s}$. During the simulation the inflow velocity is increased piecewise linearly from $v_{in}(t = 0) = 0$ up to $v_{in}(t = 4) = 1.5\,\mathrm{m/s}$. With a mean inflow velocity $\bar{v} = \frac{2}{3} \cdot v_{in} = 1.0\,\mathrm{m/s}$ and a characteristic length of $d = 0.1\,\mathrm{m}$ the characteristic Reynolds number yields $Re = 100$. A typical snapshot of the velocity field for a fully developed flow is illustrated in Figure 7.11

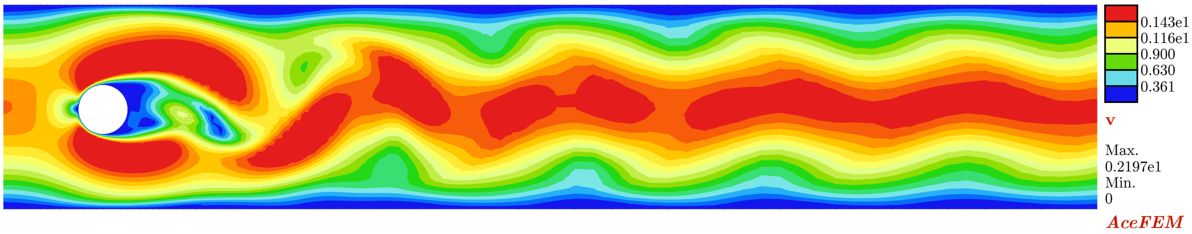

Figure 7.11: FAC - distribution of velocity field with the Houbolt method with $\Delta t = 0.005\,\mathrm{s}$ and $n_{\mathrm{ele}} = 9,728$ elements at $t = 14\,\mathrm{s}$

For a quantitative comparison of the different methods the forces acting on the cylinder over a defined time interval are measured. In precise the drag and lift coefficients are evaluated given as

$$c_D = \frac{2F_D}{\rho_f \bar{v}^2 d}, \qquad \text{and} \qquad c_L = \frac{2F_L}{\rho_f \bar{v}^2 d}\ , \tag{7.57}$$

where $F_D$ and $F_L$ are the drag and lift forces acting on the cylinder $S$ given with

$$(F_D, F_L)^T = \int_S \boldsymbol{\sigma} \cdot \boldsymbol{n}\ \mathrm{d}s\,. \tag{7.58}$$

For the presentation of the results one period of the fully developed instationary flow is extracted. The time interval starts where the lift coefficient is the lowest and has a length of approximately $\Delta t = 0.33\,\mathrm{s}$. In a first step the numerical investigations have been carried out with different mesh levels and three different element orders. Table 7.9 presents the mesh information of the successively refined finite element meshes employed in the numerical simulations including the number of elements and resulting degrees of freedom.

For comparison of the different calculations, the results for the drag coefficient are presented as an example. It should be noted that the calculated lift coefficients vary between $c_{L,min} = -1.025$ and $c_{L,max} = 0.99$ and are thus in good agreement with the reference results of Turek et al. [397], where the results are obtained based on a finite element $Q_2/P_1^{disc}$ and the Crank-Nicolson method with a time step size $\Delta t = 1/1600\,\mathrm{s}$.

Table 7.9: FAC - mesh level, number of elements ($n_{\text{ele}}$) and degrees of freedom ($n_{\text{dof}}$) for different element types

| | | $n_{\text{dof}}$ | | |
|---|---|---|---|---|
| level | $n_{\text{ele}}$ | $RT_1P_2$ | $RT_2P_3$ | $RT_3P_4$ |
| 1 | 2,432 | 34,078 | 73,006 | 126,526 |
| 2 | 5,472 | 76,654 | 164,230 | 284,638 |
| 3 | 9,728 | 136,254 | 291,934 | 505,982 |
| 4 | 15,200 | 212,878 | 456,118 | 790,558 |
| 5 | 29,792 | 417,198 | 893,926 | |

First, the accuracy of the different element orders is compared and the results for the drag coefficient obtained using the Houbolt and Crank-Nicolson method and a time step size of $\Delta t = 0.005\,\text{s}$ are shown. Figure 7.12 shows that the low-order element $RT_1P_2$ leads to a relatively poor approximation even at the finest mesh level compared to the reference solution from Turek et al. [397]. Both higher order elements perform similarly well in terms of approximation quality.

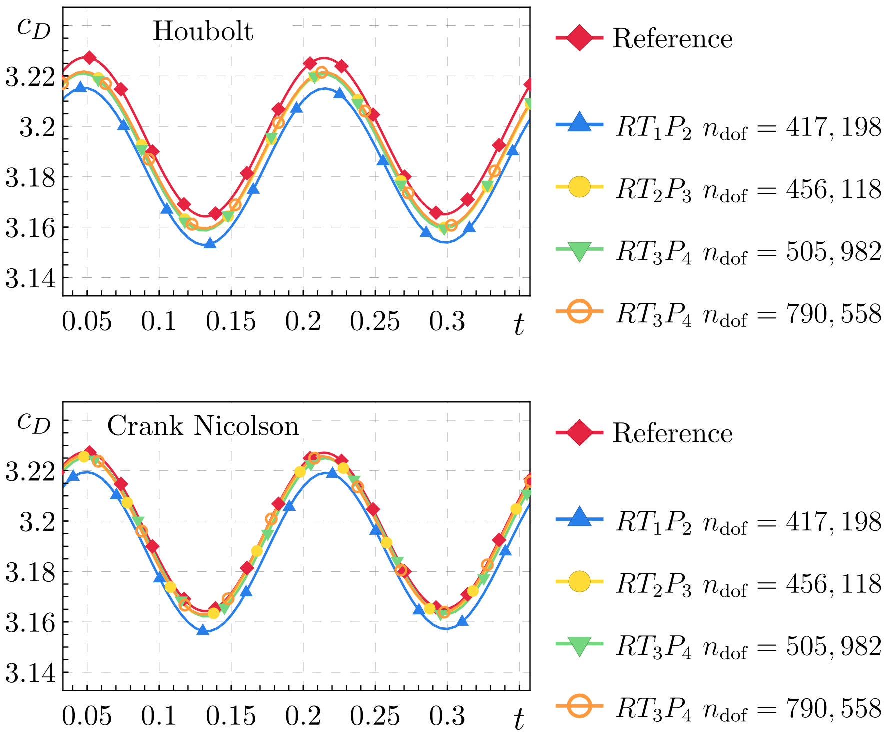

Figure 7.12: FAC - evolution of drag coefficient $c_D$ over time $t$ (in $s$) for different element orders and mesh levels, with Crank Nicolson method (bottom) and Houbolt method (top) with $\Delta t = 0.005\,\text{s}$, with reference solution from Turek et al. [397]

As a consequence of these observations, the element order $RT_2P_3$ is used for the following comparisons of the different time discretization schemes. Figure 7.13 shows the spatial convergence of the results for the four methods with a fixed time step size of $\Delta t = 0.005\,\text{s}$ and illustrates that all methods, except the Houbolt method, have the same accuracy.

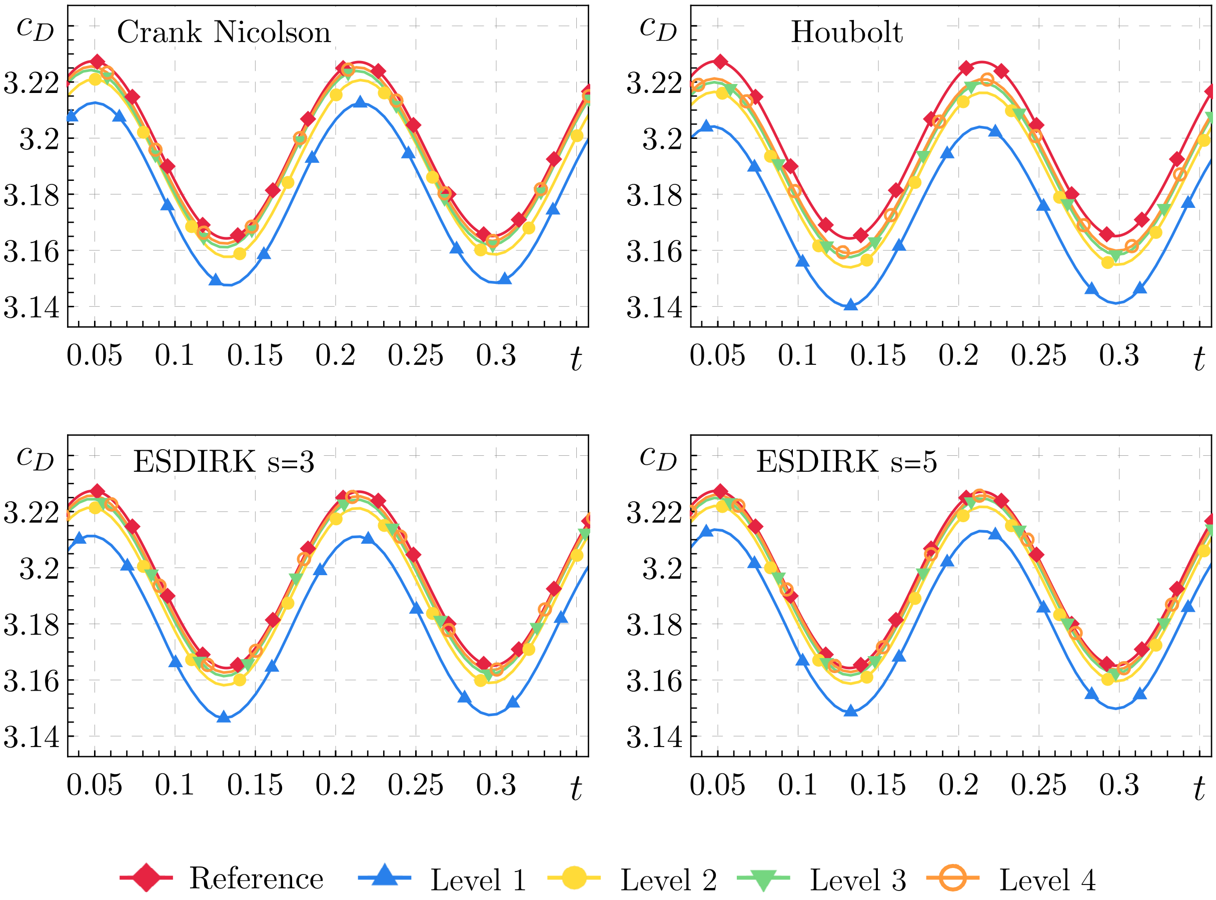

Figure 7.13: FAC - drag coefficient $c_D$ over time $t$ (in s) for different time integration methods ($RT_2P_3$, $\Delta t = 0.005\,\mathrm{s}$), with reference solution from Turek et al. [397]

To simplify the comparison, the mean error of the drag coefficient with respect to the reference values is evaluated as

$$e = \sqrt{\frac{\sum_{i=1}^{N} \left[c_D(t_i) - c_{ref}(t_i)\right]^2}{N}}\,, \tag{7.59}$$

where $N$ is the number of time steps in the considered interval. The results for a fixed time increment of $\Delta t = 0.005\,\mathrm{s}$ and different meshes, as well as for mesh level 3 and different time step sizes are shown in Figure 7.14. These graphs confirm the earlier observations that only the Houbolt method requires a smaller time step to achieve similar accuracy to the other three methods. Another finding and also one of the main results is that all schemes for solving the incompressible Navier-Stokes equations with the least-squares FEM can be used without any apparent stability problems in the studied case. From accuracy aspects, the schemes of higher order from the family of Runge-Kutta methods achieve the same results as the Crank-Nicolson method which is second-order accurate. Further increasing the time step size to investigate possible advantages in terms of efficiency of ESDIRK-3 and ESDIRK-4(3) is not reasonable for this benchmark problem, since the oscillations of the physical quantities cannot be reproduced correctly for larger time step sizes $\Delta t > 0.02\,\mathrm{s}$.

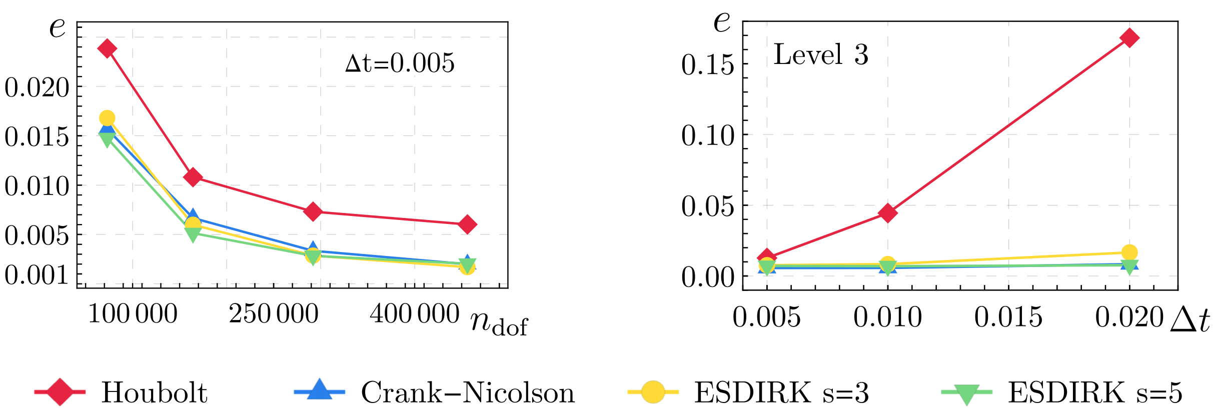

Figure 7.14: FAC - error of drag coefficient with $RT_2P_3$ on different mesh levels, for different time integration methods and different increments $\Delta t$

### Conservation of energy and mass

Another important aspect of solving unsteady flow problems is the conservation of energy and mass. In the context of this work, this issue does not take a central role and will only be briefly examined at this point for the boundary value problem presented.

First, the mass flow difference at the inlet and outlet $\Delta Q$ and the satisfaction of the continuity equation are considered by evaluating the third residual of the fluid $\mathcal{R}_3^F$ over a longer period of time. Figure 7.15 (left) presents, for all the time discretization schemes studied, the evolution of the percentage difference between inflow and outflow over a period of $T = 40\,\mathrm{s}$, computed as

$$\Delta Q = \frac{Q_{in} - Q_{out}}{Q_{in}} \cdot 100\%, \qquad \text{with} \qquad Q_{in/out} = \int_{\partial\Omega_{in/out}} \boldsymbol{v} \cdot \boldsymbol{n} \; \mathrm{d}h \; . \tag{7.60}$$

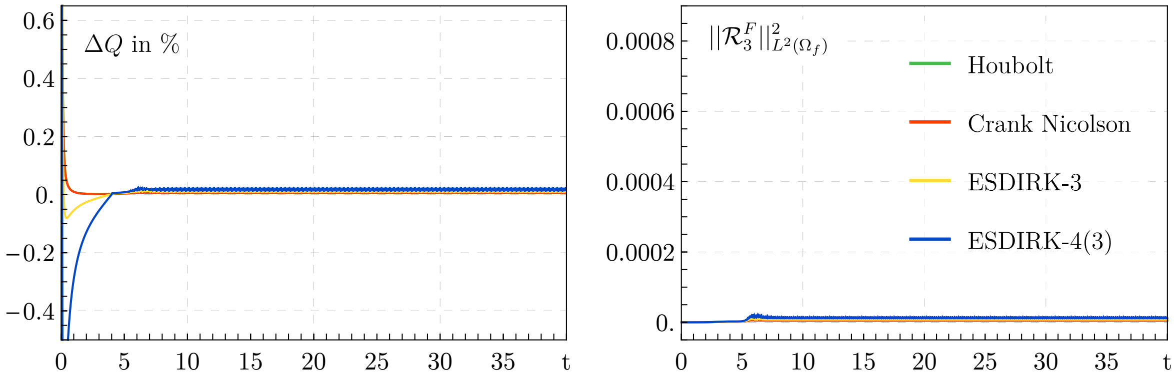

Figure 7.15: FAC - mass flow difference $\Delta Q$ (left) and residual $\mathcal{R}_3^F := \operatorname{div} \boldsymbol{v}$ (right) over time $t$ (in s) for different time integration methods with $\Delta t = 0.005\,\mathrm{s}$ (Level 3, $RT_2P_3$)

The inflow is increased up to the time $T = 4\,\mathrm{s}$ and it can be seen that the flow difference remains constant at almost zero after the final inflow velocity is reached. The conservation of mass is also visible in Figure 7.15 (right), which shows that the integral value of the squared $L^2$-norm of the residual $\mathcal{R}_3^F := \operatorname{div} \boldsymbol{v}$ remains constant well below $10^{-4}$. Thus, the condition of constant density of the incompressible fluid is fulfilled numerically as well.

In addition, to evaluate the conservation of energy, the kinetic energy over the entire fluid domain $\Omega_f$ defined as

$$E = \frac{1}{2} \int_{\Omega_f} \rho_f |\boldsymbol{v}|^2 \mathrm{d}\Omega_f \tag{7.61}$$

is considered. This is again computed for all time discretization schemes studied over a period of $T = 40\,\mathrm{s}$. The results presented in Figure 7.16 show a stable behavior over the considered period for a time increment $\Delta t = 0.005\,\mathrm{s}$.

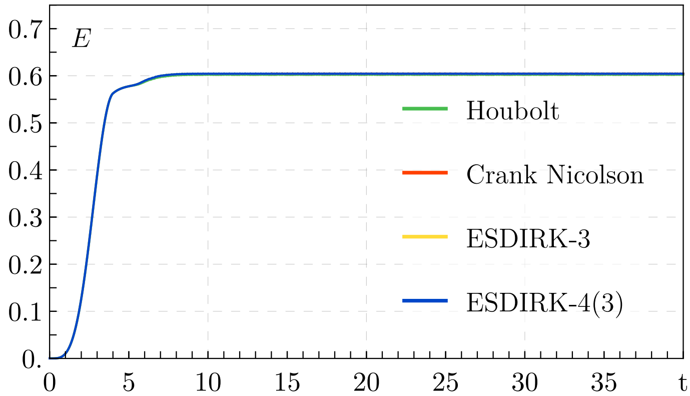

Figure 7.16: FAC - kinetic energy $E$ over time $t$ (in s) for different time integration methods with $\Delta t = 0.005\,\mathrm{s}$ (Level 3, $RT_2P_3$)

## 7.5 Numerical example: Dynamic structure problem

In this section, the application of the different time discretization schemes to solve dynamical structure problems with linear elastic material behavior is studied. For this purpose, a benchmark problem in two dimensions is used, which is a vibrating plate (VP) with an artificial body force and an exact solution, cf. Lai et al. [251]. The problem is solved with the mixed LS stress-velocity formulation given in (6.4) and the related physical weights are chosen as $\omega_{s1} = \sqrt{\Delta t/\rho_s}$ and $\omega_{s2} = 1/\sqrt{\Delta t}$. For the spatial discretization, the velocities are approximated with standard Lagrange polynomials and the stresses with vector-valued Raviart-Thomas functions. The discretization in time in this section is performed using the following algorithms: Houbolt, implicit Euler, Newmark, SDIRK-2(1), ESDIRK-2, ESDIRK-3(2), ESDIRK-3, ESDIRK-4(3). The Butcher tableaus for the different Runge-Kutta schemes can be found in Appendix C.1.

The square plate with the dimensions $\Omega_s = [0,1]^2$ is subjected to a uniform body force in both spatial directions, i.e. $\boldsymbol{f}(x_1, x_2, t) = [f, f]^T$ with

$$\begin{aligned} f(x_1, x_2, t) &= 0.2\, \sin(\pi x_1) \sin(\pi x_2) \exp(-t) \\ &\quad + (-0.4\, \cos(\pi(x_1 + x_2)) + 0.1\, \cos(\pi(x_1 - x_2)))\, \pi^2 \exp(-t)\ . \end{aligned} \tag{7.62}$$

The choice of this body force, and considering for the material parameters a first Lamé constant of $\lambda_s = 1\,\mathrm{N/m^2}$ and a shear modulus of $\mu_s = 0.5\,\mathrm{N/m^2}$, yields an exact solution for the displacements specified by

$$u_1(x_1, x_2, t) = u_2(x_1, x_2, t) = 0.2\, \sin(\pi x_1) \sin(\pi x_2) \exp(-t)\ . \tag{7.63}$$

Based on this, the exact solution for the velocities can be derived as

$$v_1(x_1,x_2,t) = v_2(x_1,x_2,t) = -0.2\,\sin(\pi x_1)\sin(\pi x_2)\exp(-t)\;. \tag{7.64}$$

The boundary conditions for the velocities are prescribed on the entire boundary. To ensure correct initialization of the start values, the velocities are set to

$$\boldsymbol{v}^0(x_1,x_2) = \begin{bmatrix} -0.2\,\sin(\pi x_1)\sin(\pi x_2) \\ -0.2\,\sin(\pi x_1)\sin(\pi x_2) \end{bmatrix}\;. \tag{7.65}$$

Depending on the time discretization method used, the accelerations and displacements at the initial time $t = 0$, and for the Houbolt method also at earlier time steps $t = -\Delta t$ and $t = -2\Delta t$, are specified depending on the initial velocities as

$$\boldsymbol{a}(x_1,x_2,t) = \boldsymbol{v}(x_1,x_2,t)\cdot(-1) \quad\Rightarrow\quad \boldsymbol{a}^0(x_1,x_2) = -\boldsymbol{v}^0(x_1,x_2)\;, \tag{7.66}$$

and

$$\begin{aligned} &\boldsymbol{u}(x_1,x_2,t) = -\boldsymbol{v}(x_1,x_2,t) \\ &\qquad\Rightarrow\quad \begin{cases} \boldsymbol{u}^0(x_1,x_2) &= -\boldsymbol{v}^0(x_1,x_2)\;, \\ \boldsymbol{u}^{-1}(x_1,x_2) &= -\boldsymbol{v}^0(x_1,x_2)\cdot\exp(\Delta t)\;, \\ \boldsymbol{u}^{-2}(x_1,x_2) &= -\boldsymbol{v}^0(x_1,x_2)\cdot\exp(2\Delta t)\;. \end{cases} \end{aligned} \tag{7.67}$$

The notation of the initial values for accelerations and displacements as a function of the initial velocities was selected at this point simply because it is convenient for the implementation in the applied software package AceFEM. Further information on the definition of the problem can be found in Lai et al. [251].

Figure 7.17 shows the solution at time $t = 1\,\mathrm{s}$, which is obtained with the time discretization method ESDIRK-2 using a time step size of $\Delta t = 10^{-3}\,\mathrm{s}$ and with a spatial discretization of $32 \times 32$ elements of order $RT_3P_4$.

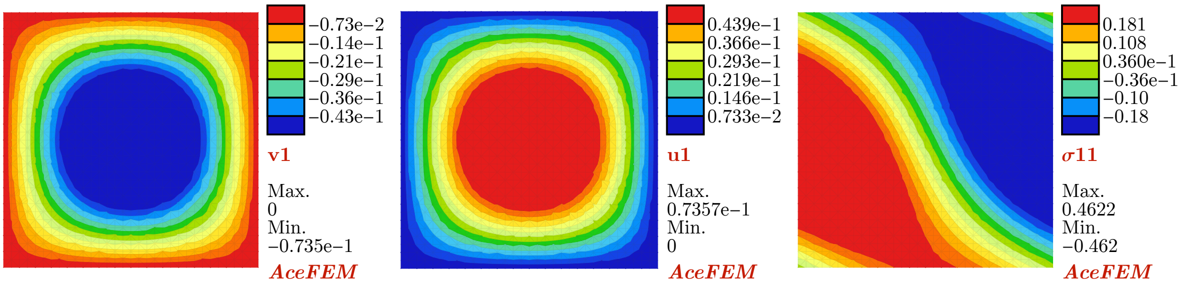

Figure 7.17: VP - distribution of velocity component $v_1$ (left in m/s), displacement $u_1$ (center in m) and stress component $\sigma_{11}$ (right in $\mathrm{N/m^2}$) at time $t = 1\,\mathrm{s}$

In order to evaluate the temporal convergence of the constructed LS SV formulation for linear elasticity, the approximated solution is compared to the exact solution for the velocities (7.64). Therefore, the problem is solved on the time interval $T = [0,1]\,\mathrm{s}$ and the norm of the global error in the velocities is evaluated at every time step as

$$e_v^{n+1} = ||\boldsymbol{v}^{h,n+1} - \boldsymbol{v}_{\text{exact}}^{n+1}||_{L^2(\Omega)} \tag{7.68}$$

Assembling all error measures given in (7.68) leads to $e_v^{all} = [e_v^1, e_v^2, ..., e_v^{n+1}]$ and for the numerical estimation of the convergence order the mean value is calculated, such that

$$e_v = \text{mean}(e^{all}) = \text{mean}([e_v^1, e_v^2, ..., e_v^{n+1}]) \ . \tag{7.69}$$

In order to evaluate the temporal error, the spatial discretization is based on a fine mesh ($n_{\text{ele}} = 8192$) and the element $RT_3P_4$, such that the space discretization errors can be considered as negligible with respect to the temporal ones. The vibrating plate problem is solved with different time discretization schemes and the simulations are advanced with varying time step sizes ranging from $\Delta t = 0.2\,\text{s}$ to $\Delta t = 0.025\,\text{s}$. The evolution of the error in the velocity is plotted in a logarithmic scale over the time step size, see Figure 7.18.

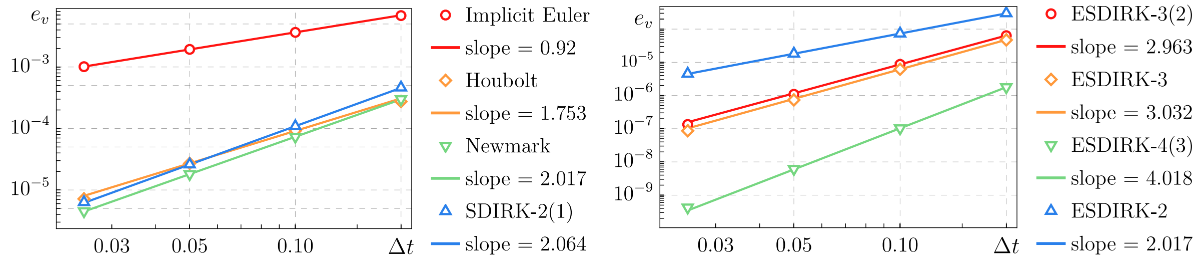

Figure 7.18: VP - $L^2$-norm of the error in velocities obtained with $n_{\text{ele}} = 8192$ elements of order $RT_3P_4$ for different time discretization methods and time step sizes $\Delta t$

All methods have in common that the error of the field variable decreases when the time step size is reduced. In addition, the magnitude of the total error is reduced as the order of accuracy of the methods increases. For all implemented time discretization methods the expected orders are achieved.

## 7.6 Adaptive time stepping methods

Robust and efficient time integration methods are of high interest in many fields of numerics and are especially important for complex problems like fluid-structure interactions. The accuracy and efficiency of time integration schemes can be additionally improved by the application of adaptive time stepping. Time step adaptability is particularly effective when flow conditions change within a time interval, as it allows the time step to be selected to correctly capture the underlying flow physics. Furthermore, the automatic adjustment of a suitable time step size enables to save computing time also for problems where the required step size is unknown in advance, since it is not necessary to perform several test simulations.

There are different approaches to control the adaptive step sizes, which are mostly based on the evaluation of a local error to determine the next time step size. A rather flexible variant is e.g. the fully implicit Richardson's extrapolation, which is applicable for quasi every one-step time discretization method. Thereby the numerical error is calculated by executing the calculation once in each time step with the step size $\Delta t$ and e.g. $\Delta t/2$. This is relatively straightforward to implement, but leads to a large increase in computational effort. Another option with less added computational cost is to use an explicit step to evaluate the local error in each implicitly computed time step. For instance, the application of Runge-Kutta schemes comes with the advantage of a simple implementation of such explicit-implicit time adaptivity. Using so-called embedded Runge-Kutta methods enables a straightforward local error estimation for step-size control.

Adaptive time stepping methods have been applied and studied in various fields for years. A small number of contributions in the field of dynamic structural mechanics include, for example, UNDERWOOD AND PARK [401], ZIENKIEWICZ AND XIE [432], DIEBELS ET AL. [127], SCHLEUPEN AND RAMM [339], or for more recent works, ROTHE ET AL. [331], RANG [319], LAI AND HUANG [250], GRAFENHORST ET AL. [171], GILBERT ET AL. [170]. Similarly, for problems in fluid dynamics, there are numerous researches on adaptive time stepping, for instance, in JOHNSON ET AL. [225], TUREK [395], GRESHO ET AL. [172], KAY ET AL. [226], JOHN AND RANG [222], COLOMÉS AND BADIA [107] and DEPARIS ET AL. [123]. Also in the field of coupled FSI problems, there have been studies in the last decades on the application of adaptive time stepping techniques, such as of WALL [408], DE SAMPAIO ET AL. [116], BIRKEN ET AL. [43], HAY ET AL. [180], MAYR [277], MAYR ET AL. [279] and FAILER AND WICK [142], to name a few.

The basic components of time adaptivity methods are on the one hand the estimation of a local error estimate and on the other hand the choice of the step size controller. For error evaluation, a classification can be made into a priori and a posteriori error estimators, depending on whether the problem needs to be solved first for evaluation or not. Within this thesis, only a posteriori error estimation is applied. For the selection of the time step sizes several approaches exist, which are generally based either on standard step-size control algorithms or on proportional integral (PI) controller. The latter are presented e.g. by GUSTAFSSON ET AL. [175], GUSTAFSSON [174] and SÖDERLIND [366]. The authors state that standard step-size control, which is based on the assumption that a local error $r$ always depends asymptotically on the step size $\Delta t$ as $r \sim \Delta t^{p+1}$ with the order $p$ of the method, may lead to step size oscillations. Therefore, the PI controller is proposed, in which not only the actual error but additionally its development is considered, to obtain a smoother step size development.

In the following section, the local error estimation based on embedded Runge-Kutta schemes, and the applied procedure to adapt the time step size using this error measure, is presented. For detailed information on estimation of numerical errors and implementation of automatic step size control, reference is made to textbooks HAIRER AND WANNER [177], HAIRER ET AL. [179], BUTCHER [77].

### 7.6.1 Error estimation based on embedded Runge-Kutta schemes

For the error estimation in this thesis embedded Runge-Kutta schemes are employed. Therein, the solution is first approximated based on a SDIRK of order $p$, and then, a second SDIRK method of order $q = p - 1$ with the same coefficients $\alpha_{jl}$ and $\gamma_j$ is used to assess the local error. This is done by exploiting the difference between the high- and low-order solutions, i. e. according to (7.40) with

$$\delta_{n+1} \approx \phi^{n+1} - \hat{\phi}^{n+1} = \Delta t \sum_{j=1}^{s} (\beta_j - \hat{\beta}_j) k_j \ . \tag{7.70}$$

Here, $\phi^{n+1}$ is the approximated solution with the method of order $p$, and $\hat{\phi}^{n+1}$ is the lower order solution evaluated based on existing stage results $k_j$, as

$$\phi^{n+1} = \phi^n + \Delta t \sum_{j=1}^{s} \beta_j k_j \qquad \text{and} \qquad \hat{\phi}^{n+1} = \phi^n + \Delta t \sum_{j=1}^{s} \hat{\beta}_j k_j \ , \tag{7.71}$$

with coefficients $\beta_j$ and $\hat{\beta}_j$ as given in the Butcher tableaus. In case of the presented mixed LS stress-velocity formulations for solid and fluid dynamics, the local error estimator can be evaluated in both domains based on the velocities or in the solid domain also based on the displacements, following

$$\boldsymbol{\delta}_v^{n+1} \approx \boldsymbol{v}^{n+1} - \hat{\boldsymbol{v}}^{n+1} = \Delta t \sum_{j=1}^{s} (\beta_j - \hat{\beta}_j)\, \boldsymbol{a}_j \tag{7.72a}$$

$$\text{or} \qquad \boldsymbol{\delta}_u^{n+1} \approx \boldsymbol{u}^{n+1} - \hat{\boldsymbol{u}}^{n+1} = \Delta t \sum_{j=1}^{s} (\beta_j - \hat{\beta}_j)\, \boldsymbol{v}_j \ . \tag{7.72b}$$

According to Hairer and Wanner [177], Hairer et al. [179], the aim of the procedure is, that the differences in all components of the quantity of interest, denoted by $v^i$, remain below a prescribed tolerance, such that, e.g. for the velocities

$$|v_{n+1}^i - \hat{v}_{n+1}^i| \leq tol^i \qquad \text{with} \qquad tol^i = \epsilon_a + \max(|v_n^i|, |v_{n+1}^i|) \cdot \epsilon_r \ . \tag{7.73}$$

Herein, the total tolerance is composed of an absolute tolerance $\epsilon_a$ and a relative part with $\epsilon_r$. Therefore, the total error estimates for velocities and displacements can be defined as

$$e_v = \sqrt{\frac{1}{n_v} \sum_{i=1}^{n_v} \left( \frac{v_{n+1}^i - \hat{v}_{n+1}^i}{tol^i} \right)^2} \qquad \text{or} \qquad e_d = \sqrt{\frac{1}{n_d} \sum_{i=1}^{n_d} \left( \frac{u_{n+1}^i - \hat{u}_{n+1}^i}{tol^i} \right)^2} \ , \tag{7.74}$$

with $n_v$ and $n_d$ denoting the degrees of freedom of the considered quantity. Note, that in case of error estimates based on different quantities, the tolerances can be chosen differently for each individual quantity and the resulting error estimate is determined in each time step as $e_r = \max[e_v, e_d]$.

### 7.6.2 Automatic step-size control

The evaluated local error estimate can be used in a next step to adapt the time step size such that the error does not exceed a user-given tolerance. Based on a standard control algorithm the size of the next time step can be computed, following e.g Hairer et al. [179], as

$$\Delta t_{new} = \Delta t_n \cdot \begin{cases} \max\left[ f_{\min}, f_{\text{save}} \cdot {e_r}^{-1/(q+1)} \right] & \text{if } e_r > 1 \\ \min\left[ f_{\max}, f_{\text{save}} \cdot {e_r}^{-1/(q+1)} \right] & \text{if } e_r \leq 1 \end{cases} . \tag{7.75}$$

Several factors are used to limit the variation of the time step size. For example, $f_{\min}$ and $f_{\max}$ define the lower and upper limits up to which the new time step may deviate from the previous one. Typical ranges for these parameters are $f_{\min} \in [0.4, 0.5]$ and $f_{\max} \in$

$[1.5, 5]$. Following Shampine and Watts [358], the maximum limiting factor can be set to $f_{\max} = 1$ after each step rejection, thus reducing the risk that the next step will also have to be repeated, when the step size is increased. Furthermore, an additional factor $f_{\text{save}}$ is used to ensure that always a value tending to be smaller than allowed by the error estimator is chosen. This can reduce the probability of a step rejection, which is performed whenever $e_r > 1$. The factor $f_{\text{save}}$ can be set as a fixed value, commonly within a range of $[0.8, 1)$, or it can depend on the number of Newton iterations, as suggested in Hairer and Wanner [177], so that

$$f_{\text{save}} = 0.9 \frac{2k_{\max} + 1}{2k_{\max} + k_n} \tag{7.76}$$

with the required Newton iterations in the actual time step $k_n$ and the maximum number of iterations $k_{\max}$. An upcoming problem in complex nonlinear simulations is, that the Newton scheme does not converge at some point of the computation. In this case, the last time step must be repeated, but the step size can not be determined based on an error estimate using the actual solution. In the context of this thesis, the time step size is decreased heuristically by $\Delta t_{new} = \kappa \Delta t$ with the choice of $\kappa \in [0.7, 0.95]$. Another way to reduce fluctuations in the step size and especially to avoid rejections of computed solutions is to include the size of previous time steps when increasing the step size, see Mayr [277] for instance. Thereby, the next time step can be averaged from the determined time step size based on the error estimate and a given number of previous time steps, which then reads

$$\Delta \bar{t}_{new} = \min \left[ \Delta t_{new},\ \theta\, \Delta t_{new} + (1-\theta) \frac{1}{N} \sum_{i=0}^{N} \Delta t_{n-i} \right] . \tag{7.77}$$

The number of considered past time steps can be modified by selecting $N$ and the weighting $\theta$ controls the influence.

If the automatic time step size control is based on a PI controller, the new time increment can be calculated according to Hairer and Wanner [177] as

$$\Delta t_{new} = f_{\text{save}} \left( \frac{1}{e_r^{n+1}} \right)^{1/p} \left( \frac{e_r^n}{e_r^{n+1}} \right)^{1/p} \frac{\Delta t_n^2}{\Delta t_{n-1}} , \tag{7.78}$$

with $e_r$ and $f_{\text{save}}$ being again any error estimate and a safety factor and the indices $n$ and $n+1$ denoting quantities of the actual and last time step.

The algorithmic procedure described above can be represented by the diagram in Figure 7.19. At the beginning of each time step all stages of the applied Runge-Kutta scheme are calculated. If in one of the stages the Newton method does not converge with the selected $\Delta t$, the time step is immediately repeated with a step size reduced by a heuristically determined factor. If all stages have been successfully solved, the local error estimate is computed, which in this case is performed using the embedded RK methods. If the value is greater than one, the result is rejected and the step is repeated. For this purpose, the new step size is determined based on the error estimator. If the value is less than one, the new step size is calculated based on the error estimator. However, there is the special case that $\Delta t$ is not increased if the last time step had to be repeated because of a step rejection or divergence in the Newton method. If the maximum time of the interval has not yet been reached, all quantities are updated next and the procedure repeats with a new time step.

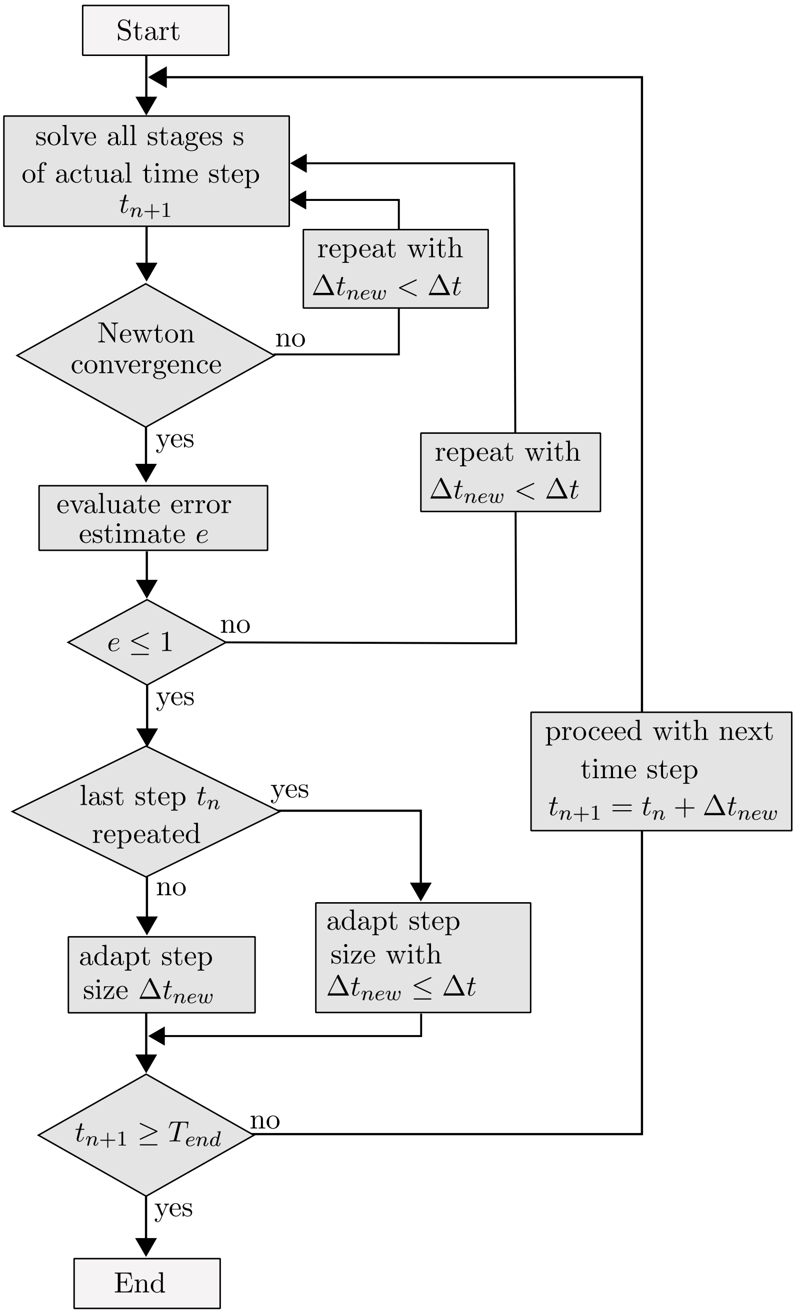

Figure 7.19: Algorithm for adaptive time stepping

## 7.7 Numerical examples: Time adaptivity for fluid and solid dynamics

The main objective of this section is to implement adaptive time-stepping control for solving unsteady flow problems and dynamic structure problems. Here, the two basic components are considered, the determination of the local error estimator and the time-stepping control. Furthermore, the impact of an adaptive time step control on the accuracy of the results and the efficiency of the simulations is investigated. For the application of time adaptivity in combination with the fluid formulation, a channel flow around a cylinder with time-dependent inflow is studied, and an oscillating cantilever beam is simulated using the solid formulation.

### 7.7.1 Flow around a cylinder with time dependent inflow

To test the application of adaptive time stepping when solving transient flow of Newtonian fluids, the benchmark problem flow around a cylinder (FAC3) in 2D with time-dependent inflow boundary conditions from Schäfer et al. [338] is used. The mixed LS stress-velocity formulation given in (4.17), with physical weighting factors $\omega_{f1} = \sqrt{\Delta t/\rho_f}$, $\omega_{f2} = 1/\sqrt{\rho_f \nu_f}$ and $\omega_{f3} = 1$ is applied. The geometry is identical to the one in Section 7.4.2. But in this case the parabolic inflow profile is applied time-dependent using a sinusoidal function as

$$\boldsymbol{v}(x_2,t) = \left( \frac{4x_2(0.41 - x_2)}{0.41^2} v_{in}(t), 0 \right)^T \qquad \text{with} \qquad v_{in}(t) = 1.5 \sin(\pi t/8) \ . \tag{7.79}$$

This leads to a Reynolds number varying in time between $0 \leq Re \leq 100$. The remaining boundary conditions are prescribed as in Section 7.4.2, with no-slip boundaries at the top and bottom wall, and stress boundary conditions at the outflow with $\boldsymbol{\sigma}_1 \cdot \boldsymbol{n} = 0$.

The computations are performed for a time range $t = [0, 8]$ s, which corresponds to half a period of the given sinusoidal function. The distribution of the velocity field at different instants is illustrated in Figure 7.20. At the beginning, the streamlines are straight and, after some time, vortices develop behind the circular cutout, since this is positioned slightly asymmetrically in the channel. At the end of the considered time interval, the inflow is again at zero which leads to a very irregular distribution of the velocity field.

The domain is discretized in space using 2432 triangular elements of order $RT_3P_4$ leading to $127,744$ degrees of freedom. For a quantitative comparison of different time integrations and adaptive time step controls, the drag and lift coefficients as defined in Eq.(7.57) are evaluated. In order to evaluate the accuracy, a solution with the fourth-order SDIRK-4(3) and a fixed time step size $\Delta t = 0.002$ s was generated, and the computed drag and lift coefficients are compared to these reference values. More precisely, the maximum values and their positions in time are compared, and then the errors are calculated using the relative Euclidean norm, which exemplarily for the lift coefficient is given by

$$e_L = \sqrt{ \left( \frac{t^{ref}_{L,\max} - t_{L,\max}}{t^{ref}_{L,\max}} \right)^2 + \left( \frac{c^{ref}_{L,\max} - c_{L,\max}}{c^{ref}_{L,\max}} \right)^2 } \ . \tag{7.80}$$

Therein, the reference values for the coefficients and the corresponding times obtained with the high-order RK read

$$(t^{ref}_{D,\max}, c^{ref}_{D,\max}) = (3.936,\ 2.927) \qquad \text{and} \qquad (t^{ref}_{L,\max}, c^{ref}_{L,\max}) = (5.690,\ 0.477) \ . \tag{7.81}$$

These values lie well within the bounds of the reference values given in Schäfer et al. [338]. A similar approach to evaluate the accuracy of adaptive time stepping schemes was also applied in, e.g., John and Rang [222]. For the discretization in time, three embedded RK schemes of second, third and fourth order, denoted as SDIRK-2(1), ESDIRK-3(2) and SDIRK-4(3), are applied. The order of the embedded schemes used to evaluate the error estimate is one order lower in all of them, i.e. $q = p - 1$. The Butcher tableaus are given in Appendix C.1. For the adaptive time stepping, the local error estimate for the velocities based on (7.74) is evaluated for different choices of the absolute and relative error tolerances $\epsilon_a$ and $\epsilon_r$. The bounding factors to stabilize the time step control are selected as $f_{\min} = 0.5$, $f_{\max} = 1.5$ and $k_{\max} = 10$, with the maximum factor set to $f_{\max} = 1$ after each step rejection or in case of a failed Newton iteration. Furthermore, the absolute size of each time step is limited to $10^{-4} \leq \Delta t \leq 0.1\,\text{s}$.

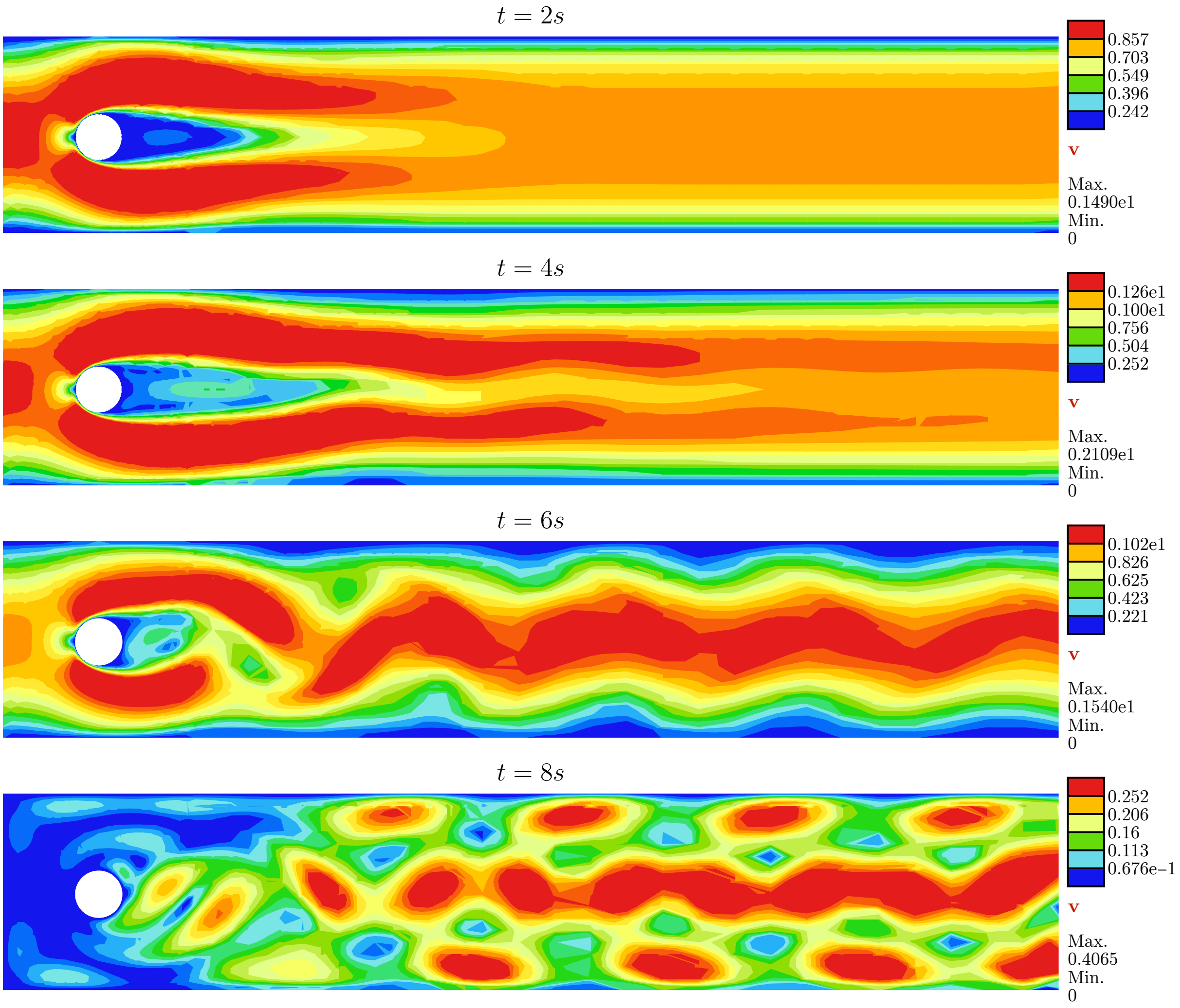

Figure 7.20: FAC3 - distribution of velocity field at different time steps $t = \{2, 4, 6, 8\}\,\text{s}$ with SDIRK-4(3) and adaptive time stepping with $\epsilon_a = 10^{-4}$

**First study:** varying $\epsilon_a$ and $\epsilon_r = 0$

In a first investigation, the relative error tolerance is set to zero, i.e. $\epsilon_r = 0$, to limit the variation possibilities, and analyze the general time step control mechanism. In Figure 7.21 the evolution of the drag and lift coefficient over time is plotted for different tolerances and compared to reference values. At this point only results obtained with SDIRK-2(1) are presented, because all methods show basically the same behavior depending on the size of the selected absolute tolerance. When considering the drag coefficient, Figure 7.21 (left), the results for all considered adaptive algorithms agree with the reference solution obtained with a fixed time step. This holds when regarding the entire time interval (top) as well as when closely zooming in. However, regarding the lift coefficient, one can already see differences for the various absolute tolerances when looking at the entire time interval. The larger the error tolerance is, the lower is the overall value of $c_L$ and furthermore the oscillations start delayed. In the close-up, one can still see differences in the result even between the two smallest tolerances taken into account. The reason for the poor performance is presumably that the typical vortices in the flow field do not develop in the first place if the time steps are too large. If the absolute tolerances are too large and the automatic time step control does not react sensitively enough to small changes in the velocity field, the vortices that actually arise are also reduced.

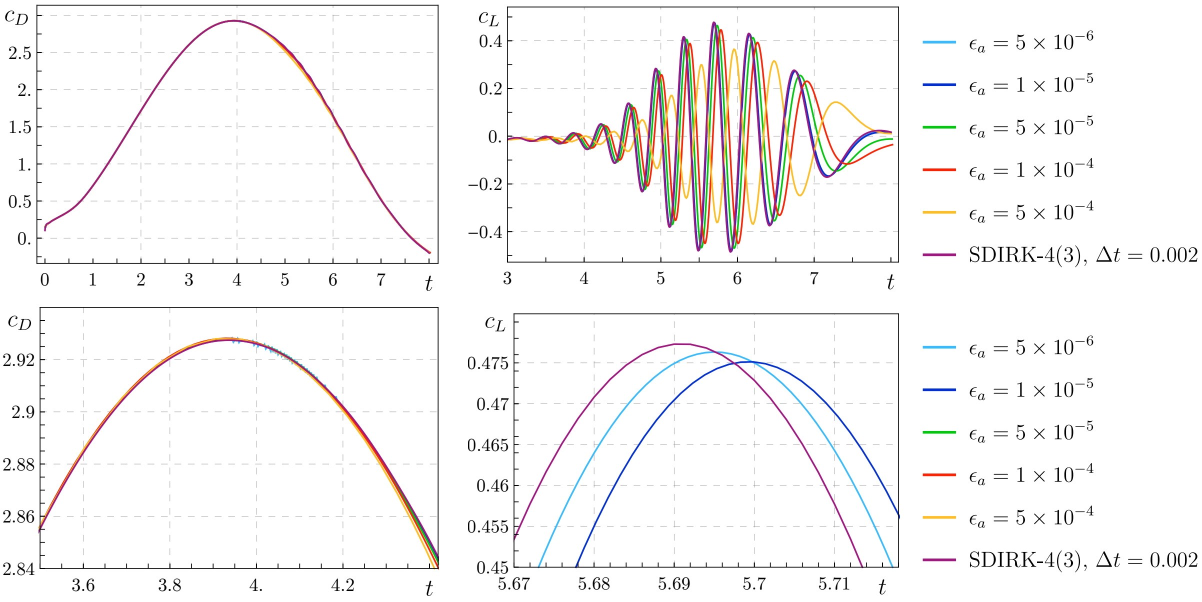

Figure 7.21: FAC3 - evolution of drag (left) and lift (right) coefficient for different tolerances $\epsilon_a$ and SDIRK-2(1)

The change of the time increment over time with the adaptive stepping control can be seen in Figure 7.22. It is visible that from the initial value $\Delta t = 0.1\,\mathrm{s}$ the step size initially increases for all variants and then starts to decrease again after a certain time. During the interval with the largest fluctuations, the minimum step size drops to a value of $\Delta t = 8.96 \times 10^{-4}\,\mathrm{s}$ for the method SDIRK-2(1). The poor approximation of the lift coefficient occurs when the time step size is lowered too late. Thereby it is not absolutely necessary that the step size is so extremely small during the period of the largest vortices. A further reduction of the absolute tolerance $\epsilon_a$ would lead to an overall reduction of the step size, so that in the range $t = [4.5, 7]\,\mathrm{s}$ such small increments are chosen that the overall computational effort becomes very large.

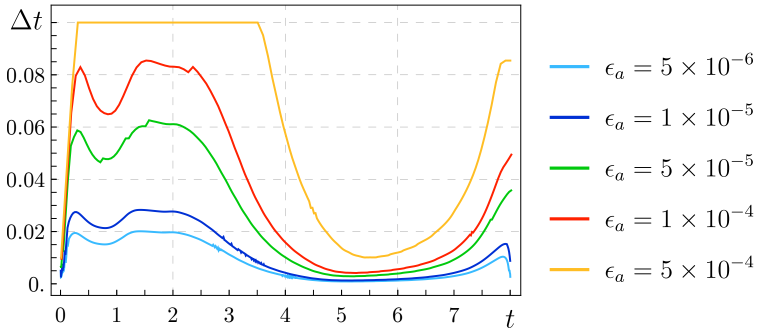

Figure 7.22: FAC3 - evolution of time step size for different tolerances $\epsilon_a$ and SDIRK-2(1)

In order to evaluate the efficiency, the computation time is measured. Therefore, all computations were preformed with the software package *AceFEM* (version 7.203), see Korelc [240; 241], Korelc and Wriggers [243] of *Mathematica* (version 12.1.1.0), see Wolfram Research Inc. [422]. The equation system is solved using the PARDISO solver (from INTEL MKL), and the simulations are executed using six cores on an Intel(R) Xeon(R) (CPU E5-2683 v4 @ 2.10GHz). It should be noted that the measured calculation time is only a rough guide, since the measurement is only based on one evaluation in each case.

For the comparison of the different methods and parameter choices, the error in the lift coefficient is evaluated as defined in (7.80) and plotted over the computation time. The error in the drag coefficient was not considered here, because the change in time step size had no noticeable effect on it. Additionally to the results with automatic time stepping for the three considered discretization methods, the problem is solved using the SDIRK-2(1) time discretization with fixed time increments $\Delta t = 0.02, 0.01, 0.005\,\text{s}$. Note that the simulations with fixed time step sizes from $\Delta t \geq 0.04\,\text{s}$ aborted for all time discretizations as soon as the flow becomes unsteady (at around $t \approx 4.2\,\text{s}$), since the Newton scheme did not converge any more. Figure 7.23 illustrates the error $e_L$ over the CPU time. Despite the adaptive time stepping, the efficiency of the considered computations is quite low compared to simulations with fixed time step sizes. This can be due to the fact that, as already mentioned, on the one hand the step size between $4.5 \leq t \leq 7$ was probably adapted smaller than necessary, which leads to an increase of the computing time. And on the other hand the error is rather large, since the time step sizes decrease late and thus too small vortices arise. Nevertheless, the highest order time integration SDIRK-4(3) is the most efficient, also for this choice of parameters for the adaptive time stepping. But at a certain point the error does not decrease further, which is probably due to the fact, that from this point on, the spatial discretization error dominates the temporal one.

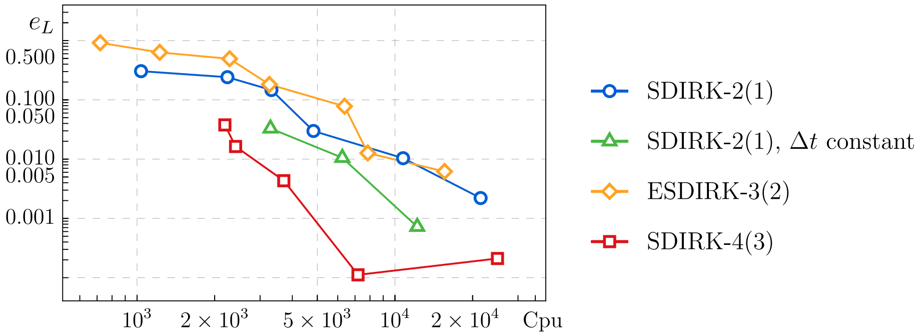

Figure 7.23: FAC3 - error $e_L$ in lift coefficient over CPU time for adaptive time stepping with different tolerances $\epsilon_a$ and constant step sizes using SDIRK-2(1)

**Second study:** different values for $\epsilon_a$ and $\epsilon_r$
Due to the finding that the efficiency of the integration methods cannot be fully exploited if only the absolute tolerance is allowed to change, the influence of varying both tolerances is also investigated in the following. Figures 7.24, 7.25 and 7.26 illustrate the evolution of the time step size and lift coefficient compared to the reference solution for the considered embedded Runge-Kutta schemes SDIRK-2(1), ESDIRK-3(2) and SDIRK-4(3). The presented results are all based on different choices for the absolute and relativ tolerance, which are required to calculate the error estimate for the automatic step control. It can

be seen, that the second- and third-order scheme require lower absolute tolerances to even roughly obtain the correct evolution of the lift coefficient. For SDIRK-2(1) the presented choice of parameters leads to smaller time step sizes, than for the time discretization ESDIRK-3(2). Thus, smaller tolerances must be set for the third-order method to obtain the same accuracy. The fourth-order SDIRK-4(3) delivers accurate results even with larger tolerances and time steps.

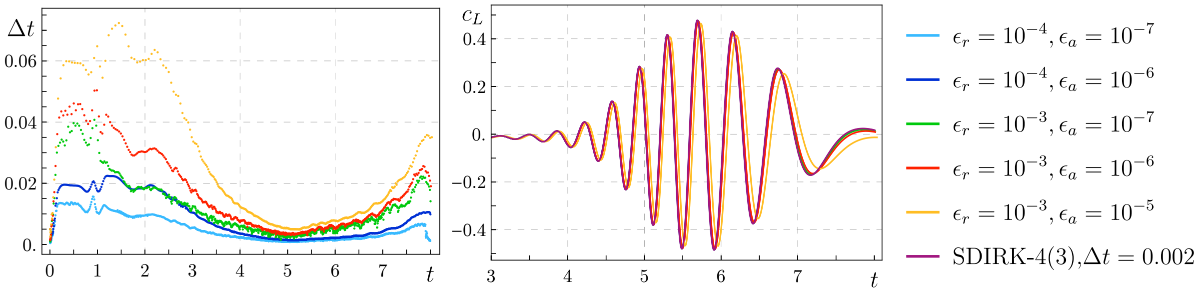

Figure 7.24: FAC3 - evolution of time step size (left) and lift coefficient (right) over time using SDIRK-2(1) with different tolerance parameters $\epsilon_r$ and $\epsilon_a$

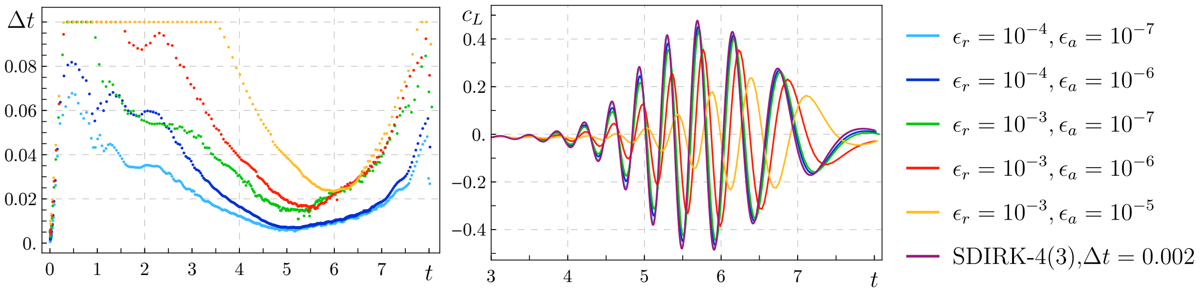

Figure 7.25: FAC3 - evolution of time step size (left) and lift coefficient (right) over time using ESDIRK-3(2) with different tolerance parameters $\epsilon_r$ and $\epsilon_a$

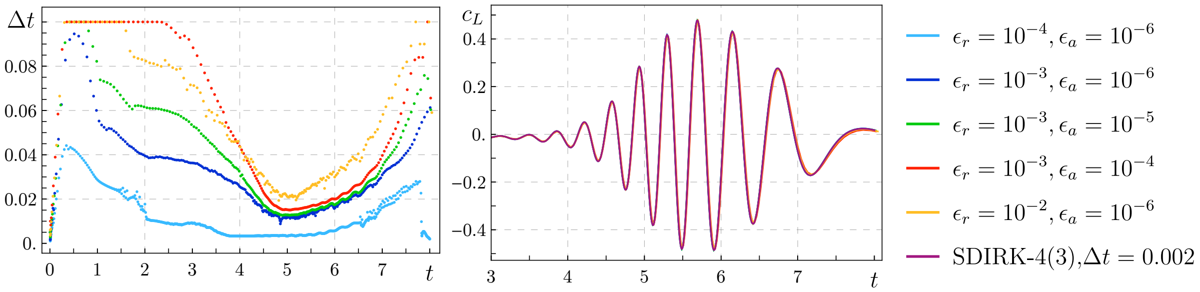

Figure 7.26: FAC3 - evolution of time step size (left) and lift coefficient (right) over time using SDIRK-4(3) with different tolerance parameters $\epsilon_r$ and $\epsilon_a$

For a rough evaluation of the efficiency, the error in the lift coefficient as given in (7.80) is again plotted over the computation time, see Figure 7.27. Compared to the results obtained with $\epsilon_r = 0$ in Figure 7.23, it can be seen that adaptive time stepping when both tolerance parameters are used can lead to a slight improvement in efficiency compared to the fixed step size calculations. In addition, the error in the lift coefficient seems to decrease only up to a certain value until a plateau is reached. This is probably due to the fact that from there on the spatial error dominates.

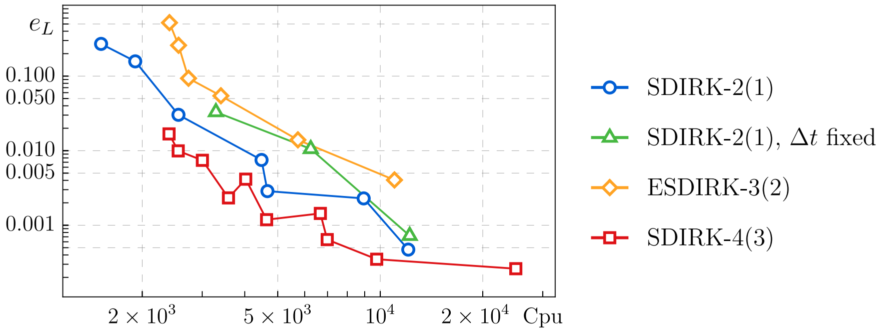

Figure 7.27: FAC3 - error $e_L$ in lift coefficient over CPU time for adaptive time stepping with different absolute and relativ tolerances and constant step sizes using SDIRK-2(1)

Overall, it can be concluded that the mechanism of automatic adjustment of the time step size works as long as some constraints are imposed. Especially in the field of fluid dynamics, it is often necessary to define an upper limit for the time step size to ensure that certain flow patterns develop at all and are not "skipped" by too coarse time steps. A possibility to take more account of the generation of vortices in the adaptive control would be e.g. to calculate the error estimator separately for the individual velocity components and to select a smaller tolerance for the vertical velocity. Furthermore, it is crucial for the efficiency of the algorithms to make the right choices. This concerns on the one hand the evaluation of the error estimator and the tolerances required therefore. And on the other hand the automatic time step control and the included safety factors. This gives the impression that the entire procedure is perhaps not quite so "automatic" after all.

### 7.7.2 Vibration of a linear elastic cantilever beam

In order to investigate the application of adaptive time stepping in combination with mixed LSFEM for solid dynamics, the stress-velocity formulation for linear-elasticity, see (6.4), is applied to solve the vibration of a dynamic cantilever beam (DCB) as also studied in SCHWARZ ET AL. [351]. The physical weights are chosen as $\omega_{s1} = \sqrt{\Delta t / \rho_s}$ and $\omega_{s2} = 1/\sqrt{\Delta t}$. The geometric dimensions of the considered domain $\Omega_s = (0, 10) \times (0, 1)\,\mathrm{m}$ and the boundary conditions are outlined in Figure 7.28.

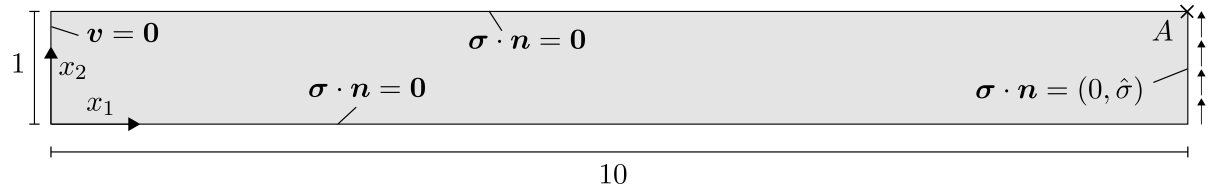

Figure 7.28: DCB - geometry and boundary conditions (unit m)

The structure is clamped at the left end, i.e. $\boldsymbol{v} = \boldsymbol{0}$, and the upper and lower edge are stress-free boundaries, i.e. $\boldsymbol{\sigma} \cdot \boldsymbol{n} = \boldsymbol{0}$. On the right edge a time-dependent shear stress is applied, which is increased linearly up to $\hat{\sigma} = 0.4\,\mathrm{kN/m^2}$ at $t = 0.5\,\mathrm{s}$ and then removed within 0.1 s. The chosen material parameters are $E = 10^4\,\mathrm{kN/m^2}$, $\nu = 0.499$ and $\rho_s = 1.2 \times 10^3\,\mathrm{kg/m^3}$. For the spatial discretization vector-valued Raviart-Thomas functions are implemented for the stresses and Lagrange polynomials are used for the velocities. In order to minimize the error based on the space discretization, the element $RT_3P_4$ based on relatively high order interpolation functions is implemented and the domain is subdivided into 1280 elements. For the discretization in time the embedded second- and fourth-order RK schemes namely SDIRK-2(1) and SDIRK-4(3) are applied. The required Butcher tableaus are given in Appendix C.1. In this section, when applying automatic time step control, in all calculations the method of averaging, see (7.77), is applied. This slightly reduces the increase of step sizes in case of strong fluctuations. Here the new $\Delta t$ is calculated based on the mean value of $N = 5$ previous time step sizes and the newly determined size, choosing $\theta = 0.5$ for the proportions. Furthermore, two different approaches are examined in which the calculation of the error estimator is based on either the velocities or the displacements, see (7.74). A combination of both error estimators with different tolerances for the considered quantities is also possible, but is not investigated here.

**Study 1)** Convergence study with constant time step size
In a first step, the temporal convergence of both methods with constant time step sizes is investigated. In order to compare the different solutions, the displacement in $x_2$-direction at the right top corner at point $A(10,0)\,\mathrm{m}$ is measured over time. The results of the displacements $u_2$ at point $A$ are shown in Figures 7.29 and 7.30 for the considered time interval of $T = [0,10]\,\mathrm{s}$ on the left side and a closer detail on the right side. Zooming in, it can be seen that for the second-order SDIRK-2(1) method, no differences in the course of the displacement are visible from a time increment of $\Delta t \leq 0.01\,\mathrm{s}$. When using the fourth-order method SDIRK-4(3) the calculation is convergent already at $\Delta t \leq 0.02\,\mathrm{s}$.

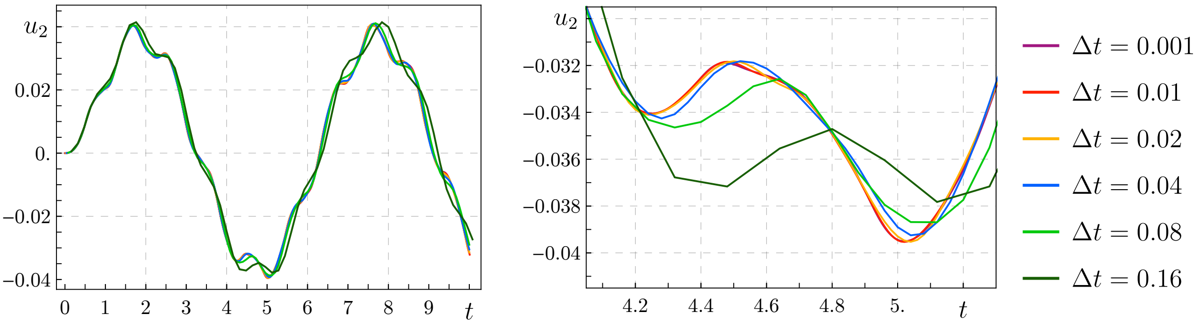

Figure 7.29: DCB - vertical displacement $u_2$ at $A(10,1)\,\mathrm{m}$ over time for SDIRK-2(1) with different constant time step sizes $\Delta t$

In order to assess and compare the accuracy of the various time integration and adaptive time stepping methods in the remainder of this section, the displacement in the $x_2$-direction at point $A(10,0)\,\mathrm{m}$ is measured over time in all simulations and compared to a reference solution. For this purpose, the solution with the SDIRK-4(3) scheme and constant step size $\Delta t = 0.002\,\mathrm{s}$ is applied as reference.

**Study 2)** Influence of limiting factors $f_{\min}$ and $f_{\max}$
In the following the effect of the control factors for adaptive time stepping on efficiency

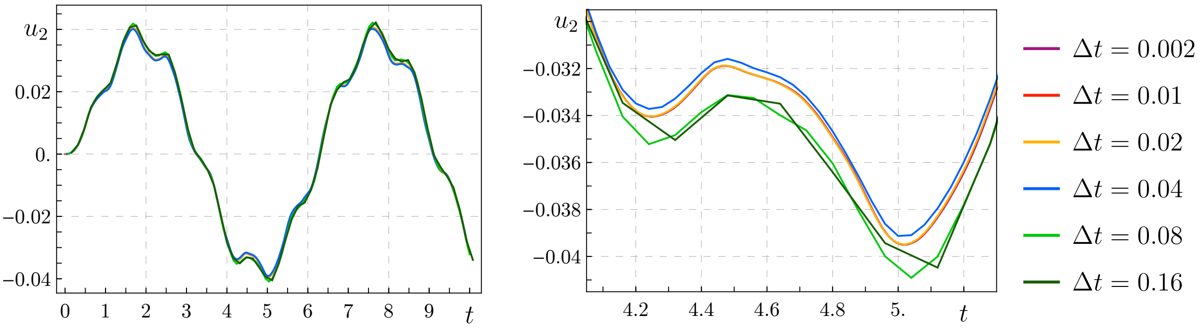

Figure 7.30: DCB - vertical displacement $u_2$ at $A(10, 1)$ m over time for SDIRK-4(3) with different constant time step sizes $\Delta t$

and accuracy is examined. Therefore, the SDIRK-2(1) method is used for time discretization and the error estimate for the automatic time stepping is evaluated based on the displacements, as defined in $(7.74)_2$. The absolute and relative tolerances for the error estimator are chosen once as $10^{-5}$ and once as $10^{-6}$.

The total number of time steps and iterations in the defined time interval and the number of step rejections are taken into account as comparison values for the efficiency. The accuracy is compared by evaluating the error of the vertical displacement relative to the reference solution as

$$err_u = \sqrt{\frac{\sum_{i=1}^{N} \left[u_2(t_i) - u_2^{ref}(t_i)\right]^2}{N}} \,. \tag{7.82}$$

Therein, $u_2^{ref}$ denotes the reference values obtained with SDIRK-4(3) and $\Delta t = 0.002\,$s, and $N$ is the number of required time steps within the regarded interval $T = [0, 10]\,$s. Table 7.10 summarizes simulation data, such as number of time steps, rejections and iterations, the average time step size and the error $err_u$ compared to the reference solution. The less restrictive the limiting factors are, the more often steps are rejected and have to be repeated. This can lead to an increase in the computational cost, which in turn may be compensated by the fact that the average accepted step size may be larger with more flexibel step size changes. The influence of the factors $f_{\min}$ and $f_{\max}$ diminishes automatically when the step size is limited by smaller error tolerances.

Table 7.10: DCB - number of accepted time steps, rejections and iterations, average time step size $\overline{\Delta t}$, and error in $u_2$ for different factors $f_{\min}$ and $f_{\max}$ and tolerances with SDIRK-2(1)

| $\epsilon_r^d = \epsilon_a^d$ | $f_{\max}$ | $f_{\min}$ | time steps | rejection | iteration | $\overline{\Delta t}$ | $err_u$ |
|---|---|---|---|---|---|---|---|
| $10^{-5}$ | 1.2 | 0.8 | 177 | 12 | 1120 | 5.67e-2 | 6.266e-4 |
| | 1.5 | 0.5 | 167 | 22 | 1127 | 6.02e-2 | 6.984e-4 |
| | 2.0 | 0.3 | 163 | 25 | 1124 | 6.16e-2 | 6.781e-4 |
| $10^{-6}$ | 1.2 | 0.8 | 542 | 2 | 3059 | 1.85e-2 | 1.537e-4 |
| | 1.5 | 0.5 | 538 | 5 | 3061 | 1.86e-2 | 1.537e-4 |
| | 2.0 | 0.3 | 537 | 6 | 3063 | 1.86e-2 | 1.534e-4 |

**Study 3)** Step size control based on velocity error estimator $e_v$
In a next step, automatic time stepping is investigated with the error estimator evaluated based on the velocities, as defined in $(7.74)_1$. The bounding factors are selected in a way that the incremental changes are as smooth as possible, with $f_{\text{max}} = 1.2$ and $f_{\text{min}} = 0.8$. The safety factor for this linear elasticity based problem is set to $f_{\text{save}} = 0.9$, since the number of Newton iterations is irrelevant.

The problem is solved in the first case using the second-order SDIRK-2(1) scheme with different absolute and relative tolerances for the error estimator and an initial step size $\Delta t = 0.01$ s. The adaption of the time increment based on the velocity error estimator with varying tolerances can be seen in Figure 7.31(left), where results within the time interval $t = [0, 5]$s are plotted. For all tolerances the step size increases at the beginning. If the values for the absolute error acceptance are chosen large, i.e. $\epsilon_a^v \geq 10^{-4}$, the time step size remains quite large, as expected, leading to a poor accuracy. This can be seen in Figure 7.32, where the evolution of the vertical displacement is shown for the entire interval (left) and for a smaller more detailed section (right). The solution obtained with high tolerances do not match the reference solution. For smaller tolerances, the time increment decreases at around $t \approx 0.5$ s, where the load application of the stress boundary condition is changed, and maintains a similar level between $0.012 \leq \Delta t \leq 0.018$ s throughout the remaining interval. The corresponding displacements agree quite well with the reference solution.

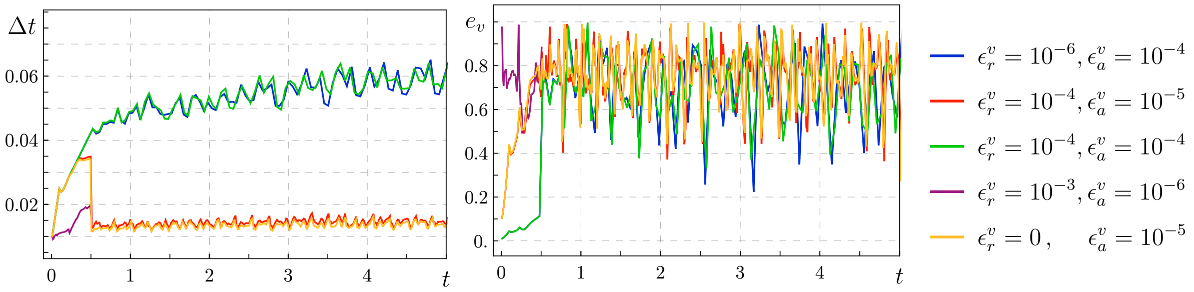

Figure 7.31: DCB - evolution of time step size $\Delta t$ (left) and error estimator $e_v$ (right) over time using SDIRK-2(1) with different tolerance parameters $\epsilon_r^v$ and $\epsilon_a^v$

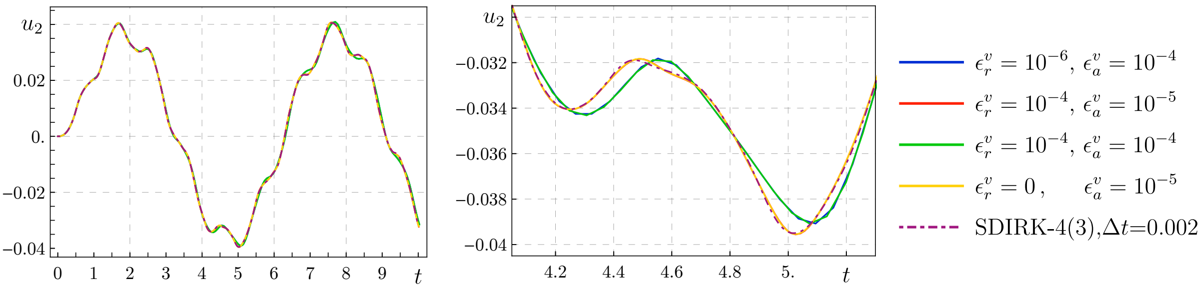

Figure 7.32: DCB - vertical displacement $u_2$ at $A(10, 1)$ m over time for SDIRK-2(1) with different tolerance parameters $\epsilon_r^v$ and $\epsilon_a^v$

For a quantitative assessment of accuracy and efficiency, all relevant data are listed in Table 7.11. As already apparent in the figures, reducing the error tolerance results in a reduction of the time step and thus also of the error. However, the variation of the relative error tolerance had little effect on the adaptive time step size adjustment. The reason is probably that the absolute error is dominant for all chosen combinations. Only the increase of the relative tolerance up to $\epsilon_r^v \geq 10^{-2}$ in combination with a small absolute tolerance $\epsilon_a^v = 10^{-5}$ affected the results by leading to larger allowable time steps. However, the absolute tolerance could not be decreased further. It is found that all calculations with an absolute tolerance $\epsilon_a^v \leq 10^{-6}$ abort at around $t \approx 0.5\,\mathrm{s}$, due to step rejections until the minimum prescribed step size $10^{-4}\,\mathrm{s}$ is reached.

Table 7.11: DCB - number of accepted time steps, rejections and iterations, average time step size $\overline{\Delta t}$, and error in $u_2$ for different tolerances $\epsilon_r^v$ and $\epsilon_a^v$ with SDIRK-2(1)

| $\epsilon_r^v$ | $\epsilon_a^v$ | time steps | rejection | iteration | $\overline{\Delta t}$ | $err_u$ |
|---|---|---|---|---|---|---|
| $10^{-4}$ | $10^{-4}$ | 180 | 25 | 1216 | 5.57e-2 | 5.839e-4 |
| $10^{-6}$ | $10^{-4}$ | 180 | 17 | 1168 | 5.57e-2 | 5.813e-4 |
| $10^{-2}$ | $10^{-5}$ | 135 | 22 | 935 | 4.11e-2 | 2.561e-4 |
| $10^{-4}$ | $10^{-5}$ | 668 | 31 | 3581 | 1.50e-2 | 1.270e-4 |
| 0 | $10^{-5}$ | 710 | 28 | 3705 | 1.41e-2 | 1.230e-4 |

Although the results with adaptive control are basically consistent with the reference solution and the accuracy can also be improved with reduction of the tolerances, see Figure 7.32, the step size changes are quite oscillatory and seem to be independent of the deformation. The same can be observed when looking at the error estimator shown in Figure 7.31 (right). Regardless of the chosen tolerances and the deformation state of the beam, the value for $e_v$ varies extremely throughout the time interval. The computations with the high-order time discretization SDIRK-4(3) yielded similar results. The automatic step size control based on the velocity error estimator is also subject to strong fluctuations there. In this case, the choice of an absolute tolerance $\epsilon_a^v < 10^{-4}$ caused the abortion of the calculation by multiple rejections of the step up to the lower limit for $\Delta t$.

**Study 4)** Step size control based on displacement error estimate $e_d$
In addition to evaluating the error estimator based on velocities, an error estimator based on displacements was also investigated for the mixed SV formulation for solid dynamics. The general procedure is the same as in the third study, in the sense that the limiting factors are chosen fixed with $f_{\min} = 0.5$ and $f_{\max} = 1.5$, the initial step size is set to $\Delta t = 0.01\,\mathrm{s}$, and the absolute and relative tolerances are varied.

The step size adjustment for different tolerance values when applying the second-order SDIRK-2(1) is illustrated in Figure 7.33(left). It can be observed, that depending on the magnitude of the tolerance, the step size first increases or directly decreases, e.g. for $\epsilon_a^d \leq 10^{-8}$. After about $t = 1\,\mathrm{s}$ the average step size stays relatively constant in the remaining interval and the fluctuations keep one level. Depending on the selected tolerances, the average size of the time increment varies considerably. This can also be seen in Table 7.12, which contains exemplary information on the simulations for the comparison. Reducing the tolerance leads to a smaller average step size and thus also to an increase in the number of calculation steps and iterations. At the same time, however, this naturally also increases the accuracy as can be seen by the smaller error.

As in the previous study, Figure 7.33 (right) shows the resulting error estimator for several adaptive calculations. The displacement based error estimator seems to vary in a slightly smaller range when using SDIRK-2(1) compared to the error estimator based on the velocities in Figure 7.31 (right). In addition, smaller step sizes, and hence errors, could be achieved in the simulations with step size control based on $e_d$, without causing the calculations with SDIRK-2(1) to abort as easily due to step rejections.

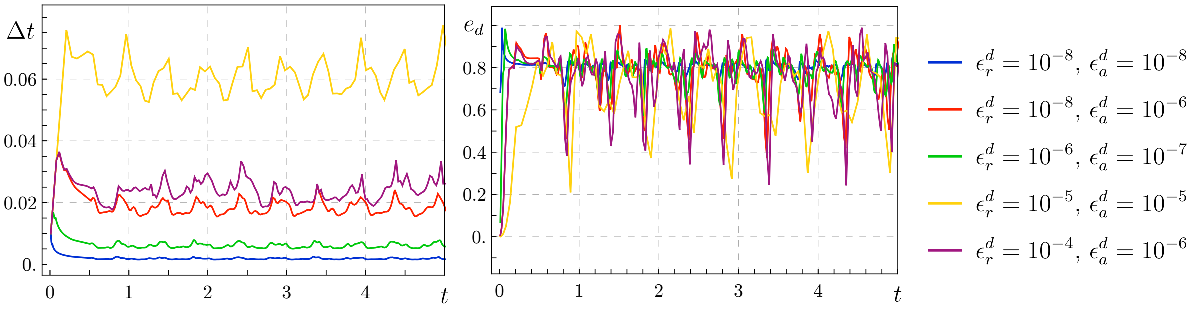

Figure 7.33: DCB - evolution of time step size $\Delta t$ (left) and error estimator $e_d$ (right) over time using SDIRK-2(1) with different tolerance parameters $\epsilon_r^d$ and $\epsilon_a^d$

Table 7.12: DCB - number of accepted time steps, rejections and iterations, average time step size $\overline{\Delta t}$, and error in $u_2$ for different tolerances $\epsilon_r^d$ and $\epsilon_a^d$ with SDIRK-2(1)

| $\epsilon_r^d$ | $\epsilon_a^d$ | time steps | rejection | iteration | $\overline{\Delta t}$ | $err_u$ |
|---|---|---|---|---|---|---|
| $10^{-5}$ | $10^{-5}$ | 167 | 22 | 1127 | 6.02e-2 | 6.984e-4 |
| $10^{-4}$ | $10^{-6}$ | 426 | 21 | 2644 | 2.35e-2 | 1.941e-4 |
| $10^{-8}$ | $10^{-8}$ | 5396 | 2 | 21952 | 1.85e-3 | 1.041e-5 |

The results using the fourth-order SDIRK-4(3) scheme for the time discretization can be found in Figure 7.34 and Table 7.13. Modification of the tolerances again shows in general the expected effect, namely that the average step size is increased or decreased depending on the accepted tolerance. Also the resulting error value becomes smaller as a consequence of tolerance reduction, but only up to a certain limit. At a choice of absolute tolerance of $\epsilon_a^d \leq 10^{-8}$ the calculation terminates due to repeated step rejection. These abortions occur depending on the choice of the relative tolerance already at $t \approx 0.5\,\mathrm{s}$ or later in the time interval. The behavior is analogous to what has already been observed for SDIRK-2(1) with adaptive step control based on the local velocity error $e_v$. When considering the error estimator $e_d$ in Figure 7.34 (right), one sees a very similar oscillating profile.

Table 7.13: DCB - number of accepted time steps, rejections and iterations, average time step size $\overline{\Delta t}$, and error in $u_2$ for different tolerances $\epsilon_r^d$ and $\epsilon_a^d$ with SDIRK-4(2)

| $\epsilon_r^d$ | $\epsilon_a^d$ | time steps | rejection | iteration | $\overline{\Delta t}$ | $err_u$ |
|---|---|---|---|---|---|---|
| $10^{-5}$ | $10^{-5}$ | 109 | 0 | 1619 | 9.20e-2 | 1.961e-4 |
| $10^{-2}$ | $10^{-7}$ | 153 | 30 | 2728 | 6.58e-2 | 2.427e-4 |
| $10^{-4}$ | $10^{-7}$ | 409 | 29 | 6549 | 2.45e-2 | 1.128e-4 |
| $10^{-9}$ | $10^{-7}$ | 512 | 5 | 7747 | 1.92e-2 | 1.229e-4 |

Remark: Both error estimators, whether based on displacements or velocities, are subject to strong fluctuations, the amount of which seems to depend on the choice or order of the time discretization. In the following, this effect will be investigated in more detail by considering the variation of the error estimator when changing the step size.

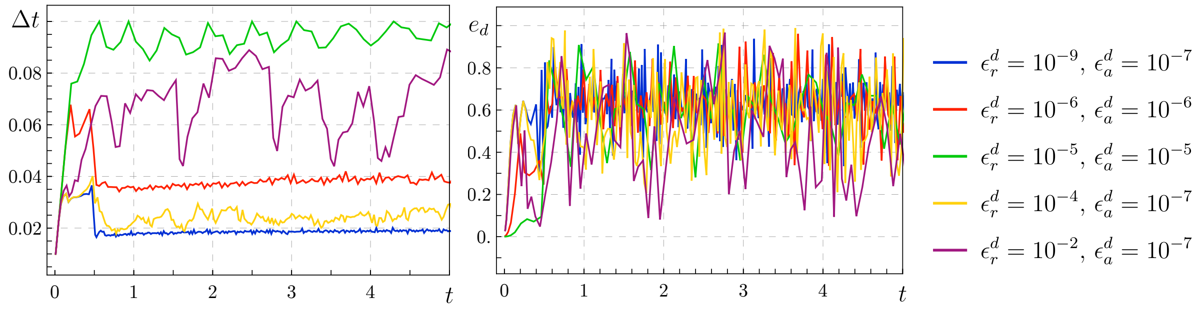

Figure 7.34: DCB - Evolution of time step size $\Delta t$ (left) and error estimator $e_d$ (right) over time using SDIRK-4(3) with different tolerance parameters $\epsilon_r^d$ and $\epsilon_a^d$

**Study 5)** Influence of step size change on error estimator
In order to investigate the origin of this behavior and the fluctuations, the evaluation of the error estimator is examined in more detail. For this purpose, the temporal development of the values for $e_v$ and $e_d$ are considered, firstly when the time step is kept constant and secondly when it is changed in a controlled manner. But the simulations are solved without adaptive time stepping in this study.

In a first step, the same spatial discretization as in the previous studies with 1280 elements is used. The absolute and relative tolerances to compute the error estimator are set depending on the time discretization to

$$\text{SDIRK-2(1)} \rightarrow \qquad \epsilon_r^v = \epsilon_a^v = 10^{-5} \qquad \text{and} \qquad \epsilon_r^d = \epsilon_a^d = 10^{-6}\ ,$$

$$\text{SDIRK-4(3)} \rightarrow \qquad \epsilon_r^v = \epsilon_a^v = 10^{-5} \qquad \text{and} \qquad \epsilon_r^d = \epsilon_a^d = 10^{-7}.$$

Figure 7.35 presents the evolution of the time step size for four different cases. First, the step size is kept constant over the entire period either with $\Delta t = 0.01\,\mathrm{s}$ or $\Delta t = 0.002\,\mathrm{s}$, and then it is decreased or increased stepwise. Arbitrary times for the change of the step size are selected here.

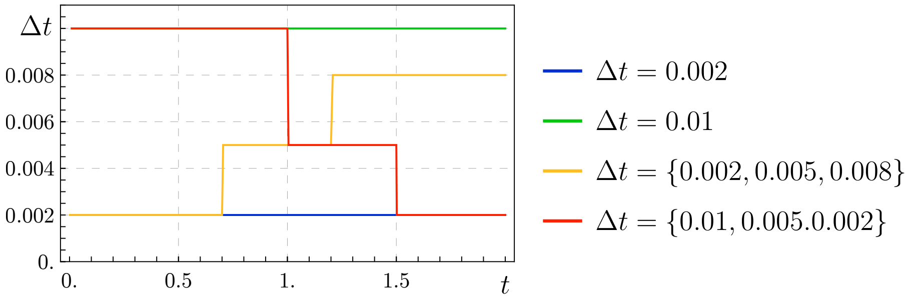

Figure 7.35: DCB - controlled change of step size $\Delta t$ at predefined times

The corresponding evolutions of the error estimators based on the velocity or displacement are illustrated for the time discretization scheme SDIRK-2(1) in Figure 7.36 and for

SDIRK-4(3) in Figure 7.37. One can recognize that the error estimators at constant step sizes (blue and green line) fluctuate slightly and take a jump at $t = 0.5\,\mathrm{s}$. But as expected, when comparing the results for $\Delta t = 0.01$ and $\Delta t = 0.002$, the overall error estimator is also lower at a smaller step size. Furthermore, apart from the jump at $t = 0.5\,\mathrm{s}$ there are no extreme peaks in the further course as long as the step size remains constant. In addition, the error magnitude with the selected tolerances for both constant step sizes is clearly less than one.

In those cases of controlled step size change, depending on whether the increment is increased or decreased, the calculation is also started with $\Delta t = 0.01$ or $\Delta t = 0.002$. Thus the error estimators at the beginning agree with one of the curves for the constant step size. When changing the step size, a clear amplitude can be recognized in the velocity error estimator $e_v$ for both time discretizations and also for the displacement error estimator $e_d$ for the fourth-order method. The peak in the curves appears regardless of whether the step size is raised or lowered. If the step size remains constant for a certain time afterwards, the values decrease again up to a level which is reasonable for the present step size. This means that with a larger step size, the error estimator is above the starting curve and vice versa. In case of such strong fluctuations adaptive step size control is difficult. It requires very large constraints on the step size control. The changes in $\Delta t$ may be only very small and possibly after each step size modification several steps need to be solved with the same increment size.

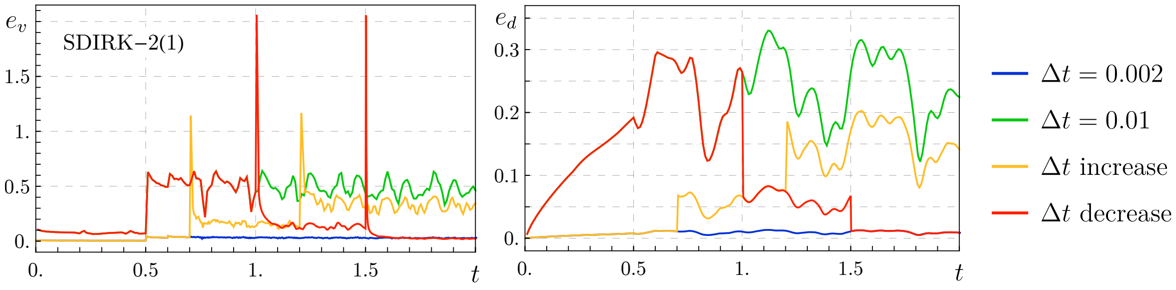

Figure 7.36: DCB - evolution of error estimator $e_v$ (left) and $e_d$ (right) using SDIRK-2(1) with constant step size and controlled step size change at predefined times

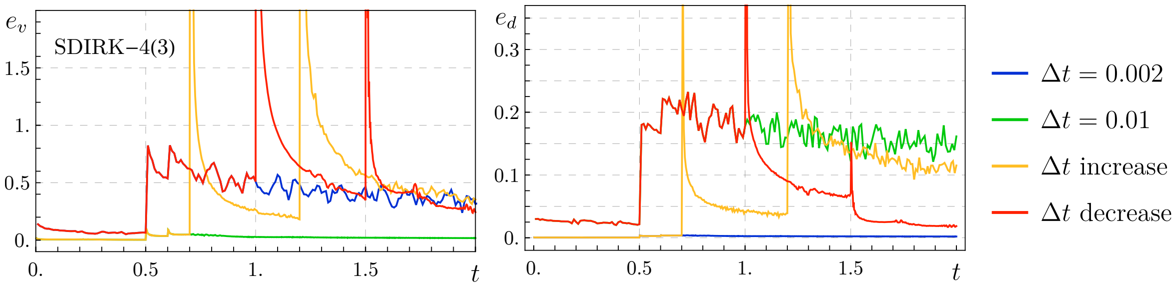

Figure 7.37: DCB - evolution of error estimator $e_v$ (left) and $e_d$ (right) using SDIRK-4(3) with constant step size and controlled step size change at predefined times

REMARK: This behavior was observed only for adaptive time stepping in combination with the mixed LS stress-velocity formulation for solid dynamics. Furthermore, the amplitudes could be reduced by improving the spatial accuracy, e.g. by increasing the number of elements or the polynomial degree. Figure 7.38 shows an example of the evolution of the error estimators when meshes with different number of elements are applied. In all cases the method SDIRK-4(3) is used and the step size is varied from $\Delta t = 0.01$ to 0.005 to 0.002 at $t = 1.0$ and $t = 1.5$. It is observed that the peaks in the error estimator when changing the time step size are smaller the finer the mesh and thus the smaller the spatial discretization error. Additionally, the maximum values of the error estimator after the first and second step size change are listed in Table 7.14. Therein a clear tendency can be noticed which shows that the values are getting smaller when the number of elements is increased. But even with 11520 elements of order $RT_3P_4$, fluctuations could not be completely avoided using this formulation, and thus the application of automatic step size control must be applied with care.

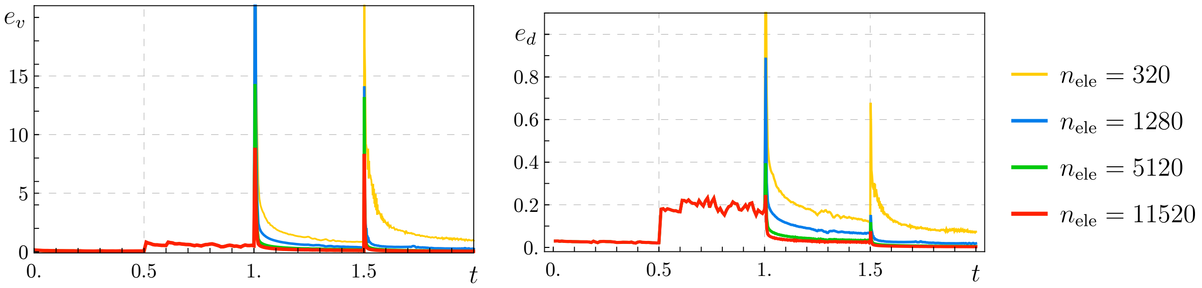

Figure 7.38: DCB - evolution of error estimator $e_v$ (left) and $e_d$ (right) using SDIRK-4(3) with controlled step size change and different meshes

Table 7.14: DCB - maximum values of error estimators after step size changes at $t_1 = 1\,\text{s}$ and $t_2 = 1.5\,\text{s}$ for meshes with different number of elements $n_{\text{ele}}$ with SDIRK-4(2)

| | | $n_{\text{ele}}$ | | | |
|---|---|---|---|---|---|
| | | 320 | 1280 | 5120 | 11520 |
| $e_v$ | $t_1$ | 60.7332 | 32.2213 | 14.3108 | 8.87911 |
| | $t_2$ | 41.7642 | 14.111 | 13.2021 | 8.3489 |
| $e_d$ | $t_1$ | 1.58485 | 0.889731 | 0.395096 | 0.245435 |
| | $t_2$ | 0.679116 | 0.152151 | 0.117975 | 0.075685 |

# 8 LSFEM for dynamic fluid-structure interaction problems

The simulation of fluid-structure interaction problems is of high interest in a wide range of fields, such as biomechanics and aerodynamics. One of the main challenging tasks herein is the fulfillment of the coupling conditions at the interface of the fluid and the solid domain. In this work, the governing equations in the fluid and solid domain are given based on LS formulations in terms of stresses and velocities. This can lead to inherently fulfilled coupling conditions when choosing appropriate interpolation functions for the unknowns. The main components for the numerical solution of dynamic fluid-structure interaction problems can be summarized, following Kayser-Herold and Matthies [230], as

- Numerical method for fluid domain
    - ○ Time discretization scheme for unsteady flows
    - ○ Consideration of moving domain, e.g. with ALE framework
- Numerical method for structure domain
    - ○ Time discretization scheme for dynamic structures
    - ○ Appropriate material formulation to account for large deformations
- Treatment of coupling conditions
- Algorithm for moving background mesh
    - ○ Mesh motion method
    - ○ Re-meshing algorithm if necessary

In this chapter, the different applied approaches for all components are explained and tested, partly separately and later on, coupled. The construction of the mixed LS formulation for dynamic FSI problems is performed step by step. Therefore, the first step is the simple coupling of the fluid and solid formulations, without ALE description and valid only for linear elastic material behavior. Thus, this first approach is only suitable for computations which are limited to small structure deformations. It serves primarily for the basic verification of the combination of both domains. It should be noted that time discretizations are straightforwardly implemented in both formulations, as these have already been tested separately for the fluid and solid formulations in previous chapters.

Subsequently, on the one hand, the least-squares SV fluid formulation in arbitrary-Lagrangian-Eulerian description is explained and, on the other hand, techniques for the computation of the background mesh motion are investigated. The different approaches to mesh deformation are first examined using an example constructed based on the FSI benchmark of Turek et al. [399] and Turek and Hron [396]. However, this is solved in a simplified way without calculating the fluid domain. Only the deformation of a solid flag is considered, which generates large deformations in the surrounding mesh domain. In addition, the fluid formulation with ALE framework is verified by calculating a channel flow in which the background mesh is manually displaced.

Next, the derived formulations are combined to solve dynamic FSI problems with large deformations. First, the coupling of the ALE fluid formulation with the SV solid for linear elasticity is tested by means of the numerical example of a flow through a channel with contracting walls. Finally, the SV fluid formulation based on the incompressible

Navier-Stokes equations in an ALE framework and the SV solid formulation for hyperelastic material behavior based on a description in the current configuration, are coupled. The final coupled LS formulation for FSI with large structure deformations is tested by means of a standard FSI benchmark, considering also the application of high-order time discretization and adaptive time stepping.

## 8.1 The coupled LS stress-velocity formulations for dynamic FSI problems

As a first step towards the solution of fluid-structure interaction problems, the equations for the fluid and the solid domain, are combined to one equation system. Assuming, that the mixed LS functional for the fluid domain is given by $\mathcal{F}^F$ and defined on $\Omega_f$ and the mixed LS solid functional is denoted by $\mathcal{F}^S$ and defined on $\Omega_s$, the associated LS FSI functional is constructed as

$$\mathcal{F}^{FSI}(\boldsymbol{\sigma}, \boldsymbol{v}) = \mathcal{F}^F(\boldsymbol{\sigma}, \boldsymbol{v}) + \mathcal{F}^S(\boldsymbol{\sigma}, \boldsymbol{v}) \ . \tag{8.1}$$

Therein, all residuals of the two individual functionals are given as a function of velocities and stresses. In the context of this work, the FSI formulations always include dynamic terms, hence a discretization in time must be used to define the relation between acceleration and velocity. Note, that the implementation of the stress-velocity solid formulations always requires a discretization in time to at least relate the displacements to the velocities even if the accelerations are dropped.

The solution of the minimization problem can be obtained by linearization and application of Newton's method $\delta\mathcal{F} + \Delta\delta\mathcal{F} = 0$. The resulting discretized linear system of equations for a typical element in matrix notation can be written as

$$\begin{bmatrix} \boldsymbol{k}^e_{vv} & \boldsymbol{k}^e_{v\sigma} \\ \boldsymbol{k}^e_{\sigma v} & \boldsymbol{k}^e_{\sigma\sigma} \end{bmatrix} \begin{bmatrix} \Delta\boldsymbol{w} \\ \Delta\boldsymbol{\beta} \end{bmatrix} = - \begin{bmatrix} \boldsymbol{r}^e_v \\ \boldsymbol{r}^e_\sigma \end{bmatrix} , \tag{8.2}$$

where $\boldsymbol{w}^I = [w^I_1 \ w^I_2]^T$ and $\boldsymbol{\beta}^J = [\beta^J_1 \ \beta^J_2]^T$ are the degrees of freedom of the velocities and stresses, which can be approximated with the interpolation matrices $\boldsymbol{N}$ and $\boldsymbol{\psi}$ as

$$\boldsymbol{v} = \sum_I \boldsymbol{N}^I \boldsymbol{w}^I, \quad \text{and} \quad \boldsymbol{\sigma} = \sum_J \boldsymbol{\psi}^J \, \boldsymbol{\beta}^J. \tag{8.3}$$

The components of the matrix as well as the right-hand-side-vector contain entries from the fluid and solid formulation, e.g. $\boldsymbol{k}^e_{vv}$ is composed of entries in $\Delta\delta_{\boldsymbol{vv}}\mathcal{F}^F$ and $\Delta\delta_{\boldsymbol{vv}}\mathcal{F}^S$. For more details on the implementation see the Appendix D.

The partial differential equation system defined on $\Omega = \Omega_f \cup \Omega_s \times [0, T]$ is completed by the specification of initial conditions and constraints on the external boundary $\partial\Omega$. As already stated in Section 3.3.3, in the case of mixed stress-velocity formulations, the entire boundary can be considered as Dirichlet type boundary since constraints are directly imposed to the primary variables. Therefore, a partition into two subsets can be performed, such that the boundary conditions for the velocities and stresses in the LS FSI functional read

$$\boldsymbol{v} = \boldsymbol{v}_D \qquad \text{on } \partial\Omega_{Dv} \times (0, T] \qquad \text{with} \qquad \partial\Omega_{Dv} \subseteq \partial\Omega \ , \tag{8.4a}$$

$$\boldsymbol{\sigma} \cdot \boldsymbol{n} = \boldsymbol{t}_D \qquad \text{on } \partial\Omega_{Ds} \times (0, T] \qquad \text{with} \qquad \partial\Omega_{Ds} \subseteq \partial\Omega \ . \tag{8.4b}$$

Here, $\boldsymbol{n}$ denotes the outward unit normal vector, $\boldsymbol{v}_D$ and $\boldsymbol{t}_D$ the prescribed values of the velocity and traction vector on the boundary. It is to be noted that both boundary subsets can belong to the solid as well as to the fluid domain. Additionally, initial conditions are set for the velocities

$$\boldsymbol{v}(t_0) = \boldsymbol{v}_0 \qquad \text{on } \Omega \qquad \text{at} \quad t = t_0 \; , \tag{8.5}$$

and according to the time discretization method also for the accelerations and displacements, as prescribed in Section 3.3.3. Further boundary conditions, which are required in case of additional equations to describe the mesh deformation, are outlined in Section 8.3.4 when presenting the mesh formulation itself.

### 8.1.1 Monolithic coupling conditions for SV formulations

Fluid-structure interaction problems require materials with fundamentally different properties to interact in a common boundary value problem. During this process, there is a reciprocal influence of both materials with regard to their kinematics. More precisely, it must be taken into account that a fluid flowing over the surface of a solid exerts normal and tangential tensile forces that cause deformations in the structure. These in turn influence the forces acting on the fluid, which affect the flow kinematics. For a correct reproduction of the interaction and mutual influence, the handling of the interface is of great importance.

An important aspect of this work is the use of LS formulations expressed in terms of stresses and velocities in both domains in order to achieve, in combination with appropriate approximation functions, an inherent fulfillment of the interface conditions. Denoting the interface between the two materials as $\Gamma_i$, the coupling conditions which are illustrated in Figure 8.1 can be specified as

$$\boldsymbol{v}_f = \boldsymbol{v}_s \qquad \text{on} \quad \Gamma_i \; , \tag{8.6a}$$

$$\boldsymbol{\sigma}_f \cdot \boldsymbol{n} = \boldsymbol{\sigma}_s \cdot \boldsymbol{n} \quad \text{on} \quad \Gamma_i \; . \tag{8.6b}$$

Herein, $\boldsymbol{n} = (n_1, ..., n_d)^T$ is the normal unit vector and $\boldsymbol{v}_i$ and $\boldsymbol{\sigma}_i$ with $i = \{f, s\}$ denote the velocities and Cauchy stresses in the fluid and solid domain, respectively. The first term involves the no-slip interface conditions of a fluid at a solid surface, and the second term states that the normal stresses of both regions at the interface must be equal.

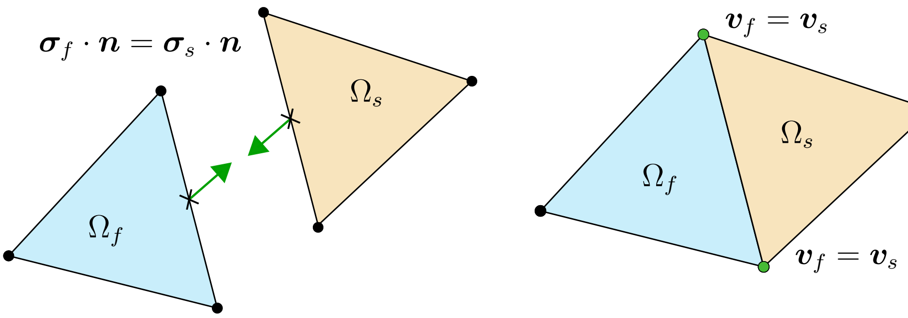

Figure 8.1: Coupling conditions on $\Gamma_i$ for a solid and fluid element

**Interpolations spaces**

As stated earlier, the coupling conditions can be automatically satisfied without additional constraints by applying conformal interpolation functions. More precisely, the approximation of the fluid and solid velocity field using standard finite element spaces in

$H^1$ guarantees consistency at the interface and satisfies (8.6a), and the application of Raviart-Thomas elements satisfies a priori the stress-coupling conditions (8.6b). For the presented mixed LS formulations with $\mathcal{F}(\boldsymbol{\sigma}, \boldsymbol{v}) : \boldsymbol{V} \times \boldsymbol{W} \rightarrow \mathbb{R}^2$ this leads to the finite element spaces

$$\boldsymbol{V}_k^h = \{\boldsymbol{v} \in H^1(\Omega)^2 : \boldsymbol{v}|_{\Omega_e} \in P_k(\Omega_e)^2 \ \ \forall\, \Omega_e\} \subseteq \boldsymbol{V} \ , \tag{8.7}$$

$$\boldsymbol{W}_m^h = \{\boldsymbol{\sigma} \in H(\mathrm{div}, \Omega)^2 : \boldsymbol{\sigma}|_{\Omega_e} \in RT_m(\Omega_e)^2 \ \ \forall\, \Omega_e\} \subseteq \boldsymbol{W} \ , \tag{8.8}$$

where $P_k(\Omega_e)$ are Lagrange interpolation polynomials of order $k$ and $RT_m(\Omega_e)$ represent vector-valued Raviart-Thomas interpolation functions of order $m$, see e.g. Raviart and Thomas [324] or Brezzi and Fortin [69]. The resulting finite elements in two dimensions will be denoted as $RT_mP_k$.

## 8.2 Numerical examples: Dynamic FSI problems with small deformations

In the previous chapters, the mixed LS formulations in terms of stresses and velocities were studied separately for unsteady fluid flow and structural dynamics problems. In the following, the proposed approaches are combined to solve FSI problems. For this purpose, the first step is to test the general coupling procedure by solving interaction problems with small deformations in the solid regime. The small deformations at the interface prevent the need to consider the motion of the background mesh in the fluid domain, which allows the use of the standard SV fluid formulation (4.17) (without ALE) for the initial numerical tests. In addition, the restriction to small strains allows the utilization of the SV solid formulation based on linear elasticity given in (6.4). Thus the resulting least-squares functional for fluid-structure interaction problems the with restriction to small strains reads

$$\mathcal{F}^{FSI}(\boldsymbol{\sigma}, \boldsymbol{v}) = \mathcal{F}^{F}(\boldsymbol{\sigma}, \boldsymbol{v}) + \mathcal{F}^{LE}(\boldsymbol{\sigma}, \boldsymbol{v}) \ . \tag{8.9}$$

For the numerical evaluations that follow, the weighting factors for the residual terms are chosen based on findings in Kayser-Herold and Matthies [231], except that the third residual of the fluid functional is left unweighted with the result that

$$\omega_{f1} = \sqrt{\frac{\Delta t}{\rho_f}} \ , \quad \omega_{f2} = \sqrt{\frac{1}{\rho_f \nu_f}} \ , \quad \omega_{f3} = 1 \ , \quad \omega_{s1} = \sqrt{\frac{\Delta t}{\rho_s}} \ , \quad \omega_{s2} = \sqrt{\frac{\mu_s}{\Delta t}} \ . \tag{8.10}$$

The boundary value problems considered in the subsequent sections are the flow around a cylinder to which a flag is attached and a flow through a channel with a solid barrier. The flow velocity and material properties are chosen in such a way that the resulting Reynolds numbers are low and the deformations in the solid remain small. In both considered problems, this leads to a final steady-state flow after a transient phase.

### 8.2.1 Steady flow around a cylinder with flag

As a first numerical example to test the presented time-dependent SV formulations to solve fluid-structure interaction problems the flow around a cylinder with a flag attached to the cutout, denoted as FAC-flag (1), is calculated. The setup is based on the benchmark problem presented in Turek et al. [399] and Turek and Hron [396], which is denoted as FSI 1. The geometry and boundary conditions of this FSI problem as depicted in Figure 8.2 are similar to the setup of the fluid example in Section 7.4.2 except of an additional elastic flag attached to the cylinder. The center of the cylinder with a diameter of $d = 0.1\,\mathrm{m}$ is situated at $(0.2, 0.2)\,\mathrm{m}$.

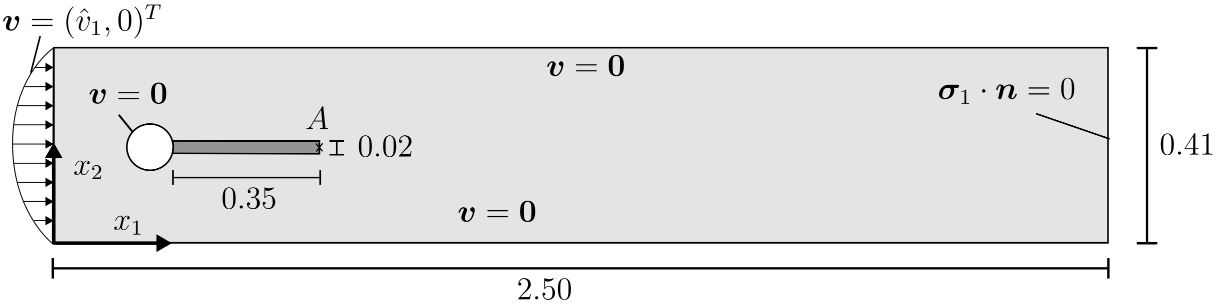

Figure 8.2: FAC-flag (1) - geometry and boundary conditions (unit m)

An inflow on the left side, pressure-related stress boundary conditions for an outflow on the right side, and no-slip boundary conditions are applied to the top and bottom walls and to the cylindrical cutout. The flag is fixed on its left boundary. Suitable outflow boundary conditions for the presented stress-velocity formulation are defined as $\boldsymbol{\sigma}_1 \cdot \boldsymbol{n} = 0$ with $\boldsymbol{\sigma}_1 = (\sigma_{11},\ \sigma_{12})^T$. For the inflow velocity in $x_1$-direction a quadratic function is defined as

$$\hat{v}_1(x_2, t) = 1.5\ v_{in}(t)\ \frac{x_2(0.41 - x_2)}{0.205^2}\ . \tag{8.11}$$

For a uniform increase of the inflow velocity, a cosine function is used, such that

$$v_{in}(t) = \begin{cases} \bar{v}\ \left(1 - \cos\left(\frac{\pi}{2}\,t\right)\right) \cdot \frac{1}{2} & \text{if} \quad t < 2.0 \\ \bar{v} & \text{if} \quad t \geq 2.0 \end{cases}\ , \tag{8.12}$$

where $\bar{v}$ is the mean inflow velocity as given in Table 8.1. The material parameters are set equivalent to specification in TUREK ET AL. [399] and also listed in Table 8.1. With a characteristic length of $L_{ch} = 0.1\,\mathrm{m}$ corresponding to the diameter of the cylinder and the given material and flow parameters, the Reynolds number is $Re = 20$.

Table 8.1: FAC-flag (1) - material parameters for steady FSI1 from TUREK ET AL. [399]

| Description | Value | Unit |
|---|---|---|
| Mean inflow velocity $\bar{v}$ | 0.2 | m/s |
| Fluid density $\rho_f$ | 1.0 $\times 10^3$ | kg/m$^3$ |
| Viscosity $\nu_f$ | 0.001 | m$^2$/s |
| Solid density $\rho_s$ | 1.0 $\times 10^3$ | kg/m$^3$ |
| Young's modulus $E$ | 1.4 $\times 10^6$ | kg/(m s$^2$) |
| Poisson ratio $\nu_s$ | 0.4 | - |

For the validation and verification of the presented approaches drag and lift forces are computed, which act in case of the FSI problem on the cylindrical cutout as well as on the flag. With $S = S_1 \cup S_2$, where $S_1$ denotes the length of the cylinder in contact with the fluid and $S_2$ denotes the interface between the fluid and the solid, the drag and lift forces are defined as

$$(F_D, F_L) = \int_S \boldsymbol{\sigma} \cdot \boldsymbol{n}\ \mathrm{d}S\,. \tag{8.13}$$

An additional measured quantity for comparison are the displacements at the right end of the flag at point $A(0.6, 0.2)$ m. The calculations are performed with different mesh refinements and the elements $RT_1P_2$ and $RT_3P_4$. Table 8.2 summarizes the information about the different meshes, including the number of elements of the solid as well as the fluid domain and the number of degrees of freedom.

Table 8.2: FAC-flag (1) - mesh level, number of elements $n_{\text{ele}}$ in fluid and solid domain and number of degrees of freedom ($n_{\text{dof}}$)

| | $n_{\text{ele}}$ | | $n_{\text{dof}}$ | |
|---|---|---|---|---|
| level | solid | fluid | $RT_1P_2$ | $RT_3P_4$ |
| 1 | 72 | 889 | 13,906 | 50,876 |
| 2 | 128 | 1,612 | 24,968 | 91,696 |
| 3 | 512 | 6,018 | 92,636 | 341,992 |
| 4 | 2,048 | 24,150 | 369,212 | 1,367,176 |

In a first step, the Houbolt time discretization is used for the fluid as well as the solid domain. Next, a combination of two different time integration schemes is investigated. Therefore, the Houbolt method is applied for the solid domain and the Crank-Nicolson method for the fluid domain.

Table 8.3: FAC-flag (1) - displacements $u_1$ and $u_2$ (in m) at point $A(0.6, 0.2)$ m, and drag $F_D$ and lift force $F_L$ (in N), obtained with the Houbolt method for both domains, reference solution from TUREK ET AL. [399]

| | level | $u_1$ | $u_2$ | $F_D$ | $F_L$ |
|---|---|---|---|---|---|
| $RT_1P_2$ | 1 | 2.8883E-5 | 4.2390E-3 | 11.4405 | 1.2411 |
| $\Delta t = 0.005\,\text{s}$ | 2 | 2.7998E-5 | 3.6978E-3 | 12.9918 | 1.1089 |
| | 3 | 2.4793E-5 | 7.2647E-4 | 14.0466 | 1.0885 |
| | 4 | 2.4097E-5 | 1.6963E-3 | 14.2390 | 1.1113 |
| $RT_1P_2$ | 1 | 2.4916E-5 | 2.2459E-3 | 11.1112 | 1.2014 |
| $\Delta t = 0.001\,\text{s}$ | 2 | 2.4482E-5 | 2.1655E-3 | 12.5154 | 1.0280 |
| | 3 | 2.3639E-5 | 1.3415E-3 | 13.8934 | 1.0646 |
| | 4 | 2.3551E-5 | 1.5963E-3 | 14.2112 | 1.0979 |
| $RT_3P_4$ | 1 | 2.4396E-5 | 1.3018E-3 | 13.9161 | 1.0892 |
| $\Delta t = 0.005\,\text{s}$ | 2 | 2.4022E-5 | 1.6584E-3 | 14.0686 | 1.1017 |
| | 3 | 2.3864E-5 | 1.6996E-3 | 14.1808 | 1.1114 |
| | 4 | 2.3798E-5 | 1.6355E-3 | 14.2338 | 1.1132 |
| $RT_3P_4$ | 1 | 2.3740E-5 | 1.4949E-3 | 13.9165 | 1.0729 |
| $\Delta t = 0.001\,\text{s}$ | 2 | 2.3569E-5 | 1.5846E-3 | 14.0701 | 1.0847 |
| | 3 | 2.3658E-5 | 1.6050E-3 | 14.1785 | 1.1049 |
| | 4 | 2.3682E-5 | 1.5876E-3 | 14.2323 | 1.1108 |
| reference | | 2.2705E-5 | 8.2088E-4 | 14.2943 | 7.638E-1 |

The results for two spatial interpolation orders ($RT_1P_2$ and $RT_3P_4$) and two different time increments ($\Delta t = 0.005\,\mathrm{s}$ and $\Delta t = 0.001\,\mathrm{s}$) are listed in Table 8.3 and Table 8.4. Regarding the combinations of the time discretization schemes, both approaches lead to similar results. When comparing the spatial convergence orders, both elements show acceptable convergence behavior.

Table 8.4: FAC-flag (1) - displacements $u_1$ and $u_2$ (in m) at point $A(0.6, 0.2)$m, and drag $F_D$ and lift force $F_L$ (in N), obtained with the Houbolt and Crank-Nicolson method for solid and fluid domain, reference solution from TUREK ET AL. [399]

| | level | $u_1$ | $u_2$ | $F_D$ | $F_L$ |
|---|---|---|---|---|---|
| $RT_1P_2$ | 1 | 2.8530E-5 | 4.2591E-3 | 11.4095 | 1.2376 |
| $\Delta t = 0.005\,\mathrm{s}$ | 2 | 2.7714E-5 | 3.6490E-3 | 12.9635 | 1.1063 |
| | 3 | 2.4721E-5 | 7.2445E-4 | 14.0400 | 1.0875 |
| | 4 | 2.4071E-5 | 1.7040E-3 | 14.2374 | 1.1113 |
| $RT_1P_2$ | 1 | 2.4682E-5 | 2.2556E-3 | 11.0576 | 1.1936 |
| $\Delta t = 0.001\,\mathrm{s}$ | 2 | 2.4294E-5 | 2.1482E-3 | 12.4632 | 1.0232 |
| | 3 | 2.3584E-5 | 1.3396E-3 | 13.8774 | 1.0627 |
| | 4 | 2.3529E-5 | 1.6005E-3 | 14.2072 | 1.0973 |
| $RT_3P_4$ | 1 | 2.4353E-5 | 1.3082E-3 | 13.9126 | 1.0882 |
| $\Delta t = 0.005\,\mathrm{s}$ | 2 | 2.4000E-5 | 1.6588E-3 | 14.0672 | 1.1014 |
| | 3 | 2.3854E-5 | 1.7000E-3 | 14.1803 | 1.1114 |
| | 4 | 2.3793E-5 | 1.6364E-3 | 14.2336 | 1.1132 |
| $RT_3P_4$ | 1 | 2.3706E-5 | 1.4970E-3 | 13.9085 | 1.0708 |
| $\Delta t = 0.001\,\mathrm{s}$ | 2 | 2.3552E-5 | 1.5837E-3 | 14.0668 | 1.0835 |
| | 3 | 2.3649E-5 | 1.6041E-3 | 14.1774 | 1.1045 |
| | 4 | 2.3689E-5 | 1.5928E-3 | 14.2320 | 1.1098 |
| reference | | 2.2705E-5 | 8.2088E-4 | 14.2943 | 7.6375E-1 |

Note that the numerical procedure at this point is not completely consistent with the one in the FSI 1 benchmark in TUREK ET AL. [399]. In this example, as mentioned initially, a small strain approach is used for the solid domain, while the reference solution is based on a hyperelastic material model. Furthermore, no mesh movement in the fluid using the Arbitrary-Lagrangian-Eulerian framework has been considered here. This can be considered as the reason for the small deviations between the displacement in $x_2$ direction as well as the lift force from the reference solution.

This example demonstrats that the Houbolt method for the time discretization of the solid formulation can be combined without difficulty with the Houbolt and Crank-Nicolson schemes for the fluid domain. The presented approaches apparently showed no stability problems for the considered fluid-structure interaction problem.

### 8.2.2 Channel with flow over a wall

The second numerical example to investigate the mixed SV formulations for the simulation of incompressible flows and elastic solid materials, is a channel flow over an elastic wall (FOW). The geometric measures and boundary conditions are illustrated in Figure 8.3. Herein, no-slip boundary conditions are prescribed on the upper and lower walls, i.e. $\boldsymbol{v} = 0$, and a parallel inflow at $x_1 = 0\,\mathrm{m}$ is defined as

$$\boldsymbol{v}(x_2, t) = \begin{bmatrix} v_{in}(t)\ 0.15\dfrac{x_2(5.0 - x_2)}{6.25} \\ 0 \end{bmatrix} . \tag{8.14}$$

The inflow velocity is linearly increased from $v_{in}(t = 0) = 0\,\mathrm{m/s}$ up to $v_{in}(t = 4) = 1\,\mathrm{m/s}$. Additionally, pressure associated stress boundary conditions are defined at the outflow by $\boldsymbol{\sigma}_1 \cdot \boldsymbol{n} = 0$ with $\boldsymbol{\sigma}_1 = [\sigma_{11}\ \sigma_{12}]^T$. The material parameters leading to laminar flow conditions after a transient initial phase are chosen as listed in Table 8.5.

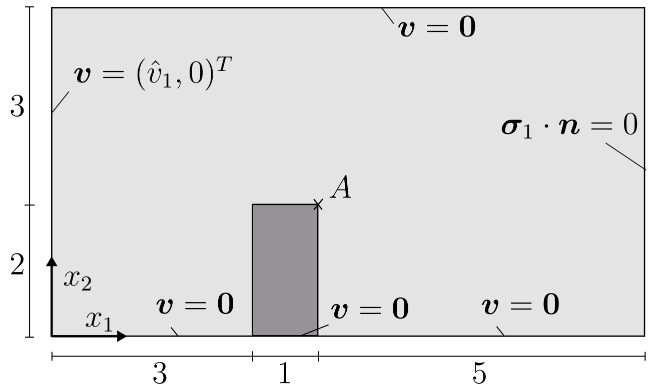

Figure 8.3: FOW - geometry, boundary conditions

Table 8.5: FOW - mat. parameters

| Description | Value & Unit |
|---|---|
| Fluid density $\rho_f$ | 1 kg/m$^3$ |
| Viscosity $\nu_f$ | 0.01 m$^2$/s |
| Solid density $\rho_s$ | 1 kg/m$^3$ |
| Young's modulus $E$ | 200 kg/(m s$^2$) |
| Poisson ratio $\nu_s$ | 0.499 |

The example is evaluated considering different spatial discretization orders, i.e. $RT_1P_2$ and $RT_3P_4$, and different time step sizes $\Delta t = \{0.1, 0.01, 0.005\}\,\mathrm{s}$. A mesh with 294 triangular elements in the solid domain and 2,281 elements in the fluid domain is selected, resulting in a number of degrees of freedom of $n_{DOF} = 36,114$ and $n_{DOF} = 134,028$ for the low- and high-order element, respectively. For the temporal discretization the Houbolt method is applied in the solid formulation, whereas the fluid equations are discretized in time using the Houbolt and Crank-Nicolson scheme, as specified in Section 7.3.

Figure 8.4 presents an example of the evolution of the velocity field, including streamlines, at different points in time. The solution is obtained with the Houbolt time discretization method for the solid domain and the Crank-Nicolson scheme for the fluid domain, a time increment of $\Delta t = 0.005\,\mathrm{s}$ and the element order $RT_3P_4$. Note that the steady-state solution is reached only after a time of about $t = 70\,\mathrm{s}$, with a main flow forming above the wall and a vortex behind the wall. The flow at the outlet is not symmetrical for the geometry considered and the velocity of the fluid at steady state is greatest in the upper two-thirds of the domain.

As a comparison value, the displacement at the point $A(4, 2)\,\mathrm{m}$ is measured over a period up to time $t = 100\,\mathrm{s}$. The results for the displacement in $x_1$-direction at $t = 100\,\mathrm{s}$ are presented in Table 8.6 and the development over time for the time step sizes $\Delta t = 0.1\,\mathrm{s}$ and $\Delta t = 0.005$,s is depicted in Figure 8.5.

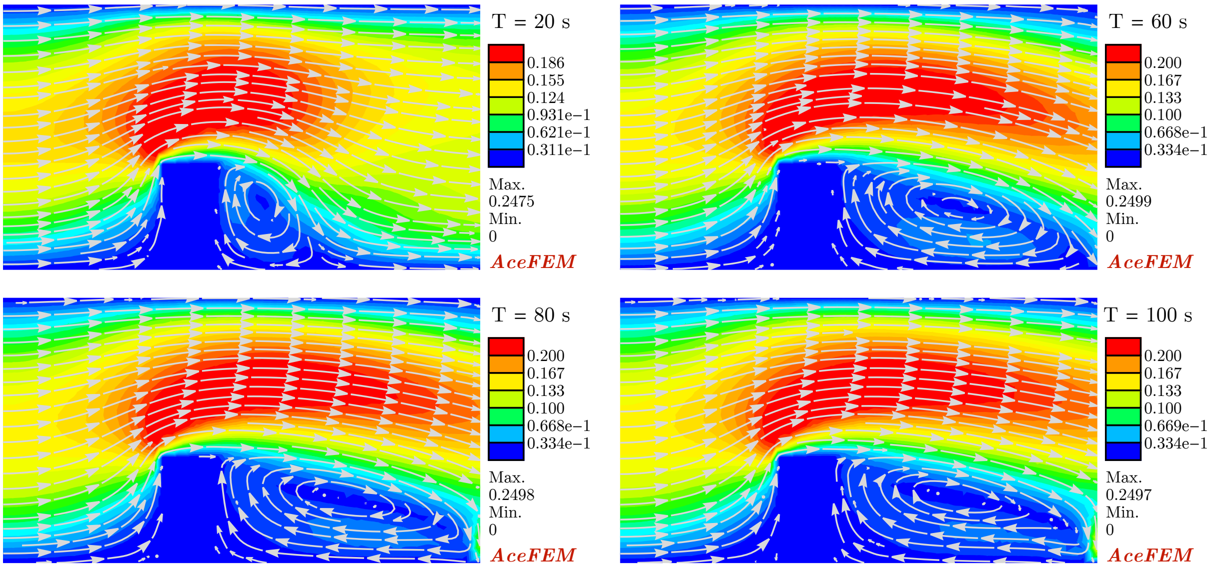

Figure 8.4: FOW - Velocity field $|\boldsymbol{v}|$ at $t = [20, 60, 80, 100]$ s

Table 8.6: FOW - displacement $u_1$ (in m) at point $A = (4, 2)$ m for different element orders and time increments using two combinations of time discretizations for solid and fluid

| | Houbolt - Houbolt | | Houbolt - Crank-Nicolson | |
|---|---|---|---|---|
| $\Delta t$ | $RT_1P_2$ | $RT_3P_4$ | $RT_1P_2$ | $RT_3P_4$ |
| 0.1 | 1.06991E-2 | 6.83221E-3 | 1.01341E-2 | 6.57799E-3 |
| 0.01 | 5.43573E-3 | 5.26811E-3 | 5.39330E-3 | 5.25144E-3 |
| 0.005 | 5.30739E-3 | 5.18737E-3 | 5.27137E-3 | 5.17466E-3 |

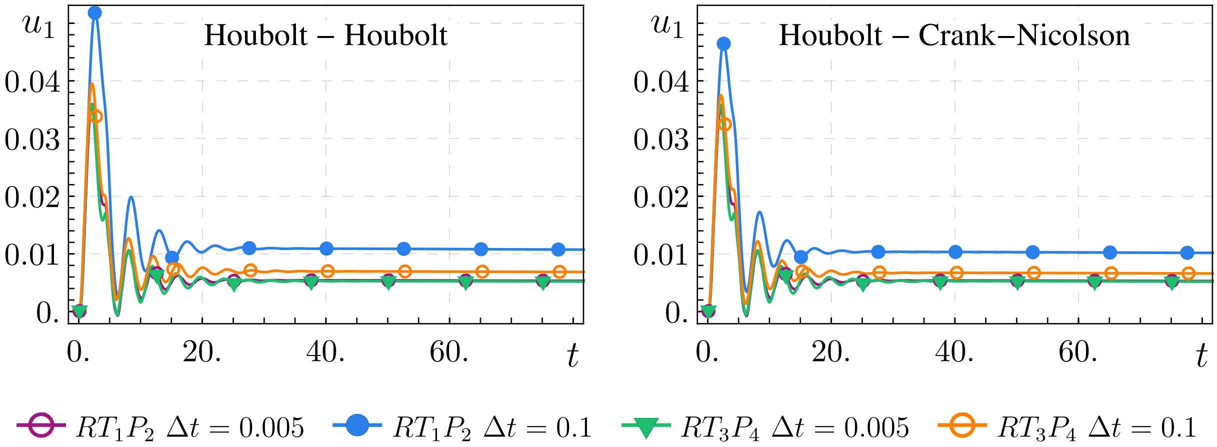

Figure 8.5: FOW - displacement $u_1(A)$ (in m) over time $t$ (in s) for different element orders, time discretization methods and time increments

Both combinations of time discretization methods are stable for all time steps considered and yield similar results. The two element orders converge with decreasing time step size up to a displacement of about $u_1(A) = 0.0052\,\text{m}$, with the high-order element yielding better results than the low-order spatial discretization also at larger time steps.

## 8.3 The fluid formulation with a moving domain

So far, the FSI calculations are based on small deformations in the solid domain $\Omega_s$, thus also the fluid domain $\Omega_f$ does not undergo large changes. In order to perform simulations with large displacements in both regions and to be able to simulate real interactions, the fluid domain needs to be capable of moving. For this purpose, the background mesh in the fluid domain, which is introduced as a third domain $\Omega_m$, also needs to be calculated. Additionally, the displacements or velocities of this mesh must be taken into account in the governing equations of the fluid. This is achieved by introducing the Arbitrary-Lagrangian-Eulerian framework.

### 8.3.1 The Arbitrary-Lagrangian-Eulerian framework

This approach is based on a combination of the two classical descriptions of motion in continuum mechanics, which are the Lagrangian and the Eulerian description as explained in Section 2.1.2. To illustrate the correlation between the different configurations Figure 2.1 can be extended. For the application of the ALE framework, an arbitrary reference domain $\hat{\Omega}$ is introduced, as shown in Figure 8.6. This domain consists of a set of reference points $\hat{Q}$ and in general it depends on time. Furthermore, additional mappings $\Phi_t : \hat{\Omega} \to \Omega_0$ and $\phi_t : \hat{\Omega} \to \Omega_t$ are defined, which are assumed to be invertible and differentiable. The mixed ALE form was developed with the objective to use the advantages of both classical methods while minimizing the disadvantages, see Donea et al. [132]. The basic ideas of the ALE framework are presented by, e.g., Hirt et al. [197] and Hughes et al. [207].

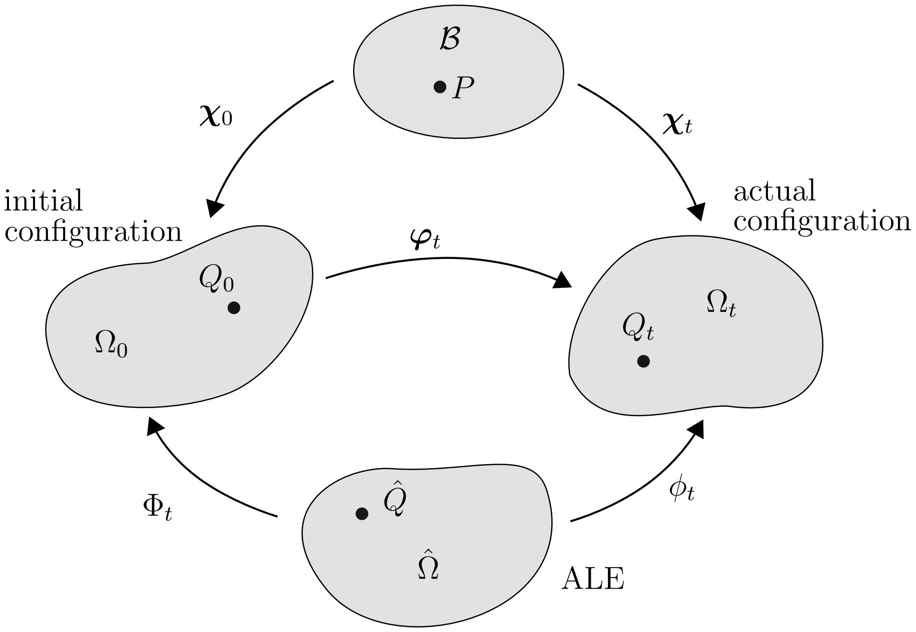

Figure 8.6: Different configurations and related mappings

Basic advantages of a Lagrangian description of motion, where the nodes of the mesh follow the moving material particles, see Figure 8.7(top), are the simple handling of free surfaces and interfaces and a straightforward treatment of materials with time-dependent constitutive relations. However, the method has the disadvantage that large distortions of the considered continuum require additional relocation of the mesh. In case of an Eulerian description in which the mesh remains fixed, see Figure 8.7(center), and the material deforms independently, large deformations of the material can be handled without the requirement of constructing new meshes. However, a precise definition of interfaces is difficult. With the introduction of an arbitrary reference domain in ALE description, the mesh can take an arbitrary deformation. The relation between the Eulerian, Lagrangian and mixed ALE framework is illustrated in Figure 8.7. Therein, the boundary of the domain is defined as Lagrangian, as it usually applies e.g. to the fluid-structure interface in FSI problems.

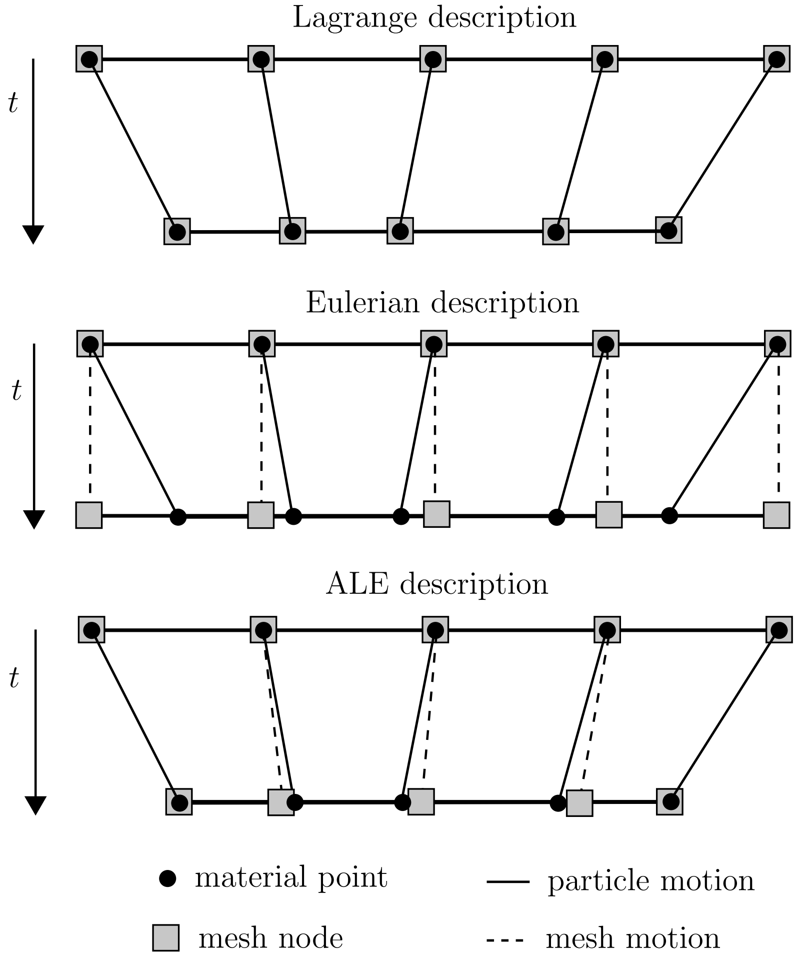

Figure 8.7: Mesh and material motion in Lagrangian, Eulerian and ALE description in 1D with Lagrangian boundary in ALE description, according to Donea et al. [132]

The ALE description was initially developed for the application in the scope of fluid-structure interaction problems, see e.g. Hughes et al. [207] and Donea et al. [131]. However, the advantages of this method have long been exploited in a wide range of areas whenever partial differential equations are to be solved on deforming domains. For example, the ALE framework is commonly applied in solid dynamics when large deformations occur as in the context of metal forming processes, see Haber [176], Schreurs et al. [340], Gadala and Wang [160], Askes et al. [6], for instance. There are various investigations in the field of fluid dynamics with different focuses, such as the preservation of the accuracy of higher order time integrations or the handling of free boundaries, to be found e.g. in Fullsack [159], Duarte et al. [134] and Étienne et al. [141].

Considerable research on the application of the ALE description within FSI problems addresses issues such as different techniques for computing the mesh motion and handling large deformations without leading to self-penetrating elements or irreversible distortions in the mesh. A small selection of interesting works on these topics from the beginning of the 21th century is provided, e.g., by the following publications of Kjellgren and Hyvärinen [239], Behr and Arora [34], Geuzaine et al. [166], and Wall et al. [410]. More recent studies with a focus on approaches considering an additional phantom domain, extended hyperelasticity formulations, or mesh-Jacobian-based stiffening (MJBS) include, for instance, Wick [415], Bazilevs et al. [29], Hilger et al. [195], Takizawa et al. [379], and Shamanskiy and Simeon [357]. Further detailed descriptions of mesh moving methods can be found in, among others, Donea et al. [132], Bazilevs et al. [27], Souli and Benson [367] and Richter [329].

In the following, all necessary components for the calculation of FSI problems with large deformations will be explained. For this purpose, the fluid formulation in the ALE kinematics description is introduced first. Then the employed technique for the calculation of the mesh motion is presented.

### 8.3.2 Stress-velocity fluid formulation in ALE description

The incompressible Navier-Stokes equations in the ALE description can be constructed based on (2.70) by adding a convective term considering the difference between the velocity of the fluid and the reference frame, i.e. the velocity of the background mesh. The resulting system of equations reads

$$\rho_f \; \boldsymbol{a} + \rho_f \nabla \boldsymbol{v} \cdot (\boldsymbol{v} - \hat{\boldsymbol{v}}) - 2 \rho_f \nu_f \; \operatorname{div}(\nabla^s \boldsymbol{v}) + \nabla p - \boldsymbol{f} = \boldsymbol{0} \;, \tag{8.15a}$$

$$\operatorname{div} \boldsymbol{v} = 0 \;. \tag{8.15b}$$

Therein, $\boldsymbol{a} = \frac{\partial \boldsymbol{v}}{\partial t}$ denotes again the acceleration vector, $\boldsymbol{v}$ the velocity vector, $p$ the pressure, $\rho_f$ and $\nu_f$ the fluid density and viscosity, and $\hat{\boldsymbol{v}}$ the mesh velocity. The given equation system is transformed into a first-order system, similarly as in Section 4, by introducing the Cauchy stresses as additional variables and eliminating the pressure. The resulting functional in terms of stresses and velocities reads

$$\begin{aligned} \mathcal{F}^F_{ALE}(\boldsymbol{\sigma}, \boldsymbol{v}) = \frac{1}{2} \Big( & ||\omega_{f1} \left(\rho_f \boldsymbol{a}(\boldsymbol{v}) - \operatorname{div} \boldsymbol{\sigma} + \rho_f \nabla \boldsymbol{v} \cdot (\boldsymbol{v} - \hat{\boldsymbol{v}}) - \boldsymbol{f}\right)||^2_{L^2(\Omega_f)} \\ & + ||\omega_{f2} \left(\operatorname{dev} \boldsymbol{\sigma} - 2 \rho_f \nu_f \nabla^s \boldsymbol{v}\right)||^2_{L^2(\Omega_f)} + \; ||\omega_{f3} \left(\operatorname{div} \boldsymbol{v}\right)||^2_{L^2(\Omega_f)} \Big) \;, \end{aligned} \tag{8.16}$$

with appropriate positive weighting factors $\omega_{f1}$, $\omega_{f2}$ and $\omega_{f3}$. This formulation is also presented in Averweg et al. [8], with its application in combination with a linear elastic solid formulation to solve a quasi-stationary FSI problem. For the solution of dynamic FSI problems, the accelerations can be approximated using various time discretization schemes as explained in Section 7.3, for instance. The construction of the first and second variations of the functional with respect to the unknowns, which are required to solve the minimization problem, are built in the same way as given in Section 4.2. The mesh velocity and displacement, which is relevant to determine the new fluid reference configuration, can be computed using a number of different techniques as outlined in the following.

### 8.3.3 Mesh motion techniques

For FSI calculations which are based on the ALE framework it is important to choose an appropriate mesh motion approach to compute the background mesh in the fluid domain. A suitable mesh motion technique has to satisfy certain characteristics, i.e.

- The mesh has to comply with the structure displacement at the FSI interface, such that $\hat{\boldsymbol{u}} = \boldsymbol{u}_s$ and $\hat{\boldsymbol{v}} = \boldsymbol{v}_f = \boldsymbol{v}_s$ on $\Gamma_i$, with $\hat{\boldsymbol{u}}$ and $\hat{\boldsymbol{v}}$ denoting the mesh displacements and velocities, respectively.
- Inside the domain it can have an arbitrary shape as long as no element is inverted, i.e. $J_m = \det \boldsymbol{F}_m = \det(\boldsymbol{I} + \nabla \hat{\boldsymbol{u}}) > 0$.
- For long-term studies accumulation of mesh distortion occurring in path-dependent approaches should be avoided.

There are several approaches to mesh updating in the literature based on different techniques. In general, a distinction can be made between mesh moving and re-meshing. Both operations are often applied in combination with the main goal to shift the mesh nodes as long as possible and then to re-mesh them when the distortion is too large. In case of re-meshing of a region, there is a rearrangement of the elements and possibly even of the nodes. The process can lead to some disadvantages that are important to consider. First, a projection error can occur when transferring the solution from the old to the new mesh. Furthermore, frequent re-meshing can lead to high computational costs if the entire domain is always regenerated. In the context of this work, re-meshing is avoided and the focus is on a mesh movement that is as smooth as possible.

Various techniques can be chosen to calculate the displacement of the mesh nodes. For example, a rather simple way is to solve an auxiliary Laplace problem such that the displacements within the domain are defined as a harmonic extension of the known boundary values to the fluid domain, see for instance Wu and Cai [425] and Formaggia et al. [152]. However, this approach usually does not provide good results for large deformations at the fluid-structure interface and is thus limited to simulations with small mesh deformations. The solution of the biharmonic equation allows to model also large deformations since it is more regular, refer to e.g. Richter [327], Wick [415] and Shamanskiy and Simeon [357]. However, this method usually comes with higher computational cost.

Another common approach is to solve an additional linear elasticity equation, see Sackinger et al. [333], sometimes in combination with a Jacobian-based stiffening, to assign higher stiffness to the smaller elements, which are generally located close to the interface. This method is used among others for example in Johnson and Tezduyar [224] and Stein et al. [372]. A similar method is utilized by Suito et al. [376] and Takizawa et al. [379], for instance, except that instead of the equations for linear elasticity, hyperelastic material behavior is assumed for the mesh. Authors Hilger et al. [195] also investigate an elastic approach for mesh deformation and introduce additionally a new method based on a mesh phantom domain. Thus, the mesh deformation is not limited to the domain of the fluid but can move beyond it, allowing large deformations to be simulated without re-meshing.

In the scope of this thesis, the mesh motion in the interior of the fluid domain is governed by the equations of linear elasticity with an additional local stiffening, as described in the next sections.

### 8.3.4 Mesh motion based on linear elasticity with local stiffening

Considering the mesh domain $\Omega_m \in \mathbb{R}^d$ bounded by $\partial\Omega_m$, the governing equations to model the behavior of the mesh based on the balance principles read

$$\operatorname{div} \boldsymbol{\sigma}_m + \boldsymbol{f} = \boldsymbol{0} \quad \text{on} \quad \Omega_m \ , \tag{8.17}$$

with the Cauchy stresses $\boldsymbol{\sigma}_m$ and an external force $\boldsymbol{f}$. The stresses are defined by the constitutive equations for linear elasticity as given in 2.4.2. For a straightforward application of the mesh boundary conditions at the interface between the solid and the fluid domain, the velocities are chosen as unknowns for the mesh equations, in accordance with the LS formulations. Thus, the Cauchy stresses are defined using Hooke's law as

$$\boldsymbol{\sigma}_m = \lambda_m \operatorname{tr}(\nabla^s \boldsymbol{u}_m(\boldsymbol{v}_m))\, \boldsymbol{I} + 2\mu_m\, \nabla^s \boldsymbol{u}_m(\boldsymbol{v}_m) \tag{8.18}$$

with pseudo-material parameters as the first and second Lamé constants $\lambda_m$ and $\mu_m$, and the mesh displacement and velocity in the fluid domain denoted by $\boldsymbol{u}_m$ and $\boldsymbol{v}_m$, respectively. Considering that there are no tractions applied to the mesh and therefore omitting Neumann-type boundaries, the domain $\Omega_m$ is bounded by

$$\partial\Omega_m = \partial\Omega_{Dm} \cup \Gamma_i \qquad \text{and} \qquad \partial\Omega_{Dm} \cap \Gamma_i = \emptyset \ . \tag{8.19}$$

Meaning that the boundary is composed of the subset $\Gamma_i$ representing the fluid-structure interface and the remaining part defined as $\partial\Omega_{Dm}$, where both subsets are Dirichlet-type boundaries. Therefore, the corresponding boundary conditions are specified as

$$\boldsymbol{v}_m = \boldsymbol{v}_f = \boldsymbol{v}_s \qquad \text{on} \qquad \Gamma_i \tag{8.20a}$$

$$\boldsymbol{v}_m = \boldsymbol{v}_D \qquad \text{on} \qquad \partial\Omega_{Dm} \ . \tag{8.20b}$$

Remark: Due to a convenient implementation, the mesh boundary conditions at the interface are always based on the solution of the last time step. Considering a time discretization method, the boundary conditions thus correspond in semi-discrete form to $\boldsymbol{v}_m^{n+1} = \boldsymbol{v}_f^n = \boldsymbol{v}_s^n$ on $\Gamma_i$.

For the mesh domain a standard Galerkin variational approach is applied. Assuming, that no external forces exist and that no traction boundary conditions are applied, the weak form of the linear elasticity problem consists of finding $\boldsymbol{v}_m \in H^1(\Omega_m)^d$ such that

$$\int\limits_{\Omega_m} \boldsymbol{\sigma}_m(\boldsymbol{v}_m) : \nabla^s \delta\boldsymbol{u}_m \ \mathrm{d}V = 0 \qquad \forall\ \delta\boldsymbol{u}_m \in H^1(\Omega_m)^d \ , \tag{8.21}$$

where $\delta\boldsymbol{v}_m$ is a test function fulfilling $\delta\boldsymbol{v}_m = \boldsymbol{0}$ on $\partial\Omega_m\ \forall\ \delta\boldsymbol{v}_m \in H^1(\Omega_m)^d$. For the discretization in space Lagrange interpolation functions with equivalent order as those for the velocities in the solid and fluid domains are selected. The approximation space $\boldsymbol{V} := H^1(\Omega_m)$ is defined as

$$\boldsymbol{V}_k := \{\boldsymbol{v}_m \in H^1(\Omega)^d : \boldsymbol{v}_m|_{\Omega_e} \in P_k(\Omega_e)^d \ \ \forall\, \Omega_e \in \Omega_m\} \subseteq \boldsymbol{V} \ , \tag{8.22}$$

where $P_k$ denote Lagrange interpolation functions of order $k$ on triangles in $d = 2$ or tetrahedrals in $d = 3$. The discretization in time is performed with the same time integration procedure as used in the solid domain, such that the correlation between the displacements and the actual velocities is defined by one of the terms given in Section 7.3.

**Local stiffening**

For the approach based on linear elasticity, the mesh motion can be controlled with the help of the pseudo-material parameters, which enables to vary the stiffness of each mesh element individually. In the following example, changes in the modulus of elasticity $E_m$ and Poisson's ratio $\nu_m$ are considered, from which the Lamé constants are determined as

$$\lambda_m = \frac{E_m\,\nu_m}{(1+\nu_m)(1-2\nu_m)} \qquad \text{and} \qquad \mu_m = \frac{E_m}{2(1+\nu_m)} \tag{8.23}$$

The Young's modulus of each element can be modified by multiplication with different factors, depending, for example, on the deformation, the quality of the elements, the compression and the element size. With an initial modulus defined as $E^e_{m,0}$, which may be the same or varying throughout the domain $\Omega_m$, the elastic modulus for each element at time $t_{n+1}$ is then given as

$$E^e_m(t_{n+1}) = E^e_{m,0} \prod_{i=1}^{b} f^e_i(t_{n+1}) \ , \tag{8.24}$$

where a number of $b$ affecting quantities are taken into account. Another commonly used approach especially in combination with linear elastic mesh equations is the mesh-Jacobian-based stiffening (MJBS), first introduced in Tezduyar et al. [388]. In this case, the Jacobi determinant in the integral of the mesh equations is either dropped or the degree with which it enters the integrals is adjusted. Different schemes exist in which either the Jacobi matrix of the transformation from the parameter space to the physical space is used for scaling, or the determinant of the deformation gradient. When omitting the Jacobi determinant of the transformation matrix $\boldsymbol{J}^e = (\partial \boldsymbol{X}/\partial \boldsymbol{\xi})^e$, this can be interpreted as a local change of the elasticity modulus defined as

$$E^e_m = \frac{E^e_{m,0}}{\det \boldsymbol{J}^e} \ . \tag{8.25}$$

This version of the MJBS leads to a stiffening of smaller elements compared to larger ones, which is usually very appropriate, since elements near the interface where large deformations occur are typically smaller. To account for the deformation of mesh elements, the determinant of the deformation matrix $\boldsymbol{F}^e = (\partial \boldsymbol{x}/\partial \boldsymbol{X})^e$ can be used for scaling the Young's modulus, as presented e.g. in Richter [329], which reads

$$E^e_m = \frac{E^e_{m,0}}{\det \boldsymbol{F}^e} \qquad \text{or} \qquad E^e_m = E^e_{m,0}\left(\det \boldsymbol{F}^e + \frac{1}{\det \boldsymbol{F}^e}\right) \ . \tag{8.26}$$

This leads to an increase in element stiffness when $J^e = \det \boldsymbol{F}^e$ approaches zero, and in the second term also when $J^e$ becomes large. If instead one uses the transformation matrix from the parameter space to the deformed configuration, such that

$$E^e_m = \frac{E^e_{m,0}}{\det \boldsymbol{j}^e} \qquad \text{with} \qquad \boldsymbol{j}^e = (\partial \boldsymbol{X}/\partial \boldsymbol{\xi})^e \ , \tag{8.27}$$

then both the different initial size of the individual elements is taken into account and the change in element size due to the deformation. For more details on the MJBS reference is made to, e.g., Johnson and Tezduyar [224], Stein et al. [372] and Takizawa et al. [379].

**Mesh quality**

In the subsequent section, different approaches for local mesh stiffening are compared. To evaluate the effectiveness of the various mesh moving techniques, a measure of mesh quality is introduced as in Zavattieri et al. [428], which is defined for triangles in 2D as

$$Q_e = C \, \frac{A_e}{P_e^2} \ . \tag{8.28}$$

Here, $A_e$ is the element area, $P_e$ the perimeter of the element, and $C$ is a constant to render the quality of equilateral elements equal to one, which is $C = 20.784619$ for triangles.

## 8.4 Numerical examples: Mesh motion and fluid in ALE description

With an appropriate mesh motion technique and the reformulation of the fluid equations in an Arbitrary-Lagrangian-Eulerian framework, to handle a changing shape of the fluid domain, the presented LS approach is applicable to model large deformations, which is an indispensable requirement to address real world fluid-structure interaction problems. In this section, numerical investigations are presented that address the search for appropriate local stiffening methods to enable smooth mesh deformation and a verification of the ALE formulation for fluids.

### 8.4.1 Dynamic flag with large deformations in moving mesh domain

The next example is designed to find approaches that allow the largest possible deformations without re-meshing. For this purpose, the factors for the local stiffening of the mesh given in (8.24) are investigated as well as mesh-Jacobian-based stiffening and also combinations of both. The underlying geometry is the same as presented in Figure 8.2, except that in this case only the solid flag is modeled surrounded by a linear elastic mesh, i.e. without the calculation of the fluid domain, such that $\Omega = \Omega_s \cup \Omega_m$, see Figure 8.8. The material behavior in the solid domain is defined by the LS stress-velocity formulation for hyperelasticity given in (6.16) and the mesh domain is solved with the variational approach for linear elasticity stated in (8.21). In this example, the physical weights in (6.16) are chosen such that

$$\omega_{s1} = \sqrt{\frac{\Delta t}{\rho_s}} \ , \quad \omega_{s2} = \sqrt{\frac{1}{\mu_s \Delta t}} \ , \quad \omega_{s3} = 1 \ , \tag{8.29}$$

with the solid density $\rho_s$, the shear modulus $\mu_s$ and the time step size $\Delta t$. The boundary conditions for the solid and mesh domain are illustrated in Figure 8.8. The mesh velocities, here denoted with $\boldsymbol{v}_m$, are set to zero at all outer edges and at the cylinder. The flag is fixed at the left end and the remaining edges have stress-free boundary conditions, i.e. $\boldsymbol{\sigma} \cdot \boldsymbol{n} = \boldsymbol{0}$. Additionally, the mesh velocity is prescribed according to (8.20a) at the interface of the mesh and solid domain defined by $\Gamma_i = \partial\Omega_s \cap \partial\Omega_m$.

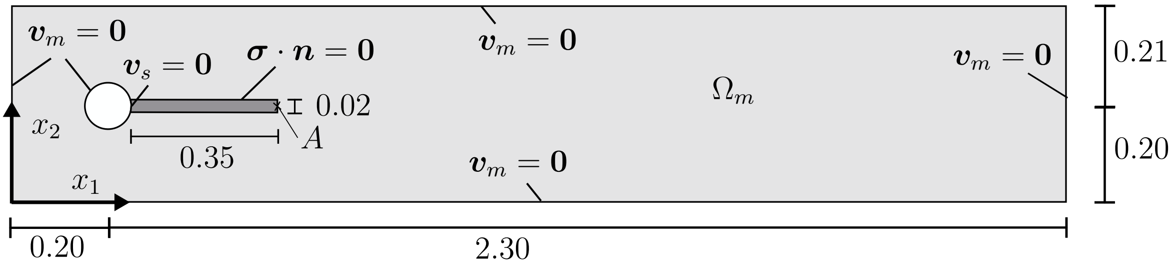

Figure 8.8: Flag in mesh domain - geometry and boundary conditions (unit m)

The choice of this numerical study is mainly motivated by the fact that the same geometry will be used later to compute a fully coupled dynamic FSI benchmark problem. This study is performed before the fully coupled analysis, which is computationally much more expensive, to ensure that the mesh motion is regular and that no excessive distortions appear. In order to create a large deformation in the mesh, the solid material parameters are chosen from the solid benchmark example in Turek and Hron [396], named as CSM3, and stated in Table 8.7. In this case, the elastic flag undergoes vibrations due to an applied body force and reaches a maximum and minimum vertical displacement of about $u_2^{\max} = 1.55 \cdot 10^{-3}\,\mathrm{m}$ and $u_2^{\min} = -1.29 \cdot 10^{-1}\,\mathrm{m}$ at the tip (point $A$ in Figure 8.8). The overall deformations that occur in the solid body in this example are larger than those arising later in the dynamic FSI example. Therefore it is assumed that a mesh configuration that leads to a mesh with good quality in this example is also suitable for the FSI problem.

Table 8.7: Flag in mesh domain - material parameters according to the dynamic benchmark problem CSM3 from Turek and Hron [396]

| Description | Value | Unit |
|---|---|---|
| Solid density $\rho_s$ | $1.0 \cdot 10^3$ | $\mathrm{kg/m^3}$ |
| Young's modulus $E_s$ | $1.4 \cdot 10^6$ | $\mathrm{kg/(m\ s^2)}$ |
| Poisson ratio $\nu_s$ | 0.4 | – |
| Body force $\boldsymbol{f}$ | $(0,\text{-}2.0)^T$ | $\mathrm{kg/(ms)^2}$ |
| Poisson ratio mesh $\nu_m$ | 0.3 | – |

For the discretization in space, vector valued Raviart-Thomas interpolation functions with order $m = 1$ and for the velocities Lagrange polynomials with $k = 2$ are chosen, leading to the solid element denoted as $RT_1P_2$. The mesh velocities are approximated with Lagrange interpolation functions of the same order as for the solid velocity field. In this study, the mesh displacement is investigated for three different mesh levels with the number of elements being 72, 128 or 512 in $\Omega_s$ and 889, 1612 or 6018 in $\Omega_m$. The first mesh is presented exemplarily in Figure 8.9. The discretization in time is performed with a second-order Runge-Kutta scheme denoted as ESDIRK-2 and given in Section 7.3, using a time step size $\Delta t = 0.01\,\mathrm{s}$. A stopping criterion is implemented, such that calculations are automatically aborted as soon as the quality of an element, defined in (8.28), becomes less than zero.

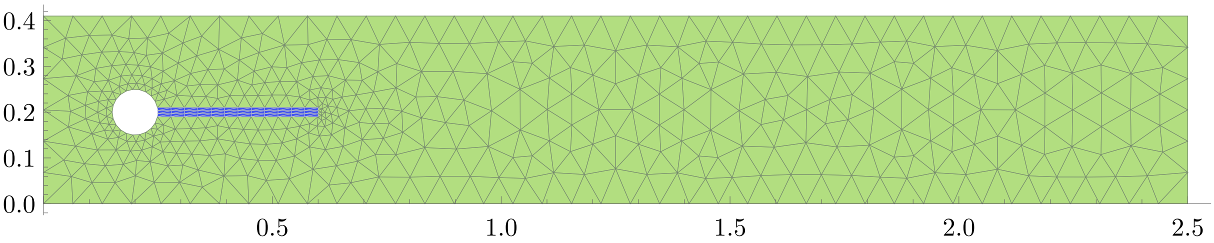

Figure 8.9: Flag in mesh domain - mesh level 1 with 72 solid elements in $\Omega_s$ and 889 mesh elements in $\Omega_m$ in undeformed configuration (unit m)

### Approach 1: uniform $E_m$ on $\Omega_m$

In a first attempt, the element stiffness is not modified locally, and a global elasticity modulus of $E_m^e = 1\,\mathrm{kg/(m\ s^2)}$ is set on the entire domain $\Omega_m$. With this choice, the computation aborts at $t = 0.31\,\mathrm{s}$ at which point the mesh deformation takes the form as illustrated in Figure 8.10 (left), where a detail of the domain is presented with $0.15 < x_1 < 0.8$ and $x_2 < 0.25$. It is visible that the elements close to the tip of the flag where the largest solid displacement occurs are extremely compressed. This is also reflected in the quality of the individual elements which is shown in Figure 8.10 on the right. The quality of most elements in the domain exceeds $Q_e > 0.75$. However, in areas where large deformations are present, especially directly at the interface, the quality decreases. This reveals, that if the mesh parameters are constant over the entire mesh domain only FSI problems with moderate solid motions can be solved without re-meshing. Mesh elements close to the fluid-structure interface should have a higher stiffness, than elements further from the interface in regions with less movement of the background mesh.

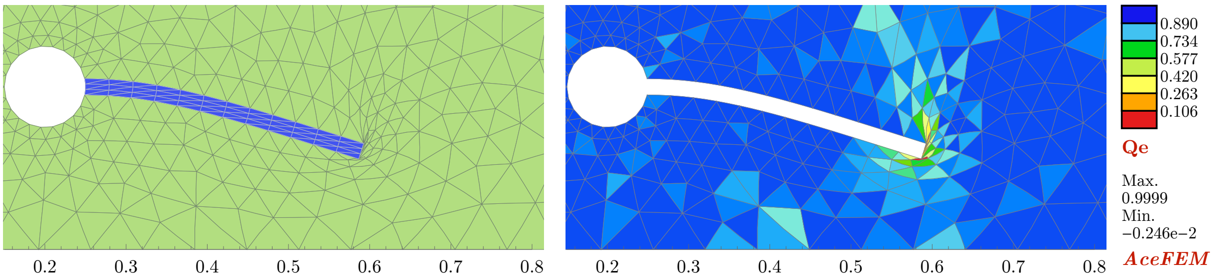

Figure 8.10: Flag in mesh domain - plot of deformed mesh with global elasticity modulus $E_m^e = 1\,\mathrm{kg/(m\ s^2)}$ (left) and quality of elements (right) at $t = 0.31\,\mathrm{s}$

### Approach 2: locally defined $E_{mi}$ on $\Omega_{mi}$ with $i = \{1, 2, 3\}$

For a first attempt to vary the stiffness locally, the mesh domain is divided into three regions with different elastic moduli. The following divisions are selected depending on the total number of elements $n_{\text{ele}}$:

$$\Omega_{m1} := \quad \text{all mesh elements in contact with the solid} \qquad \rightarrow E_{m1}$$

$$\Omega_{m2} := \begin{cases} \{0.235 < x_1 < 0.67\,\&\,0.09 < x_2 < 0.3\} \setminus \Omega_{m1} & \text{if } n_{\text{ele}} = 961 \\ \{0.235 < x_1 < 0.65\,\&\,0.125 < x_2 < 0.28\} \setminus \Omega_{m1} & \text{if } n_{\text{ele}} = 1740 \\ \{0.245 < x_1 < 0.62\,\&\,0.158 < x_2 < 0.242\} \setminus \Omega_{m1} & \text{if } n_{\text{ele}} = 6530 \end{cases} \qquad \rightarrow E_{m2}$$

$$\Omega_{m3} := \quad \Omega_m \setminus \{\Omega_{m1} \cup \Omega_{m2}\} \qquad \rightarrow E_{m3}$$

The partitioning of the domain $\Omega_m$ is depicted in Figure 8.11 (left) as an example for mesh level 1. Different combinations of Young's moduli are investigated and compared. Presented here are example results for $E_{mi} = \{10, 5, 1\}\,\mathrm{kg/(m\ s)}^2$. The simulation with this set of parameters is not aborted caused by a quality measure of $Q_e < 0$. Nevertheless, at the time of the largest displacement of $u_2(A)$ at about $t = 0.5\,\mathrm{s}$ it is clearly visible that the elements in the region $\Omega_{m3}$, in which the specified stiffness is the lowest, are strongly compressed and also the quality decreases significantly, see Figure 8.11 (right).

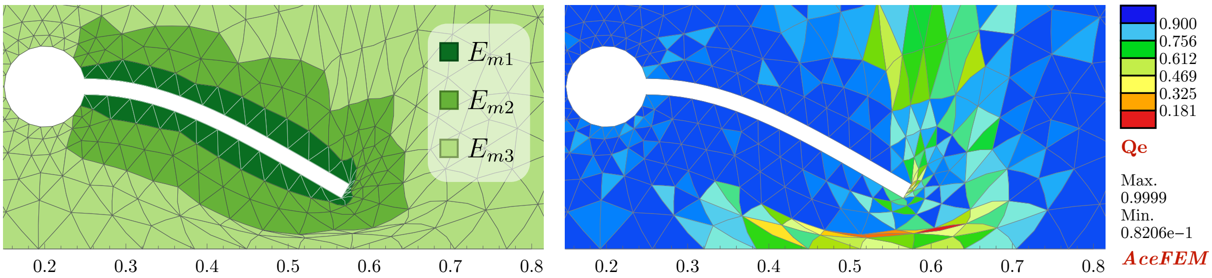

Figure 8.11: Flag in mesh domain - plot of deformed mesh (left) and quality of elements (right) with different E-moduli $E_{mi} = \{10, 5, 1\}\,\mathrm{kg/(m\ s)}^2$ at $t = 0.5\,\mathrm{s}$

The distortion of the mesh can be influenced and thus the quality slightly improved, by different choices of elasticity moduli. To compare several parameter sets, the quality over time for different combinations is sketched in Figure 8.12 (left). In each time step the quality of the worst element is considered. It is shown that depending on the stiffness distribution, the minimum quality at the time of the largest displacement around $t \approx 0.5\,\mathrm{s}$ and $t \approx 1.4\,\mathrm{s}$ is modified little or, in case of a poor choice, the calculation stops due to elements with a negativ quality measure, i.e. $Q_e < 0$. This method has a limited practical usability, especially since the values have to be readjusted depending on the mesh and the magnitude of the maximum deformation.

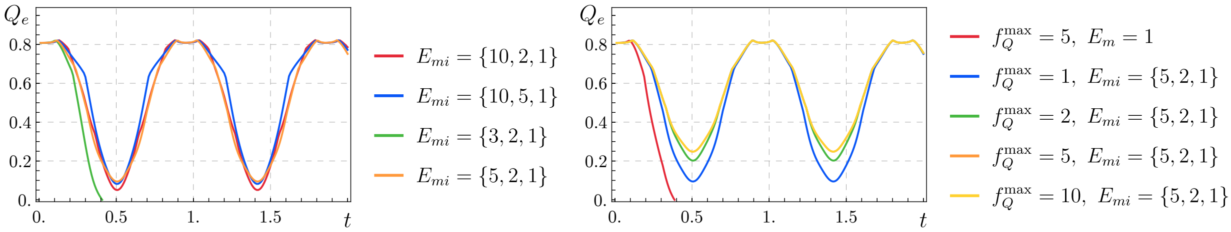

Figure 8.12: Flag in mesh domain - quality measure $Q_e$ over time for different combinations of E-moduli (left) and additional scaling with $f_Q^e$ (right)

## Approach 3: local stiffening based on element quality

In a next test, a factor is simply defined based on the quality of the elements. This increases the Young's modulus in each element as the quality decreases, see (8.24), in the way that $E_m^e = E_{m,0}^e\, f_Q^e$. The underlying function for the factor $f_Q^e$ depending on the quality $Q_e$ is given by

$$f_Q^e = \min\left[\frac{1}{Q_e},\ f_Q^{\max}\right] \tag{8.30}$$

and the course is shown in Figure 8.13 (left). Thereby an upper limit is defined with $f_Q^{\max}$. The initial Young's modulus is prescribed on the entire domain as $E_{m,0}^e = 1\,\mathrm{kg/(m\ s^2)}$.

With the maximum factor chosen between $f_Q^{\max} = [2, 10]$ the computations are aborted between $0.35 < t < 0.43\,\mathrm{s}$, because a minimum quality below zero occurs. With this approach, using only the factor $f_Q^e$ to control the stiffness, no variant is found in which the calculation with mesh level 1 succeeded without being aborted.

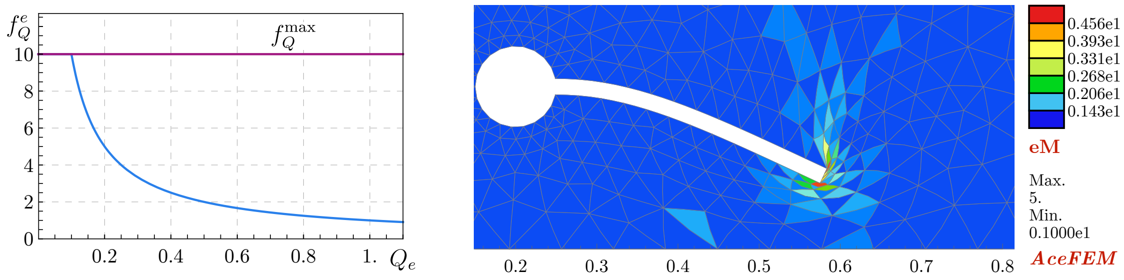

Figure 8.13: Flag in mesh domain - factor to increase stiffness depending on quality (left) and resulting distribution of E-modulus on deformed domain at $t = 0.39\,\mathrm{s}$ with $f_Q^{\max} = 5$

The underlying reason is well visible in Figure 8.13 (right). Increasing the stiffness only based on the quality of the individual elements leads to a too unbalanced distribution of the E-modulus. With this method, neighboring elements can have an extremely different stiffness, leading to frequent overlapping of the elements. However, the scaling based on the element quality can provide an improvement of element deformation if additionally the stiffness is specified separately in individual regions as described in the second approach. This is visible by evaluating $Q_e$ over time in Figure 8.12 (right) In this diagram, results for different factors $f_Q^{\max}$ are plotted where the elastic moduli in the subdomains are set to $E_{mi} = \{5, 2, 1\}$. In addition, the figure includes the curve of $Q_e$ when the initial modulus is uniform and only a stiffening with the factor $f_Q$ is applied. One can see that the first calculation are terminated because the minimum element quality is below zero. By increasing the influence of $f_Q^e$, the measure of the quality in the worst element can be improved, up to a certain level.

### Approach 4: local stiffening based on element displacement

A more uniform distribution of stiffness than in the last examples can be achieved if a local factor is determined based on the displacement of each element. For this purpose, the following functions are used in a further analysis

$$f^e_{u,lin} = \min\left[(1 + f_u^{\max}) \cdot \left(\frac{u^e_{\max}}{u^n_{\max}}\right),\ f_u^{\max}\right] \,, \tag{8.31a}$$

$$f^e_{u,exp} = \min\left[(f_u^{\max})^\wedge\!\left(\frac{u^e_{\max}}{u^n_{\max}}\right),\ f_u^{\max}\right] \,, \tag{8.31b}$$

with a linear and an exponential course as depicted in Figure 8.14 (left). Within this function $u^e_{\max} = \max(u_1^I, u_2^I)$ denotes the maximum displacement of the nodes within the considered element, which is scaled by the maximum displacement $u^n_{\max}$ of the last time step on the entire domain $\Omega_m$, and the factor $f_u^{\max}$ defines again the upper bound of the local factor.

A linear influence of the displacement on the stiffness is insufficient to avoid highly distorted elements. All calculations in which the E-modulus is scaled by $f^e_{u,lin}$, with a choice

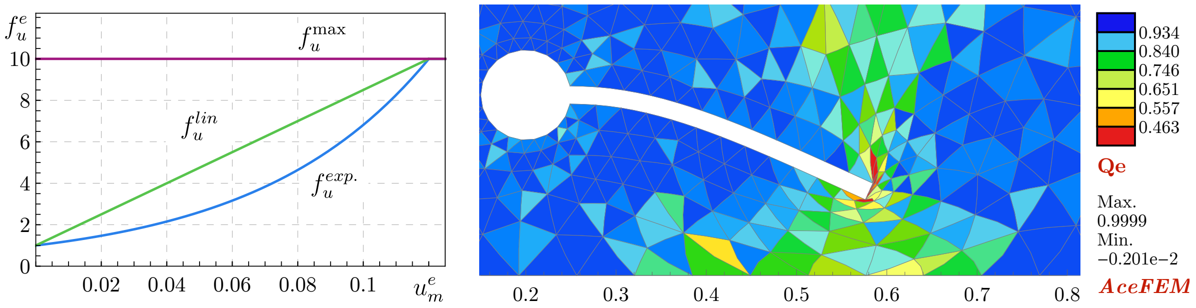

Figure 8.14: Flag in mesh domain - factor to increase stiffness depending on displacement (left) and quality of elements with linear scaling and $f_u^{\max} = 20$ at $t = 0.38$ (right)

of $f_u^{\max} \in [2, 50]$, are terminated before the maximum flag deformation is reached due to the stopping criterion $Q_e < 0$. Figure 8.14 (right) illustrates the quality of the distorted mesh with $f_u^{\max} = 20$ at the time of termination $t = 0.38\,\mathrm{s}$. The triangles surrounding the tip of the flag are strongly skewed.

Increasing the stiffness based on an exponential function of the displacement yielded the curves of the quality measure over time shown in Figure 8.15 (left). The graph shows that only for a limited range of the maximum factor $f_u^{\max} \in [20, 30]$ acceptable results are obtained without damage in the mesh. This study reveals on the one hand that a linear influence of the displacement on the stiffness is too small, on the other hand that the effect can be improved by an exponential function, although this too is very limited. Thus, the application of this scaling alone is not suitable to solve problems with large mesh deformations. Even though the distribution of stiffness over the domain appears reasonable, see Figure 8.15 (right), with higher values where large deformations occur and a modulus of elasticity close to one where no deformations occur. This plot presents the deformed configuration at $t = 0.5\,\mathrm{s}$ obtained with an exponential scaling and $f_u^{\max} = 20$.

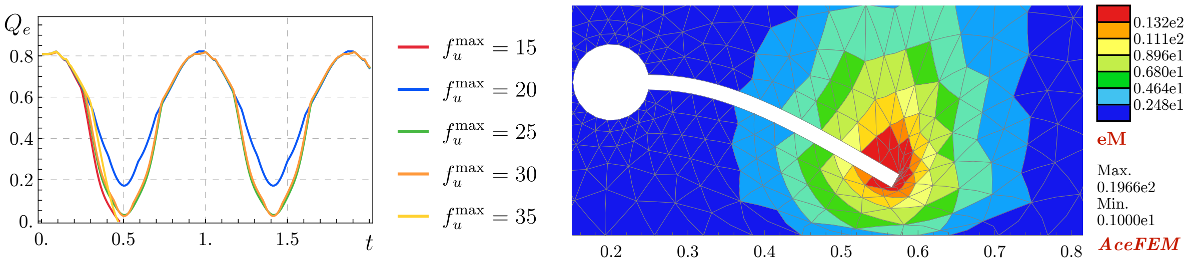

Figure 8.15: Flag in mesh domain - quality measure $Q_e$ over time for exponential scaling with $f_{u,exp}^e$ (left) and E-modulus on deformed domain at $t = 0.5\,\mathrm{s}$ with $f_u^{\max} = 20$

### Approach 5: mesh-Jacobian-based stiffening (MJBS)

A further study examines stiffening based on the transformation matrices of the mesh, where the modulus of elasticity is scaled either by the determinant of $\boldsymbol{J}^e = (\partial \boldsymbol{X} / \partial \boldsymbol{\xi})^e$ or $\boldsymbol{j}^e = (\partial \boldsymbol{x} / \partial \boldsymbol{\xi})^e$, see (8.25) and (8.27), respectively. In the first variant, the stiffness of the individual elements is thus simply determined depending on their initial size, and in the second, the change in volume of the individual elements is also taken into account. Thus, the local elasticity modulus in each element is defined as

$$E^e_{mJ} = E^e_{m,0} \cdot f^e_J \qquad \text{with} \qquad f^e_J = \frac{1}{\det \boldsymbol{J}^e} \tag{8.32a}$$

$$\text{or} \qquad E^e_{mj} = E^e_{m,0} \cdot f^e_j \qquad \text{with} \qquad f^e_j = \frac{1}{\det \boldsymbol{j}^e}\ . \tag{8.32b}$$

This approach has been tested for all three mesh levels. The evolution of the quality measure over time is presented in Figure 8.16 (left). Notice that in both variants for the first and second mesh the minimum element quality remains greater than 0.2. For the first mesh a significant improvement is visible at the times of maximum solid deformation when the volume change of the elements is taken into account, i.e. with Eq.(8.32b). In case of the finest mesh the calculation even aborts if in the scaling of the Young's modulus the deformation is neglected, i.e. when using (8.32a). The explanation for this is apparent in Figure 8.16 (right), which shows the element quality on the deformed domain at the time of collapse at $t = 0.47\,\mathrm{s}$. In the lower region where the elements are relatively large, and therefore the stiffness scaled by $f^e_J$ comparably low, the elements are strongly compressed.

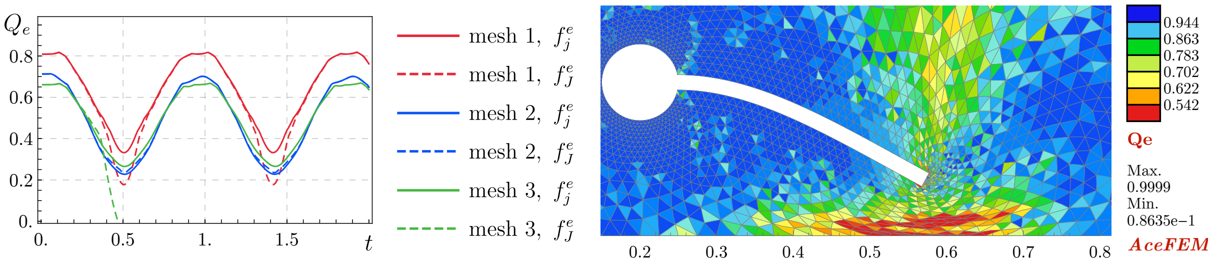

Figure 8.16: Flag in mesh domain - quality measure $Q_e$ over time for both MJBS approaches (left), and element quality on deformed mesh 3 at $t = 0.47\,\mathrm{s}$ with $E^e_{mJ}$ (right)

**Conclusion:**

In general, local stiffening of elements is required to account for large deformations in the mesh domain without the need for re-meshing due to overly distorted elements. The modulus of elasticity can be determined individually based on various functions in each element. For example, the influencing variable can be a defined quality measure, the deformation or change in volume or area. In the considered example, stiffening based on the determinant of the transformation matrix to the current configuration (8.32b) proved to be the most effective approach. However, a combination of a mesh partitioning with different predefined E-moduli, and additional application of factors for local stiffening based on element quality and displacement yielded satisfactory results for the finest mesh. The resulting mesh deformations at time $t = 0.5\,\mathrm{s}$, where the maximum flag deflection occurs, are presented in Figure 8.17. In both versions, the total deformation of the mesh is distributed very regularly among the individual elements. This is also reflected in the quality measure $Q_e$. The distribution of this quantity over the entire mesh domain in Figure 8.18 shows that even at the time of the largest deformation for the finest mesh, the quality of the individual elements remains acceptable.

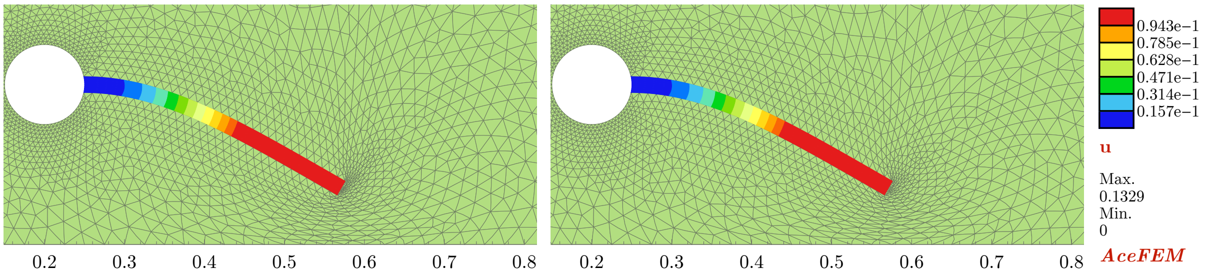

Figure 8.17: Flag in mesh domain - deformed configuration of mesh level 3 and solid displacement at $t = 0.5\,\text{s}$, left: combination of different factors with $f_u^{\max} = 5$, $f_Q^{\max} = 2$, $E_{mi} = \{5, 2, 1\}$ , right: stiffening with MJBS (8.32b)

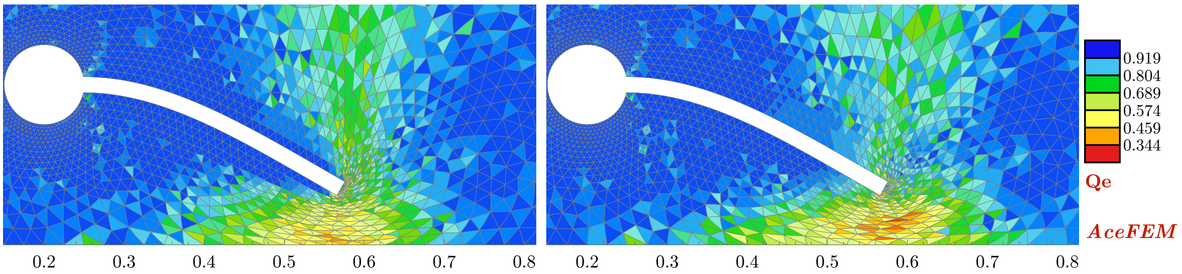

Figure 8.18: Flag in mesh domain - quality measure with mesh level 3 at $t = 0.5\,\text{s}$, left: combination of different factors with $f_u^{\max} = 5$, $f_Q^{\max} = 2$, $E_{mi} = \{5, 2, 1\}$, right: stiffening with MJBS (8.32b)

### 8.4.2 Channel flow with moving background mesh

Before the presented LS stress-velocity fluid formulation in ALE description (4.17) is applied to coupled FSI problems, a simple channel flow with a moving background mesh is calculated for verification. The mesh is solved based on the equations for linear elasticity given in 8.3.4. The problem with the domain $\Omega_f = \Omega_m = [0, L] \times [0, H]$, as shown in Figure 8.19, consists of a straight channel with a parabolic inflow in $x_1$-direction given by

$$\hat{v}_f(x_2, t) = 1.2 \frac{(H - x_2)\, x_2}{H^2}\, \lambda_v(t) \; , \tag{8.33}$$

which is applied depending on time with the following function

$$\lambda_v(t) = \begin{cases} \sin\left[0.5\,\pi\, t\right] & \text{if} \quad t \leq 1\,\text{s} \\ 1 & \text{if} \quad t > 1\,\text{s} \end{cases} \; . \tag{8.34}$$

The height and length of the geometry are chosen as $H = 0.5\,\text{m}$ and $L = 1\,\text{m}$. The top and bottom walls have no-slip boundary conditions and at the outflow the stress component is defined as $\boldsymbol{\sigma}_1 \cdot \boldsymbol{n} = 0$. The mesh is fixed at all outer edges, i. e. $\boldsymbol{v}_m = 0$. A displacement in $x_2$-direction is imposed on the horizontal centerline to generate a deformation of the background mesh. The function, which is applied to all nodes between $\frac{1}{8}L \leq x_1 \leq \frac{7}{8}L$ is

$$\hat{u}_m(x_1, t) = \left( 0.09074 - \frac{1.659 x_1}{L} + \frac{9.244 x_1^2}{L^2} - \frac{15.17 x_1^3}{L^3} + \frac{7.585 x_1^4}{L^4} \right) \lambda_u(t) \; , \tag{8.35}$$

and is constructed in such a way that the slope at the edge is very small and gradually increases toward the center of the channel. Additionally, the change over time is defined by a sinus function given by $\lambda_u(t) = \sin[0.5\,\pi\,t]$. The obtained function as a function of time and spatial $x_1$-coordinate can be seen in Figure 8.20 for the range $L/8 < x_1 < 7/8L$ and the time interval $0 < t < 10\,\text{s}$. The material parameters for the fluid and the mesh are defined as listed in Table 8.8.

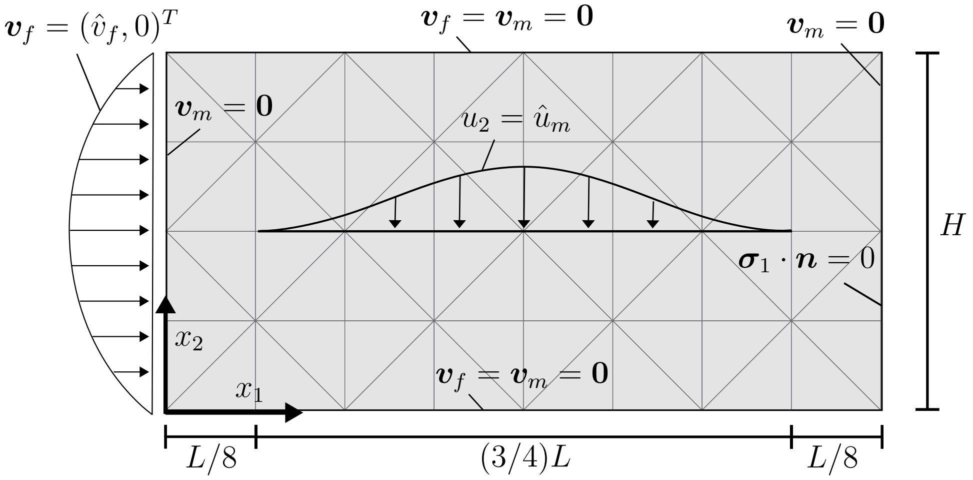

Figure 8.19: Channel ALE - geometry and boundary conditions

The domain is discretized in space by a structured grid with a partition $16 \times 32$, leading to 1024 triangular elements of order $RT_1P_2$ in $\Omega_f$ and of order $P_2$ in $\Omega_m$. For the time discretization the second-order Runge-Kutta scheme denoted as ESDIRK-2 and presented in Section 7.3 is used.

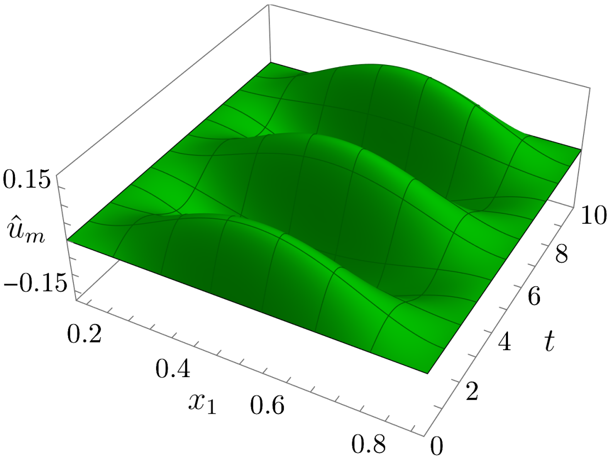

Figure 8.20: Channel ALE - function $\hat{u}_m(x_1, t)$ for mesh deformation over time

Table 8.8: Channel ALE - parameters

| Description | Value & Unit |
|---|---|
| Fluid density $\rho_f$ | 1 kg/m$^3$ |
| Viscosity $\nu_f$ | 0.001 m$^2$/s |
| Mesh elasticity $E_m$ | 1 kg/(m s$^2$) |
| Mesh Poisson ratio $\nu_m$ | 0.3 |

To validate the SV fluid formulation in ALE description, several quantities are evaluated over time while the mesh is moving. On the one hand, the flow velocity of the fluid in $x_1$-direction in the center of the domain at $\boldsymbol{x} = (0.5, 0.25)\,\text{m}$ is measured. On the other hand, the enstrophy $Z$ and kinetic energy $E$ in the domain at each instant are calculated. These are defined as

$$Z = \frac{1}{2}\int_{\Omega_f} \boldsymbol{\omega}^2 \;\mathrm{d}V = \frac{1}{2}\int_{\Omega_f} (\nabla \times \boldsymbol{v})^2 \;\mathrm{d}V \tag{8.36}$$

and

$$E = \frac{1}{2} \int_{\Omega_f} \rho_f |\boldsymbol{v}|^2 \, \mathrm{d}V \ , \tag{8.37}$$

where $\boldsymbol{\omega}$ denotes the vorticity, computed as the curl of the velocity vector. The evolution of all quantities over time is shown in Figure 8.21, where the kinetic energy has been increased by a factor of 50 for better visualization. Furthermore, the mesh displacement in $x_2$-direction in the center of the domain is depicted, reflecting the applied sinusoidal function. In the graph it is clearly visible that the course of the fluid quantities remains unaffected by the deformation of the background mesh. This can also be observed in the illustration of the velocity field distribution in Figure 8.22, in which the contour lines remain unchanged regardless the mesh deformation.

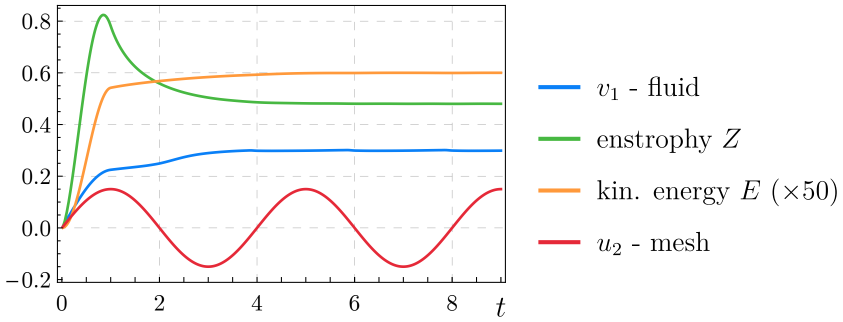

Figure 8.21: Channel ALE - evolution over time of fluid velocity $v_1$ and mesh displacement $u_2$ at $(L/2, H/2)$, enstrophy $Z$ and kinetic energy $E$ over domain $\Omega_f$

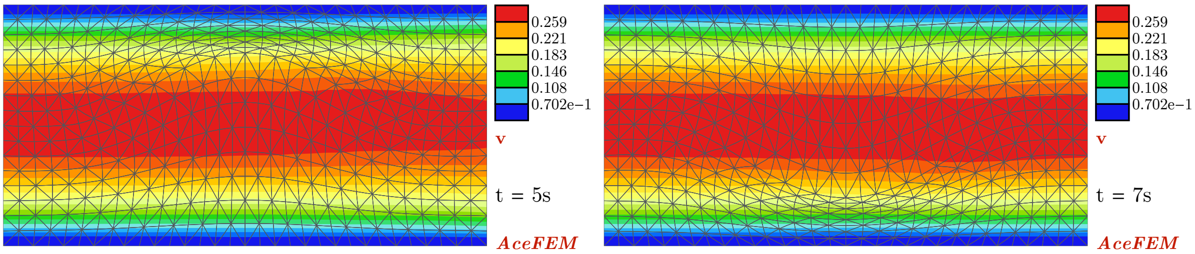

Figure 8.22: Channel ALE - distribution of fluid velocity $\boldsymbol{v}$ at $t = 5\,\mathrm{s}$ (left) and $t = 7\,\mathrm{s}$ (right) with deformed background mesh (unit m/s)

## 8.5 Numerical examples: Dynamic FSI problems with large deformations

In the previous sections, the necessary elements for the computation of monolithically coupled dynamic FSI problems using the mixed least-squares FEM have been derived and verified independently. Moreover, the basic coupling of the stress-velocity formulations for the fluid without consideration of a moving domain and the solid for linear elasticity has already been tested. Without the possibility of deformation in the fluid domain, only examples with small deformations could be solved. For the numerical solution of FSI problems with large deformations, the motion of the fluid domain must be considered. Therefore, the LS stress-velocity fluid formulation in Arbitrary-Lagrangian-Eulerian description and suitable approaches for the computation of the background grid were presented and tested in previous sections. This section aims to combine the approaches tested separately and to study the coupling by means of examples.

In a first step, the coupling of the fluid ALE functional and the SV solid functional for linear elasticity is tested by evaluating a channel flow with elastic contracting wall. This combination enables the solution of FSI problems with large deformations in the fluid domain, but is valid only for small strains in the solid domain. In order to compute interaction problems considering also large strains, the fluid ALE formulation is coupled in a next step with the stress-velocity formulation for hyperelasticity. As a final example, the flow around a cylinder with an attached flag undergoing large deformations is analyzed. Various time integration methods are applied to solve this complex problem, with attention to higher order methods and the use of adaptive time stepping.

### 8.5.1 Channel flow with contracting linear elastic walls

The first numerical example in this section serves as a first test to couple the SV fluid formulation in an ALE framework (4.17) with moving background mesh to the SV solid formulation for linear elasticity (6.3). The mesh deformation is considered by solving the equations of linear elasticity given in 8.3.4. Thus the resulting least-squares functional for fluid-structure interaction problems considering a moving fluid domain, but with restriction to small strains in the solid regime is given by

$$\mathcal{F}^{FSI}(\boldsymbol{\sigma},\boldsymbol{v}) = \mathcal{F}^{F}_{ALE}(\boldsymbol{\sigma},\boldsymbol{v}) + \mathcal{F}^{LE}(\boldsymbol{\sigma},\boldsymbol{v}) \ . \tag{8.38}$$

The weighting factors for the residual terms in the fluid and solid formulation in this example are chosen as

$$\omega_{f1} = \sqrt{\frac{\Delta t}{\rho_f}} \ , \quad \omega_{f2} = \sqrt{\frac{1}{\rho_f \nu_f}} \ , \quad \omega_{f3} = 1 \ , \quad \omega_{s1} = \sqrt{\frac{\Delta t}{\rho_s}} \ , \quad \omega_{s2} = \sqrt{\frac{\mu_s}{\Delta t}} \ . \tag{8.39}$$

The considered domain consists of a rectangular mesh-fluid region $\Omega_f = \Omega_m$ bounded at the top and bottom by a solid region $\Omega_s$, as illustrated in Figure 8.23. The fluid has no prescribed inflow, but zero normal stress at the right and left boundary. A flow is created by compressing the fluid area through movement of the upper and lower solid walls. Therefore, a time dependent velocity in vertical direction is applied to the solid boundary according to

$$\hat{v}_s(x_1,t) = (0.32\,x_1^2 - 0.32\,x_1^3 + 0.08\,x_1^4)\ \lambda_v(t) \ , \tag{8.40}$$

with the sinusoidal function

$$\lambda_v(t) = \sin[0.5\,\pi\,t] \ . \tag{8.41}$$

On the left and right boundary, the solid as well as the mesh are fixed. In addition to the inherent fulfillment of the fluid-solid coupling conditions at the interface $\Gamma_i$ for velocities $\boldsymbol{v}_s = \boldsymbol{v}_f$ and tension vector $\boldsymbol{\sigma}_s \cdot \boldsymbol{n} = \boldsymbol{\sigma}_f \cdot \boldsymbol{n}$, the mesh velocities are prescribed based on the velocities of the solid, i.e. $\boldsymbol{v}_m = \boldsymbol{v}_s$. For implementation reasons, the known solid values of the previous time steps are used here. The material parameters for all three domains are given in Table 8.9.

The time discretization for this example is performed using the second-order Houbolt method, cf. (7.35), with a constant time step size $\Delta t = 0.02\,\mathrm{s}$. And for the space, Lagrange interpolation functions of order two for the velocities in all domains are used, and vector-valued Raviart-Thomas interpolations for the stresses in fluid and solid domain, leading to the elements denoted as $RT_1P_2$ (solid, fluid) and $P_2$ (mesh). The calculations are performed with a mesh consisting of 384 triangular elements in each domain, i.e. 192 in each solid wall.

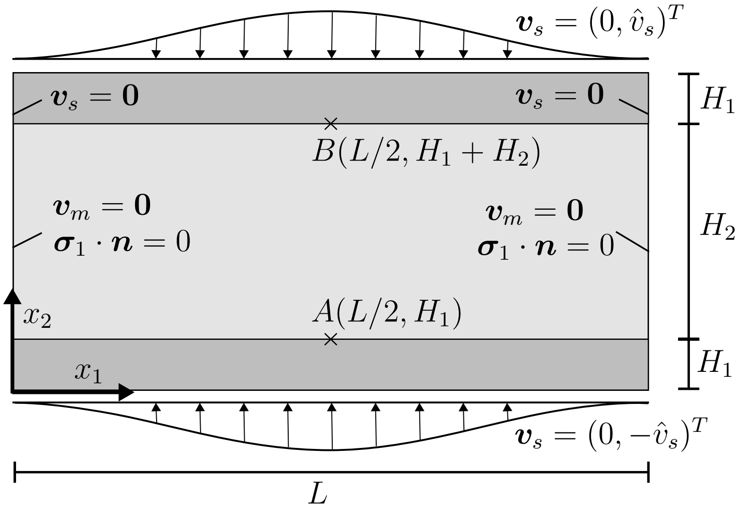

Figure 8.23: Channel contracting - geometry and boundary conditions with $L = 2\,\text{m}$, $H_1 = 0.1\,\text{m}$, $H_2 = 0.5\,\text{m}$

Table 8.9: Channel contracting - material parameters

| Parameter | Value & Unit |
|---|---|
| Density $\rho_f$ | 1 kg/m$^3$ |
| Viscosity $\nu_f$ | 0.002 m$^2$/s |
| Density $\rho_s$ | 1 kg/m$^3$ |
| Elasticity $E_s$ | 100 kg/m$^3$ |
| Poisson ratio $\nu_s$ | 0.4 |
| Elasticity $E_m$ | 1 kg/(m s$^2$) |
| Poisson ratio $\nu_m$ | 0.3 |

To verify the correct transfer of the solid velocities as boundary conditions to the background mesh of the fluid domain, the velocities as well as displacements in $x_2$-direction at the midpoint of the upper and lower interfaces are measured over time. The resulting mesh and solid/fluid quantities measured at points $A = (1, 0.1)\,\text{m}$ and $B = (1, 0.6)\,\text{m}$ are plotted for a time interval $t = [0, 11]\,\text{s}$ in Figure 8.24. The graphs demonstrate that the values for the velocities, which are directly applied as boundary conditions to the mesh, as well as for the displacements, which are calculated by means of the time discretization method, are in agreement.

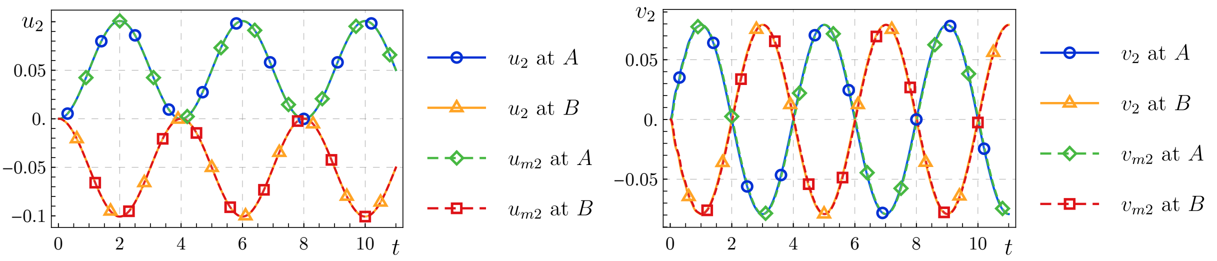

Figure 8.24: Channel contracting - evolution of displacement (left) and velocity (right) of solid/fluid $(u_2, v_2)$ and mesh $(u_{m2}, v_{m2})$ at center points $A(1, 0.1)\,\text{m}$ and $B(1, 0.6)\,\text{m}$ of lower and upper interface (units m, m/s)

The satisfaction of the interface conditions between fluid and solid domain can be observed in figures 8.25 and 8.26. In the former, the velocity components at time $t = 11\,\text{s}$ are depicted. At that moment, the walls move back towards their initial position, causing fluid to flow back into the channel. This is reflected in the $v_1$ velocity, with positiv values on the left half of the channel and negativ ones on the right side. The component in $x_1$-

direction is much larger in the fluid domain than in the solid, which hardly moves in this direction. However, the velocity component $v_2$ has a similar magnitude in both domains with maximum values in the center of the channel consistent with the applied boundary conditions.

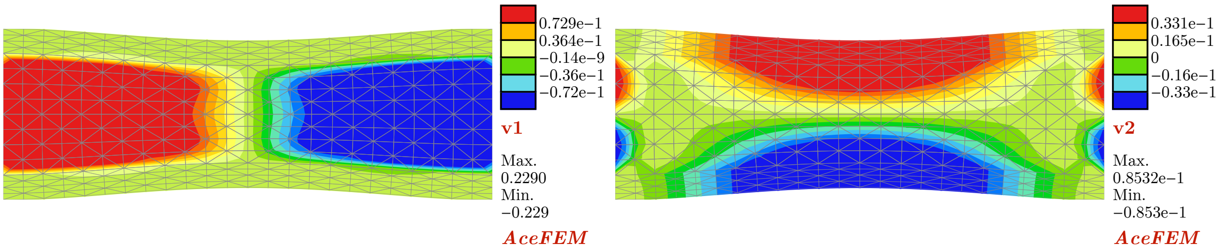

Figure 8.25: Channel contracting - distribution of velocity components in solid and fluid domains at $t = 11\,\mathrm{s}$ (units m/s)

For the stresses, the components $\sigma_{11}$ and $\sigma_{22}$ are shown as examples in Figure 8.26. Here, the normal stresses in $x_1$-direction are much higher in the walls than in the fluid. In a separate representation of the stresses in both domains with individual plot ranges, the stress component in the fluid domain becomes visible as well. The stress component $\sigma_{22}$ at the considered time at maximum compression is highest in the center, as well as at the edges in the solid area due to the clamping of the walls on the right and left end.

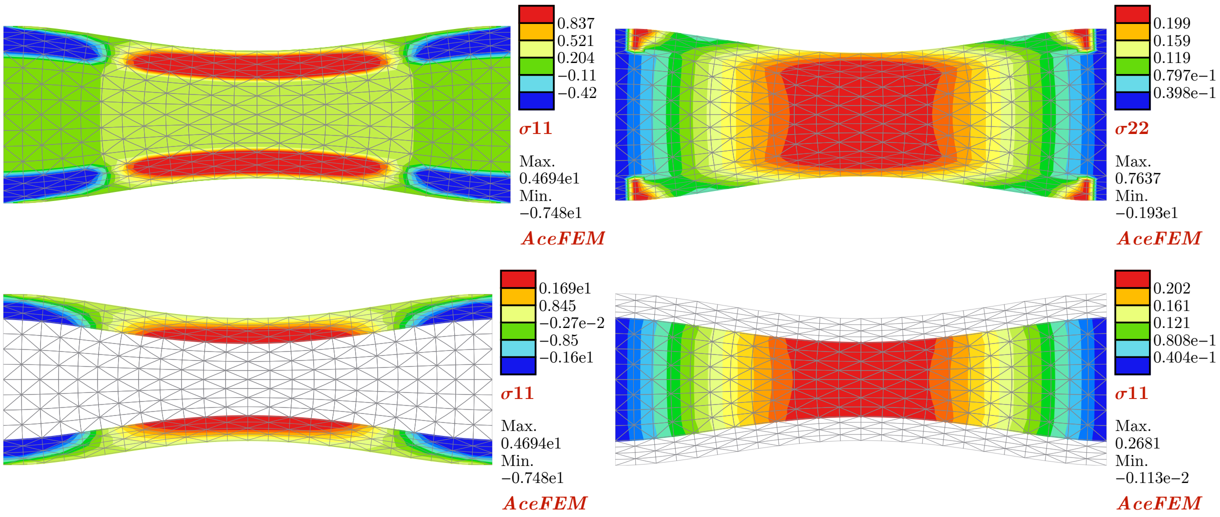

Figure 8.26: Channel contracting - distribution of stress components in solid and fluid domains together (top) and normal stress $\sigma_{11}$ in both domains separately (bottom) at $t = 10\,\mathrm{s}$ (units $\mathrm{N/m^2}$)

Remark: This numerical example has demonstrated the basic implementation of the monolithic coupling of the mixed LS SV formulations including the consideration of a deformable fluid domain. However, it should be noted that the SV formulation used here for the solid based on the linear elasticity approach is valid only for small strains. In order to determine the true stresses in the case of large deformations, e.g. hyperelastic material behavior must be taken into account.

### 8.5.2 Unsteady flow around a cylinder with flag

In the examples considered so far, the assumption of linear-elastic material behavior in the solid has been made. For the calculation of FSI problems with large strains, this simplified assumption is not valid. Therefore, the stress-velocity formulation based on the hyperelastic material behavior according to St. Venant-Kirchhoff type is used in the following, which is defined in (6.16). The SV fluid ALE formulation given in (8.16) is used to be able to account for mesh deformations. Thus the resulting least-squares functional for dynamic fluid-structure interaction problems reads

$$\mathcal{F}^{FSI}(\boldsymbol{\sigma}, \boldsymbol{v}) = \mathcal{F}^{F}_{ALE}(\boldsymbol{\sigma}, \boldsymbol{v}) + \mathcal{F}^{HE}(\boldsymbol{\sigma}, \boldsymbol{v}) \; . \tag{8.42}$$

For the solid formulation the Lagrangian description is used with the actual configuration as reference frame. This is implemented by generating the shape functions, using the construction rules specified in 3.2, directly in the current configuration with $\boldsymbol{x} = \boldsymbol{X} + \boldsymbol{u}$. Thus, the stress degrees of freedom in the solid formulation correspond to the Cauchy stresses. Consequently, these match the stress degrees of freedom in the fluid formulation, allowing the coupling conditions (8.6b) to be automatically satisfied by the appropriate choice of shape functions, as defined in (8.8) and (8.22).

The setup is based on the benchmark problem described in Turek et al. [399] and Turek and Hron [396] denoted as FSI 2. The geometry and boundary conditions of this FSI problem are similar to the steady-case problem as depicted in Figure 8.2 in Section 8.2.1 except for the magnitude of the mean inflow velocity in $x_1$-direction defined in (8.11). Furthermore, the mesh velocity is set to zero at all outer edges and on the cylinder, such that all relevant boundary conditions are displayed together in Figure 8.27.

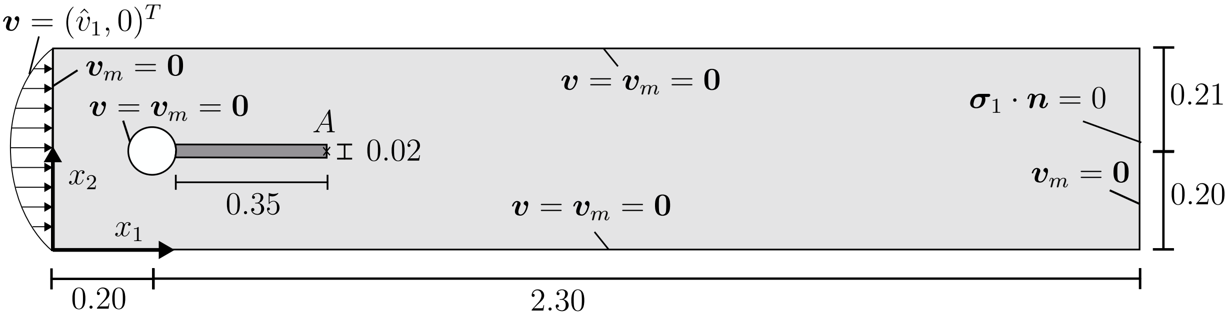

Figure 8.27: FAC-flag (2) - geometry and boundary conditions (unit m)

The material parameters are set equivalent to specification in Turek et al. [399] and listed in Table 8.10. With the characteristic length of $L_{ch} = 0.1\,\text{m}$, corresponding to the diameter of the cylinder, and the given material and flow parameters, the Reynolds number is $Re = 100$. The mesh deformation is considered by solving the equations of linear elasticity given in Section 8.3.4. For a smooth deformation of the fluid background mesh local stiffening based on mesh-Jacobian-based stiffening is included. Through this, the mesh stiffness is determined individually for each element, depending on the current size of the respective element, with decreasing stiffness as the size increases. As a result, elements near the fluid-structure interface with an initially smaller area, see Figure 8.28, and those that are strongly compressed, generally have a higher resistance to deformation, avoiding strong mesh distortions.

Table 8.10: FAC-flag (2) - material parameters for FSI2 from Turek et al. [399] and chosen pseudo-material parameter for linear elastic mesh deformation

| Description | Value | Unit |
|---|---|---|
| Mean inflow velocity $\bar{v}$ | 1.0 | m/s |
| Fluid density $\rho_f$ | 1.0 $\times 10^3$ | kg/m$^3$ |
| Viscosity $\nu_f$ | 0.001 | m$^2$/s |
| Solid density $\rho_s$ | 10 $\times 10^3$ | kg/m$^3$ |
| Young's modulus $E$ | 1.4 $\times 10^6$ | kg/(m s$^2$) |
| Poisson ratio $\nu_s$ | 0.4 | - |
| Young's modulus $E_m$ | 1 | kg/(m s$^2$) |
| Poisson ratio $\nu_m$ | 0.3 | - |

For the following numerical example, the weighting factors are chosen such that the individual residual terms have the same unit. The units of the individual residuals for the fluid and solid formulation are

$$\left[\mathcal{R}_1^F\right] = \frac{\text{kg}}{\text{m}^2\,\text{s}^2}\,, \qquad \left[\mathcal{R}_2^F\right] = \frac{\text{kg}}{\text{m}\,\text{s}^2}\,, \qquad \left[\mathcal{R}_3^F\right] = \frac{1}{\text{s}}\,,$$

$$\left[\mathcal{R}_1^{HE}\right] = \frac{\text{kg}}{\text{m}^2\,\text{s}^2}\,, \qquad \left[\mathcal{R}_2^{HE}\right] = \frac{\text{kg}}{\text{m}\,\text{s}^2}\,, \qquad \left[\mathcal{R}_3^{HE}\right] = \frac{\text{kg}}{\text{m}\,\text{s}^2}\,.$$

The residuals can all be transformed into the same unit with the resulting unit of the functional being $\left[\mathcal{F}^{FSI}\right]$ =kg/(sm)$^2$, by choosing the following weights

$$\omega_{f1} = \sqrt{\frac{f_{dt} L_{ch}}{\rho_f v_0^2}}\,, \qquad \omega_{f2} = \sqrt{\frac{1}{\rho_f \nu_f v_0}}\,, \qquad \omega_{f3} = \sqrt{L_{ch} \rho_f Re}\,,$$

$$\omega_{s1} = \sqrt{\frac{f_{dt} L_{ch}}{\rho_s v_0^2}}\,, \qquad \omega_{s2} = \sqrt{\frac{1}{\rho_s v_0 L_{ch}}}\,, \qquad \omega_{s3} = \sqrt{\frac{1}{\rho_s v_0 L_{ch}}}\,.$$

The parameters therein are characteristic quantities, such as characteristic length $L_{ch}$, bulk velocity $v_0$, i.e. mean inflow velocity, and Reynolds number $Re$. In addition, the choice of time step size is taken into account by the factor $f_{dt} = \Delta t / \Delta t_0$, where the characteristic step size $\Delta t_0$ is chosen as the initial increment for adaptive time stepping.

Remark: Various combinations of weighting factors have been investigated, and the selection presented here provided the best results in terms of stability and accuracy for the studied problem. Overall, the coupled formulation shows a high sensitivity to the magnitude of the chosen weights. As stated also in Rasmussen [321], Rasmussen et al. [323] and Kayser-Herold [227], especially for complex problems such as monolithic coupled FSI calculations, the choice of residual weightings is extremely important for the quality of the solution or even for the solvability of the numerical problem.

The calculations are performed with different mesh refinements generated using Gmsh, cf. Geuzaine and Remacle [165], and the element of order $RT_2P_3$. The grids are constructed in a way such that elements close to the interface and the cylinder are smallest and get larger towards the outer walls. An example mesh is shown in Figure 8.28, where the domains are discretized with 257 solid and 2329 fluid triangular elements, respectively. Table 8.11 summarizes the information on the different meshes, including the number of elements in the solid as well as the fluid domain, and the number of degrees of freedom.

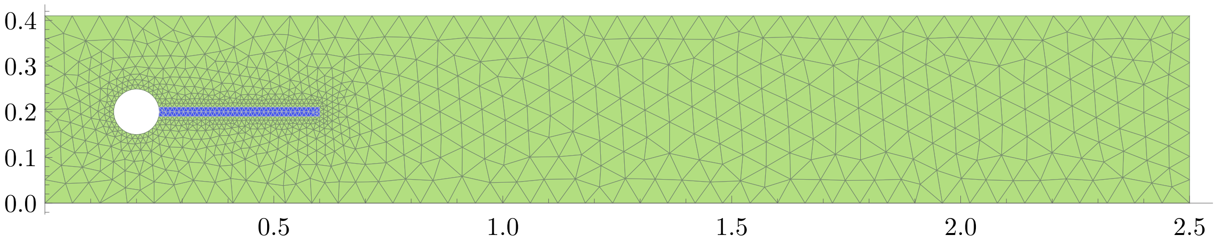

Figure 8.28: FAC-flag (2) - example meshing generated with Gmsh, mesh level 3 (unit m)

Different integration methods are used for the temporal discretization, always taking the same method in all domains, i.e. fluid, solid and mesh. The presented approaches are validated, verified and compared by evaluating the drag and lift forces acting on the cylindrical cutout as well as on the flag, and the displacements at the right end of the flag at point $A(0.6, 0.2)$ m to reference values from Turek et al. [397; 399]. With $S = S_1 \cup S_2$, where $S_1$ denotes the length of the cylinder in contact with the fluid and $S_2$ denotes the interface between the fluid and the solid, the drag and lift forces are defined as

$$(F_D, F_L) = \int_S \boldsymbol{\sigma} \cdot \boldsymbol{n} \, \mathrm{d}S \, . \tag{8.43}$$

Table 8.11: FAC-flag (2) - mesh level, number of elements in fluid and solid domain and number of degrees of freedom ($n_{\mathrm{dof}}$)

| level | solid | fluid | $n_{\mathrm{dof}}$ |
|---|---|---|---|
| 1 | 100 | 1018 | 43,800 |
| 2 | 157 | 1600 | 68,418 |
| 3 | 257 | 2329 | 100,194 |
| 4 | 484 | 2811 | 125,916 |
| 5 | 726 | 3534 | 161,622 |

**Verification using the Houbolt method:**
In a first step, a mesh convergence study is performed using the Houbolt method, which is second-order accurate in time. A constant time step size with $\Delta t = 1.25 \times 10^{-3}$ s and a maximum time $t = 20$ s are chosen for all considered mesh levels. The resulting course of the drag force $F_D$ and lift force $F_L$ as well as the flag displacement $u_1$ and $u_2$ for the mesh level 5 is shown in Figures 8.29. For comparison, the minimum and maximum reference values from Turek et al. [399] are included, showing the agreement of the obtained results. Furthermore, it can be seen that the flow is fully developed and becomes periodic approximately from time $t > 10$ s.

For an evaluation of the convergence behavior, the minimum and maximum values at fully developed flow are listed in Tables 8.12 and 8.13 for different mesh levels. In addition, for a better comparison, an average relative error of the forces and displacements, denoted by

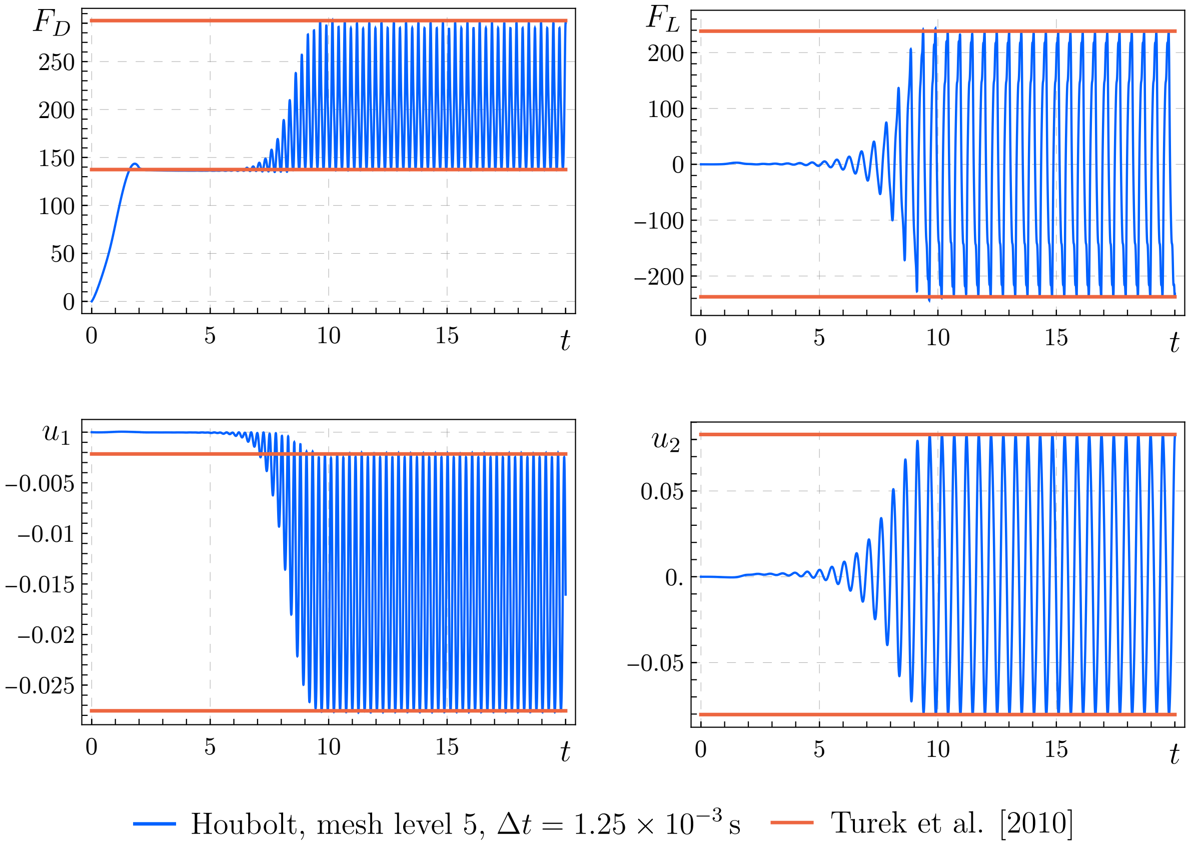

Figure 8.29: FAC-flag (2) - evolution of drag force, lift force and displacements, obtained with Houbolt method, $\Delta t = 1.25 \times 10^{-3}$ and mesh level 5 (units $[F]$=N, $[u]$=m, $[t]$=s)

$err_F$ and $err_u$ respectively, is given. For this purpose, the norm of the relative differences between the obtained results and the reference values is calculated. As an example, for drag and lift forces the formula is

$$\begin{aligned} err_F = \Bigg( &\left( \frac{F_{D,\min} - F^{\mathrm{ref}}_{D,\min}}{F^{ref}_{D,\min}} \right)^2 + \left( \frac{F_{D,\max} - F^{ref}_{D,\max}}{F^{ref}_{D,\max}} \right)^2 \\ &+ \left( \frac{F_{L,\min} - F^{ref}_{L,\min}}{F^{ref}_{L,\min}} \right)^2 + \left( \frac{F_{L,\max} - F^{ref}_{L,\max}}{F^{ref}_{L,\max}} \right)^2 \Bigg)^{\frac{1}{2}} . \end{aligned} \tag{8.44}$$

The relative error of the displacements is calculated in the same way. According to the presented data, convergent behavior can be observed with an error below 2% and 4% for the forces and displacements, respectively, at mesh level 5 with 161.622 degrees of freedom.

In a next step, the flow around a cylinder is solved with the Houbolt time discretization and different constant time step sizes to evaluate the temporal convergence. For calculations with $\Delta t \geq 5.0 \times 10^{-3}$ the simulations are aborted due to divergence in the Newton scheme as soon as the oscillations of the flag started to increase. The results obtained with smaller step sizes correspond to the reference values. As an example for comparison, a section of the drag and lift force curves are shown in Figure 8.30. These results are

Table 8.12: FAC-flag (2) - mesh convergence, drag and lift forces (in N) and mean relative error compared to reference values from TUREK ET AL. [399]

| level | $F_{D,\min}$ | $F_{D,\max}$ | $F_{L,\min}$ | $F_{L,\max}$ | $err_F$ |
|---|---|---|---|---|---|
| 1 | 134.340 | 264.674 | -215.505 | 215.723 | 0.164580 |
| 2 | 131.749 | 279.039 | -225.855 | 227.660 | 0.090529 |
| 3 | 136.675 | 283.517 | -225.621 | 231.584 | 0.064915 |
| 4 | 136.778 | 286.998 | -230.299 | 232.941 | 0.042098 |
| 5 | 136.791 | 290.467 | -234.999 | 235.273 | 0.018370 |
| ref. | 137.41 | 292.71 | -237.19 | 238.41 | |

Table 8.13: FAC-flag (2) - mesh convergence, flag displacement at $A(0.6, 0.2)\,\mathrm{m}$ (in m) and mean relative error compared to reference values from TUREK ET AL. [399]

| level | $u_{1,\min}$ | $u_{1,\max}$ | $u_{2,\min}$ | $u_{2,\max}$ | $err_u$ |
|---|---|---|---|---|---|
| 1 | -0.023972 | -0.0015997 | -0.074529 | 0.076616 | 0.305452 |
| 2 | -0.026644 | -0.0019131 | -0.078326 | 0.081192 | 0.119395 |
| 3 | -0.026670 | -0.0019255 | -0.078598 | 0.081240 | 0.113016 |
| 4 | -0.026880 | -0.0019674 | -0.079264 | 0.081693 | 0.090451 |
| 5 | -0.027688 | -0.0020745 | -0.080321 | 0.082845 | 0.035467 |
| ref. | -0.02755 | -0.00215 | 0.0803 | 0.0829 | |

obtained with different constant time step sizes and mesh level 5. In this case, the data of TUREK ET AL. [397] are shown as a reference, which are available as curves for the entire time interval. In the detail view it can be seen that the characteristic curves of the reference are reproduced well with the applied least-squares approach. Furthermore, when comparing the different time step sizes, only very small deviations can be seen overall, with the two smallest time steps agreeing fairly well.

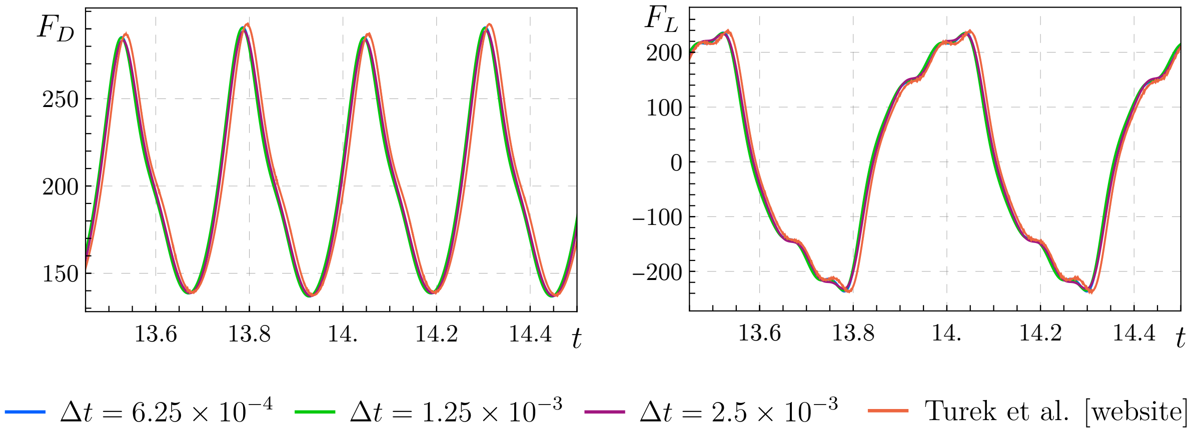

Figure 8.30: FAC-flag (2) - evolution of drag and lift force, obtained with Houbolt method, different time step sizes and mesh level 5, reference taken from TUREK ET AL. [397] (units $[F]$=N, $[t]$=s)

**High-order time discretization and adaptive time step control:**
Next, the application of high-order time integration methods in combination with the LSFEM to solve FSI problems with large deformations is investigated. For this purpose, various Runge-Kutta methods with different number of stages are implemented. Moreover, adaptive time stepping is applied, in which the error estimator is determined without significant additional computational cost using embedded RK methods. All simulations are performed with mesh level 5 and element $RT_2P_3$.

The applied schemes are singly-diagonally implicit RK methods with temporal order of two to three denoted as SDIRK-2(1), ESDIRK-2(1) and ESDIRK-3(2). Therein, the first number indicates the order $p$ of the applied method for solving the respective time steps and the second number indicates the order $q = p - 1$ of the embedded method for evaluating the error estimator for adaptive time step control. The butcher tableaus with required parameters for the individual stages are given in Appendix C.1. Detailed information on the implementation of RK schemes for the temporal discretization of LS stress-velocity formulations is provided in Section 7.3. The most relevant equations are (7.46) and (7.47), describing the accelerations or displacements in terms of the actual velocities in the respective stage and further known values from previous stages.

As outlined in Section 7.6.1, the error estimator can be determined based on different quantities with embedded Runge-Kutta methods. Relying on the results in Section 7.7.2, which revealed that the mixed LS SV formulation for the solid is relatively sensitive to the change in time step sizes, the error estimator is evaluated based on the velocities in the fluid domain in the following. More precisely, the error at each time step is evaluated with all velocity node values $v^i$ in the fluid domain as

$$e_v = \sqrt{\frac{1}{n_v} \sum_{i=1}^{n_v} \left( \frac{v^i_{n+1} - \hat{v}^i_{n+1}}{\epsilon_a + \max(|v^i_n|, |v^i_{n+1}|) \cdot \epsilon_r} \right)^2} \,. \tag{8.45}$$

The absolute and relative error tolerances $\epsilon_a$ and $\epsilon_r$ are chosen differently to control the magnitude of the time step size and thus the error. The automatic step size control is performed as specified in Section 7.6.2 using (7.75). The bounding factors to stabilize the time step control are selected as $f_{\min} = 0.9$, $f_{\max} = 1.1$ and $k_{\max} = 10$. In case of a failed Newton iteration, the new step size in the following step is set to $\Delta t_{new} = 0.95 \Delta t$. Additionally, if a step rejection or a failure in the Newton iteration occurred in the second last time step, the step size in the subsequent five time steps is not allowed to increase, i.e. the maximum factor is set to $f_{\max} = 1$, and a further rejection is not allowed. This limitation aims to stabilize the calculation in case of fluctuations caused by time step size changes. To further slightly reduces the increase of step sizes in case of strong varying magnitudes, the method of averaging, see (7.77), is applied. Here, the new $\Delta t$ is calculated based on the mean value of $N = 5$ previous time step sizes and the newly determined size, choosing $\theta = 0.5$ for the proportions in (7.77). Furthermore, the absolute size of each time step is limited to $10^{-4} \leq \Delta t \leq 0.05\,\mathrm{s}$ and the initial time step is chosen as $\Delta t_0 = 0.01\,\mathrm{s}$.

To compare the different RK methods several results are summarized in Table 8.14. The table includes the chosen relative and absolute tolerances for the calculation of the error estimator and the resulting average time step sizes and number of Newton iterations for the entire simulation interval $t \in [0, 20]\,\mathrm{s}$. The average step size is calculated based on all accepted time steps, i.e. without the ones that are rejected or in which Newton's method diverged. The number of Newton iterations, however, contains all iterations that were performed during the calculation process, i.e. also those within the time steps that had to be repeated. Furthermore, for a rough comparison of the methods regarding their accuracy, the error of the drag and lift force as well as the flag displacement is again evaluated. It can be seen that, as expected, the average time step size decreases with smaller tolerances, and thus the magnitudes of the errors reduce as well. Here, the absolute error tolerance is mainly decisive.

Table 8.14: FAC-flag (2) - Number of total Newton iterations, average time step size $\overline{\Delta t}$ (in s), and mean relative errors for different methods and tolerances

| method | $\epsilon_r$ | $\epsilon_a$ | iterations | $\overline{\Delta t}$ $\times 10^{-3}$ | $err_F$ | $err_u$ |
|---|---|---|---|---|---|---|
| SDIRK-2(1) | $10^{-5}$ | $10^{-3}$ | 56073 | 5.768 | 0.024002 | 0.025223 |
|  | $10^{-5}$ | $10^{-4}$ | 128059 | 2.051 | 0.006053 | 0.014778 |
|  | $10^{-2}$ | $10^{-5}$ | 66515 | 4.263 | 0.011748 | 0.016400 |
| ESDIRK-2(1) | $10^{-4}$ | $10^{-4}$ | 78697 | 3.572 | 0.007634 | 0.016868 |
|  | $10^{-4}$ | $10^{-5}$ | 148978 | 1.726 | 0.011191 | 0.015138 |
|  | $10^{-2}$ | $10^{-6}$ | 56303 | 5.495 | 0.013422 | 0.025868 |
| ESDIRK-3(2) | $10^{-6}$ | $10^{-4}$ | 121037 | 7.125 | 0.014610 | 0.020768 |
|  | $10^{-4}$ | $10^{-5}$ | 85207 | 5.648 | 0.008731 | 0.015539 |
|  | $10^{-6}$ | $10^{-5}$ | 119123 | 3.621 | 0.004844 | 0.012960 |
| Houbolt | - | - | 52329 | 2.500 | 0.033562 | 0.069385 |
|  | - | - | 95347 | 1.250 | 0.018370 | 0.035467 |
|  | - | - | 178311 | 0.625 | 0.013328 | 0.024979 |

The calculations reveal that the range for the selection of reasonable tolerances is relatively small. One reason for this is that if too large tolerances are chosen, the calculations not only become inaccurate, but also frequent divergences occur in the Newton method due to relatively large chosen time step sizes. If the tolerances are chosen far too high, the computations may not be controlled by the actual step size control based on the error estimator, but mainly by the step size reductions after a failed Newton procedures. This effect is visible when looking at the results of the calculation with ESDIRK-3(2) choosing $\epsilon_r = 10^{-6}$ and $\epsilon_a = 10^{-4}$. Despite the large average time step size $\overline{\Delta t} \approx 7 \times 10^{-3}\,$s, the number of total iterations is very high even compared to simulations with smaller time increments. This is not only due to the fact that larger step sizes require more iterations per time step, but in this case mainly because the Newton method has failed many times due to the large step size. Another reason is that too small tolerances obviously reduce the time steps extremely at some points of the calculation, which in turn leads to the occurrence of numerical instabilities.

In order to provide a rough estimate of the efficiency of the adaptive step size control, the data of the Houbolt method with different constant time increments is also included in Table 8.14 for comparison. Using the embedded RK methods with adaptive step size, fewer iterations are needed and the errors still tend to be smaller. But it can also be noticed that with raising the order of the integration procedure, i.e. with increasing the number of stages, the number of iterations rises and thus, consequently, also the computational costs.

The adjustment of the time step size is depicted for some examples in Figure 8.31. As can be seen, the RK methods with automatic step size control are especially efficient because the initial phase of the FSI problem, in which no large velocities and deformations are present, can be solved with relatively large step sizes. At the beginning of the simulation, the step size increases in all cases starting from the selected initial value $\Delta t_0 = 0.1\,\mathrm{s}$. In the example of the third-order ESDIRK there is an increase until the selected maximum step size of $\Delta t_{\max} = 0.05\,\mathrm{s}$ is reached. When the normal stresses at the interface become higher and the flag starts to vibrate, the step size is automatically decreased with all embedded Runge-Kutta methods. The close-up shows that the step size with the ESDIRK-3(2) is always above that of the second-order methods, although the tolerances for the accuracy are chosen smaller. Despite the fact that more stages have to be evaluated per time step, the average larger increment leads to a lower number of total iterations being required, cf. Table 8.14. And considering these results, it could be concluded that the high-order method is more efficient.

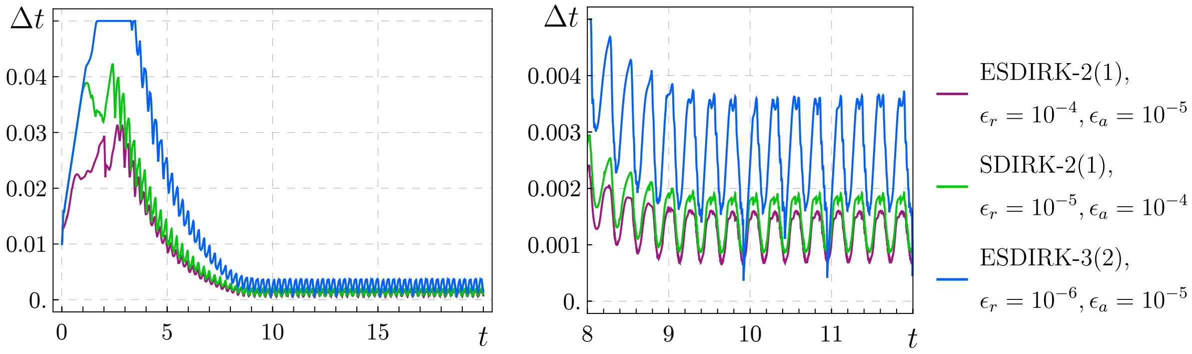

Figure 8.31: FAC-flag (2) - evolution of time step size $t \in [0, 20]\,\mathrm{s}$ (left) and zoom (right), obtained with RK methods with adaptive time stepping and mesh 5 (units $[F]$=N, $[t]$=s)

Figures 8.32 and 8.33 illustrate the courses of the drag and lift forces obtained with the RK methods and time adaptivity. These calculations with mesh level 5 show that the results are consistent with the reference values and only small differences between the different methods can be seen in the zoom. The magnitude of the amplitudes is similar with only a small shift of the phase.

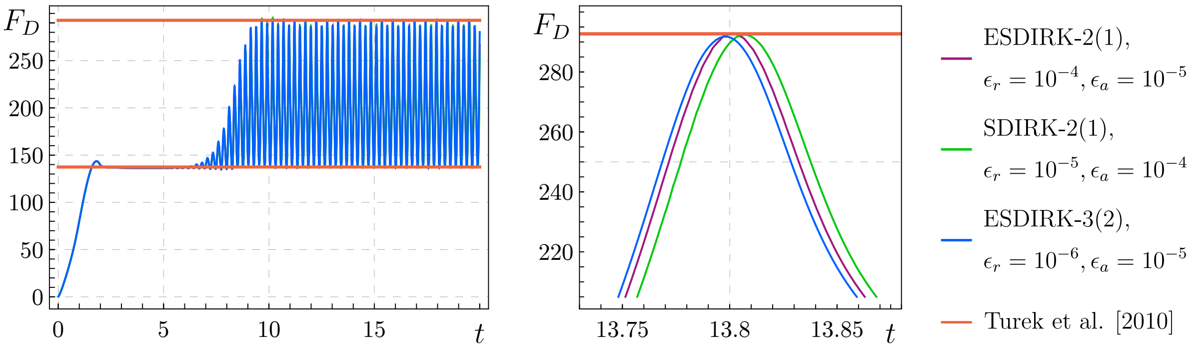

Figure 8.32: FAC-flag (2) - evolution of drag force on $t \in [0, 20]\,\mathrm{s}$ (left) and zoom (right), obtained with RK methods with adaptive time stepping and mesh 5 (units $[F]$=N, $[t]$=s)

As already mentioned, the comparison of the efficiency based on the number of iterations of course only serves as a rough guide. For a more definite statement, the computing time

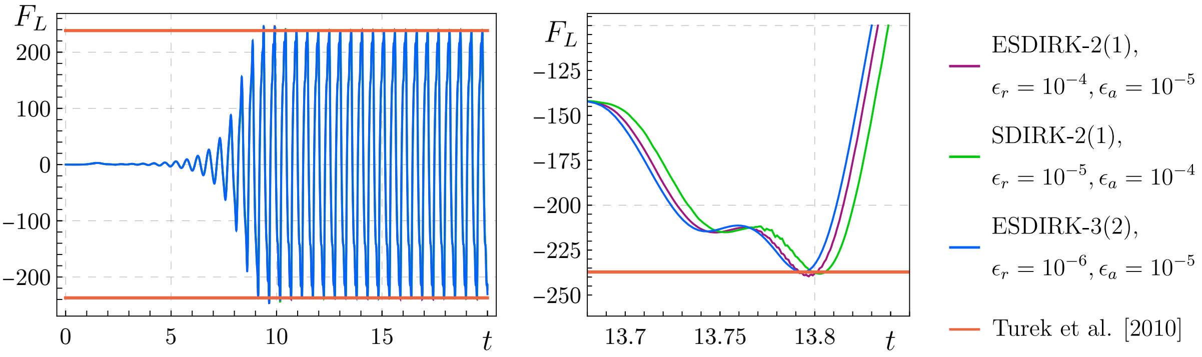

Figure 8.33: FAC-flag (2) - evolution of lift force on $t \in [0, 20]$ s (left) and zoom (right), obtained with RK methods with adaptive time stepping and mesh 5 (units $[F]$=N, $[t]$=s)

would have to be evaluated, for example, but this is not as straightforward to implement in practice. In addition, the error measure calculated here based on the drag and lift forces as well as displacements only provides a rough statement about the accuracy, since only the amplitudes are taken into account. For a more precise evaluation, the frequency would have to be included, for example, or the total deviation in a defined interval.

Finally, the solution to this benchmark problem for different flag configurations is visualized in Figures 8.35 and 8.34. Four different time points within one period of the flag oscillation are selected to display the velocity in the fluid region and the displacement in the solid region.

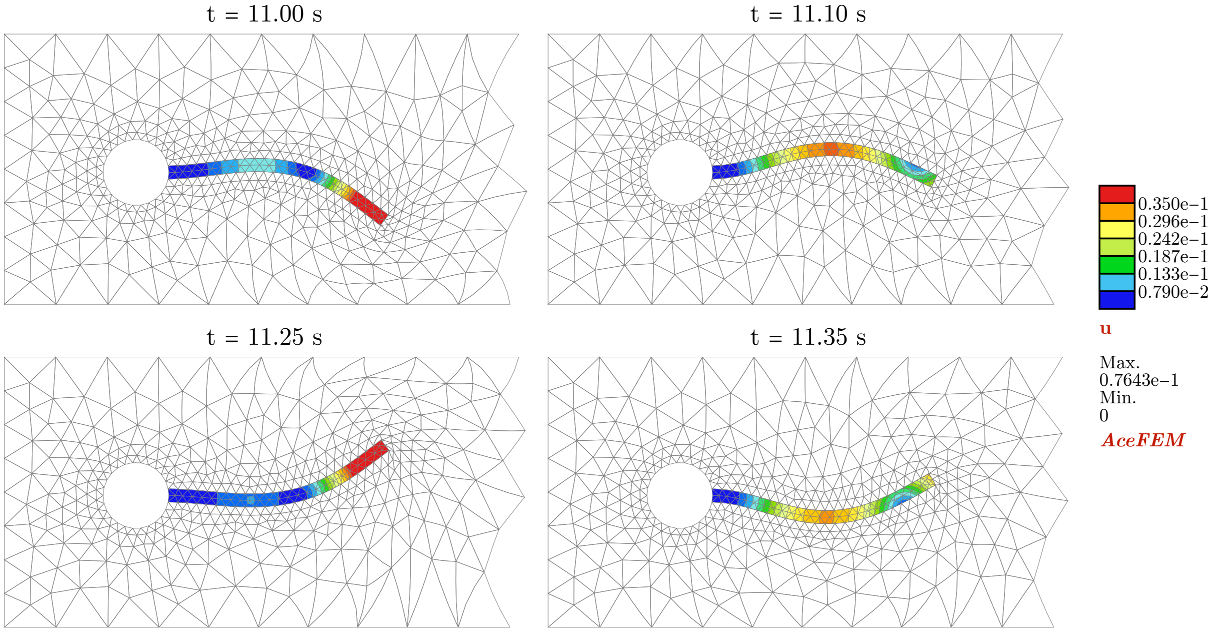

Figure 8.34: FAC-flag (2) - distribution of displacement field $|\boldsymbol{u}|$ (in m) at different times within one period of flag oscillation

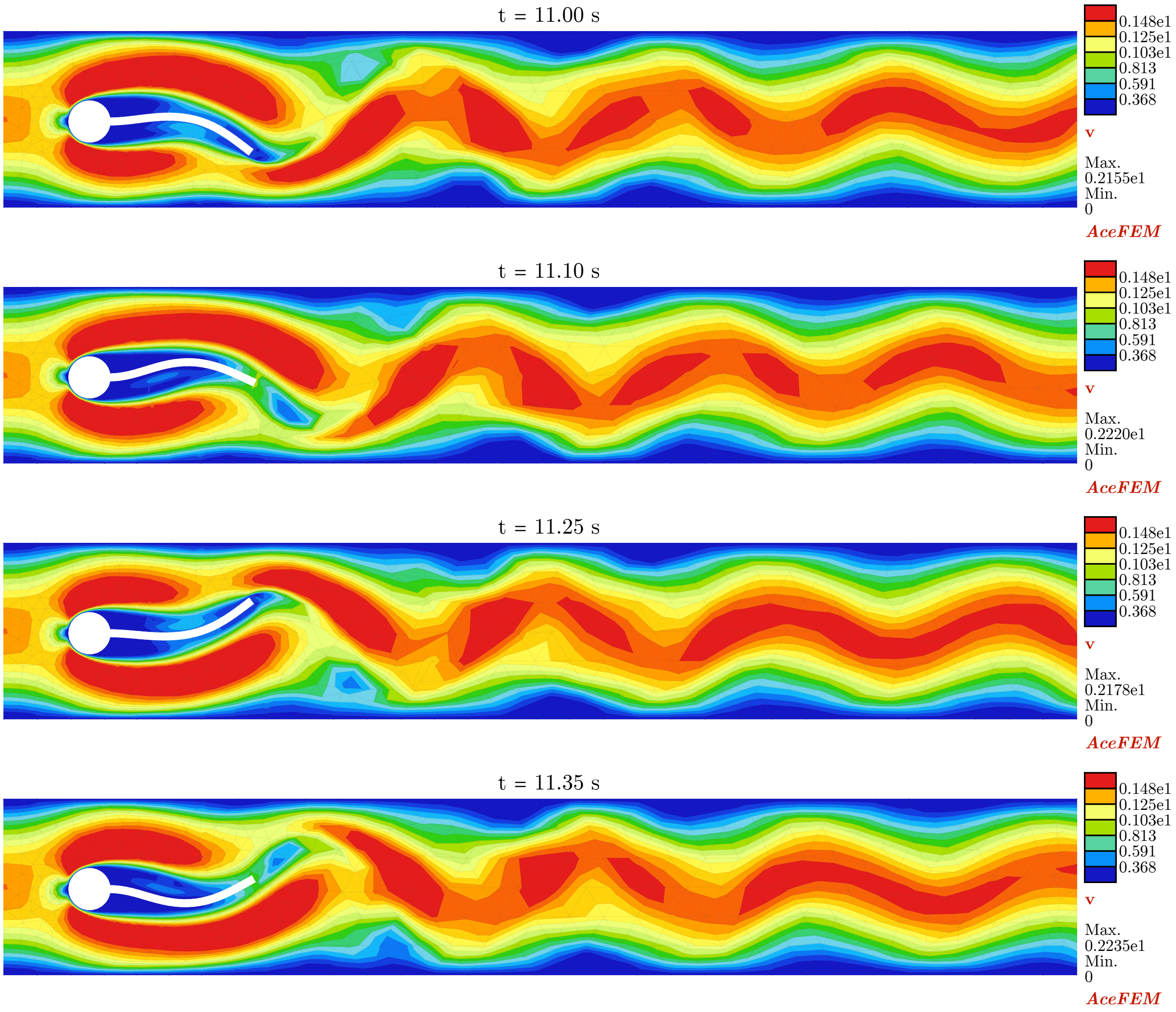

Figure 8.35: FAC-flag (2) - distribution of total velocity field $|\boldsymbol{v}|$ (in m/s) at different times within one period of flag oscillation

# 9 Conclusion and Outlook

The present thesis dealt with the construction and analysis of least-squares finite element formulations to solve dynamic fluid, structure and fluid-structure interaction problems. In detail various time discretization schemes were introduced and their application in the different fields was investigated, considering also adaptive time stepping. Further, all components for solving monolithically coupled FSI problems undergoing large deformations were derived and studied. Additionally, least-squares finite elements for the solution of non-Newtonian fluid flow were constructed and studies in 2D and 3D were performed, including also the assimilation of numerical and experimental data.

**Conclusion**
After the introduction to give a brief review on the state of the art in the considered field of research, the basic mechanical background for the work was provided. Therefore, kinematic relationships, stress quantities and the essential balance equations of continuum mechanics were first defined. Furthermore, the laws of material modeling for fluid and solid mechanics were stated. In this context, the Lagrangian and Eulerian descriptions were provided. Subsequent, an overview on the finite element method in general and on the specifics of the least-squares FEM was given. Details on interpolation spaces and the construction of interpolation functions were outlined. This included a brief description of implementation aspects that allow the creation of shape functions in different given configurations. Furthermore, theoretical basics on assimilation of data using the LSFEM, including data preparation using the Kriging interpolation were presented.

The derivation of least-squares finite element formulations for dynamic flow of incompressible Newtonian and non-Newtonian fluids based on the Navier-Stokes equations were outlined. First, the LS stress-velocity formulation for steady flow of non-Newtonian fluids was applied to solve two-dimensional problems. The spatial convergence behavior was investigated using an example with an analytical solution and the results yielded the expected orders of convergence for the element formulations considered. In addition, some studies have been carried out on the flow behavior of non-Newtonian fluids as a function of various factors. For this purpose, e.g. the influence of the Reynolds number or of the different parameters of the Carreau-Yasuda viscosity model were analyzed. Two typical benchmark problems, named driven cavity and flow over a backward facing step, were chosen for this study. A further numerical example consisting of a flow through a channel with smooth contraction was applied to show the assimilation of data to the numerical computation. It was demonstrated that the additional data has a positive effect on the quality of the least-squares solution especially with low-order spatial interpolation and thus, for example, the problem of mass loss could be greatly reduced.

In a next step, three-dimensional flow problems were solved using the LS stress-velocity-pressure formulation including the Carreau-Yasuda viscosity model. A benchmark problem in 3D with analytical solution was chosen to evaluate the convergence behavior of the proposed approach. Then, the flow of blood through a simplified geometry of a carotid bifurcation was simulated. Initially, the approach was verified and the convergence was evaluated. Next, the incorporation of experimental data measured in the internal artery was investigated. A distinction was made between the inclusion of data only at individual positions of cross-sectional surfaces or at all nodes of the surfaces. Especially the incorporation of experimental data on the whole cross-sectional area exhibited a great influence and produced results that were closer to the measured data in the remaining region. In order to investigate the positive effect of data assimilation in both arterial branches, finally also numerical data were used for this example. An improvement was observed, particularly with regard to mass loss.

A major aspect of this thesis was the investigation of different time discretization methods for the LS SV formulations. For this purpose, first the basic concept of these methods for solving first order partial differential equations was explained and illustrated by applying them to a simple 1D example. Then, aspects of the implementation of different methods specifically for the fluid and solid SV formulations were outlined. The application of these methods to the solution of unsteady flow and dynamic solid problems was subsequently studied in detail. The focus was on the evaluation of the temporal order of convergence in combination with the SV formulations and on a comparison of the efficiency of the different methods. Concluding, the expected theoretical order of convergence in time was achieved in most cases. Slight reductions in order occurred only for the high-order time discretization methods when solving the Navier-Stokes equations.

To further increase efficiency in time-dependent problems, adaptive time-stepping methods can be applied. In this work, embedded Runge-Kutta methods were implemented for this purpose. These offer the possibility of computing local error estimators without significant additional computational cost. The procedure for the computation of these error estimators was explained in detail and furthermore general information on automatic control of the time steps was provided. The performance of automatic time-stepping with error estimators based on embedded Runge-Kutta methods was then tested for a flow and a solid problem. The simulations showed the efficiency of the adaptivity in time, but also revealed that some caution is needed for the applicability in combination with the LSFEM. It appeared that in some cases the SV formulations respond sensitively to changes in time step sizes, thus requiring some attention when applying automatic time step control.

Finally, the presented stress-velocity formulations for fluid and solid dynamics were coupled to solve fluid-structure interaction problems. In a first step, the general idea of this thesis for coupling and inherently fulfilled interface conditions using suitable function spaces was presented. Next, the coupling was tested using numerical FSI examples with small deformations. Then, all required components for the handling of large deformations in FSI problems were specified. More precisely, the fluid formulation in an Arbitrary-Lagrangian-Eulerian description was introduced to account for a moving domain. Additional, details on the computation of the fluid background mesh were given. The fluid ALE formulation was verified by a channel flow with moving background mesh. The different approaches to mesh motion were compared by means of a numerical example consisting of a vibrating beam causing large deformations in the surrounding mesh domain. The focus was on the determination of local mesh stiffness in order to generate the most uniform and smooth deformation possible.

In the end, the separately tested components are coupled to solve FSI problems with large deformations. The coupling of the LS SV fluid ALE formulation with mesh deformation based on a linear elastic approach with the LS SV solid formulation is tested with a flow through a channel with linear elastic material behavior. For this purpose, the channel walls are compressed and pulled apart through boundary conditions on the outer walls.

The calculated values confirm the correct coupling at the interface. In a final benchmark problem, the monolithic coupling of the fluid ALE formulation with the solid formulation for hyperelastic material behavior is examined, along with the application of various time discretization methods including adaptive time stepping. Comparison of the time discretizations applied in terms of efficiency and accuracy revealed that the use of adaptive time stepping for solving monolithically coupled FSI problems with LSFEM can be quite advantageous, provided that the parameter choice for the step size control is appropriate.

### Outlook

It was shown that the least-squares finite element method is suitable to be applied in a variety of different fields. The straightforward way to construct first-order systems in terms of quantities of interest is of great advantage especially for solving FSI problems. The stress-velocity formulations have proven to be promising for monolithic coupling due to the possible inherent fulfillment of the interface conditions. For more specific applications, such as simulating blood flows with fluid-structure interaction, the formulations for non-Newtonian fluids could be coupled with the least-squares stress-velocity solid formulation. Furthermore, the investigated time integration methods could also be implemented to the formulation for non-Newtonian fluids to enable transient behavior. In the field of solid mechanics the SV formulations could be reformulated for further material laws to cover, e.g. transversal isotropy or plasticity. The former could be of interest, for example, in the context of correct modeling of blood vessels. Another interesting point of investigation in the modeling of realistic blood flows in medical engineering is the inclusion of patient-specific data. In this context, the straightforward assimilation of data into numerical simulations, as presented in this work for pure fluid flows, may be promising. In all fields, a further improvement of the results shown for adaptive mesh refinement algorithms can be investigated. Therein, the advantage of an error indicator without additional computational cost provided by the least-squares functional can be used.

# A Appendix: Spatial discretization

## A.1 Lagrange shape functions

The approximation functions for cubic triangles in the actual configuration can be constructed according to Zienkiewicz and Taylor [431] as

$$\begin{aligned} N^i(x,y) &= \frac{1}{2}(3L_i-1)(3L_i-2)L_i \quad \text{for} \quad i=1,2,3 \\ N^4(x,y) &= \frac{9}{2}L_1L_2\,(3L_1-1), \quad N^5(x,y) = \frac{9}{2}L_1L_2\,(3L_2-1) \\ N^6(x,y) &= \frac{9}{2}L_2L_3\,(3L_2-1), \quad N^7(x,y) = \frac{9}{2}L_2L_3\,(3L_3-1) \\ N^8(x,y) &= \frac{9}{2}L_3L_1\,(3L_3-1), \quad N^9(x,y) = \frac{9}{2}L_3L_1\,(3L_1-1) \\ N^{10}(x,y) &= 27\,L_1L_2L_3 \end{aligned} \tag{A.1}$$

with area coordinates $L_1, L_2$ and $L_3$ defined in (3.27). The first three nodes are corner nodes, the nodes four to nine are located on the edges and node ten is an internal node, see Figure 3.2.

# B Appendix: LSFEM for non-Newtonian fluids

## B.1 Algorithmic procedure for implementation of LS SV formulation to solve steady flow of non-Newtonian fluids in 2D including data assimilation

- Initialization of basic variables

  $\boldsymbol{w}^I = \left[w_1^I, w_2^I\right]^T, \quad \boldsymbol{\beta}^J = \left[\beta_1^J, \beta_2^J\right]^T$

  $\boldsymbol{w}^I$ DOF for velocities at node $I$
  $\boldsymbol{\beta}^J$ DOF for stresses at node $J$

- Discretization in space

  1. velocities: $v_i^h = \sum\limits_I N^I w_i^I \;, \quad v_{i,j}^h = \sum\limits_I N_{,j}^I \, w_i^I$ and $v_{i,i}^h = \sum\limits_I N_{,i}^I \, w_i^I$
  2. stresses: $\sigma_{ij}^h = \sum\limits_J \psi_j^J \beta_i^J$ and $\sigma_{ij,j}^h = \sum\limits_J \psi_{j,j}^J \, \beta_i^J$

- Discretized LS functional for non-Newtonian fluid flow with data assimilation

  $$\mathcal{F}^*(\boldsymbol{\sigma}^h, \boldsymbol{v}^h) = \mathcal{F}^F(\boldsymbol{\sigma}^h, \boldsymbol{v}^h) + \frac{1}{2} \sum_{i=1}^{M} \zeta_i (\boldsymbol{d}_i - \boldsymbol{H}_i \cdot \boldsymbol{v}^h)^2$$

  with $\mathcal{F}^F(\boldsymbol{\sigma}^h, \boldsymbol{v}^h) = \frac{1}{2}\left( ||\omega_1 \mathcal{R}_1||^2_{L^2(\Omega_e)} + ||\omega_2 \mathcal{R}_2||^2_{L^2(\Omega_e)} + ||\omega_3 \mathcal{R}_3||^2_{L^2(\Omega_e)} \right)$ ,

  and $\mathcal{R}_1 := \operatorname{div} \boldsymbol{\sigma}^h - \rho_f \nabla \boldsymbol{v}^h \cdot \boldsymbol{v}^h + \boldsymbol{f}$ , $\quad \mathcal{R}_2 := \operatorname{dev} \boldsymbol{\sigma}^h - 2\eta(\dot{\gamma}^h) \nabla^s \boldsymbol{v}^h$,

  $\mathcal{R}_3 := \operatorname{div} \boldsymbol{v}^h$,

  $\eta(\dot{\gamma}) = \eta_\infty + (\eta_0 - \eta_\infty)\left[1 + (\lambda \, \dot{\gamma})^a\right]^{\frac{n-1}{a}}$ and $\dot{\gamma} = \sqrt{2(\nabla^s \boldsymbol{v}^h : \nabla^s \boldsymbol{v}^h)}$

- Element RHS-vector $\boldsymbol{P}^e$ and system-matrix $\boldsymbol{K}^e$

  DOF vector of element $e$: $\quad \boldsymbol{D}^e = [\boldsymbol{w}^1, ..., \boldsymbol{w}^K, \boldsymbol{\beta}^1, ..., \boldsymbol{\beta}^N]^T$

  with $K$ and $N$ denoting the number of nodes

  ```
  FOR each element e DO
      $\boldsymbol{P}^e = \frac{\partial \mathcal{F}^*}{\partial \boldsymbol{D}^e}$   and   $\boldsymbol{K}^e = \frac{\partial \boldsymbol{P}^e}{\partial \boldsymbol{D}^e}$
  END DO
  ```

## B.2 Algorithmic procedure for implementation of LS SVP formulation to solve steady flow of non-Newtonian fluids in 3D including data assimilation

- Initialization of basic variables

$$\boldsymbol{w}^I = \left[w_1^I, w_2^I, w_3^I\right]^T, \quad \boldsymbol{\beta}^J = \left[\beta_{11}^J, \beta_{12}^J, \beta_{13}^J, \beta_{22}^J, \beta_{23}^J, \beta_{33}^J\right]^T, \quad q^L$$

  $\boldsymbol{w}^I$ DOF for velocities at node $I$
  $\boldsymbol{\beta}^J$ DOF for stresses at node $J$ (with $\boldsymbol{\sigma} = \boldsymbol{\sigma}^T$)
  $q^L$ DOF for pressure at node $L$

- Discretization in space

  1. velocities: $v_i^h = \sum\limits_I N^I w_i^I$ , $\quad v_{i,j}^h = \sum\limits_I N_{,j}^I \, w_i^I$ $\quad$ and $\quad v_{i,i}^h = \sum\limits_I N_{,i}^I \, w_i^I$
  2. stresses: $\sigma_{ij}^h = \sum\limits_J N^J \beta_{ij}^J$ $\quad$ and $\quad \sigma_{ij,j}^h = \sum\limits_J N_{,j}^J \, \beta_{ij}^J$
  3. pressure: $p^h = \sum\limits_L N^L q^L$

- Discretized LS functional for non-Newtonian fluid flow with data assimilation

$$\mathcal{F}^*(\boldsymbol{\sigma}^h, \boldsymbol{v}^h, p^h) = \mathcal{F}(\boldsymbol{\sigma}^h, \boldsymbol{v}^h, p^h) + \frac{1}{2}\sum_{i=1}^{M} \zeta_i(\boldsymbol{d}_i - \boldsymbol{H}_i \cdot \boldsymbol{v}^h)^2$$

  with $\quad \mathcal{F}(\boldsymbol{\sigma}^h, \boldsymbol{v}^h, p^h) = \dfrac{1}{2}\left(||\omega_1 \mathcal{R}_1||^2_{L^2(\Omega_e)} + ||\omega_2 \mathcal{R}_2||^2_{L^2(\Omega_e)} + ||\omega_3 \mathcal{R}_3||^2_{L^2(\Omega_e)}\right)$ ,

  and $\quad \mathcal{R}_1 := \operatorname{div} \boldsymbol{\sigma}^h - \rho \nabla \boldsymbol{v}^h \cdot \boldsymbol{v}^h + \boldsymbol{f}$ , $\quad \mathcal{R}_2 := \boldsymbol{\sigma}^h - 2\eta(\dot{\gamma}) \nabla^s \boldsymbol{v}^h + p^h \mathbf{1}$,

  $\mathcal{R}_3 := \operatorname{div} \boldsymbol{v}^h$,

$$\eta(\dot{\gamma}) = \eta_\infty + (\eta_0 - \eta_\infty)\left[1 + (\lambda\,\dot{\gamma})^a\right]^{\frac{n-1}{a}} \quad \text{and} \quad \dot{\gamma} = \sqrt{2(\nabla^s \boldsymbol{v}^h : \nabla^s \boldsymbol{v}^h)}$$

- Element RHS-vector $\boldsymbol{P}^e$ and system-matrix $\boldsymbol{K}^e$

  DOF vector of element $e$: $\quad \boldsymbol{D}^e = [\boldsymbol{w}^1, ..., \boldsymbol{w}^K, \boldsymbol{\beta}^1, ..., \boldsymbol{\beta}^N, q^1, ..., q^N]^T$

  with $K$ and $N$ denoting the number of nodes

```
FOR each element e DO
    $\boldsymbol{P}^e = \frac{\partial \mathcal{F}^*}{\partial \boldsymbol{D}^e}$    and    $\boldsymbol{K}^e = \frac{\partial \boldsymbol{P}^e}{\partial \boldsymbol{D}^e}$
END DO
```

## B.3 Body force for flow of non-Newtonian fluid in cubical domain

The body force expression for the three dimensional numerical example of non-Newtonian fluid flow in a cubical domain is given by

$$\boldsymbol{f} = \begin{bmatrix} \rho_f(-v_a v_{3,3} + v_3 v_{a,3}) - \mu_e'(2v_{a,1}\gamma_{e,1} - v_{3,3}\gamma_{e,2} + (v_{3,a} + v_{a,3})\gamma_{e,3}) \\ -\mu_e(2v_{a,aa} + v_{a,33}) + (2\pi\cos[2\pi x_1]\sin[2\pi x_2]\sin[2\pi x_3]) \\ \\ \rho_f(-v_a v_{3,3} + v_3 v_{a,3}) - \mu_e'(-v_{3,3}\gamma_{e,1} + 2v_{a,2}\gamma_{e,2} + (v_{3,a} + v_{a,3})\gamma_{e,3}) \\ -\mu_e(2v_{a,aa} + v_{a,33}) + (2\pi\sin[2\pi x_1]\cos[2\pi x_2]\sin[2\pi x_3]) \\ \\ \rho_f(2v_a v_{3,a} + v_3 v_{3,3}) - \mu_e'((v_{3,a} + v_{a,3})(\gamma_{e,1} + \gamma_{e,2}) + 2v_{3,3}\gamma_{e,3}) \\ -\mu_e(2v_{3,aa} + v_{3,33}) + (2\pi\sin[2\pi x_1]\sin[2\pi x_2]\cos[2\pi x_3]) \end{bmatrix} \tag{B.1}$$

with

$$
\begin{aligned}
v_a &= -2x_3\cos[\pi x_1]\cos[\pi x_2]\exp[\pi(-x_3^2 + 0.25)] \\
v_3 &= \sin[\pi(x_1 + x_2)]\exp[\pi(-x_3^2 + 0.25)] - \sin[\pi(x_1 + x_2)] \\
v_{a,1} &= 2\pi x_3\sin[\pi x_1]\cos[\pi x_2]\exp[\pi(-x_3^2 + 0.25)] \\
v_{a,2} &= 2\pi x_3\cos[\pi x_1]\sin[\pi x_2]\exp[\pi(-x_3^2 + 0.25)] \\
v_{a,3} &= (4\pi x_3^2 - 2)\cos[\pi x_1]\cos[\pi x_2]\exp[\pi(-x_3^2 + 0.25)] \\
v_{3,a} &= \pi\cos[\pi(x_1 + x_2)]\exp[\pi(-x_3^2 + 0.25)] - \pi\cos[\pi(x_1 + x_2)] \\
v_{3,3} &= -v_{a,1} - v_{a,2} \\
v_{a,aa} &= 2\pi^2 x_3\cos[\pi x_1]\cos[\pi x_2]\exp[\pi(-x_3^2 + 0.25)] \\
v_{a,12} &= -2\pi^2 x_3\sin[\pi x_1]\sin[\pi x_2]\exp[\pi(-x_3^2 + 0.25)] \\
v_{a,13} &= (-4(\pi x_3)^2 + 2\pi)\sin[\pi x_1]\cos[\pi x_2]\exp[\pi(-x_3^2 + 0.25)] \\
v_{a,23} &= (-4(\pi x_3)^2 + 2\pi)\cos[\pi x_1]\sin[\pi x_2]\exp[\pi(-x_3^2 + 0.25)] \\
v_{a,33} &= 4\pi x_3(-2\pi x_3^2 + 3)\cos[\pi x_1]\cos[\pi x_2]\exp[\pi(-x_3^2 + 0.25)] \\
v_{3,aa} &= -\pi^2\sin[\pi(x_1 + x_2)](\exp[\pi(-x_3^2 + 0.25)] - 1) \\
v_{3,a3} &= -2\pi^2 x_3\cos[\pi(x_1 + x_2)]\exp[\pi(-x_3^2 + 0.25)] \\
v_{3,33} &= -v_{a,13} - v_{a,23} \\
\gamma_e &= \sqrt{5v_{a,1}^2 + 5v_{a,2}^2 + 6v_{a,1}v_{a,2} + 2(v_{3,a} + v_{a,3})^2} \\
\mu_e &= \mu_\infty + (\mu_0 - \mu_\infty)(1 + (\lambda^a\gamma_e^a))^{\frac{(n-1)}{a}} \\
\mu_e' &= \frac{\mathrm{d}\mu_e}{\mathrm{d}\gamma_e} \\
\gamma_{e,1} &= ((5v_{a,1} + 3v_{a,2})v_{a,aa} + (3v_{a,1} + 5v_{a,2})v_{a,12} + 2(v_{3,a} + v_{a,3})(v_{3,aa} + v_{a,13}))/\gamma_e \\
\gamma_{e,2} &= ((3v_{a,1} + 5v_{a,2})v_{a,aa} + (5v_{a,1} + 3v_{a,2})v_{a,12} + 2(v_{3,a} + v_{a,3})(v_{3,aa} + v_{a,23}))/\gamma_e \\
\gamma_{e,3} &= ((5v_{a,1} + 3v_{a,2})v_{a,13} + (3v_{a,1} + 5v_{a,2})v_{a,23} + 2(v_{3,a} + v_{a,3})(v_{3,a3} + v_{a,33}))/\gamma_e
\end{aligned}
$$

# C Appendix: Time discretization

## C.1 Butcher tableaus for applied ESDIRK schemes

The parameters for various explicit-singly-diagonal-implicit Runge-Kutta methods with stage number $s$ and order $p$ with the corresponding reference literatures are given in the following Butcher tableaus.

Table C.1: ESDIRK-3 with s=4, p=3, from Montlaur et al. [281]

$$\begin{array}{c|cccc}
0 & 0 & & & \\
1 & \frac{1}{2} & \frac{1}{2} & & \\
\frac{3}{2} & \frac{5}{8} & \frac{3}{8} & \frac{1}{2} & \\
1 & \frac{7}{18} & \frac{1}{3} & -\frac{2}{9} & \frac{1}{2} \\
\hline
 & \frac{7}{18} & \frac{1}{3} & -\frac{2}{9} & \frac{1}{2}
\end{array}$$

Table C.2: ESDIRK-2 with s=2, p=2, (Crank-Nicolson)

$$\begin{array}{c|cc}
0 & 0 & \\
1 & 1/2 & 1/2 \\
\hline
 & 1/2 & 1/2
\end{array}$$

## C.2 Butcher tableaus for applied embedded ESDIRK and SDIRK schemes

The parameters for different embedded ESDIRK and SDIRK methods with number of stages $s$, order $p$ and order of the embedded scheme $q$ with the corresponding reference literatures are given in the following Butcher tableaus.

Table C.3: ESDIRK-2(1), s=3, p=2 q=1, from Rang [318]

$$\begin{array}{c|ccc}
0 & 0 & & \\
2-\frac{2}{\sqrt{2}} & 1-\frac{\sqrt{2}}{2} & 1-\frac{\sqrt{2}}{2} & \\
1 & \frac{1}{2\sqrt{2}} & \frac{1}{2\sqrt{2}} & 1-\frac{\sqrt{2}}{2} \\
\hline
\beta_i & \frac{1}{2\sqrt{2}} & \frac{1}{2\sqrt{2}} & 1-\frac{\sqrt{2}}{2} \\
\hdashline
\hat{\beta}_i & \frac{1}{2}-\frac{\sqrt{2}}{8} & \frac{1}{2}-\frac{\sqrt{2}}{8} & \frac{\sqrt{2}}{4}
\end{array}$$

Table C.4: SDIRK-2(1) with s=2, p=2, q=1, from Ellsiepen and Hartmann [138]

$$\begin{array}{c|cc}
\alpha & \alpha & \\
1 & 1-\alpha & \alpha \\
\hline
\beta_i & 1-\alpha & \alpha \\
\hdashline
\hat{\beta}_i & 1-\hat{\alpha} & \hat{\alpha}
\end{array}$$

with

$$\alpha = 1-\frac{1}{2}\sqrt{2}, \quad \hat{\alpha} = 2-\frac{5}{4}\sqrt{2}$$

Table C.5: SDIRK-4(3), s=5, p=4 q=3, from Hairer and Wanner [177]

| | | | | | |
|---|---|---|---|---|---|
| $\frac{1}{4}$ | $\frac{1}{4}$ | | | | |
| $\frac{3}{4}$ | $\frac{1}{2}$ | $\frac{1}{4}$ | | | |
| $\frac{11}{20}$ | $\frac{17}{50}$ | $-\frac{1}{25}$ | $\frac{1}{4}$ | | |
| $\frac{1}{2}$ | $\frac{371}{1360}$ | $-\frac{137}{2720}$ | $\frac{15}{544}$ | $\frac{1}{4}$ | |
| $1$ | $\frac{25}{24}$ | $-\frac{49}{48}$ | $\frac{125}{16}$ | $-\frac{85}{12}$ | $\frac{1}{4}$ |
| $\beta_i$ | $\frac{25}{24}$ | $-\frac{49}{48}$ | $\frac{125}{16}$ | $-\frac{85}{12}$ | $\frac{1}{4}$ |
| $\hat{\beta}_i$ | $\frac{59}{48}$ | $-\frac{17}{96}$ | $\frac{225}{32}$ | $-\frac{85}{12}$ | $0$ |

Table C.6: ESDIRK-3(2) with s=4, p=3, q=2, from Bijl et al. [41]

| | | | | |
|---|---|---|---|---|
| $0$ | $0$ | | | |
| $\frac{1767732205903}{2027836641118}$ | $\frac{1767732205903}{4055673282236}$ | $\frac{1767732205903}{4055673282236}$ | | |
| $\frac{3}{5}$ | $\frac{2746238789719}{10658868560708}$ | $\frac{-640167445237}{6845629431997}$ | $\frac{1767732205903}{4055673282236}$ | |
| $1$ | $\frac{1471266399579}{7840856788654}$ | $\frac{-4482444167858}{7529755066697}$ | $\frac{11266239266428}{11593286722821}$ | $\frac{1767732205903}{4055673282236}$ |
| $\beta_i$ | $\frac{1471266399579}{7840856788654}$ | $\frac{-4482444167858}{7529755066697}$ | $\frac{11266239266428}{11593286722821}$ | $\frac{1767732205903}{4055673282236}$ |
| $\hat{\beta}_i$ | $\frac{2756255671327}{12835298489170}$ | $\frac{-10771552573575}{22201958757719}$ | $\frac{9247589265047}{10645013368117}$ | $\frac{2193209047091}{5459859503100}$ |

Table C.7: ESDIRK-4(3) with s=6, p=4, q=3, from Bijl et al. [41]

| | | | | | | |
|---|---|---|---|---|---|---|
| $0$ | $0$ | | | | | |
| $\frac{1}{2}$ | $\frac{1}{4}$ | $\frac{1}{4}$ | | | | |
| $\frac{83}{250}$ | $\frac{8611}{62500}$ | $\frac{-1743}{31250}$ | $\frac{1}{4}$ | | | |
| $\frac{31}{50}$ | $\frac{5012029}{34652500}$ | $\frac{-654441}{2922500}$ | $\frac{174375}{388108}$ | $\frac{1}{4}$ | | |
| $\frac{17}{20}$ | $\frac{15267082809}{155376265600}$ | $\frac{-71443401}{120774400}$ | $\frac{730878875}{902184768}$ | $\frac{2285395}{8070912}$ | $\frac{1}{4}$ | |
| $1$ | $\frac{82889}{524892}$ | $0$ | $\frac{15625}{83664}$ | $\frac{69875}{102672}$ | $\frac{-2260}{8211}$ | $\frac{1}{4}$ |
| $\beta_i$ | $\frac{82889}{524892}$ | $0$ | $\frac{15625}{83664}$ | $\frac{69875}{102672}$ | $\frac{-2260}{8211}$ | $\frac{1}{4}$ |
| $\hat{\beta}_i$ | $\frac{4586570599}{29645900160}$ | $0$ | $\frac{178811875}{945068544}$ | $\frac{814220225}{1159782912}$ | $\frac{-3700637}{11593932}$ | $\frac{61727}{225920}$ |

# D Appendix: LSFEM for FSI

## D.1 Algorithmic procedure for implementation of LS SV formulations to solve dynamic FSI problems

- Initialization of basic variables

$$\boldsymbol{w}^I = \begin{bmatrix} w_1^I \\ w_2^I \end{bmatrix}, \quad \boldsymbol{\beta}^J = \begin{bmatrix} \beta_1^J \\ \beta_2^J \end{bmatrix}, \qquad \begin{array}{l} \boldsymbol{w}^I \text{ DOF for velocities of node } I \\ \boldsymbol{\beta}^J \text{ DOF for stresses at interpolation site } J \end{array}$$

- Time discretization
  1. Read history values (e.g. $\boldsymbol{v}_n^I, \boldsymbol{u}_n^I, \boldsymbol{u}_{n-1}^I, \boldsymbol{u}_{n-2}^I$)
  2. Approximate time dependent quantities at actual time step $n+1$ for each node $I$ ($\boldsymbol{u}^I{}_{n+1}$, $\boldsymbol{a}^I{}_{n+1}$)
  3. Write $\boldsymbol{v}^I{}_{n+1}, \boldsymbol{u}^I{}_{n+1}$ to history

- Space discretization
  1. Velocities: $v_i^h = \sum\limits_I N^I {w_i}^I, \quad v_{i,j}^h = \sum\limits_I N_{,j}^I \, w_i^I \quad$ and $\quad v_{i,i}^h = \sum\limits_I N_{,i}^I {w_i}^I$

     Displacements: $u_i^h = \sum\limits_I N^I {u_i}^I \quad$ and $\quad u_{i,j}^h = \sum\limits_I N_{,j}^I \, u_i^I$

     Accelerations: ${a_i}^h = \sum\limits_I N^I a_i^I$

     ($u_i^I$ and $a_i^I$ from the time discretization)
  2. Stresses $\sigma_{ij}^h = \sum\limits_J \psi_j^J \, \beta_i^J, \quad \sigma_{ij,j}^h = \sum\limits_J \psi_{j,j}^J \, \beta_i^J$

     and $\quad \operatorname{dev} \sigma_{ij}^h = \sigma_{ij}^h - \frac{1}{3}\sigma_{mm}^h \delta_{ij}$ with the Kronecker delta $\delta_{ij}$

- Discretized LS functional for FSI

  fluid: $\mathcal{F}^F(\boldsymbol{\sigma}^h, \boldsymbol{v}^h) = \frac{1}{2}\left( \left|\left|\omega_{f1}\mathcal{R}_1^F\right|\right|_{L^2(\Omega_e)}^2 + \left|\left|\omega_{f2}\mathcal{R}_2^F\right|\right|_{L^2(\Omega_e)}^2 + \left|\left|\omega_{f3}\mathcal{R}_3^F\right|\right|_{L^2(\Omega_e)}^2 \right)$ ,

  with $\mathcal{R}_1^F$, $\mathcal{R}_2^F$ and $\mathcal{R}_3^F$ depending on chosen formulation with or without ALE

  solid: $\mathcal{F}^S(\boldsymbol{\sigma}^h, \boldsymbol{v}^h) = \frac{1}{2}\left( \left|\left|\omega_{s1}\mathcal{R}_1^S\right|\right|_{L^2(\Omega_e)}^2 + \left|\left|\omega_{s2}\mathcal{R}_2^S\right|\right|_{L^2(\Omega_e)}^2 + \left|\left|\omega_{s3}\mathcal{R}_3^S\right|\right|_{L^2(\Omega_e)}^2 \right)$ ,

  with $\mathcal{R}_1^S$, $\mathcal{R}_2^S$ and $\mathcal{R}_3^S$ depending on chosen material law for the structure

  FSI: $\quad \mathcal{F}^{FSI}(\boldsymbol{\sigma}^h, \boldsymbol{v}^h) = \mathcal{F}^F(\boldsymbol{\sigma}^h, \boldsymbol{v}^h) + \mathcal{F}^S(\boldsymbol{\sigma}^h, \boldsymbol{v}^h)$

- Element RHS-Vector $\boldsymbol{P}^e$ and System-Matrix $\boldsymbol{S}^e$

  $\boldsymbol{D}^e = [\boldsymbol{d}^1, ..., \boldsymbol{d}^K, \boldsymbol{\beta}^1, ..., \boldsymbol{\beta}^M]^T$ DOF vector of element $e$ with $K$ and $M$ denoting the number of interpolation sites

```
FOR each element e DO
    $\boldsymbol{P}^e = \frac{\partial \mathcal{F}^{FSI}}{\partial \boldsymbol{D}^e}$    and    $\boldsymbol{S}^e = \frac{\partial \boldsymbol{P}^e}{\partial \boldsymbol{D}^e}$
END DO
```

# List of Figures

2.1 Configuration of a continuum body and displacement of a material point . 12

2.2 Concept of stresses - traction vectors acting on cut surface . . . . . . . . . 17

2.3 A viscous fluid sheared between two plates with apparent linear and non-linear velocity profiles, compare SIGLOCH [363] . . . . . . . . . . . . . . . . . 26

2.4 Characteristic behavior of different generalized Newtonian fluids: relation between shear rate $\dot{\gamma}$ and shear stress $\tau$ (left) or viscosity $\eta$ (right) . . . . 29

2.5 Viscosity function for different values of the parameters $n$ (left) and $\lambda$ (right) with the Carreau-Yasuda model . . . . . . . . . . . . . . . . . . . . 29

3.1 Triangulation $\Omega_h$ of an arbitrary domain $\Omega$ in 2D using triangular elements with element domain $\Omega^e$ and mapping from parameter space $\hat{\Omega}_e$ to physical space . . . . . . . . . . . . . . . . . . . . . . . . . . . . . . . . . . . 31

3.2 Order of corner, edge and inner nodes in triangular elements $P_k$ with $k = \{1, 2, 3\}$ for linear, quadratic and cubic Lagrange polynomials (left to right) 35

3.3 Area coordinates for construction of Lagrange shape functions on triangles, according to ZIENKIEWICZ AND TAYLOR [431] . . . . . . . . . . . . . . . 36

3.4 Order of interpolation sites and naming of Raviart-Thomas shape functions for elements $RT_0$, $RT_1$ and $RT_2$ . . . . . . . . . . . . . . . . . . . . . . 37

3.5 Construction of Raviart-Thomas functions for $RT_1$ and $RT_2$ based on $\mathbf{\Psi}_0^{j,1}$ and Lagrange functions defined on subtriangles . . . . . . . . . . . . . . . 38

5.1 SD - geometry and boundary conditions for flow in a square domain (left) and exact solution for total velocity field (right, in m/s) . . . . . . . . . . . 53

5.2 SD - solution for total velocity field (left, in m/s), pressure (center, in N/m$^2$) and stresses $\sigma_{12}$ (right, in N/m$^2$) for a mesh size of 128 triangles using element $RT_2P_3$ . . . . . . . . . . . . . . . . . . . . . . . . . . . 54

5.3 SD - $L^2$-norm of the discretization error in approximation of velocities $\boldsymbol{v}$ and stresses $\boldsymbol{\sigma}$ for different element orders and mesh sizes . . . . . . . . . . 55

5.4 LDC - geometry and boundary conditions (left, in m) and solution for the total velocity field (right, in m/s) . . . . . . . . . . . . . . . . . . . . . . 55

5.5 LDC - velocity profiles at centerlines in $x_1$- and $x_2$-direction obtained with element $RT_2P_3$ and different mesh sizes compared to reference solution from KIM AND REDDY [234] (units [$h$]=[$x$]=m and [$v$]=m/s) . . . . . . . . . . 56

5.6 LDC - influence of parameter $n$ on velocity profiles (units [$x$]=m and [$v$]=m/s)) . . . . . . . . . . . . . . . . . . . . . . . . . . . . . . . . . . . 57

5.7 LDC - influence of parameter $\lambda$ on velocity profiles (units [$x$]=m and [$v$]=m/s)) . . . . . . . . . . . . . . . . . . . . . . . . . . . . . . . . . . . 57

5.8 BFS - geometry and boundary conditions with length $h = 0.5\,\mathrm{m}$ . . . . . . 58

5.9 BFS - structured mesh exemplary for element length $h = 1/4\,\mathrm{m}$ . . . . . . 58

5.10 BFS - distribution of total velocity field $|\boldsymbol{v}|$ obtained with mesh level 3 . . 59

5.11 BFS - velocity profiles for different mesh levels at $x_1 = 7\,\mathrm{m}$ (top) and $x_2 = 15\,\mathrm{m}$ (bottom) compared to reference solution from GARTLING [162] for $Re = 800$ . . . . . . . . . . . . . . . . . . . . . . . . . . . . . . . . 59

5.12 BFS - shear stress $\boldsymbol{\sigma}_1 \cdot \boldsymbol{n}$ at bottom wall and points of reattachment compared to reference solution from KIM AND REDDY [234] for different Reynolds numbers . . . . . . . . . . . . . . . . . . . . . . . . . . . . 61

5.13 BFS - reattachment point $x_R$ depending on different values for $\lambda$ and $n$ . . 61

5.14 BFS - shear stress $\boldsymbol{\sigma}_1 \cdot \boldsymbol{n}$ at bottom wall for different values $n$ . . . . . . . 62

5.15 BFS - shear stress $\boldsymbol{\sigma}_1 \cdot \boldsymbol{n}$ at bottom wall for different values $\lambda$ . . . . . . . 62

5.16 NC - geometry for channel with smooth 4:1 narrowing . . . . . . . . . . . 63

5.17 NC - mesh structure (left) and total velocity field for mesh level M3 with element $RT_2P_3$ (right, in m/s) . . . . . . . . . . . . . . . . . . . . . . . . 63

5.18 NC - velocity profiles (in m/s) without data assimilation (mesh levels M2, M3, M4) and with data assimilation at cut $C3$ (for mesh M2) . . . . . . . 65

5.19 Cube - error of total velocity $\varepsilon_v$ and pressure $\varepsilon_p$ compared to exact solution over element length in logarithmic scale for different element orders . . . . 67

5.20 Cube - velocity field $|\boldsymbol{v}|$ in planes $x_1 = 0$, $x_2 = 0$ and $x_3 = 0$ (in m/s) . . . 68

5.21 Carotid - pressure field (left, in N/m$^2$) and viscosity (right, in kg/(m s)) on a mesh with element length $h = 1/12$m . . . . . . . . . . . . . . . . . 68

5.22 Carotid - geometry and boundary conditions artery bifurcation (in mm) . . 69

5.23 Carotid - velocity field $|\boldsymbol{v}|$ (left, in m/s) and pressure field $p$ (right, in N/m$^2$) 70

5.24 Carotid - velocity field (left, in m/s), pressure field $p$ (center, in N/m$^2$) and vector plot showing secondary flow (right) in cut plane $C1$ . . . . . . . . . 71

5.25 Carotid - absolute error in velocity compared to Galerkin reference solution (left) and mass loss (right) with different mesh levels and element orders . 71

5.26 Carotid - velocity profiles (in m/s) along centerlines $A$ (top) and $B$ (bottom) in planes $C1, C3, C5$, obtained with element $P_2P_3P_2$ and different mesh levels (axis in m) . . . . . . . . . . . . . . . . . . . . . . . . . . 72

5.27 Carotid - velocity profiles (in m/s) along centerlines $A$ (top) and $B$ (bottom) in planes $C1, C3, C5$, results without data assimilation and with experimental data assimilation on line and on whole plane (axis in m) . . . . 73

5.28 Carotid - interpolation of experimental velocity data (in m/s) on planes $C2$ (top) and $C4$ (bottom) in internal carotid artery (axis in m) . . . . . . 74

5.29 Carotid - velocity profiles (in m/s) along centerlines $A$ (top) and $B$ (bottom) in planes $C2$-$C4$, results without data assimilation and with numerical data assimilation on planes only in ICA ($C1, C5$) and on planes in ICA & ECA ($C1, C5, C6$) (axis in m) . . . . . . . . . . . . . . . . . . . . . . . 75

7.1 Schematic visualization of the solution of initial value problems, division in subintervals (left) and explicit function integration (right) . . . . . . . . 83

7.2 Schematic visualization of the upwind finite difference scheme . . . . . . . 88

7.3 Spatial discretization using FD scheme for advection equation in 1D (left) and analytical solution at different times (right) . . . 88

7.4 Approximation at different times steps (dashed line) compared to exact solution (solid line) obtained with implicit Euler (left) and RK method with parameters corresponding to Crank-Nicolson method (right) with 100 grid points . . . 92

7.5 TGV - distribution of the velocity components $v_1$ (left), $v_2$ (center) and the total velocity $|\boldsymbol{v}|$ (right) at time $t = 1\,\mathrm{s}$, obtained with ESDIRK-2 and $RT_3P_4$ (in m/s) . . . 100

7.6 TGV - distribution of the stress components $\sigma_{11}$ (left), $\sigma_{12}$ (center) and $\sigma_{22}$ (right) at time $t = 1\,\mathrm{s}$, obtained with ESDIRK-2 and $RT_3P_4$ (in N/m$^2$) . . . 101

7.7 TGV - $L^2$-norm of the error in velocities and stresses obtained with ESDIRK-2 for different element orders and mesh levels . . . 102

7.8 TGV - $L^2$-norm of the error in velocities obtained with $n_{\mathrm{ele}} = 8192$ elements of order $RT_3P_4$ for different time discretization methods and time step sizes $\Delta t$ . . . 102

7.9 TGV - $L^2$-norm of error in velocities for different $\Delta t$ ($n_{\mathrm{ele}} = 512$, $RT_3P_4$) . . . 103

7.10 FAC - geometry and boundary conditions (unit m) . . . 103

7.11 FAC - distribution of velocity field with the Houbolt method with $\Delta t = 0.005\,\mathrm{s}$ and $n_{\mathrm{ele}} = 9,728$ elements at $t = 14\,\mathrm{s}$ . . . 104

7.12 FAC - evolution of drag coefficient $c_D$ over time $t$ (in $s$) for different element orders and mesh levels, with Crank Nicolson method (bottom) and Houbolt method (top) with $\Delta t = 0.005\,\mathrm{s}$, with reference solution from Turek et al. [397] . . . 105

7.13 FAC - drag coefficient $c_D$ over time $t$ (in s) for different time integration methods ($RT_2P_3$, $\Delta t = 0.005\,\mathrm{s}$), with reference solution from Turek et al. [397] . . . 106

7.14 FAC - error of drag coefficient with $RT_2P_3$ on different mesh levels, for different time integration methods and different increments $\Delta t$ . . . 107

7.15 FAC - mass flow difference $\Delta Q$ (left) and residual $\mathcal{R}_3^F := \operatorname{div} \boldsymbol{v}$ (right) over time $t$ (in s) for different time integration methods with $\Delta t = 0.005\,\mathrm{s}$ (Level 3, $RT_2P_3$) . . . 107

7.16 FAC - kinetic energy $E$ over time $t$ (in s) for different time integration methods with $\Delta t = 0.005\,\mathrm{s}$ (Level 3, $RT_2P_3$) . . . 108

7.17 VP - distribution of velocity component $v_1$ (left in m/s), displacement $u_1$ (center in m) and stress component $\sigma_{11}$ (right in N/m$^2$) at time $t = 1\,\mathrm{s}$ . . . 109

7.18 VP - $L^2$-norm of the error in velocities obtained with $n_{\mathrm{ele}} = 8192$ elements of order $RT_3P_4$ for different time discretization methods and time step sizes $\Delta t$ . . . 110

7.19 Algorithm for adaptive time stepping . . . 114

7.20 FAC3 - distribution of velocity field at different time steps $t = \{2, 4, 6, 8\}$ s with SDIRK-4(3) and adaptive time stepping with $\epsilon_a = 10^{-4}$ . . . . . . . . 116

7.21 FAC3 - evolution of drag (left) and lift (right) coefficient for different tolerances $\epsilon_a$ and SDIRK-2(1) . . . . . . . . . . . . . . . . . . . . . . . . . 117

7.22 FAC3 - evolution of time step size for different tolerances $\epsilon_a$ and SDIRK-2(1) 117

7.23 FAC3 - error $e_L$ in lift coefficient over CPU time for adaptive time stepping with different tolerances $\epsilon_a$ and constant step sizes using SDIRK-2(1) . . . 118

7.24 FAC3 - evolution of time step size (left) and lift coefficient (right) over time using SDIRK-2(1) with different tolerance parameters $\epsilon_r$ and $\epsilon_a$ . . . . . . 119

7.25 FAC3 - evolution of time step size (left) and lift coefficient (right) over time using ESDIRK-3(2) with different tolerance parameters $\epsilon_r$ and $\epsilon_a$ . . . . . . 119

7.26 FAC3 - evolution of time step size (left) and lift coefficient (right) over time using SDIRK-4(3) with different tolerance parameters $\epsilon_r$ and $\epsilon_a$ . . . . . . 119

7.27 FAC3 - error $e_L$ in lift coefficient over CPU time for adaptive time stepping with different absolute and relativ tolerances and constant step sizes using SDIRK-2(1) . . . . . . . . . . . . . . . . . . . . . . . . . . . . . . . . . 120

7.28 DCB - geometry and boundary conditions (unit m) . . . . . . . . . . . . 120

7.29 DCB - vertical displacement $u_2$ at $A(10, 1)$ m over time for SDIRK-2(1) with different constant time step sizes $\Delta t$ . . . . . . . . . . . . . . . . . . 121

7.30 DCB - vertical displacement $u_2$ at $A(10, 1)$ m over time for SDIRK-4(3) with different constant time step sizes $\Delta t$ . . . . . . . . . . . . . . . . . . 122

7.31 DCB - evolution of time step size $\Delta t$ (left) and error estimator $e_v$ (right) over time using SDIRK-2(1) with different tolerance parameters $\epsilon_r^v$ and $\epsilon_a^v$ . 123

7.32 DCB - vertical displacement $u_2$ at $A(10, 1)$ m over time for SDIRK-2(1) with different tolerance parameters $\epsilon_r^v$ and $\epsilon_a^v$ . . . . . . . . . . . . . . . . 123

7.33 DCB - evolution of time step size $\Delta t$ (left) and error estimator $e_d$ (right) over time using SDIRK-2(1) with different tolerance parameters $\epsilon_r^d$ and $\epsilon_a^d$ . 125

7.34 DCB - Evolution of time step size $\Delta t$ (left) and error estimator $e_d$ (right) over time using SDIRK-4(3) with different tolerance parameters $\epsilon_r^d$ and $\epsilon_a^d$ . 126

7.35 DCB - controlled change of step size $\Delta t$ at predefined times . . . . . . . . 126

7.36 DCB - evolution of error estimator $e_v$ (left) and $e_d$ (right) using SDIRK-2(1) with constant step size and controlled step size change at predefined times . . . . . . . . . . . . . . . . . . . . . . . . . . . . . . . . . . . . 127

7.37 DCB - evolution of error estimator $e_v$ (left) and $e_d$ (right) using SDIRK-4(3) with constant step size and controlled step size change at predefined times . . . . . . . . . . . . . . . . . . . . . . . . . . . . . . . . . . . . 127

7.38 DCB - evolution of error estimator $e_v$ (left) and $e_d$ (right) using SDIRK-4(3) with controlled step size change and different meshes . . . . . . . . . . . . 128

8.1 Coupling conditions on $\Gamma_i$ for a solid and fluid element . . . . . . . . . . . 131

8.2 FAC-flag (1) - geometry and boundary conditions (unit m) . . . . . . . . . 133

8.3 FOW - geometry, boundary conditions . . . . . . . . . . . . . . . . . . . . . . 136

8.4 FOW - Velocity field $|\boldsymbol{v}|$ at $t = [20, 60, 80, 100]$ s . . . . . . . . . . . . . . . . 137

8.5 FOW - displacement $u_1(A)$ (in m) over time $t$ (in s) for different element orders, time discretization methods and time increments . . . . . . . . . . 137

8.6 Different configurations and related mappings . . . . . . . . . . . . . . . . 138

8.7 Mesh and material motion in Lagrangian, Eulerian and ALE description in 1D with Lagrangian boundary in ALE description, according to Donea et al. [132] . . . . . . . . . . . . . . . . . . . . . . . . . . . . 139

8.8 Flag in mesh domain - geometry and boundary conditions (unit m) . . . . 145

8.9 Flag in mesh domain - mesh level 1 with 72 solid elements in $\Omega_s$ and 889 mesh elements in $\Omega_m$ in undeformed configuration (unit m) . . . . . . . . . 146

8.10 Flag in mesh domain - plot of deformed mesh with global elasticity modulus $E^e_m = 1\,\mathrm{kg/(m\ s^2)}$ (left) and quality of elements (right) at $t = 0.31\,\mathrm{s}$ . . . . 146

8.11 Flag in mesh domain - plot of deformed mesh (left) and quality of elements (right) with different E-moduli $E_{mi} = \{10, 5, 1\}\,\mathrm{kg/(m\ s)^2}$ at $t = 0.5\,\mathrm{s}$ . . . 147

8.12 Flag in mesh domain - quality measure $Q_e$ over time for different combinations of E-moduli (left) and additional scaling with $f^e_Q$ (right) . . . . . . . 147

8.13 Flag in mesh domain - factor to increase stiffness depending on quality (left) and resulting distribution of E-modulus on deformed domain at $t = 0.39\,\mathrm{s}$ with $f^{\max}_Q = 5$ . . . . . . . . . . . . . . . . . . . . . . . . . . . . . . . . 148

8.14 Flag in mesh domain - factor to increase stiffness depending on displacement (left) and quality of elements with linear scaling and $f^{\max}_u = 20$ at $t = 0.38$ (right) . . . . . . . . . . . . . . . . . . . . . . . . . . . . . . . 149

8.15 Flag in mesh domain - quality measure $Q_e$ over time for exponential scaling with $f^e_{u,exp}$ (left) and E-modulus on deformed domain at $t = 0.5\,\mathrm{s}$ with $f^{\max}_u = 20$ . . . . . . . . . . . . . . . . . . . . . . . . . . . . . . . . . 149

8.16 Flag in mesh domain - quality measure $Q_e$ over time for both MJBS approaches (left), and element quality on deformed mesh 3 at $t = 0.47\,\mathrm{s}$ with $E^e_{mJ}$ (right) . . . . . . . . . . . . . . . . . . . . . . . . . . . . . . . 150

8.17 Flag in mesh domain - deformed configuration of mesh level 3 and solid displacement at $t = 0.5\,\mathrm{s}$, left: combination of different factors with $f^{\max}_u = 5$, $f^{\max}_Q = 2$, $E_{mi} = \{5, 2, 1\}$ , right: stiffening with MJBS (8.32b) . . . . . . 151

8.18 Flag in mesh domain - quality measure with mesh level 3 at $t = 0.5\,\mathrm{s}$, left: combination of different factors with $f^{\max}_u = 5$, $f^{\max}_Q = 2$, $E_{mi} = \{5, 2, 1\}$, right: stiffening with MJBS (8.32b) . . . . . . . . . . . . . . . . . . . . . 151

8.19 Channel ALE - geometry and boundary conditions . . . . . . . . . . . . 152

8.20 Channel ALE - function $\hat{u}_m(x_1, t)$ for mesh deformation over time . . . . . 152

8.21 Channel ALE - evolution over time of fluid velocity $v_1$ and mesh displacement $u_2$ at $(L/2, H/2)$, enstrophy $Z$ and kinetic energy $E$ over domain $\Omega_f$ . . . . . . . . . . . . . . . . . . . . . . . . . . . . . . . . . . . 153

8.22 Channel ALE - distribution of fluid velocity $\boldsymbol{v}$ at $t = 5\,\mathrm{s}$ (left) and $t = 7\,\mathrm{s}$ (right) with deformed background mesh (unit m/s) . . . . . . . . . . . . . 153

8.23 Channel contracting - geometry and boundary conditions with $L = 2\,\mathrm{m}$, $H_1 = 0.1\,\mathrm{m}$, $H_2 = 0.5\,\mathrm{m}$ . . . . . . . . . . . . . . . . . . . . . . . . . . 155

8.24 Channel contracting - evolution of displacement (left) and velocity (right) of solid/fluid $(u_2, v_2)$ and mesh $(u_{m2}, v_{m2})$ at center points $A(1, 0.1)\,\mathrm{m}$ and $B(1, 0.6)\,\mathrm{m}$ of lower and upper interface (units m, m/s) . . . . . . . . . . . 155

8.25 Channel contracting - distribution of velocity components in solid and fluid domains at $t = 11\,\mathrm{s}$ (units m/s) . . . . . . . . . . . . . . . . . . . . . . 156

8.26 Channel contracting - distribution of stress components in solid and fluid domains together (top) and normal stress $\sigma_{11}$ in both domains separately (bottom) at $t = 10\,\mathrm{s}$ (units N/m$^2$) . . . . . . . . . . . . . . . . . . . . . 156

8.27 FAC-flag (2) - geometry and boundary conditions (unit m) . . . . . . . . . 157

8.28 FAC-flag (2) - example meshing generated with Gmsh, mesh level 3 (unit m) 159

8.29 FAC-flag (2) - evolution of drag force, lift force and displacements, obtained with Houbolt method, $\Delta t = 1.25 \times 10^{-3}$ and mesh level 5 (units $[F]$=N, $[u]$=m, $[t]$=s) . . . . . . . . . . . . . . . . . . . . . . . . . . . . . . . . 160

8.30 FAC-flag (2) - evolution of drag and lift force, obtained with Houbolt method, different time step sizes and mesh level 5, reference taken from TUREK ET AL. [397] (units $[F]$=N, $[t]$=s) . . . . . . . . . . . . . . . . . . 161

8.31 FAC-flag (2) - evolution of time step size $t \in [0, 20]\,\mathrm{s}$ (left) and zoom (right), obtained with RK methods with adaptive time stepping and mesh 5 (units $[F]$=N, $[t]$=s) . . . . . . . . . . . . . . . . . . . . . . . . . . . . . . . . 164

8.32 FAC-flag (2) - evolution of drag force on $t \in [0, 20]\,\mathrm{s}$ (left) and zoom (right), obtained with RK methods with adaptive time stepping and mesh 5 (units $[F]$=N, $[t]$=s) . . . . . . . . . . . . . . . . . . . . . . . . . . . . . . . . 164

8.33 FAC-flag (2) - evolution of lift force on $t \in [0, 20]\,\mathrm{s}$ (left) and zoom (right), obtained with RK methods with adaptive time stepping and mesh 5 (units $[F]$=N, $[t]$=s) . . . . . . . . . . . . . . . . . . . . . . . . . . . . . . . . 165

8.34 FAC-flag (2) - distribution of displacement field $|\boldsymbol{u}|$ (in m) at different times within one period of flag oscillation . . . . . . . . . . . . . . . . . . . . . 165

8.35 FAC-flag (2) - distribution of total velocity field $|\boldsymbol{v}|$ (in m/s) at different times within one period of flag oscillation . . . . . . . . . . . . . . . . . . 166

## List of Tables

2.1 Characteristics of Lagrangian and Eulerian description of motion . . . . . . 14

2.2 Definition and characteristics of common deformation and strain tensors . 16

2.3 Summary of relevant characteristics and relations of common stress tensors 18

2.4 Local statements of balance equations in Lagrangian and Eulerian description 22

5.1 SD - mesh level, number of elements ($n_{\text{ele}}$) and degrees of freedom ($n_{\text{dof}}$) for different element types . . . 54

5.2 LDC - material and viscosity model parameters . . . 56

5.3 BFS - mesh level, minimum element length $h$, number of elements ($n_{\text{ele}}$) and degrees of freedom ($n_{\text{dof}}$) for discretizations with element $RT_2P_3$ . . . 60

5.4 BFS - reattachment length $x_R$ for different Reynolds numbers by changing the dynamic viscosity . . . 60

5.5 NC - mesh level, number of elements ($n_{\text{ele}}$), number of degrees of freedom ($n_{\text{dof}}$) and results for mass loss (difference of inflow and outflow in %) and absolute velocity error (in cuts $C1$, $C2$, $C4$) compared to numerical reference solution . . . 64

5.6 Cube - material and model parameters . . . 67

5.7 Carotid - material and model parameters . . . 69

5.8 Carotid - mesh level, number of elements ($n_{\text{ele}}$) and number of degrees of freedom ($n_{\text{dof}}$) for different element types . . . 70

5.9 Carotid - effect of experimental data assimilation on mass loss (in %), obtained with element $P_2P_3P_2$ and mesh level M2 . . . 73

5.10 Carotid - effect of data assimilation in ICA ($C1, C5$) or ICA & ECA ($C1, C5, C6$) with element $P_2P_3P_2$ and mesh level M2 or M5, mass loss (difference of in- and outflow in %) and velocity error ($C2$-$C4$) . . . 76

7.1 General Butcher tableau for fully implicit RK with $s$ stages (left) and for SDIRK with $s = 4$ stages (right) . . . 86

7.2 Characteristics of Runge-Kutta methods . . . 87

7.3 Solution $z(x_i, t_n)$ with implicit Euler and FD upwind scheme at discrete grid points $x_i$ at different time steps $t_n$ . . . 89

7.4 General Butcher tableau for 2-stage ESDIRK-2 (Crank-Nicolson) . . . 90

7.5 Solution $z(x_i, t_n)$ with implicit Runge-Kutta (s=2) and FD upwind scheme at discrete grid points $x_i$ at different time steps $t_n$ . . . 91

7.6 List of used RK methods with number of all stages $s$, number of implicitly evaluated stages, order $p$, order of embedded method $q$, and source literature 98

7.7 TGV - mesh level, number of elements ($n_{\text{ele}}$) and degrees of freedom ($n_{\text{dof}}$) for different element types . . . 101

7.8 TGV - Parameters for Crank-Nicolson method presented in (7.39) . . . 103

7.9 FAC - mesh level, number of elements ($n_{\text{ele}}$) and degrees of freedom ($n_{\text{dof}}$) for different element types . . . 105

7.10 DCB - number of accepted time steps, rejections and iterations, average time step size $\overline{\Delta t}$, and error in $u_2$ for different factors $f_{\min}$ and $f_{\max}$ and tolerances with SDIRK-2(1) . . . 122

7.11 DCB - number of accepted time steps, rejections and iterations, average time step size $\overline{\Delta t}$, and error in $u_2$ for different tolerances $\epsilon_r^v$ and $\epsilon_a^v$ with SDIRK-2(1) . . . 124

7.12 DCB - number of accepted time steps, rejections and iterations, average time step size $\overline{\Delta t}$, and error in $u_2$ for different tolerances $\epsilon_r^d$ and $\epsilon_a^d$ with SDIRK-2(1) . . . 125

7.13 DCB - number of accepted time steps, rejections and iterations, average time step size $\overline{\Delta t}$, and error in $u_2$ for different tolerances $\epsilon_r^d$ and $\epsilon_a^d$ with SDIRK-4(2) . . . 125

7.14 DCB - maximum values of error estimators after step size changes at $t_1 = 1\,\mathrm{s}$ and $t_2 = 1.5\,\mathrm{s}$ for meshes with different number of elements $n_{\mathrm{ele}}$ with SDIRK-4(2) . . . 128

8.1 FAC-flag (1) - material parameters for steady FSI1 from TUREK ET AL. [399] . . . 133

8.2 FAC-flag (1) - mesh level, number of elements $n_{\mathrm{ele}}$ in fluid and solid domain and number of degrees of freedom ($n_{\mathrm{dof}}$) . . . 134

8.3 FAC-flag (1) - displacements $u_1$ and $u_2$ (in m) at point $A(0.6, 0.2)\,\mathrm{m}$, and drag $F_D$ and lift force $F_L$ (in N), obtained with the Houbolt method for both domains, reference solution from TUREK ET AL. [399] . . . 134

8.4 FAC-flag (1) - displacements $u_1$ and $u_2$ (in m) at point $A(0.6, 0.2)$m, and drag $F_D$ and lift force $F_L$ (in N), obtained with the Houbolt and Crank-Nicolson method for solid and fluid domain, reference solution from TUREK ET AL. [399] . . . 135

8.5 FOW - mat. parameters . . . 136

8.6 FOW - displacement $u_1$ (in m) at point $A = (4, 2)\,\mathrm{m}$ for different element orders and time increments using two combinations of time discretizations for solid and fluid . . . 137

8.7 Flag in mesh domain - material parameters according to the dynamic benchmark problem CSM3 from TUREK AND HRON [396] . . . 145

8.8 Channel ALE - parameters . . . 152

8.9 Channel contracting - material parameters . . . 155

8.10 FAC-flag (2) - material parameters for FSI2 from TUREK ET AL. [399] and chosen pseudo-material parameter for linear elastic mesh deformation . . . 158

8.11 FAC-flag (2) - mesh level, number of elements in fluid and solid domain and number of degrees of freedom ($n_{\mathrm{dof}}$) . . . 159

8.12 FAC-flag (2) - mesh convergence, drag and lift forces (in N) and mean relative error compared to reference values from TUREK ET AL. [399] . . . 161

8.13 FAC-flag (2) - mesh convergence, flag displacement at $A(0.6, 0.2)\,\mathrm{m}$ (in m) and mean relative error compared to reference values from TUREK ET AL. [399] . . . 161

8.14 FAC-flag (2) - Number of total Newton iterations, average time step size $\overline{\Delta t}$ (in s), and mean relative errors for different methods and tolerances . . 163
C.1 ESDIRK-3 with s=4, p=3, from MONTLAUR ET AL. [281] . . . . . . . . . 175
C.2 ESDIRK-2 with s=2, p=2, (Crank-Nicolson) . . . . . . . . . . . . . . . . . . 175
C.3 ESDIRK-2(1), s=3, p=2 q=1, from RANG [318] . . . . . . . . . . . . . . . . 175
C.4 SDIRK-2(1) with s=2, p=2, q=1, from ELLSIEPEN AND HARTMANN [138] 175
C.5 SDIRK-4(3), s=5, p=4 q=3, from HAIRER AND WANNER [177] . . . . . . 176
C.6 ESDIRK-3(2) with s=4, p=3, q=2, from BIJL ET AL. [41] . . . . . . . . . 176
C.7 ESDIRK-4(3) with s=6, p=4, q=3, from BIJL ET AL. [41] . . . . . . . . . 177

# References

[1] S. Abarbanel, D. Gottlieb, and M. Carpenter. On the Removal of Boundary Errors Caused by Runge-Kutta Integration of Non-Linear Partial Differential Equations. *SIAM Journal on Scientific Computing*, 17, 1996.

[2] L. Agati, S. Cimino, G. Tonti, F. Cicogna, V. Petronilli, L. De Luca, C. Iacoboni, and G. Pedrizzetti. Quantitative analysis of intraventricular blood flow dynamics by echocardiographic particle image velocimetry in patients with acute myocardial infarction at different stages of left ventricular dysfunction. *Eur Heart J Cardiovasc Imaging*, 15(11):1203–1212, 2014.

[3] R. Alexander. Diagonally Implicit Runge-Kutta Methods for Stiff O.D.E.'s. *SIAM Journal on Numerical Analysis*, 14(6):1006–1021, 1977.

[4] J. Argyris, I. Fried, and D. Scharpf. The TET 20 and TEA 8 elements for the matrix displacement method. *The Aeronautical Journal*, 72(691):618–623, 1968.

[5] J. H. Argyris and S. Kelsey. Energy theorems and structural analysis. *Aircraft engineering*, 23, 1954.

[6] H. Askes, A. Rodrıguez-Ferran, and A. Huerta. Adaptive analysis of yield line patterns in plates with the arbitrary Lagrangian–Eulerian method. *Computers & structures*, 70(3):257–271, 1999.

[7] F. Auteri, N. Parolini, and L. Quartapelle. Numerical Investigation on the Stability of Singular Driven Cavity Flow. *J. Comput. Phys.*, 183(1):1–25, 2002.

[8] S. Averweg, A. Schwarz, C. Nisters, and J. Schröder. A least-squares finite element approach to model fluid-structure interaction problems. *Proceedings in Applied Mathematics and Mechanics*, 19(1):e201900204, 2019.

[9] S. Averweg, A. Schwarz, C. Nisters, and J. Schröder. Implicit time discretization schemes for mixed least-squares finite element formulations. *Computer Methods in Applied Mechanics and Engineering*, 368:113111, 2020.

[10] S. Averweg, A. Schwarz, C. Nisters, and J. Schröder. A least-squares finite element formulation to solve incompressible non-Newtonian fluid flow. *Proceedings in Applied Mathematics and Mechanics*, 20(1):e202000169, 2021.

[11] S. Averweg, A. Schwarz, C. Schwarz, and J. Schröder. Least-squares formulation to solve non-Newtonian fluid flow and application of data assimilation in 2D. *Proceedings in Applied Mathematics and Mechanics*, 21(1):e202100022, 2021.

[12] S. Averweg, A. Schwarz, C. Schwarz, and J. Schröder. 3D modeling of generalized Newtonian fluid flow with data assimilation using the least-squares finite element method. *Computer Methods in Applied Mechanics and Engineering*, 392:114668, 2022.

[13] I. Babuška. The finite element method with lagrangian multipliers. *Numerische Mathematik*, 20(3):179–192, 1973.

[14] C. Bahriawati and C. Carstensen. Three MATLAB implementations of the lowest-order Raviart-Thomas MFEM with a posteriori error control. *Computational methods in applied mathematics*, 5(4):333–361, 2005.

[15] D. Balzani, D. Brands, A. Klawonn, O. Rheinbach, and J. Schröder. On the mechanical modeling of anisotropic biological soft tissue and iterative parallel solution strategies. *Archive of Applied Mechanics*, 80:479–488, 2010.

[16] D. Balzani, D. Böse, D. Brands, R. Erbel, A. Klawonn, O. Rheinbach, and J. Schröder. Parallel simulation of patient-specific atherosclerotic arteries for the enhancement of intravascular ultrasound diagnostics. *Engineering Computations*, 29(8):888–906, 2012.

[17] D. Balzani, S. Deparis, S. Fausten, D. Forti, A. Heinlein, A. Klawonn, A. Quarteroni, O. Rheinbach, and J. Schröder. Numerical modeling of fluid–structure interaction in arteries with anisotropic polyconvex hyperelastic and anisotropic viscoelastic material models at finite strains. *International journal for numerical methods in biomedical engineering*, 32(10):e02756, 2016.

[18] D. Balzani, A. Heinlein, A. Klawonn, O. Rheinbach, and J. Schröder. Comparison of arterial wall models in fluid-structure interaction simulations. *Computational Mechanics*, 2023.

[19] K.-J. Bathe. *Finite Element Procedure.* Prentice-Hall, 1996.

[20] K.-J. Bathe. *Finite-Element-Methoden.* Springer-Verlag, Berlin, 2nd edition, 2002.

[21] K.-J. Bathe and G. Ledezma. Benchmark problems for incompressible fluid flows with structural interactions. *Computers & structures*, 85(11-14):628–644, 2007.

[22] K.-J. Bathe and H. Zhang. A mesh adaptivity procedure for CFD and fluid-structure interactions. *Computers & Structures*, 87(11-12):604–617, 2009.

[23] Y. Bazilevs and K. Takizawa. *Advances in Computational Fluid-Structure Interaction and Flow Simulation: New Methods and Challenging Computations.* Birkhäuser Basel, 1st edition, 2016.

[24] Y. Bazilevs, V. M. Calo, Y. Zhang, and T. J. R. Hughes. Isogeometric Fluid-structure Interaction Analysis with Applications to Arterial Blood Flow. *Computational Mechanics*, 38(4):310–322, 2006.

[25] Y. Bazilevs, J. Gohean, T. Hughes, R. Moser, and Y. Zhang. Patient-specific isogeometric fluid–structure interaction analysis of thoracic aortic blood flow due to implantation of the Jarvik 2000 left ventricular assist device. *Computer Methods in Applied Mechanics and Engineering*, 198(45-46):3534–3550, 2009.

[26] Y. Bazilevs, M. Hsu, J. Kiendl, R. Wüchner, and K. Bletzinger. 3D Simulation of Wind Turbine Rotors at Full Scale. Part II: Fluid - Structure Interaction Modeling with Composite Blades. *Int. J. Numer. Meth. Fluids*, 65:236–253, 2011.

[27] Y. Bazilevs, K. Takizawa, and T. Tezduyar. *Computational Fluid-Structure Interaction: Methods and Applications.* 2013.

[28] Y. Bazilevs, K. Takizawa, T. E. Tezduyar, M.-C. Hsu, N. Kostov, and S. McIntyre. Aerodynamic and FSI analysis of wind turbines with the ALE-VMS and ST-VMS methods. *Archives of Computational Methods in Engineering*, 21(4):359–398, 2014.

[29] Y. Bazilevs, A. Korobenko, X. Deng, and J. Yan. Novel structural modeling and mesh moving techniques for advanced fluid–structure interaction simulation of wind turbines. *International Journal for Numerical Methods in Engineering*, 102(3-4): 766–783, 2015.

[30] Y. Bazilevs, K. Kamran, G. Moutsanidis, D. Benson, and E. Oñate. A new formulation for air-blast fluid–structure interaction using an immersed approach. Part I: basic methodology and FEM-based simulations. *Computational Mechanics*, 60(1): 83–100, Jul 2017.

[31] Y. Bazilevs, G. Moutsanidis, J. Bueno, K. Kamran, D. Kamensky, M. Hillman, H. Gomez, and J. Chen. A new formulation for air-blast fluid–structure interaction using an immersed approach: part II—coupling of IGA and meshfree discretizations. *Computational Mechanics*, 60(1):101–116, Jul 2017.

[32] Y. Bazilevs, K. Takizawa, T. Tezduyar, M.-C. Hsu, Y. Otoguro, H. Mochizuki, and M. Wu. ALE and space–time variational multiscale isogeometric analysis of wind turbines and turbomachinery. In *Parallel Algorithms in Computational Science and Engineering*, pages 195–233. Springer, 2020.

[33] Y. Bazilevs, K. Takizawa, T. Tezduyar, M.-C. Hsu, Y. Otoguro, H. Mochizuki, and M. Wu. Wind turbine and turbomachinery computational analysis with the ALE and space-time variational multiscale methods and isogeometric discretization. *Journal of Advanced Engineering and Computation*, 4(1), 2020.

[34] M. Behr and D. Arora. Shear-slip mesh update method: Implementation and applications. *Computer Methods in Biomechanics and Biomedical Engineering*, 6(2): 113–123, 2003.

[35] B. Bell and K. Surana. A Space-Time Coupled p-Version Least-Squares Finite Element Formulation for Unsteady Fluid Dynamics Problems. *Int. J. Numer. Meth. Eng.*, 37:3545–3569, 1994.

[36] B. Bell and K. Surana. p-Version Least Squares Finite Element Formulation for two-dimensional, incompressible, non-Newtonian isothermal and non-isothermal fluid flow. *International Journal for Numerical Methods in Fluids*, 18:127–162, 1994.

[37] B. Bell and K. Surana. A space-time coupled p-version least squares finite element formulation for unsteady two-dimensional Navier-Stokes equations. *International Journal for Numerical Methods in Engineering*, 39:2593–2618, 1996.

[38] L. Bertagna, M. D'Elia, M. Perego, and A. Veneziani. *Data Assimilation in Cardiovascular Fluid–Structure Interaction Problems: An Introduction*, pages 395–481. Springer Basel, 2014.

[39] B. Bharadvaj, R. Mabon, and D. Giddens. Steady flow in a model of the human carotid bifurcation. Part I - flow visualization. *Journal of Biomechanics*, 15(5):349 – 362, 1982.

[40] B. Bharadvaj, R. Mabon, and D. Giddens. Steady flow in a model of the human carotid bifurcation. part ii—laser-doppler anemometer measurements. *Journal of Biomechanics*, 15(5):363 – 378, 1982.

[41] H. Bijl, M. Carpenter, V. Vatsa, and C. Kennedy. Implicit Time Integration Schemes for the Unsteady Compressible Navier-Stokes Equations: Laminar Flow. *Journal of Computational Physics*, 179(1):313 – 329, 2002.

[42] R. B. Bird, R. C. Armstrong, and O. Hassager. *Dynamics of Polymeric Liquids*, volume I of *Fluid Mechanics*. Wiley, New York, 1987.

[43] P. Birken, K. Quint, S. Hartmann, and A. Meister. A time-adaptive fluid-structure interaction method for thermal coupling. *Computing and visualization in science*, 13(7):331–340, 2010.

[44] F. J. Blom. A monolithical fluid-structure interaction algorithm applied to the piston problem. *Computer Methods in Applied Mechanics and Engineering*, 167(3): 369 – 391, 1998.

[45] J. Blum, F.-X. L. Dimet, and I. M. Navon. Data Assimilation for Geophysical Fluids. In R. M. Temam and J. J. Tribbia, editors, *Special Volume: Computational Methods for the Atmosphere and the Oceans*, volume 14 of *Handbook of Numerical Analysis*, pages 385–441. Elsevier, 2009.

[46] P. Bochev. *Least-Squares Finite Element Methods for the Stokes and Navier-Stokes equations*. Phd thesis, Virginia Polytechnic Institute and State University, Blacksburg, Virginia, 1994.

[47] P. Bochev. Experiences with negative norm least-square methods for the Navier Stokes equations. *Electron. Trans. Numer. Anal.*, 6:44–62, 1997.

[48] P. Bochev and J. Choi. A comparative study of least-squares, SUPG and Galerkin methods for convection problems. *International Journal of Computational Fluid Dynamics*, 15(2):127–146, 2001.

[49] P. Bochev and J. Choi. Improved least-squares error estimates for scalar hyperbolic problems. *Computational Methods in Applied Mathematics*, 1(2):115–124, 2001.

[50] P. Bochev and M. Gunzburger. Analysis of least squares finite element methods for the Stokes equations. *Mathematics of Computation*, 63(208):479–506, 1994.

[51] P. Bochev and M. Gunzburger. Analysis of weighted least squares finite element methods for the Stokes equations. *Mathematics of Computation*, 63:479–506, 1994.

[52] P. Bochev and M. Gunzburger. Least-squares methods for the velocity-pressure-stress formulation of the Stokes equations. *Computer Methods in Applied Mechanics and Engineering*, 126:267–287, 1995.

[53] P. Bochev and M. Gunzburger. Finite element methods of least-squares type. *SIAM Review*, 40:789–837, 1998.

[54] P. Bochev and M. Gunzburger. *Least-Squares Finite Element Methods*. Springer-Verlag, New York, 1st edition, 2009.

[55] P. Bochev, Z. Cai, T. Manteuffel, and S. McCormick. First-order system least-squares for the Navier-Stokes equations. In *NASA Conference Publication*, pages 41–56. Citeseer, 1996.

[56] P. Bochev, Z. Cai, T. Manteuffel, and S. McCormick. Analysis of velocity-flux least-squares methods for the Navier-Stokes equations, part I. *SIAM Journal on Numerical Analysis*, 35:990–1009, 1998.

[57] P. Bochev, T. A. Manteuffel, and S. F. McCormick. Analysis of Velocity-Flux Least-Squares Principles for the Navier-Stokes Equations: Part II. *SIAM Journal on Numerical Analysis*, 36(4):1125–1144, 1999.

[58] T. Bodnár, Galdi, G., and S. Nečasová. *Fluid-Structure Interaction and Biomedical Applications*. Springer, 2014.

[59] D. Boffi, F. Brezzi, and M. Fortin. *Mixed Finite Element Methods and Applications*. Springer, 2013.

[60] P. Bolton. *A least-squares finite element method for the Stokes and Navier-Stokes equations*. PhD thesis, UMIST, 2002.

[61] P. Bolton and R. Thatcher. On mass conservation in least-squares methods. *Journal of Computational Physics*, 203:287–304, 2005.

[62] P. Bolton and R. W. Thatcher. A Least-squares Finite Element Method for the Navier-Stokes Equations. *Journal of Computational Physics*, 213(1):174–183, 2006.

[63] A. Bose and G. Carey. Least-squares p-r finite element methods for incompressible non-Newtonian flows. *Computer Methods in Applied Mechanics and Engineering*, 180(3):431 – 458, 1999.

[64] O. Botella and R. Peyret. Benchmark spectral results on the lid-driven cavity flow. *Computers & Fluids*, 27(4):421–433, 1998.

[65] M. Boulakia, E. Burman, M. A. Fernández, and C. Voisembert. Data assimilation finite element method for the linearized Navier-Stokes equations in the low Reynolds regime. *Inverse Problems*, 36(8):085003, 2020.

[66] D. Braess. *Finite Elemente*. Springer-Verlag, Berlin, 2nd edition, 1997.

[67] F. Brezzi. On the existence, uniqueness and approximation of saddle-point problems arising from Lagrangian multipliers. *Publications mathématiques et informatique de Rennes*, (S4):1–26, 1974.

[68] F. Brezzi and J. Douglas. Stabilized mixed methods for the Stokes problem. *Numerische Mathematik*, 53(1):225–235, 1988.

[69] F. Brezzi and M. Fortin. *Mixed and Hybrid Finite Element Methods*. Springer-Verlag, NewYork, 1991.

[70] P. Bringmann and C. Carstensen. An adaptive least-squares FEM for the Stokes equations with optimal convergence rates. *Numerische Mathematik*, 135(2):459–492, 2017.

[71] A. Brooks and T. Hughes. Streamline upwind/Petrov-Galerkin formulations for convection dominated flows with particular emphasis on the incompressible Navier-Stokes equations. *Computer Methods in Applied Mechanics and Engineering*, 32: 199–259, 1982.

[72] H.-J. Bungartz and M. Schäfer. *Fluid-structure interaction: modelling, simulation, optimisation*, volume 53. Springer Science & Business Media, 2006.

[73] H.-J. Bungartz, M. Mehl, and M. Schäfer. *Fluid Structure Interaction II : Modelling, Simulation, Optimization.* Springer-Verlag Berlin Heidelberg, 2010.

[74] E. Burman and L. Oksanen. Data assimilation for the heat equation using stabilized finite element methods. *Numerische Mathematik*, 139(3):505–528, 2018.

[75] K. Burrage and L. Petzold. On Order Reduction for Runge-Kutta Methods Applied to Differential/Algebraic Systems and to Stiff Systems of ODEs. *Siam Journal on Numerical Analysis*, 27:447–456, 04 1990.

[76] J. C. Butcher. *The Numerical Analysis of Ordinary Differential Equations: Runge-Kutta and General Linear Methods.* Wiley-Interscience, New York, NY, USA, 1987.

[77] J. C. Butcher. *Numerical methods for ordinary differential equations.* John Wiley & Sons, 2016.

[78] Z. Cai and G. Starke. First-order system least squares for the stress-displacement formulation: Linear elasticity. *SIAM Journal on Numerical Analysis*, 41:715–730, 2003.

[79] Z. Cai and G. Starke. Least-squares methods for linear elasticity. *SIAM Journal on Numerical Analysis*, 42:826–842, 2004.

[80] Z. Cai and C. Westphal. An adaptive mixed lest-squares finite element method for viscoelastic fluids of oldroyd type. *Journal of Non-Newtonian Fluid Mechanics*, 159: 72–80, 2009.

[81] Z. Cai, T. Manteuffel, and S. McCormick. First-order system least squares for velocity-vorticity-pressure form of the Stokes equations, with application to linear elasticity. 3:150–159, 1995.

[82] Z. Cai, T. A. Manteuffel, and S. F. McCormick. First-Order System Least Squares for the Stokes Equation, with Application to Linear Elasticity. *SIAM Journal on Numerical Analysis*, 34:1727–1741, 1997.

[83] Z. Cai, T. Manteuffel, S. McCormick, and S. Parter. First-order system least squares (FOSLS) for planar linear elasticity: Pure traction problem. *SIAM Journal on Numerical Analysis*, 35:320–335, 1998.

[84] Z. Cai, C.-O. Lee, T. Manteuffel, and S. McCormick. First-order system least squares for linear elasticity: Numerical results. *SIAM Journal on Scientific Computing*, 21: 1706–1727, 2000.

[85] Z. Cai, C.-O. Lee, T. Manteuffel, and S. McCormick. First-order system least squares for the Stokes and linear elasticity equations: Further results. *SIAM Journal on Scientific Computing*, 21:1728–1739, 2000.

[86] Z. Cai, B. Lee, and P. Wang. Least-squares methods for incompressible Newtonian fluid flow: Linear stationary problems. *SIAM Journal on Numerical Analysis*, 42 (2):843–859, 2004.

[87] Z. Cai, J. Korsawe, and G. Starke. An adaptive least squares mixed finite element method for the stress-displacement formulation of linear elasticity. *Numerical Methods for Partial Differential Equations*, 21:132–148, 2005.

[88] G. Carey and B.-N. Jiang. Least-Squares Finite Elements for First-Order Hyperbolic Systems. *International Journal for Numerical Methods in Engineering*, 26:81–93, 1988.

[89] M. Carpenter, D. Gottlieb, S. Abarbanel, and W. Don. The Theoretical Accuracy of Runge-Kutta Time Discretizations for the Initial Boundary Value Problem: A Study of the Boundary Error. *SIAM Journal on Scientific Computing*, 16:1241–1252, 1995.

[90] P. Carreau, I. MacDonald, and R. Bird. A nonlinear viscoelastic model for polymer solutions and melts—II. *Chemical Engineering Science*, 23(8):901–911, 1968.

[91] P. J. Carreau. Rheological equations from molecular network theories. *Transactions of the Society of Rheology*, 16(1):99–127, 1972.

[92] S. Carstens and D. Kuhl. Higher-order accurate implicit time integration schemes for transport problems. *Archive of Applied Mechanics*, 82(8):1007–1039, 2012.

[93] J. R. Cash. Diagonally Implicit Runge-Kutta Formulae with Error Estimates. *IMA Journal of Applied Mathematics (Institute of Mathematics and Its Applications)*, 24, 1979.

[94] J. Cebral. *Loose coupling algorithms for fluid-structure interaction.* PhD thesis, George Mason University, 1996.

[95] V. Chabannes, G. Pena, and C. Prud'homme. High-order fluid–structure interaction in 2d and 3d application to blood flow in arteries. *Journal of Computational and Applied Mathematics*, 246:1–9, 2013.

[96] C. Chang. A mixed finite element method for the Stokes problem: an acceleration-pressure formulation. *Applied Mathematics and Computation*, 36(2):135–146, 1990.

[97] C. Chang and J. Nelson. Least-squares finite element method for the Stokes problem with zero residual of mass conservation. *SIAM J. Sci. Comput.*, 34(2):480–489, 1997.

[98] T. Chen, C. Cox, H. Lee, and K. Tung. Least-squares finite element methods for generalized Newtonian and viscoelastic flows. *Applied Numerical Mathematics*, 60: 1024–1040, 2010.

[99] T.-F. Chen. Semidiscrete least squares methods for linear convection-diffusion problem. *Computers & Mathematics with Applications*, 24(11):29–44, 1992.

[100] T.-F. Chen. Semidiscrete least squares methods for linear hyperbolic systems. *Numerical Methods for Partial Differential Equations*, 8(5):423–442, 1992.

[101] R. Chhabra and J. Richardson. *Non-Newtonian flow in the process industries: fundamentals and engineering applications.* Butterworth-Heinemann, 1999.

[102] J.-P. Chilès and P. Delfiner. *Geostatistics: Modeling Spatial Uncertainty.* Wiley, 1999.

[103] J.-P. Chilès and N. Desassis. *Handbook of Mathematical Geosciences*, chapter Fifty Years of Kriging. Springer, Cham., 2018.

[104] C.-K. Cho and S. Kim. An essentially non-oscillatory Crank–Nicolson procedure for incompressible Navier–Stokes equations. *International Journal for Numerical Methods in Fluids*, 56(8):1351–1357, 2008.

[105] J. Chung and G. M. Hulbert. A Time Integration Algorithm for Structural Dynamics With Improved Numerical Dissipation: The Generalized-$\alpha$ Method. *Journal of Applied Mechanics*, 60(2):371–375, 06 1993.

[106] R. W. Clough. The finite element method in plane stress analysis. *Proc. 2nd ASCE Conference on Electronic Computation*, pages 345–378, 1960.

[107] O. Colomés and S. Badia. Segregated Runge–Kutta methods for the incompressible Navier–Stokes equations. *International Journal for Numerical Methods in Engineering*, 105(5):372–400, 2016.

[108] R. Courant, E. Isaacson, and M. Rees. On the solution of nonlinear hyperbolic differential equations by finite differences. *Communications on Pure and Applied Mathematics*, 5(3):243–255, 1952.

[109] J. Crank and P. Nicolson. A practical method for numerical evaluation of solutions of partial differential equations of the heat-conduction type. *Advances in Computational Mathematics*, 6(1):207–226, 1996.

[110] N. Cressie. The origins of kriging. *Mathematical Geology*, 22(3):239–252, 1990.

[111] M. Crochet, A. Davies, and K. Walters. *Numerical simulation of non-Newtonian flow.* Elsevier, 2012.

[112] M. M. Cross. Rheology of non-Newtonian fluids: A new flow equation for pseudoplastic systems. *Journal of Colloid Science*, 20(5):417 – 437, 1965.

[113] I. Currie. *Fundamental mechanics of fluids.* CRC Press, 1974.

[114] C. F. Curtiss and J. O. Hirschfelder. Integration of Stiff Equations. *Proceedings of the National Academy of Sciences*, 38(3):235–243, 1952.

[115] H. Dalimunthe and K. Surana. p-Version least squares finite element formulation for three-dimensional, incompressible, non-isothermal, non-Newtonian fluid flow. *Computers & Structures*, 58(1):85–105, 1996.

[116] P. de Sampaio, P. Hallak, A. Coutinho, and M. Pfeil. A stabilized finite element procedure for turbulent fluid–structure interaction using adaptive time–space refinement. *International Journal for Numerical Methods in Fluids*, 44(6):673–693, 2004.

[117] H. De Sterck, T. Manteuffel, S. McCormick, and L. Olson. Least-squares finite element methods and algebraic multigrid solvers for linear hyperbolic PDEs. *SIAM Journal on Scientific Computing*, 26(1):31–54, 2004.

[118] H. De Sterck, T. Manteuffel, S. McCormick, and L. Olson. Numerical conservation properties of H (div)-conforming least-squares finite element methods for the Burgers equation. *SIAM Journal on Scientific Computing*, 26(5):1573–1597, 2005.

[119] J. Deang and M. Gunzburger. Issues related to least-squares finite element methods for the Stokes equations. *SIAM Journal on Scientific Computing*, 20(3):878–906, 1998.

[120] J. Degroote. Partitioned simulation of fluid-structure interaction. *Archives of computational methods in engineering*, 20(3):185–238, 2013.

[121] J. Degroote, K.-J. Bathe, and J. Vierendeels. Performance of a new partitioned procedure versus a monolithic procedure in fluid–structure interaction. *Computers & Structures*, 87(11-12):793–801, 2009.

[122] M. D'Elia and A. Veneziani. Uncertainty quantification for data assimilation in a steady incompressible Navier-Stokes problem. *ESAIM: Mathematical Modelling and Numerical Analysis - Modélisation Mathématique et Analyse Numérique*, 47(4): 1037–1057, 2013.

[123] S. Deparis, M. Deville, F. Menghini, L. Pegolotti, and A. Quarteroni. Application of the Rosenbrock methods to the solution of unsteady 3D incompressible Navier-Stokes equations. *Computers & Fluids*, 179:112–122, 2019.

[124] A. Deshpande, J. Krishnan, and S. Kumar. *Rheology of Complex Fluids.* Springer, New York, 2010.

[125] W. G. Dettmer and D. Perić. A computational framework for fluid–structure interaction: Finite element formulation and applications. *Computer Methods in Applied Mechanics and Engineering*, 195(41):5754 – 5779, 2006.

[126] W. G. Dettmer and D. Perić. A Fully Implicit Computational Strategy for Strongly Coupled Fluid-Solid Interaction. *Archives of Computational Methods in Engineering*, 14(3):205–247, 2007.

[127] S. Diebels, P. Ellsiepen, and W. Ehlers. Error-controlled Runge-Kutta time integration of a viscoplastic hybrid two-phase model. *Technische Mechanik*, 19(19-27): 125, 1999.

[128] X. Ding and T. Tsang. On First-Order Formulations of the Least-Squares Finite Element Method for Incompressible Flows. *International Journal of Computational Fluid Dynamics*, 17:183–197, 2003.

[129] J. Donea and A. Huerta. *Finite element methods for flow problems.* John Wiley and Sons, 2003.

[130] J. Donea and L. Quartapelle. An introduction to finite element methods for transient advection problems. *Computer Methods in Applied Mechanics and Engineering*, 95 (2):169–203, 1992.

[131] J. Donea, S. Giuliani, and J. Halleux. An arbitrary lagrangian-eulerian finite element method for transient dynamic fluid-structure interactions. *Computer Methods in Applied Mechanics and Engineering*, 33(1):689 – 723, 1982.

[132] J. Donea, A. Huerta, J.-P. Ponthot, and A. Rodríguez-Ferran. *Arbitrary Lagrangian–Eulerian Methods*, chapter 14. John Wiley & Sons, Ltd, 2004.

[133] E. Dowell and K. Hall. Modeling of fluid-structure interaction. *Annual Review of Fluid Mechanics*, 33(1):445–490, 2001.

[134] F. Duarte, R. Gormaz, and S. Natesan. Arbitrary Lagrangian–Eulerian method for Navier–Stokes equations with moving boundaries. *Computer Methods in Applied Mechanics and Engineering*, 193(45-47):4819–4836, 2004.

[135] R. Dwight. Bayesian inference for data assimilation using Least-Squares Finite Element methods. *IOP Conference Series: Materials Science and Engineering*, 10: 012224, 2010.

[136] E. Eason. A review of least-squares methods for solving partial differential equations. *International Journal for Numerical Methods in Engineering*, 10:1021–1046, 1976.

[137] N. Edgar and K. Surana. p-version least-squares finite-element formulation for axisymmetric incompressible Newtonian and non-Newtonian fluid flow with heat transfer. *Numerical Heat Transfer, Part B: Fundamentals*, 27(2):213–235, 1995.

[138] P. Ellsiepen and S. Hartmann. Remarks on the interpretation of current non-linear finite element analyses as differential-algebraic equations. *International Journal for Numerical Methods in Engineering*, 51(6):679–707, 2001.

[139] A. Eringen. *Mechanics of Continua.* John Wiley and Sons, 1967.

[140] V. Ervin. Computational bases for RTk and BDMk on triangles. *Computers & Mathematics with Applications*, 64(8):2765–2774, 2012.

[141] S. Étienne, A. Garon, and D. Pelletier. Perspective on the geometric conservation law and finite element methods for ALE simulations of incompressible flow. *Journal of Computational Physics*, 228(7):2313–2333, 2009.

[142] L. Failer and T. Wick. Adaptive time-step control for nonlinear fluid–structure interaction. *Journal of Computational Physics*, 366:448–477, 2018.

[143] C. Felippa and K. Park. Staggered transient analysis procedures for coupled mechanical systems: Formulation. *Computer Methods in Applied Mechanics and Engineering*, 24(1):61 – 111, 1980.

[144] C. Felippa, K. C. Park, and J. A. Deruntz. Stabilization of staggered solution procedures for fluid–structure interaction analysis. *Computational Methods for Fluid-Structure Interaction Problems*, 26:95–124, 1977.

[145] C. Felippa, K. C. Park, and C. Farhat. Partitioned analysis of coupled system. *Computer Methods in Applied Mechanics and Engineering*, 190:3247–3270, 1998.

[146] C. A. Felippa. A historical outline of matrix structural analysis: A play in three acts. Technical report, CU-CAS-00-13, Center for Aerospace Structures, University of Colorado, 2000.

[147] Z. Feng and K. Surana. p-Version least squares finite element formulation for three-dimensional, isothermal, incompressible, non-Newtonian fluid flow. *Computers & Structures*, 57(5):799–816, 1995.

[148] M. Fernández, M. Landajuela, and M. Vidrascu. Fully decoupled time-marching schemes for incompressible fluid/thin-walled structure interaction. *Journal of Computational Physics*, 297:156–181, 2015.

[149] J. Ferziger and M. Perić. *Numerische Strömungsmechanik.* 2008. ISBN 978-3-662-46543-1. doi: 10.1007/978-3-662-46544-8.

[150] G. Fix and M. Gunzburger. On Least Squares Approximations to Indefinite Problems of the Mixed Type. *International Journal for Numerical Methods in Engineering*, 12:453–469, 1978.

[151] G. Fix, M. Gunzburger, and R. Nicolaides. On finite element methods of the least squares type. *Computational Methods in Applied Mathematics*, 5:87–98, 1979.

[152] L. Formaggia, A. Quarteroni, and A. Veneziani. *Cardiovascular Mathematics: Modeling and Simulation of the Circulatory System*, volume 1. 2009.

[153] C. Förster, W. A. Wall, and E. Ramm. Artificial added mass instabilities in sequential staggered coupling of nonlinear structures and incompressible viscous flows. *Computer Methods in Applied Mechanics and Engineering*, 196(7):1278 – 1293, 2007.

[154] A. Fortin, R. Guénette, and R. Pierre. On the discrete evss method. *Computer methods in applied mechanics and engineering*, 189(1):121–139, 2000.

[155] S. Frei, B. Holm, T. Richter, T. Wick, and H. Yang, editors. *Fluid-Structure Interaction: Modeling, Adaptive Discretisations and Solvers.* De Gruyter, 2017.

[156] B. Froehle and P.-O. Persson. A high-order discontinuous Galerkin method for fluid–structure interaction with efficient implicit–explicit time stepping. *Journal of Computational Physics*, 272:455–470, 2014.

[157] G. Fu and W. Kuang. A monolithic divergence-conforming HDG scheme for a linear fluid-structure interaction model. *SIAM Journal on Numerical Analysis*, 60 (2):631–658, 2022.

[158] T. Führer and M. Karkulik. Space-time least-squares finite elements for parabolic equations. *Computers & Mathematics with Applications*, 92:27–36, 2021.

[159] P. Fullsack. An arbitrary Lagrangian-Eulerian formulation for creeping flows and its application in tectonic models. *Geophysical Journal International*, 120(1):1–23, 1995.

[160] M. Gadala and J. Wang. ALE formulation and its application in solid mechanics. *Computer Methods in Applied Mechanics and Engineering*, 167(1-2):33–55, 1998.

[161] G. P. Galdi and R. Rannacher. *Fundamental trends in fluid-structure interaction*, volume 1. World Scientific, 2010.

[162] D. Gartling. A test problem for outflow boundary conditions—flow over a backward-facing step. *International Journal for Numerical Methods in Fluids*, 11(7):953–967, 1990.

[163] M. W. Gee, U. Küttler, and W. A. Wall. Truly monolithic algebraic multigrid for fluid-structure interaction. *International Journal for Numerical Methods in Engineering*, 85:987–1016, 2011.

[164] M. Gerritsma. Direct minimization of the discontinuous least-squares spectral element method for viscoelastic fluids. *Journal of Scientific Computing*, 27(1):245–256, 2006.

[165] C. Geuzaine and J.-F. Remacle. Gmsh: A 3-D finite element mesh generator with built-in pre- and post-processing facilities. *International Journal for Numerical Methods in Engineering*, 79(11):1309–1331, 2009.

[166] P. Geuzaine, C. Grandmont, and C. Farhat. Design and analysis of ale schemes with provable second-order time-accuracy for inviscid and viscous flow simulations. *Journal of Computational Physics*, 191(1):206–227, 2003.

[167] J. Ghaboussi and X. Wu. *Numerical Methods in Computational Mechanics.* Boca Raton: CRC Press, 2016.

[168] H. Giesekus. A simple constitutive equation for polymer fluids based on the concept of deformation-dependent tensorial mobility. *Journal of Non-Newtonian Fluid Mechanics*, 11(1-2):69–109, 1982.

[169] F. Gijsen, F. van de Vosse, and J. Janssen. The influence of the non-Newtonian properties of blood on the flow in large arteries: steady flow in a carotid bifurcation model. *Journal of Biomechanics*, 32(6):601 – 608, 1999.

[170] R. Gilbert, M. Grafenhorst, S. Hartmann, and Z. Yosibash. Simulating the temporal change of the active response of arteries by finite elements with high-order time-integrators. *Computational Mechanics*, 64(6):1669–1684, 2019.

[171] M. Grafenhorst, J. Rang, and S. Hartmann. Time-adaptive finite element simulations of dynamical problems for temperature-dependent materials. *Journal of Mechanics of Materials and Structures*, 12(1):57–91, 2016.

[172] P. Gresho, D. Griffiths, and D. Silvester. Adaptive time-stepping for incompressible flow part i: Scalar advection-diffusion. *SIAM Journal on Scientific Computing*, 30 (4):2018–2054, 2008.

[173] M. Gurtin. *An introduction to continuum mechanics.* Academic press, 1982.

[174] K. Gustafsson. Control-theoretic techniques for stepsize selection in implicit runge-kutta methods. *ACM Transactions on Mathematical Software (TOMS)*, 20(4):496–517, 1994.

[175] K. Gustafsson, M. Lundh, and G. Söderlind. Api stepsize control for the numerical solution of ordinary differential equations. *BIT Numerical Mathematics*, 28(2):270–287, 1988.

[176] R. Haber. A mixed Eulerian-Lagrangian displacement model for large-deformation analysis in solid mechanics. *Computer Methods in Applied Mechanics and Engineering*, 43(3):277–292, 1984.

[177] E. Hairer and G. Wanner. *Solving Ordinary Differential Equations II.* Springer: Berlin, 1996.

[178] E. Hairer, C. Lubich, and M. Roche. *The numerical solution of differential-algebraic systems by Runge-Kutta methods.* Springer, Berlin, Heidelberg, 1989.

[179] E. Hairer, S. Nørsett, and G. Wanner. *Solving Ordinary Differential Equations I Nonstiff problems.* Springer, Berlin, second edition, 2000.

[180] A. Hay, S. Etienne, D. Pelletier, and A. Garon. hp-adaptive time integration for ale simulation of fluid-structure interaction problems. In *53rd AIAA Aerospace Sciences Meeting*, 2015.

[181] M. Heil, A. Hazel, and J. Boyle. Solvers for large-displacement fluid–structure interaction problems: segregated versus monolithic approaches. *Computational Mechanics*, 43(1):91–101, 2008.

[182] W. Herschel and R. Bulkley. Konsistenzmessungen von Gummi-Benzollösungen. *Kolloid-Zeitschrift*, 39(4):291–300, 1926.

[183] A. Hessenthaler. *Multilevel convergence analysis: parallel-in-time integration for fluid-structure interaction problems with applications in cardiac flow modeling.* PhD thesis, Universität Stuttgart, 2020.

[184] A. Hessenthaler, N. Gaddum, O. Holub, R. Sinkus, O. Röhrle, and D. Nordsletten. Experiment for validation of fluid-structure interaction models and algorithms. *International Journal for Numerical Methods in Biomedical Engineering*, 33(9):e2848, 2017.

[185] A. Hessenthaler, O. Röhrle, and D. Nordsletten. Validation of a non-conforming monolithic fluid-structure interaction method using phase-contrast MRI. *International journal for numerical methods in biomedical engineering*, 33(8):e2845, 2017.

[186] A. Hessenthaler, M. Balmus, O. Röhrle, and D. Nordsletten. A class of analytic solutions for verification and convergence analysis of linear and nonlinear fluid-structure interaction algorithms. *Computer methods in applied mechanics and engineering*, 362:112841, 2020.

[187] A. Hessenthaler, R. Falgout, J. Schroder, A. de Vecchi, D. Nordsletten, and O. Röhrle. Time-periodic steady-state solution of fluid-structure interaction and cardiac flow problems through multigrid-reduction-in-time. *Computer Methods in Applied Mechanics and Engineering*, 389:114368, 2022.

[188] J. Heys, C. DeGroff, T. Manteuffel, S. McCormick, and H. Tufo. Modeling 3-D compliant blood flow with FOSLS. *Biomedical sciences instrumentation*, 40:193–199, 2004.

[189] J. Heys, T. Manteuffel, S. McCormick, and J. Ruge. First-order system least-squares (FOSLS) for coupled fluid-elastic problems. *Journal of Computational Physics*, 195: 560–575, 2004.

[190] J. Heys, C. DeGroff, T. Manteuffel, and S. McCormick. First-order system least-squares (FOSLS) for modeling blood flow. *Medical Engineering & Physics*, 28(6): 495–503, 2006.

[191] J. Heys, E. Lee, T. Manteuffel, and S. McCormick. On mass-conserving least-squares methods. *SIAM Journal on Scientific Computing*, 28(3):1675–1693, 2006.

[192] J. Heys, E. Lee, T. Manteuffel, S. McCormick, and J. Ruge. Enhanced mass conservation in least-squares methods for Navier-Stokes equations. *SIAM Journal on Scientific Computing*, 31:2303–2321, 2009.

[193] J. Heys, T. Manteuffel, S. McCormick, M. Milano, J. Westerdale, and M. Belohlavek. Weighted least-squares finite elements based on particle imaging velocimetry data. *Journal of Computational Physics*, 229(1):107–118, 2010.

[194] J. J. Heys, E. Lee, T. A. Manteuffel, and S. F. McCormick. An alternative least-squares formulation of the Navier-Stokes equations with improved mass conservation. *Journal of Computational Physics*, 226:994–1006, 2007.

[195] D. Hilger, N. Hosters, F. Key, S. Elgeti, and M. Behr. A novel approach to fluid-structure interaction simulations involving large translation and contact. In *Conference on Isogeometric Analysis and Applications*, pages 39–56. Springer, 2018.

[196] M. Hirschhorn, V. Tchantchaleishvili, R. Stevens, J. Rossano, and A. Throckmorton. Fluid–structure interaction modeling in cardiovascular medicine–A systematic review 2017–2019. *Medical engineering & physics*, 78:1–13, 2020.

[197] C. Hirt, A. Amsden, and J. Cook. An arbitrary Lagrangian-Eulerian computing method for all flow speeds. *Journal of computational physics*, 14(3):227–253, 1974.

[198] G. Holzapfel. *Nonlinear Continuum Mechanics - A Continuum Approach for Engineering.* John Wiley and Sons, 2000.

[199] N. Hosters. *Spline-based methods for fluid-structure interaction.* PhD thesis, RWTH Aachen University, 2018.

[200] N. Hosters, J. Helmig, A. Stavrev, M. Behr, and S. Elgeti. Fluid–structure interaction with NURBS-based coupling. *Computer Methods in Applied Mechanics and Engineering*, 332:520–539, 2018.

[201] J. Houbolt. A recurrence matrix solution for the dynamic response of elastic aircraft. *Journal of the Aeronautical Sciences*, 17(9):540–550, 1950.

[202] J. Hron and S. Turek. A monolithic FEM solver for an ALE formulation of fluid-structure interaction with configuration for numerical benchmarking. *European Conference on Computational Fluid Dynamics ECCOMAS CFD*, 2006.

[203] M.-C. Hsu and Y. Bazilevs. Blood vessel tissue prestress modeling for vascular fluid–structure interaction simulation. *Finite Elements in Analysis and Design*, 47 (6):593–599, 2011.

[204] H. H. Hu, N. Patankar, and M. Zhu. Direct Numerical Simulations of Fluid–Solid Systems Using the Arbitrary Lagrangian-Eulerian Technique. *Journal of Computational Physics*, 169(2):427 – 462, 2001.

[205] B. Hübner, E. Walhorn, and D. Dinkler. A monolithic approach to fluid–structure interaction using space–time finite elements. *Computer Methods in Applied Mechanics and Engineering*, 193(23):2087 – 2104, 2004.

[206] T. Hughes. *The finite element method: linear static and dynamic finite element analysis*. Courier Corporation, 1987.

[207] T. Hughes, W. Liu, and T. Zimmermann. Lagrangian-Eulerian finite element formulation for incompressible viscous flows. *Computer Methods in Applied Mechanics and Engineering*, 29(3):329–349, 1981.

[208] T. Hughes, L. Franca, and M. Balestra. A new finite element formulation for computational fluid dynamics: V. Circumventing the babuska-brezzi condition: a stable Petrov-Galerkin formulation for the Stokes problem accommodating equal-order interpolations. *Computational Methods in Applied Mathematics*, 59:85–99, 1986.

[209] T. Hughes, K. Takizawa, Y. Bazilevs, T. Tezduyar, and M.-C. Hsu. Computational cardiovascular analysis with the variational multiscale methods and isogeometric discretization. In *Parallel Algorithms in Computational Science and Engineering*, pages 151–193. Springer, 2020.

[210] S. Hussain, F. Schieweck, and S. Turek. An efficient and stable finite element solver of higher order in space and time for nonstationary incompressible flow. *International Journal for Numerical Methods in Fluids*, 73(11):927–952, 2013.

[211] M. Igelbüscher. *Mixed and Hybrid Finite Element Formulations in Solid Mechanics - Application and Analysis for Nonlinearities*. PhD thesis, 2021.

[212] M. Igelbüscher, J. Schröder, and A. Schwarz. A mixed least-squares finite element formulation with explicit consideration of the balance of moment of momentum, a numerical study. *GAMM-Mitteilungen*, 43(2):e202000009, 2020.

[213] J. Janela, A. Moura, and A. Sequeira. A 3D non-Newtonian fluid–structure interaction model for blood flow in arteries. *Journal of Computational and applied Mathematics*, 234(9):2783–2791, 2010.

[214] J. Jansson, N. Degirmenci, and J. Hoffman. Adaptive unified continuum FEM modeling of a 3D FSI benchmark problem. *International journal for numerical methods in biomedical engineering*, 33(9):e2851, 2017.

[215] S. Jeong and E. Lee. Weighted norm least squares finite element method for Poisson equation in a polyhedral domain. *Journal of Computational and Applied Mathematics*, 299:35–49, 2016.

[216] D. Jespersen. A least-squares decomposition method for solving elliptic equations. *Math. Comp.*, 31:873–880, 1977.

[217] B.-N. Jiang. A least-squares finite element method for incompressible Navier-Stokes problems. *International Journal for Numerical Methods in Fluids*, 14:843–859, 1992.

[218] B.-N. Jiang. Non-Oscillatory and Non-Diffusive Solution of Convection Problems by the Iteratively Reweighted Least-Squares Finite Element Method. *Journal of Computational Physics*, 105:108–121, 1993.

[219] B.-N. Jiang. *The least-squares finite element method, Scientific Computation.* Springer-Verlag, Berlin, 1998.

[220] B.-N. Jiang and C. Chang. Least-squares finite elements for the Stokes problem. *Computational Methods in Applied Mathematics*, 78:297–311, 1990.

[221] B.-N. Jiang, T. Lin, and L. Povinelli. Large-scale computation of incompressible viscous flow by least-squares finite element method. *Computational Methods in Applied Mathematics*, 114:213–231, 1994.

[222] V. John and J. Rang. Adaptive time step control for the incompressible Navier–Stokes equations. *Computer Methods in Applied Mechanics and Engineering*, 199 (9-12):514–524, 2010.

[223] V. John, G. Matthies, and J. Rang. A comparison of time-discretization/linearization approaches for the incompressible Navier-Stokes Equations. *Computer Methods in Applied Mechanics and Engineering*, 195: 5995–6010, 2006.

[224] A. Johnson and T. Tezduyar. Mesh update strategies in parallel finite element computations of flow problems with moving boundaries and interfaces. *Computer methods in applied mechanics and engineering*, 119(1-2):73–94, 1994.

[225] C. Johnson, R. Rannacher, and M. Boman. Numerics and hydrodynamic stability: toward error control in computational fluid dynamics. *SIAM Journal on Numerical Analysis*, 32(4):1058–1079, 1995.

[226] D. Kay, P. Gresho, D. Griffiths, and D. Silvester. Adaptive time-stepping for incompressible flow part II: Navier–Stokes equations. *SIAM Journal on Scientific Computing*, 32(1):111–128, 2010.

[227] O. Kayser-Herold. *Least-Squares Methods for the Solution of Fluid- Structure Interaction Problems.* Dissertation, Technischen Universität Braunschweig, 2006.

[228] O. Kayser-Herold and H. Matthies. Space-time adaptive solution of fluid-structure interaction problems. *In 2nd MIT Conference on Computational Fluid and Solid Mechanics, Amsterdam*, pages 1000–1004, 2003.

[229] O. Kayser-Herold and H. Matthies. Least-squares FEM, literature review. *Informatik-Bericht 2005-05, TU Braunschweig, Institut für Wissenschaftliches Rechnen*, 2005.

[230] O. Kayser-Herold and H. Matthies. Least squares finite element methods for fluid-structure interaction problems. *Computers and Structures*, 83:191–207, 2005.

[231] O. Kayser-Herold and H. Matthies. A unified least-squares formulation for fluid-structure interaction problems. *Computers and Structures*, 85:998–1011, 2007.

[232] H. B. Kim, J. R. Hertzberg, and R. Shandas. Development and validation of echo PIV. *Experiments in Fluids*, 36(3):455–462, 2004.

[233] N. Kim. *Spectral/hp Least-Squares Finite Element Analysis of Isothermal and Non-Isothermal Flows of Generalized Newtonian Fluids.* PhD thesis, Texas A&M University, 2019.

[234] N. Kim and J. Reddy. A spectral/hp least-squares finite element analysis of the Carreau–Yasuda fluids. *International Journal for Numerical Methods in Fluids*, 82 (9):541–566, 2016.

[235] N. Kim and J. Reddy. Least-squares finite element analysis of flow of a generalized Newtonian fluid past a circular cylinder. *Mechanics of Advanced Materials and Structures*, 25(14):1186–1196, 2018.

[236] N. Kim and J. Reddy. 3-D least-squares finite element analysis of flows of generalized Newtonian fluids. *Journal of Non-Newtonian Fluid Mechanics*, 266:143–159, 2019.

[237] N. Kim and J. Reddy. Least-squares finite element analysis of three-dimensional natural convection of generalized Newtonian fluids. *International Journal for Numerical Methods in Fluids*, 93(4):1292–1307, 2021.

[238] S. Kim, T. Manteuffel, and S. McCormick. First-Order System Least Squares (FOSLS) For Spatial Linear Elasticity: Pure Traction. *SIAM Journal on Numerical Analysis*, 38:1454–1482, 2000.

[239] P. Kjellgren and J. Hyvärinen. An Arbitrary Lagrangian-Eulerian finite element method. *Computational Mechanics*, 21(1):81–90, 1998.

[240] J. Korelc. Automatic generation of finite-element code by simultaneous optimization of expressions. *Theoretical Computer Science*, 187(1):231–248, 1997.

[241] J. Korelc. Multi-language and multi-environment generation of nonlinear finite element codes. *Engineering with Computers*, 18(4):312–327, 2002.

[242] J. Korelc. Automation of primal and sensitivity analysis of transient coupled problems. *Computational Mechanics*, 44:631–649, 10 2009. doi: 10.1007/s00466-009-0395-2.

[243] J. Korelc and P. Wriggers. *Automation of Finite Element Methods.* Springer International Publishing Switzerland, 2016.

[244] D. Krige. A statistical approach to some basic mine valuation problems on the witwatersrand. *Journal of the Southern African Institute of Mining and Metallurgy*, 52(6):119–139, 1951.

[245] J. Krishnan, A. Deshpande, and P. Kumar. *Rheology of complex fluids.* Springer, 2010.

[246] D. N. Ku, D. P. Giddens, C. K. Zarins, and S. Glagov. Pulsatile flow and atherosclerosis in the human carotid bifurcation. Positive correlation between plaque location and low oscillating shear stress. *Arteriosclerosis*, 5(3):293–302, May-Jun 1985.

[247] U. Küttler, M. Gee, C. Förster, A. Comerford, and W. A. Wall. Coupling strategies for biomedical fluid - structure interaction problems. *International Journal in Biomedical Engineering*, 26:305–321, 2010.

[248] J. Kwack and A. Masud. A stabilized mixed finite element method for shear-rate dependent non-Newtonian fluids: 3D benchmark problems and application to blood flow in bifurcating arteries. *Computational Mechanics*, 53(4):751–776, 2014.

[249] O. A. Ladyzhenskaya. *The mathematical theory of viscous incompressible flow*, volume 2. Gordon and Breach New York, 1969.

[250] J. Lai and J. Huang. An adaptive linear time stepping algorithm for second-order linear evolution problems. *Int. J. Numer. Anal. Mod*, 12(2):230–253, 2015.

[251] J. Lai, J. Huang, and C. Chen. Vibration Analysis of Plane Elasticity Problems by the C0-Continuous Time Stepping Finite Element Method. *Applied Numerical Mathematics*, 59(5):905–919, 2009.

[252] W. Lai, D. Rubin, and E. Krempl. *Introduction to Continuum Mechanics.* Elsevier Science, 2012.

[253] M. Landajuela, M. Vidrascu, D. Chapelle, and M. Fernández. Coupling schemes for the FSI forward prediction challenge: comparative study and validation. *International journal for numerical methods in biomedical engineering*, 33(4):e2813, 2017.

[254] U. Langer and H. Yang. Numerical simulation of fluid–structure interaction problems with hyperelastic models: A monolithic approach. *Mathematics and Computers in Simulation*, 145:186–208, 2018.

[255] P. Le Tallec and J. Mouro. Fluid structure interaction with large structural displacements. *Computer methods in applied mechanics and engineering*, 190(24-25): 3039–3067, 2001.

[256] H. Lee. A nonlinear weighted least-squares finite element method for the Oldroyd-B viscoelastic flow. *Applied Mathematics and Computation*, 219:42–434, 2012.

[257] H. Lee. An adaptively refined least-squares finite element method for generalized Newtonian fluid flows using the Carreau model. *SIAM Journal on Scientific Computing*, 36:193–218, 2014.

[258] H. Lee. Weighted least-squares finite element methods for the linearized Navier-Stokes equations. *International Journal of Computer Mathematics*, 91:1964–1985, 2014.

[259] H. Lee. A nonlinear weighted least-squares finite element method for the Carreau–Yasuda non-Newtonian model. *Journal of Mathematical Analysis and Applications*, 432(2):844 – 861, 2015.

[260] H. Lee and T. Chen. A nonlinear weighted least-squares finite element for Stokes equations. *Journal of Computational and Applied Mathematics*, 59:215–224, 2010.

[261] S.-H. Lee, S.-K. Youn, J.-H. Yeon, and B.-N. Jiang. A study on the fluid-structure interaction using LSFEM, 2000.

[262] P. Leyland, V. Carstens, F. Blom, and T. Tefy. Fully coupled fluid-structure algorithms for aeroelasticity and forced vibration induced flutter: Applications to a compressor cascade. *Revue Européenne des Éléments Finis*, 9(6-7):763–803, 2000.

[263] P. Lynn and S. Arya. Use of the least squares criterion in the finite element formulation. *International Journal for Numerical Methods in Engineering*, 6:75–88, 1973.

[264] P. Lynn and S. Arya. Finite elements formulated by the weighted discrete least squares method. *International Journal for Numerical Methods in Engineering*, 8: 71–90, 1974.

[265] M. Majidi and G. Starke. Least-Squares Galerkin Methods for Parabolic Problems I: Semidiscretization in Time. *SIAM Journal on Numerical Analysis*, 39(4):1302–1323, 2002.

[266] M. Majidi and G. Starke. Least-Squares Galerkin Methods for Parabolic Problems II: The Fully Discrete Case and Adaptive Algorithms. *SIAM Journal on Numerical Analysis*, 39(5):1648–1666, 2002.

[267] M. Make. *Spline-based methods for aerothermoelastic problems.* PhD thesis, Rheinisch-Westfälische Technische Hochschule Aachen, 2021.

[268] M. Make, T. Spenke, N. Hosters, and M. Behr. Spline-based space-time finite element approach for fluid-structure interaction problems with a focus on fully enclosed domains. *Computers & Mathematics with Applications*, 114:210–224, 2022.

[269] L. Malvern. *Introduction to the mechanics of a continuous medium.* Prentice-Hall, Inc., Englewood Cliffs, New Jersey, 1969.

[270] T. Manteuffel, S. McCormick, J. Schmidt, and C. Westphal. First-order system least squares (FOSLS) for geometrically nonlinear elasticity. *SIAM Journal on Numerical Analysis*, 44:2057–2081, 2006.

[271] M. Marino, M. von Hoegen, J. Schröder, and P. Wriggers. Direct and inverse identification of constitutive parameters from the structure of soft tissues. part 1: micro-and nanostructure of collagen fibers. *Biomechanics and Modeling in Mechanobiology*, 17: 1011–1036, 2018.

[272] J. Marsden and J. Hughes. *Mathematical Foundations of Elasticity.* Prentice-Hall, 1983.

[273] G. Matheron. Principles of geostatistics. *Economic Geology*, 58(8):1246–1266, 12 1963.

[274] H. Matthies, R. Niekamp, and J. Steindorf. Algorithms for strong coupling procedures. *Computer methods in applied mechanics and engineering*, 195(17-18):2028–2049, 2006.

[275] H. G. Matthies and J. Steindorf. Partitioned strong coupling algorithms for fluid–structure interaction. *Computers & Structures*, 81(8):805 – 812, 2003.

[276] J. Maxwell. On the dynamical theory of gases. *Philosophical transactions of the Royal Society of London*, (157):49–88, 1867.

[277] M. Mayr. *A Monolithic Solver for Fluid-Structure Interaction with Adaptive Time Stepping and a Hybrid Preconditioner.* Dissertation, Technische Universität München, München, 2016.

[278] M. Mayr, T. Klöppel, W. A. Wall, and M. Gee. A temporal consistent monolithic approach to fluid-structure interaction enabling single field predictors. *SIAM Journal on Scientific Computing*, 37(1):B30–B59, 2015.

[279] M. Mayr, W. Wall, and M. Gee. Adaptive time stepping for fluid-structure interaction solvers. *Finite Elements in Analysis and Design*, 141:55–69, 2018.

[280] C. Michler, S. Hulshoff, E. Van Brummelen, and R. De Borst. A monolithic approach to fluid–structure interaction. *Computers & Fluids*, 33(5-6):839–848, 2004.

[281] A. Montlaur, S. Fernandez-Mendez, and A. Huerta. High-order implicit time integration for unsteady incompressible flows. *International Journal for Numerical Methods in Fluids*, 70(5):603–626, 2012.

[282] B. Müller. *Mixed least squares finite element methods based on inverse stress-strain relations in hyperelasticity.* PhD thesis, Duisburg, Essen, Universität Duisburg-Essen, Diss., 2015, 2015.

[283] B. Müller and G. Starke. Stress-based finite element methods in linear and nonlinear solid mechanics. In J. Schröder and P. Wriggers, editors, *Advanced Finite Element Technologies*, CISM Courses and Lectures. Springer, 2015.

[284] B. Müller, G. Starke, A. Schwarz, and J. Schröder. A first-order system least squares method for hyperelasticity. *SIAM Journal on Scientific Computing*, 36(5):B795–B816, 2014.

[285] S. Münzenmaier. First-Order system least squares for generalized-Newtonian coupled Stokes-Darcy flow. *Numerical Methods for Partial Differential Equations*, 31 (4):1150–1173, 2015.

[286] S. Münzenmaier and G. Starke. First-order system least squares for coupled Stokes-Darcy flow. *SIAM Journal on Numerical Analysis*, 49:387–404, 2011.

[287] K. Namkoong, H. Choi, and J. Yoo. Computation of dynamic fluid–structure interaction in two-dimensional laminar flows using combined formulation. *Journal of Fluids and Structures*, 20:51–69, 2005.

[288] H. Nayak and G. Carey. Least square finite element simulation of viscoelastic fluid flow through 4:1 contraction. Technical report, Institute for Computational Engineering and Science, The University of Texas at Austin, 2003.

[289] M. Neunteufel and J. Schöberl. Fluid-structure interaction with H(div)-conforming finite elements. *Computers & Structures*, 243:106402, 2021.

[290] N. M. Newmark. *A method of computation for structural dynamics.* American Society of Civil Engineers, 1959.

[291] H. Nguyen and J. Reynen. A space-time least-square finite element scheme for advection-diffusion equations. *Computer Methods in Applied Mechanics and Engineering*, 42(3):331–342, 1984.

[292] M. Nickaeen. *Efficient FEM and Multigrid Solvers for the Least-Squares Method with Application to Non-Newtonian Fluid Flow.* PhD thesis, Technische Universität Dortmund, 2013.

[293] M. Nickaeen, A. Ouazzi, and S. Turek. Newton multigrid least-squares FEM for the V-V-P formulation of the Navier-Stokes equations. *Journal of Computational Physics*, 256:416–427, 2014.

[294] C. Nisters. *Least-squares finite element methods with applications in fluid and solid mechanics.* PhD thesis, 2018.

[295] C. Nisters and A. Schwarz. Efficient stress-velocity least-squares finite element formulations for the incompressible Navier-Stokes equations. *Computer Methods in Applied Mechanics and Engineering*, 341:333 – 359, 2018.

[296] C. Nisters, A. Schwarz, K. Steeger, and J. Schröder. A stress-velocity least-squares mixed finite element formulation for incompressible elastodynamics. *Proceedings in Applied Mathematics and Mechanics*, 15:217–218, 2015.

[297] C. Nisters, A. Schwarz, S. Averweg, and J. Schröder. *Remarks on a Fluid-Structure Interaction Scheme Based on the Least-Squares Finite Element Method at Small Strains*, pages 261–279. Springer International Publishing, Cham, 2018. ISBN 978-3-319-70563-7.

[298] W. Noll. The Foundations of Classical Mechanics in the Light of Recent Advances in Continuum Mechanics. *Studies in logic and the foundations of mathematics*, 27: 31–47, 1974.

[299] J. Oldroyd. On the formulation of rheological equations of state. *Proceedings of the Royal Society of London. Series A. Mathematical and Physical Sciences*, 200(1063): 523–541, 1950.

[300] M. Oliver and R. Webster. *Basic Steps in Geostatistics: The Variogram and Kriging.* 2015.

[301] W. Ostwald. Ueber die rechnerische Darstellung des Strukturgebietes der Viskosität. *Kolloid-Zeitschrift*, 47:176–187, 1929.

[302] K. Park and C. Felippa. *Partitioned analysis of coupled systems*, chapter 3. North Holland, 1983.

[303] D. Pathria. The correct formulation of intermediate boundary conditions for runge–kutta time integration of initial boundary value problems. *SIAM Journal on Scientific Computing*, 18(5):1255–1266, 1997. ISSN 1064-8275.

[304] G. Pena and C. Prud'homme. Construction of a high order fluid–structure interaction solver. *Journal of Computational and Applied Mathematics*, 234(7):2358–2365, 2010.

[305] P. Perrochet and P. Azérad. Space-Time Integrated Least-Squares: Solving a Pure Advection Equation with a Pure Diffusion Operator. *Journal of Computational Physics*, 117(2):183–193, 1995.

[306] P.-O. Persson, J. Peraire, and J. Bonet. A High Order Discontinuous Galerkin Method for Fluid-Structure Interaction. *Collection of Technical Papers - 18th AIAA Computational Fluid Dynamics Conference*, 2007.

[307] N. Phan-Thien and R. Tanner. A new constitutive equation derived from network theory. *Journal of Non-Newtonian Fluid Mechanics*, 2(4):353–365, 1977.

[308] S. Piperno, C. Farhat, and B. Larrouturou. Partitioned procedures for the transient solution of coupled aroelastic problems Part I: Model problem, theory and two-dimensional application. *Computer Methods in Applied Mechanics and Engineering*, 124(1):79 – 112, 1995.

[309] J. Pontaza. *Least-squares variational principles and the finite element method: theory, form, and model for solid and fluid mechanics.* PhD thesis, Texas A&M University, 2003.

[310] J. Pontaza. Least-squares variational principles and the finite element method: theory, formulations, and models for solid and fluid mechanics. *Finite Elements in Analysis and Design*, 41(7-8):703–728, 2005.

[311] J. Pontaza. A least-squares finite element form for unsteady incompressible flows with improved velocity-pressure coupling. *Journal of Computational Physics*, 217: 563–588, 2006.

[312] J. Pontaza and J. Reddy. Spectral/*hp* least-squares finite element formulation for the Navier-Stokes equation. *Journal of Computational Physics*, 190:523–549, 2003.

[313] J. Pontaza and J. Reddy. Space-time coupled spectral/*hp* least-squares finite element formulation for the incompressible Navier-Stokes equation. *Journal of Computational Physics*, 197:418–459, 2004.

[314] J. Pontaza and J. Reddy. Least-squares finite element formulations for viscous incompressible and compressible fluid flows. *Computer Methods in Applied Mechanics and Engineering*, 195(19-22):2454–2494, 2006.

[315] M. Proot and M. Gerritsma. Mass- and momentum conservation of the least-squares spectral element method for the Stokes problem. *Journal of Computational Physics*, 27:389–401, 2006.

[316] P. Rajaraman, T. Manteuffel, M. Belohlavek, E. McMahon, and J. Heys. Echocardiographic particle imaging velocimetry data assimilation with least square finite element methods. *Computers & Mathematics with Applications*, 68(11):1569–1580, 2014.

[317] P. Rajaraman, T. A. Manteuffel, M. Belohlavek, and J. Heys. Combining existing numerical models with data assimilation using weighted least-squares finite element methods. *International Journal for Numerical Methods in Biomedical Engineering*, 33(1):e02783, 2017.

[318] J. Rang. Design of DIRK schemes for solving the Navier-Stokes equations. Technical report, TU Braunschweig, Braunschweig, 2007.

[319] J. Rang. Adaptive timestep control for the generalised-$\alpha$ method. In C. T. J. P. Moitinho de Almeida, P. Diez and N. Pares, editors, *VI International Conference on Adaptive Modeling and Simulation*, pages 559–570, 2013.

[320] R. Rannacher. Finite element methods for the incompressible Navier-Stokes equations. In G. P. Galdi and R. Rannacher, editors, *Fundamental directions in mathematical fluid mechanics*, pages 191–293. 2000. ISBN 3-7643-6414-9 and 978-3-7643-6414-4.

[321] C. Rasmussen. *Least-squares finite element formulation for fluid-structure interaction.* PhD thesis, Air Force Institute of Technology Air University, 2009.

[322] C. Rasmussen, R. Canfield, and J. Reddy. The Least-Squares Finite Element Method Applied to Fluid-Structure Interaction Problems. In *8th AIAA/ASME/ASCE/AHS/ASC Structures, Structural Dynamics, and Materials Conference*, 2007.

[323] C. Rasmussen, R. Canfield, and J. Reddy. Advantages and Disadvantages of a Simultaneously Coupled Least-Squares Finite Element Formulation for Fluid-Structure Interaction. In *12th AIAA/ISSMO Multidisciplinary Analysis and Optimization Conference*, 2008.

[324] P.-A. Raviart and J. Thomas. A mixed finite element method for 2-nd order elliptic problems. Mathematical aspects of finite element methods. In *Mathematical aspects of finite element methods*, pages 292–315. Springer-Verlag New York, 1977.

[325] P. J. Rayner, A. M. Michalak, and F. Chevallier. Fundamentals of data assimilation applied to biogeochemistry. *Atmospheric Chemistry and Physics*, 19(22):13911–13932, 2019.

[326] J. Reddy. *An introduction to continuum mechanics.* Cambridge university press, 2013.

[327] T. Richter. Numerical methods for fluid-structure interaction problems. *Institute for Applied Mathematics, University of Heidelberg, Germany*, 2010.

[328] T. Richter. A monolithic geometric multigrid solver for fluid-structure interactions in ALE formulation. *International journal for numerical methods in engineering*, 104(5):372–390, 2015.

[329] T. Richter. *Fluid-Structure Interactions: Models, Analysis and Finite Elements.* Springer Publishing Company, Incorporated, 2017. ISBN 3319639692.

[330] R. Rivlin. Large elastic deformations of isotropic materials II. some uniqueness theorems for pure homogeneous deformation. *Philosophical Transactions of the Royal Society*, 240:491–508, 1948.

[331] S. Rothe, A.-W. Hamkar, K. Quint, and S. Hartmann. Comparison of diagonal-implicit, linear-implicit and half-explicit runge–kutta methods in non-linear finite element analyses. *Archive of Applied Mechanics*, 82(8):1057–1074, 2012.

[332] S. Rugonyi and K. Bathe. On finite element analysis of fluid flows fully coupled with structural interactions. *CMES - Computer Modeling in Engineering and Sciences*, 2(2):195–212, 2001. ISSN 1526-1492.

[333] P. Sackinger, P. Schunk, and R. Rao. A newton–raphson pseudo-solid domain mapping technique for free and moving boundary problems: a finite element implementation. *Journal of Computational Physics*, 125(1):83–103, 1996.

[334] E. Salonen and J. Freund. Weighting in the least squares finite element method. In H. Mang, F. Rammerstorfer, and J. Eberhardsteiner, editors, *Proceedings of the Fifth World Congress on Comput Mech*, number 5. Vienna University of Technology, Austria, 2002.

[335] B. Sanderse and B. Koren. Accuracy analysis of explicit Runge-Kutta methods applied to the incompressible Navier-Stokes equations. *Journal of Computational Physics*, 231:3041–3063, 2012.

[336] P. Saramito. *Complex fluids.* Springer, 2016.

[337] S. Sathe and T. Tezduyar. Modeling of fluid–structure interactions with the space–time finite elements: contact problems. *Computational Mechanics*, 43(1):51–60, 2008.

[338] M. Schäfer, S. Turek, F. Durst, E. Krause, and R. Rannacher. Benchmark computations of laminar flow around a cylinder. In *Flow simulation with high-performance computers II*, pages 547–566. Springer, 1996.

[339] A. Schleupen and E. Ramm. Local and global error estimations in linear structural dynamics. *Computers & Structures*, 76(6):741–756, 2000.

[340] P. Schreurs, F. Veldpaus, and W. Brekelmans. Simulation of forming processes, using the arbitrary Eulerian-Lagrangian formulation. *Computer methods in applied mechanics and engineering*, 58(1):19–36, 1986.

[341] J. Schröder, A. Schwarz, and K. Steeger. *Adavanced Finite Element Technologies*, chapter Least-squares finite element formulations for isotropic and anisotropic elasticity at small and large strains, pages 131–175. CISM Courses and Lectures. Springer, 2016.

[342] W. Schröder. *Notes on numerical fluid mechanics and multidisciplinary design, Summary of Flow Modulation and Fluid-Structure Interaction Findings*, volume 109. Springer-Verlag, Berlin, 2010.

[343] R. Schussnig and T. Fries. Coupled multiphysics modeling of aortic dissection. In *World Congress in Computational Mechanics and ECCOMAS Congress*, volume 400, 2021.

[344] R. Schussnig, D. Pacheco, and T. Fries. Efficient split-step schemes for fluid–structure interaction involving incompressible generalised Newtonian flows. *Computers & Structures*, 260:106718, 2022.

[345] A. Schwarz. *Least-Squares Mixed Finite Elements for Solid Mechanics.* Phd-thesis, University Duisburg-Essen, 2009.

[346] A. Schwarz and R. P. Dwight. Data Assimilation for Navier-Stokes using the Least-Squares Finite-Element Method. *International Journal for Uncertainty Quantification*, 8(5):383–403, 2018.

[347] A. Schwarz, J. Schröder, and K. Steeger. A Modified Least-Squares Finite Element Formulation for Small Strain Plasticity. *Proc. of ICCSM2009*, 2009.

[348] A. Schwarz, J. Schröder, and G. Starke. A modified Least-Squares Mixed Finite Element with Improved Momentum Balance. *International Journal for Numerical Methods in Engineering*, 81:286–306, 2010.

[349] A. Schwarz, J. Schröder, and G. Starke. A modified least-squares mixed finite element with improved momentum balance. *International Journal for Numerical Methods in Engineering*, 81:286–306, 2010.

[350] A. Schwarz, J. Schröder, G. Starke, and K. Steeger. Least-squares mixed finite elements for hyperelastic material models. In *Report of the Workshop 1207 at the "Mathematisches Forschungsinstitut Oberwolfach" entitled "Advanced Computational Engineering", organized by O. Allix, C. Carstensen, J. Schröder, P. Wriggers*, pages 470–472, 2012.

[351] A. Schwarz, K. Steeger, and J. Schröder. Weighted overconstrained least-squares mixed finite elements for static and dynamic problems in quasi-incompressible elasticity. *Computational Mechanics*, 54(3):603–612, 2014.

[352] A. Schwarz, M. Nickaeen, S. Serdas, C. Nisters, A. Ouazzi, J. Schröder, and S. Turek. A comparative study of mixed least-squares FEMs for the incompressible Navier-Stokes equations. *International Journal of Computational Engineering Science*, 17 (1), 2018.

[353] A. Schwarz, C. Nisters, S. Averweg, and J. Schröder. *Stress-Velocity Mixed Least-Squares FEMs for the Time-Dependent Incompressible Navier-Stokes Equations*, pages 137–144. Springer International Publishing, Cham, 2018. ISBN 978-3-319-73441-5.

[354] A. Schwarz, K. Steeger, M. Igelbüscher, and J. Schröder. Different approaches for mixed LSFEMs in hyperelasticity: Application of logarithmic deformation measures. *International Journal for Numerical Methods in Engineering*, 115(9):1138–1153, 2018.

[355] D. A. Serino, J. W. Banks, W. D. Henshaw, and D. W. Schwendeman. A stable added-mass partitioned (amp) algorithm for elastic solids and incompressible flow. *Journal of Computational Physics*, 399:108923, 2019.

[356] A. Shabana. *Computational Continuum Mechanics.* Cambridge University Press, 2008.

[357] A. Shamanskiy and B. Simeon. Mesh moving techniques in fluid-structure interaction: robustness, accumulated distortion and computational efficiency. *Computational Mechanics*, 67(2):583–600, 2021.

[358] L. Shampine and H. Watts. The art of writing a Runge-Kutta code. II. *Applied Mathematics and Computation*, 5(2):93–121, 1979.

[359] J. Sheldon, S. Miller, and J. Pitt. A hybridizable discontinuous Galerkin method for modeling fluid–structure interaction. *Journal of Computational Physics*, 326: 91–114, 2016.

[360] J. P. Sheldon, S. T. Miller, and J. S. Pitt. Methodology for comparing coupling algorithms for fluid-structure interaction problems. *World Journal of Mechanics*, 4 (02):54, 2014.

[361] J. P. Sheldon, S. T. Miller, and J. S. Pitt. An improved formulation for hybridizable discontinuous galerkin fluid-structure interaction modeling with reduced computational expense. *Communications in Computational Physics*, 24, 2018.

[362] G. Sieber. *Numerical Simulation of Fluid-Structure Interaction using loose coupling methods.* PhD thesis, Technische Universität, 2002.

[363] H. Sigloch. *Technische Fluidmechanik.* Springer Vieweg, Berlin, Heidelberg, 2017.

[364] J.-F. Sigrist. *Fluid-structure interaction: an introduction to finite element coupling.* John Wiley & Sons, 2015.

[365] P. Silvester. High-order polynomial triangular finite elements for potential problems. *International Journal of Engineering Science*, 7(8):849–861, 1969.

[366] G. Söderlind. Automatic control and adaptive time-stepping. *Numerical Algorithms*, 31(1):281–310, 2002.

[367] M. Souli and D. J. Benson. *Arbitrary Lagrangian Eulerian and Fluid-Structure Interaction: Numerical Simulation.* Wiley, 2013.

[368] A. Spencer. *Continuum mechanics.* Mineola, N.Y. : Dover Publications, 1980.

[369] G. Starke. Adaptive least squares finite element methods in elasto-plasticity. *Proccedings 7th International Conference on Large Scale Scientific Computations*, pages 676–682, 2009.

[370] G. Starke, B. Müller, A. Schwarz, and J. Schröder. Stress-displacement least squares mixed finite element approximation for hyperelastic materials. In *Report of the Workshop 1207 at the "Mathematisches Forschungsinstitut Oberwolfach" entitled "Advanced Computational Engineering", organized by O. Allix, C. Carstensen, J. Schröder, P. Wriggers*, pages 467–469, 2012.

[371] K. Steeger. *Least-squares mixed finite elements for geometrically nonlinear solid mechanics.* PhD thesis, 2017.

[372] K. Stein, T. Tezduyar, and R. Benney. Mesh moving techniques for fluid-structure interactions with large displacements. *Journal of Applied Mechanics*, 70:58–63, 2003.

[373] M. Stein. *Interpolation of Spatial Data: Some Theory For Kriging.* Springer, New York, 1999.

[374] J. Steindorf. *Partitionierte Verfahren für Probleme der Fluid-Struktur-Wechselwirkung.* PhD thesis, Mechanik-Zentrum, 2003.

[375] K. Subbaraj and M. Dokainish. A survey of direct time-integration methods in computational structural dynamics II. Implicit methods. *Computers and Structures*, 32(6):1387 – 1401, 1989.

[376] H. Suito, K. Takizawa, V. Huynh, D. Sze, and T. Ueda. Fsi analysis of the blood flow and geometrical characteristics in the thoracic aorta. *Computational mechanics*, 54 (4):1035–1045, 2014.

[377] K. Surana, M. Engelkemier, J. Reddy, and P. Tenpas. k-Version Least Squares Finite Element Processes for 2-D Generalized Newtonian Fluid Flows. *International Journal for Computational Methods in Engineering Science and Mechanics*, 8(4): 243–261, 2007.

[378] K. Surana, K. Deshpande, A. Romkes, and J. Reddy. Computations of Numerical Solutions in Polymer Flows Using Giesekus Constitutive Model in the hpk Framework with Variationally Consistent Integral Forms. *International Journal for Computational Methods in Engineering Science and Mechanics*, 10(5):317–344, 2009.

[379] K. Takizawa, T. Tezduyar, and R. Avsar. A low-distortion mesh moving method based on fiber-reinforced hyperelasticity and optimized zero-stress state. *Computational Mechanics*, 65(6), 2020.

[380] O. Talagrand and P. Courtier. Variational assimilation of meteorological observations with the adjoint vorticity equation. i: Theory. *Quarterly Journal of the Royal Meteorological Society*, 113(478):1311–1328, 1987.

[381] L. Tang and T. Tsang. A least-squares finite element method for time dependent incompressible flows with thermal convection. *International Journal for Numerical Methods in Fluids*, 17:271–289, 1993.

[382] L. Tang, T. Cheng, and T. Tsang. Transient solutions for three-dimensional lid-driven cavity flows by a least-squares finite element method. *International Journal for Numerical Methods in Fluids*, 21(5):413–432, 1995.

[383] L. Tang, J. Wright, and T. Tsang. Simulations of 2D and 3D thermocapillary flows by a least-squares finite element method. *International journal for numerical methods in fluids*, 28(6):983–1007, 1998.

[384] G. Taylor and A. Green. Mechanism of the production of small eddies from large ones. *Proceedings of the Royal Society of London. Series A - Mathematical and Physical Sciences*, 158(895):499–521, 1937.

[385] R. L. Taylor. On completeness of shape functions for finite element analysis. *International Journal for Numerical Methods in Engineering*, 4(1):17–22, 1972.

[386] T. Terahara, K. Takizawa, T. Tezduyar, Y. Bazilevs, and M.-C. Hsu. Heart valve isogeometric sequentially-coupled fsi analysis with the space–time topology change method. *Computational Mechanics*, 65(4):1167–1187, 2020.

[387] T. Tezduyar and S. Sathe. Modelling of fluid–structure interactions with the space–time finite elements: solution techniques. *International Journal for Numerical Methods in Fluids*, 54(6-8):855–900, 2007.

[388] T. Tezduyar, M. Behr, S. Mittal, and A. Johnson. Computation of unsteady incompressible flows with the stabilized finite element methods: Space-time formulations, iterative strategies and massively parallel implementations. *ASME PRESSURE VESSELS PIPING DIV PUBL PVP., NY(USA)*, 246:7–24, 1992.

[389] T. Tezduyar, S. Sathe, R. Keedy, and K. Stein. Space–time finite element techniques for computation of fluid–structure interactions. *Computer methods in applied mechanics and engineering*, 195(17-18):2002–2027, 2006.

[390] T. Tezduyar, S. Sathe, T. Cragin, B. Nanna, B. Conklin, J. Pausewang, and M. Schwaab. Modelling of fluid–structure interactions with the space–time finite elements: Arterial fluid mechanics. *International Journal for Numerical Methods in Fluids*, 54(6-8):901–922, 2007.

[391] T. Tezduyar, K. Takizawa, C. Moorman, S. Wright, and J. Christopher. Space–time finite element computation of complex fluid–structure interactions. *International Journal for Numerical Methods in Fluids*, 64(10-12):1201–1218, 2010.

[392] T. Tezduyar, K. Takizawa, and T. Kuraishi. Space–time computational FSI and flow analysis: 2004 and beyond. In *Current Trends and Open Problems in Computational Mechanics*, pages 537–544. Springer, 2022.

[393] C. Truesdell and W. Noll. The nonlinear field theories of mechanics. In S. Flügge, editor, *Encyclopedia of Physics*, number III/3. Springer, 1965.

[394] C. Truesdell and R. Toupin. The classical field theories. In S. Flügge, editor, *Encyclopedia of Physics*, number III/1. Springer, 1960.

[395] S. Turek. A comparative study of time-stepping techniques for the incompressible Navier-Stokes equations: from fully implicit non-linear schemes to semi-implicit projection methods. *International Journal for Numerical Methods in Fluids*, 22(10): 987–1011, 1996. ISSN 1097-0363.

[396] S. Turek and J. Hron. *Proposal for Numerical Benchmarking of Fluid-Structure Interaction between an Elastic Object and Laminar Incompressible Flow*, pages 371–385. Springer-Verlag Berlin Heidelberg, 2010.

[397] S. Turek, C. Becker, S. Kilian, M. Möller, S. Buijssen, D. Göddecke, M. Köster, R. Münster, H. Wobker, M. Geveler, D. Ribbrock, and P. Zajac. High performance finite elements, http://www.featflow.de/en/index.html.

[398] S. Turek, J. Hron, M. Madlik, M. Razzaq, H. Wobker, and J. Acker. Numerical simulation and benchmarking of a monolithic multigrid solver for fluid-structure interaction problems with application to hemodynamics. *Computational Science and Engineering*, 73:193–220, 2010.

[399] S. Turek, J. Hron, M. Razzaq, H. Wobker, and M. Schäfer. Numerical Benchmarking of Fluid-Structure Interaction: A Comparison of Different Discretization and Solution Approaches. In H.-J. Bungartz, M. Mehl, and M. Schäfer, editors, *Fluid Structure Interaction II*, pages 413–424, Berlin, Heidelberg, 2010. Springer Berlin Heidelberg.

[400] M. J. Turner, R. W. Clough, H. C. Martin, and L. J. Topp. Stiffness and deflection analysis of complex structures. *Journal of the aeronautical sciences*, 23(9):805–824, 1956.

[401] P. Underwood and K. Park. A variable-step central difference method for structural dynamics analysis-part 2. implementation and performance evaluation. *Computer methods in applied mechanics and engineering*, 23(3):259–279, 1980.

[402] V. Vallala, J. Reddy, and K. Surana. Alternative least-squares finite element models of Navier-Stokes equations for power-law fluids. *Engineering Computations*, 28:828–852, 2011.

[403] E. van Brummelen, K. van der Zee, and R. de Borst. Space/time multigrid for a fluid–structure-interaction problem. *Applied Numerical Mathematics*, 58(12):1951–1971, 2008.

[404] P. van Leeuwen. Efficient nonlinear data-assimilation in geophysical fluid dynamics. *Computers & Fluids*, 46(1):52–58, 2011.

[405] A. van Zuijlen and H. Bijl. A higher-order time integration algorithm for the simulation of nonlinear fluid-structure interaction. *Nonlinear Analysis: Theory, Methods & Applications*, 63(5-7):e1597–e1605, 2005.

[406] M. von Hoegen, M. Marino, J. Schröder, and P. Wriggers. Direct and inverse identification of constitutive parameters from the structure of soft tissues. part 2: dispersed arrangement of collagen fibers. *Biomechanics and Modeling in Mechanobiology*, 18: 897–920, 2019.

[407] H. Wackernagel. *Ordinary Kriging*, pages 79–88. Springer Berlin Heidelberg, Berlin, Heidelberg, 2003.

[408] W. Wall. *Fluid-Struktur-Interaktion mit stabilisierten Finiten Elementen.* PhD thesis, Universität Stuttgart, 1999.

[409] W. Wall, S. Genkinger, and E. Ramm. A strong coupling partitioned approach for fluid–structure interaction with free surfaces. *Computers & Fluids*, 36(1):169–183, 2007.

[410] W. A. Wall, A. Gerstenberger, P. Gamnitzer, C. Förster, and E. Ramm. *Large Deformation Fluid-Structure Interaction – Advances in ALE Methods and New Fixed Grid Approaches*, pages 195–232. Springer Berlin Heidelberg, Berlin, Heidelberg, 2006.

[411] M. Waseem. *Monolithic Weighted Least-Squares Finite Element Method for non-Newtonian Fluids with non-isothermal Effects.* PhD thesis, Technische Universität Dortmund, 2020.

[412] F. Wei, J. Westerdale, E. McMahon, M. Belohlavek, and J. Heys. Weighted least-squares finite element method for cardiac blood flow simulation with echocardiographic data. *Computational and Mathematical Methods in Medicine*, page 371315, 2012.

[413] J. Westerdale, M. Belohlavek, E. McMahon, P. Jiamsripong, J. Heys, and M. Milano. Flow velocity vector fields by ultrasound particle imaging velocimetry: in vitro comparison with optical flow velocimetry. *Journal of Ultrasound in Medicine*, 30 (2):187–195, 2011.

[414] F. White. *Viscous Fluid Flow.* McGraw-Hill Higher Education, 2nd edition, 1991.

[415] T. Wick. Fluid-structure interactions using different mesh motion techniques. *Comput. Struct.*, 89(13-14):1456–1467, 2011.

[416] T. Wick. Flapping and contact FSI computations with the fluid–solid interface-tracking/interface-capturing technique and mesh adaptivity. *Computational Mechanics*, 53(1):29–43, 2014.

[417] D. Wickert. *Least-Squares, Continuous Sensitivity Analysis for Nonlinear Fluid-Structure Interaction.* PhD thesis, Air Force Institute of Technology, AFIT Scholar, 2009.

[418] D. Wickert and R. Canfield. Least-Squares Continuous Sensitivity Analysis of an Example Fluid-Structure Interaction Problem. In *49th AIAA/ASME/ASCE/AHS/ASC Structures, Structural Dynamics, and Materials Conference*, 2008.

[419] D. Wickert, R. Canfield, and J. Reddy. Continuous Sensitivity Analysis of Fluid-Structure Interaction Problems Using Least-Squares Finite Elements. In *12th AIAA/ISSMO Multidisciplinary Analysis and Optimization Conference*, 2008.

[420] R. Williams, K. Burrage, I. Cameron, and M. Kerr. A four-stage index 2 diagonally implicit runge–kutta method. *Applied Numerical Mathematics*, 40(3):415–432, 2002.

[421] D. Winterscheidt and K. Surana. p-version least squares finite element formulation for two dimensional, incompressible fluid flow. *International Journal for Numerical Methods in Fluids*, 18:43–69, 1994.

[422] Wolfram Research Inc. Mathematica, Version 13.0.0. URL `https://www.wolfram.com/mathematica`. Champaign, IL, 2021.

[423] C. Wood, A. J. Gil, O. Hassan, and J. Bonet. A partitioned coupling approach for dynamic fluid–structure interaction with applications to biological membranes. *International Journal for Numerical Methods in Fluids*, 57(5):555–581, 2008.

[424] P. Wriggers. *Nonlinear Finite Element Methods.* Springer Berlin Heidelberg, 2008.

[425] Y. Wu and X. C. Cai. A fully implicit domain decomposition based ALE framework for three-dimensional fluid-structure interaction with application in blood flow computation. *Journal of Computational Physics*, 258:524–537, 2014.

[426] Z. Yang and D. Mavriplis. Higher-Order Time Integration Schemes for Aeroelastic Applications on Unstructured Meshes. *AIAA Journal*, 45(1):138–150, 2007.

[427] K. Yasuda, R. Armstrong, and R. Cohen. Shear flow properties of concentrated solutions of linear and star branched polystyrenes. *Rheologica Acta*, 20(2):163–178, 1981.

[428] P. Zavattieri, E. Dari, and G. BUSCAGLIA. Optimization strategies in unstructured mesh generation. *International Journal for Numerical Methods in Engineering*, 39 (12):2055–2071, 1996.

[429] S. Zhou and L. Hou. A weighted least-squares finite element method for phan-thien–tanner viscoelastic fluid. *Journal of Mathematical Analysis and Applications*, 436: 66–78, 2016.

[430] O. Zienkiewicz and A. Chan. Coupled problems and their numerical solution. In *Advances in computational nonlinear mechanics*, pages 139–176. Springer, 1989.

[431] O. Zienkiewicz and R. Taylor. *The Finite Element Method - Volume I: The Basis.* Butterworth Heinemann, 5th edition, 2000.

[432] O. Zienkiewicz and Y. Xie. A simple error estimator and adaptive time stepping procedure for dynamic analysis. *Earthquake engineering & structural dynamics*, 20 (9):871–887, 1991.

[433] O. Zienkiewicz, D. Owen, and K. Lee. Least square-finite element for elasto-static problems. Use of 'reduced' integration. *International Journal for Numerical Methods in Engineering*, 8:341–358, 1974.

[434] O. C. Zienkiewicz and Y. K. Cheung. *The Finite Element Method in Structural and Soild Mechanics.* McGraw Hill, London, 1967.

Der Lebenslauf ist in der Online-Version aus Gründen des Datenschutzes nicht enthalten.

## In dieser Schriftenreihe bisher erschienene Berichte:

| | |
|---|---|
| Nr. 1 (2004) | *Ein Modell zur Beschreibung finiter anisotroper elasto-plastischer Deformationen unter Berücksichtigung diskreter Rissausbreitung*, J. Löblein, Dissertation, 2004. |
| Nr. 2 (2006) | *Polyconvex Anisotropic Energies and Modeling of Damage applied to Arterial Walls*, D. Balzani, Dissertation, 2006. |
| Nr. 3 (2006) | *Kontinuumsmechanische Modellierung ferroelektrischer Materialien im Rahmen der Invariatentheorie*, H. Romanowski, Dissertation, 2006. |
| Nr. 4 (2007) | *Mehrskalen-Modellierung polykristalliner Ferroelektrika basierend auf diskreten Orientierungsverteilungsfunktionen*, I. Kurzhöfer, Dissertation, 2007. |
| Nr. 5 (2007) | *Proceedings of the First Seminar on the Mechanics of Multifunctional Materials*, J. Schröder, D.C. Lupascu, D. Balzani (Ed.), Tagungsband, 2007. |
| Nr. 6 (2008) | *Zur Modellierung und Simulation diskreter Rissausbreitungsvorgänge*, O. Hilgert, Dissertation, 2008. |
| Nr. 7 (2009) | *Least-Squares Mixed Finite Elements for Solid Mechanics*, A. Schwarz, Dissertation, 2009. |
| Nr. 8 (2010) | *Design of Polyconvex Energy Functions for All Anisotropy Classes*, V. Ebbing, Dissertation, 2010. |
| Nr. 9 (2012) | *Modeling of Electro-Mechanically Coupled Materials on Multiple Scales*, M.-A. Keip, Dissertation, 2012. |
| Nr. 10 (2012) | *Geometrical Modeling and Numerical Simulation of Heterogeneous Materials*, D. Brands, Dissertation, 2012. |
| Nr. 11 (2012) | *Modeling and simulation of arterial walls with focus on damage and residual stresses*, S. Brinkhues, Dissertation, 2012. |
| Nr. 12 (2014) | *Proceedings of the Second Seminar on the Mechanics of Multifunctional Materials*, J. Schröder, D.C. Lupascu, M.-A. Keip, D. Brands (Ed.), Tagungsband, 2014. |
| Nr. 13 (2016) | *Mixed least squares finite element methods based on inverse stress-strain relations in hyperelasticity*, B. Müller, Dissertation, 2016. |
| Nr. 14 (2016) | *Electromechanical Modeling and Simulation of Thin Cardiac Tissue Constructs*, R. Frotscher, Dissertation, 2016. |
| Nr. 15 (2017) | *Least-squares mixed finite elements for geometrically nonlinear solid mechanics*, K. Steeger, Dissertation, 2017. |

| | |
|---|---|
| Nr. 16 (2017) | *Scale-Bridging of Elasto-Plastic Microstructures using Statistically Similar Representative Volume Elements*, L. Scheunemann, Dissertation, 2017. |
| Nr. 17 (2018) | *Modeling of Self-healing Polymers and Polymeric Composite Systems*, S. Specht, Dissertation, 2017. |
| Nr. 18 (2018) | *Proceedings of the Third Seminar on the Mechanics of Multifunctional Materials*, J. Schröder, D.C. Lupascu, H. Wende, D. Brands (Ed.), Tagungsband, 2018. |
| Nr. 19 (2018) | *Least-squares finite element methods with applications in fluid and solid mechanics*, C. Nisters, Dissertation, 2018. |
| Nr. 20 (2018) | *A two-scale homogenization scheme for the prediction of magneto-electric product properties*, M. Labusch, Dissertation, 2018. |
| Nr. 21 (2019) | *Modeling the passive mechanical response of soft tissues: constitutive modeling approaches, efficient parameter selection and subsequent adjustments due to residual stresses*, M. von Hoegen, Dissertation, 2019 |
| Nr. 22 (2019) | *Constitutive modeling of female pelvic floor dysfunctions and reconstructive surgeries using prosthetic mesh implants*, A. Bhattarai, Dissertation, 2019 |
| Nr. 23 (2019) | *A contribution to stress-displacement based mixed galerkin finite elements for hyperelasticity*, N. Viebahn, Dissertation, 2019 |
| Nr. 24 (2020) | *Gefrier- und Auftauprozesse in gesättigten porösen Materialien - ein Modellierungskonzept im Rahmen der Theorie poröser Medien*, W.M. Bloßfeld, Dissertation, 2020 |
| Nr. 25 (2021) | *Electromechanical modelling and simulation of hiPSC-derived cardiac cell cultures*, A. Jung, Dissertation, 2021 |
| Nr. 26 (2021) | *Mixed and Hybrid Least-Squares FEM in Nonlinear Solid Mechanics*, M. Igelbüscher, Dissertation, 2021 |
| Nr. 27 (2023) | *The Material Point Method for dynamic Metal Processing*, S. Maassen, Dissertation, 2023 |